Joint Institute for Nuclear Research

FUNDAMENTAL INTERACTIONS & NEUTRONS, NUCLEAR STRUCTURE, ULTRACOLD NEUTRONS, RELATED TOPICS

XXVI International Seminar
on Interaction of Neutrons with Nuclei

Xi'an, China, May 28 – June 1, 2018

Proceedings of the Seminar

Dubna • 2019

Organized by

Frank Laboratory of Neutron Physics, JINR
The State Key Laboratory of Intense Pulsed Radiation Simulation and Effect, NINT, China
Shaanxi Key Laboratory of Advanced Nuclear Energy and Technology, XJTU, China

Organizing Committee

W. I. Furman (JINR, Russia), Honorary Chairman; *Lv Min* (Academician of CAS, China), Honorary Chairman; *Wang Naiyan* (Academician of CAS, CIAE, China), Honorary Chairman; *Hei Dongwei* (NINT, China), Co-Chairman; *Wang Sheng* (XJTU, China), Co-Chairman; *V. N. Shvetsov* (JINR, Russia), Co-Chairman; *E. Lychagin* (JINR, Russia); *Qiu Mengtong* (NINT, China); *Hu Huasi* (XJTU, China); *Song Zhaohui* (NINT, China); *Weng Xiufeng* (NINT, China)

The contributions are reproduced directly from the originals presented
by the Organizing Committee.

This collection of papers reflects the present state of neutron-aided investigations of the properties of the nucleus, including fundamental symmetries, properties of the neutron itself, neutron-excited reactions, and the parameters of the nucleus that determine the reaction cross section, as well as the latest theoretical development of all these problems. The works on experimental investigations in the physics of fission by neutrons of various energies are presented in great detail. The present state of experiments on the physics of ultracold neutrons and facilities to obtain them is described at length. The status achieved by now of the latest (from the viewpoint of technique) experiments and environment studies is covered as well.

В сборнике представлено современное состояние исследований свойств ядра с помощью нейтронов: фундаментальных симметрий и свойств самого нейтрона, возбуждаемых им реакций и параметров ядра, определяющих их сечения, а также последние теоретические разработки всех этих вопросов. Очень детально представлены работы по всем аспектам, связанным с экспериментальными исследованиями физики деления ядра нейтронами различных энергий. Достаточно полно описано современное состояние экспериментов по физике ультрахолодных нейтронов и установок для их получения, а также достигнутый к настоящему времени статус методически новейших экспериментов и результаты экологических исследований.

CONTENTS

Neutron Sources

Calculations, Methodical Aspects

Preface

The annual International Seminar on Interactions of Neutrons with Nuclei (ISINN-26) was held from May 28 to June 1 in Xi'an, the ancient capital of China. This year, for the first time ISINN-26 was jointly organized by its founder and long-term organizer – the Frank Laboratory of Neutron Physics (FLNP) of JINR, the Northwest Institute of Nuclear Technology (NINT), Xi'an Jiaotong University (XJTU) and the Chinese Radiation Physics Society (CRPS). The Seminar drew the attention of specialists from the major nuclear centers of China – the Institute of Nuclear Physics and Chemistry (INPC) of the Chinese Academy of Engineering Physics, the Chinese Institute for Radiation Protection (CIRP), the Chinese Institute of Atomic Energy (CIAE), the Institute of High Energy Physics (IHEP), universities of Lanzhou, Beijing, Sichuan and others. The Seminar brought together a large group of researchers from the JINR Member States, as well as from Egypt, Italy, Pakistan, the Republic of Korea, the United States, France and Japan. The scientific program of the Seminar included 23 invited talks, 47 oral presentations and 64 posters presented (for more details, see http://isinn.jinr.ru/past-isinns/isinn-26/program.html).

Opening the Conference, the co-chairman of the Organizing Committee, NINT Director Prof. Hei Dongwei pointed out that he was very pleased to see the participants of ISINN-26 in Xi'an, the capital of ancient China, which played an important role in history as a link between the West and the East. The co-chairman of the Seminar, FLNP Director V.N. Shvetsov, thanked his colleagues from China for the work done on the organization of ISINN-26 – a conference that every year for 26 years already has been gathering scientists from around the world. It was attended by about 170 people from 12 countries. The participants of the Seminar were greeted by the Head of the Department of International Cooperation and Exchange of XJTU, Prof. Liang Li and the Honorary Chairman of ISINN-26 W.I. Furman (JINR), who expressed the hope that the traditional exchange of knowledge between experienced and young researchers will continue. And the fact that the conference attracted a large number of young people means that neutron research has a future.

The first plenary sessions were opened with invited talks by W.I. Furman (FLNP JINR) ("Experimental and Theoretical Aspects of Nuclear Fission Induced by Resonance Neutrons"), V.N. Shvetsov ("Nuclear Planetology"), Tang Jingyu ("Status of CSNS and Back-n White Neutron Facility"), Giuseppe Tagliente ("The n_TOF Facility at CERN"), Peter Geltenbort ("Fundamental Neutron Physics at the ILL"), Ruan Xichao ("Progress of Neutron Reaction Data Measurements at CIAE"), Gong Jian ("Prospects for Studying Neutron Scattering in China").

The second day of the Seminar also included only plenary sessions with invited talks by A.I. Frank (FLNP JINR) "Group Delay Time and Neutron Optics", Yoshie Otake "RIKEN Accelerator-Driven Neutron Source, RANS and Neutron Application", S.A. Kulikov "Development of Neutron Detectors for the Spectrometers of the IBR-2 Reactor" and K. Mukhin "Cold Neutron Source for IBR-2 Reactor on Pelletized Mesitylene Beads". They were devoted both to problems of fundamental nuclear physics, and purely practical problems. Lively discussions were triggered by the reports on research using neutron-activation analysis, development of neutron detectors and an original cold moderator at the IBR-2M reactor of FLNP JINR.

The third and fourth days of the Seminar were held in the form of two parallel sessions and a joint 3-hour poster session. They covered a wide range of issues ranging from the violation of fundamental symmetries in nuclear fission to discussions of parameters of neutron sources on high-current proton accelerators operating in Russia and just recently put into operation in China, as well as experiments on them.

As usual, the session devoted to nuclear fission was very informative, featuring the reports by Yu.M. Chuvilskii (SINP MSU) ("Resonance Interference as a Common Origin of Pseudo-T-Noninvariant ROT Effect in Fission and other Neutron-Induced Reactions"), D. Berikov (FLNP

JINR) ("Measurement of T-Odd Effects in the Neutron-Induced Fission of ^{235}U at a Hot Source of Polarized Resonance Neutrons in Munich"), N. Carjan (FLNR JINR) ("Acceleration Induced Neutron Emission from Heavy Nuclei"), Zhiming Wang (Beijing University) ("Study of Five-Dimensional Potential-Energy Surfaces for Actinide Isotopes in the Double-Center Oscillator Model"), A.M. Vorobyev (RNC KI PNPI) ("Search for Scission Neutrons in the Measurements of Angular and Energy Distributions of Prompt Fission Neutrons for $^{233-235}$U, ^{239}Pu and ^{252}Cf"), and A.M. Gagarski (RNC KI PNPI) ("Angular Distributions and Anisotropy of Fission Fragments from Neutron-Induced Fission of ^{232}Th, $^{233,235,\,238}$U, ^{239}Pu, ^{nat}Pb and ^{209}Bi in Intermediate Energy Range 1–200 MeV").

Great interest was aroused by the reports devoted to the study of collinear cluster fission presented in the reports of Yu.V. Pyatkov (FLNR JINR) "Manifestation of Pear-Shaped Clusters in Collinear Cluster Tri-Partition (CCT)" and D.V. Kamanin (FLNR JINR) "Detailed Analysis of the Data Indicating True Quaternary Fission of Low Excited Actinides". Unusual properties of this exotic nuclear fission mode still trigger heated discussions and criticisms, which, in turn, initiate new experiments.

In other parallel sessions the reports made by V.N. Shvetsov on the results of the search for water on Mars by NASA's Curiosity rover using an instrument developed by the Space Research Institute of RAS with the participation of FLNP and LRB of JINR, and by Prof. Chaoqiang Huang (INPC) about neutron reflectometry studies at the CMRR research reactor were met with great interest. A large number of results were presented on the preparation of measurements and first experiments on the new Chinese pulsed neutron source CSNS (reports by Yonghao Chen, Taofeng Wang, Liying Zhang and Jie Bao) and at the spallation neutron source RADEX of INR RAS in Troitsk (report by D.V. Khliustin).

Lively discussions were sparked by the reports of E.V. Lychagin (FLNP JINR), Lv Ning (RFUE, China), Wenshou Zhang (NINT), Dongming Wang (University of Xi'an) and Li Xuesong (NINT) devoted to the development of promising experimental techniques. The wide geography of the speakers of the session dedicated to the application of neutron activation analysis in ecology and archeology inspired an active discussion of the presented results.

Many interesting talks were presented at the session devoted experiments with fast neutron. Long-term collaboration of FLNP group led by Yu.M. Gledenov, the team from NRC NUM (Ulaanbaatar) led by G. Khuukhenkhuu and the group from IHIP PU (Beijng) led by Guohui Zhang reported new results of (n,α)-reaction study. Xuesong Li from NINT reported on feasibility analysis of unfolding fast neutron spectrum by using (n, n'γ)-reaction.

During a three-hour poster session, there was an opportunity to discuss in detail a lot of interesting experiments performed by numerous young Chinese participants of the Seminar, as well as by researchers from other countries. Among them we note the talks of N. Fedorov (FLNP JINR) on new results obtained with tagged neutrons, Lv Ning (RFUE) about design and implementation of Matryoshka-type neutron spectrometer, D.N. Grozdanov (FLNP JINR) on use of resonance neutrons from IREN source for prompt NAA.

Summing up the results of the conference at the final plenary session, NINT Director Hei Dongwei and FLNP Director V.N. Shvetsov noted the success of the first experience of hosting the International Seminar on Interaction of Neutrons with Nuclei, ISINN-26 in China and expressed the hope for the implementation of plans for further joint organization and holding of future meetings of this series. This will help to strengthen and develop real cooperation between JINR and institutes and universities of China.

All ISINN-26 organizers are looking forward to the next ISINN meetings at Dubna and China.

Co-chairman of ISINN-26
V.N. Shvetsov

Neutrons Properties and Fundamental Interactions

Group Delay Time and Neutron Optics

A. Frank[1,*], V. Bushuev[2]

[1] *Frank Laboratory of Neutron Physics, Joint Institute for Nuclear Research, 141980, Dubna, Russia*
[2] *Lomonosov Moscow State University, 119991, Moscow, Russia*
frank@nf.jinr.ru

The concept of group delay time (GDT) was introduced into the theory by D. Bohm and E.P. Wigner as a measure of time shift of a wave packet interacting with a stationary potential structure. It was widely used in the analysis of a number of quantum problems, at the same time playing the role of some sort of "theoretical clock". Later on, A.I. Baz proposed to measure the time of scattering by the potential of a particle with a magnetic moment, calculating the precession angle in a magnetic field presets in the potential region. Subsequently, it became clear that neutron experiments enabled implementation of the Larmor clock based on the constant precession frequency, and the Larmor time measured by it was closely related to the GDT. In the case of neutron reflection from resonant multilayer structures, the GDT can be much longer than in the case of total reflection. Moreover, under certain circumstances, it can be negative. The latter can also be measured by the Larmor clock method. In addition, the GDT concept has proved useful for clarifying new aspects of neutron wave propagation in a refractive matter.

Introduction

The problem of interaction time in quantum mechanics has been the subject of intense discussion for many decades. Apparently, for the first time, the question of how much time a particle spends in the potential region was formulated in [1]. In the 50s, the concept 'interaction time' acquired its mathematical formulation in the works by L. Eisenbud [2], D. Bohm [3], and E.P. Wigner [4]. To date, the number of publications devoted to this problem has reached several dozens. In this paper, let us refer only to reviews [5, 6]. The diversity of opinions expressed in this discussion is largely due to differences in the definition of the physical clock or time measuring procedure.

A very common definition of interaction time going back to works [1–4] is the so-called group delay time (GDT), formerly often referred to as 'phase delay time'

$$\Delta t = \hbar \left(d\varphi / dE \right), \tag{1}$$

where φ is the phase shift of a plane wave passing between points *x1* and *x2* that enclose the area of interaction (potential). Formula (1) corresponds to the total time spent by the particle when passing between *x1* and *x2*, including delay τ associated with the interaction itself. Obviously, to determine the actual time of interaction, it is necessary to subtract the time of free propagation in the absence of potential.

An important step in the study of the issue was made in 1966 by A.I. Baz [7]. Referring to the problem of the time of particle scattering on a spherical potential with effective range r_0, he defined the quantum clock as follows: "Let us suppose that inside a

sphere $R > r_0$ there is an infinitely small homogeneous field B directed along the Z-axis, and for $r > R$ field B equals zero. Moreover, let us assume that the scattered particles have a spin $s=1/2$ and a magnetic moment $\mu=2s\mu$. Let the spin (and the magnetic moment) of the particles incident on the potential be polarized along the X-axis. If the particle enters sphere $r=R$, where field B is in effect, the magnetic moment begins to precess with the Larmor frequency

$$\omega_L = 2\mu B/\hbar. \tag{2}$$

Therefore, the spin of the particles scattered and gone beyond sphere $r=R$ will be rotated through a certain angle θ relative to its initial direction. One can calculate this angle and consequently find the average time spent inside the sphere $r=R$: $t(E) = \theta/\omega_L$».

The 'Larmor time' measured by such a clock has a close connection with the GDT. Indeed, the angle of the Larmor precession θ can be identified as phase difference $\Delta\varphi$ of the two wave function components corresponding to the two values of the spin projection on the Z-axis, which differ in values. According to A.I. Baz, having determined the time delay associated with the interaction as $\Delta t_L = \Delta\varphi/\omega_L$, and taking into account that in (2) $2\mu B=\Delta E$, we obtain $\Delta t_L = \hbar(\Delta\varphi/\Delta E)$ that coincides with (1) in the limit $B \to 0$.

V.F. Rybachenko used A.I. Baz's method to calculate the time during which the particle tunnels through the potential barrier [8]. Owing to works [7, 8], the term 'Larmor clock' has become deeply embedded in scientific literature.

Larmor clock and neutron spin echo

With a progress of a technique of neutron experiment, it has become possible to put the Larmor clock into practice. To measure the time of neutron interaction with an object by means of this method, the object should be placed in an area with a magnetic field, where the neutron spin should precess. We assume that the magnetic field is normal to the plane of the spin. Thus, the task is to measure the precession angle $\theta = \omega_L \cdot \tau$, where τ is the measured interaction time. In this case, the complete precession angle is determined by the time spent in the precession region $\Phi = \omega_L(t+\tau)$, where the time of flight $t = L/V$, V is the velocity, and L is the length of the region with the magnetic field. With a reasonable length L, time τ is several orders of magnitude shorter than time of flight t. The relative smallness of τ together with the requirement of practical measurability of phase θ imposes a lower limit on the Larmor frequency ω_L. Therefore, the $\omega_L t$ factor becomes sufficiently high. This means that in such a measurement it is necessary to ensure a very high degree of beam monochromatization, so that the dispersion of the Larmor phase was not too high: $\Delta\Phi_L = \omega_L t(\Delta v/v) \ll 1$. Otherwise, the beam will be depolarized and the measurements will become impossible. In practice, this requirement is difficult to meet, since the necessary degree of monochromatization leads to unacceptably great intensity loss.

The problem of monochromatization can be avoided by using the neutron spin echo method [9]. In this case, neutrons pass not one, but two precessing paths of the opposite precession direction successively. If the neutron velocity is constant all the way, the total Larmor phase becomes zero for all neutron velocities, provided

$$\int_{L_1} B d\ell = \int_{L_2} B d\ell \tag{3}.$$

The degree of monochromatization is limited only by the extent to which condition (3) can be fulfilled. Placing the sample in one of the precession path results in a phase change by $\omega_L \tau$.

Several experiments based on this idea were carried out using the spin-echo spectrometer of the Laue-Langevin Institute [10-12]. The Larmor clock method was applied applied to measure the time delay caused by the difference between the classic neutron velocity in vacuum and in a refractive medium. In this experiment, the time measurement error was 3.7×10^{-10} seconds, despite the fact that the total time of neutron flight through two regions with a field was 0.017 seconds, i.e. eight orders of magnitude longer. In addition, the time of Bragg reflection from a multilayer periodic structure and the time of tunneling at the resonance of a quasi-bound state in a three-layer structure analogous to a Fabry-Perot interferometer were measured. In these cases, the delay measured by the Larmor clock was about 10^{-7} seconds.
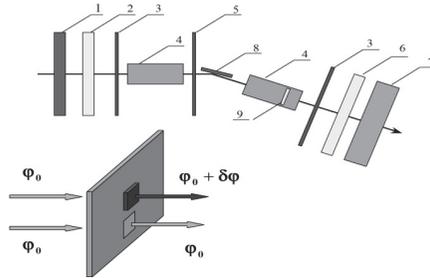
Fig.1. Design of the experiment on the measurement of the delay time of the sample passage, using the Larmor clock method. 1 – velocity selector, 2 - polarizer, 3 - $\pi/2$-flippers, 4 – precession solenoids, 5-π-flipper, 6 – analyzer of polarization, 7 – position-sensitive detector, 8 – multilayer mirror monochromator, 9 – sample location. Below is the position of the sample in one of the two beams shaped by the aperture.

Group delay time at reflection from resonant structures

The characteristic delay time of total neutron reflection is about several nanoseconds. To significantly increase the GDT in [13] it was proposed to reflect neutrons from multilayer structures. As a result of multiple interference and formation of standing waves in such structures, one can also speak of emergence of resonant modes.

Fig. 2 shows the calculation results for the neutron reflection from two three-layer Ni/Ti/Ni structures with the parameters indicated at the top. Structure 2 differs from structure 1 in the first and the third layers being swapped. In both cases, a sharp and sufficiently deep dip associated with excitation of the waveguide mode is observed on the reflection curve in the vicinity of 144 neV. For structure 1, the derivative of the phase has its maximum in this point, which corresponds to the GDT $\tau_{max} = 370$ ns. For structure 2, the reflection phase has a pronounced S-shaped form with a negative derivative in this region, which leads to a negative delay time with $\tau_{min} = -85$ ns. However, the negative value of the GDT does not contradict the principle of causality [14,15]. The two lower plots of Fig. 2 show the calculation results for the short-time pulse reflection — the Gaussian wave packet – from the same structures. It can be seen that in the case of the negative GDT (the right lower plot), the maximum of the reflected packet does slightly outpace the maximum of the incident flow. However, it occurs

due to a change in the pulse shape. The difference in the areas under the curves is obviously due to the neutron passage through the structure
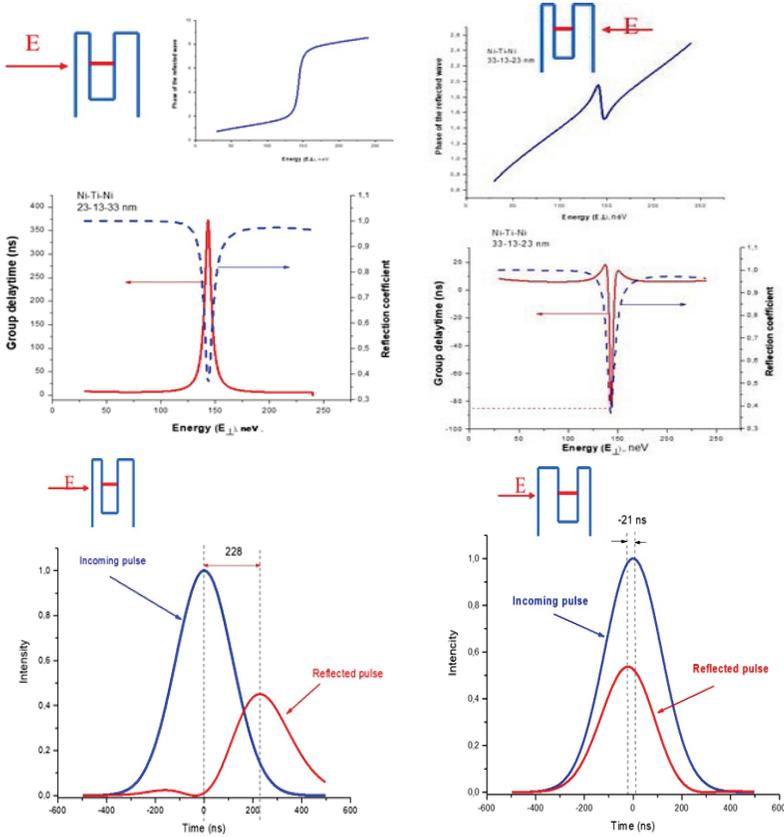
Fig.2. Above: reflection coefficient and the GDT for three-layer structures differing in the order of the layers. Below: relative magnitude and time relations between short wave packets incident and reflected from the same structures.

Group delay time and neutron velocity in a refractive substance

Above, we mentioned the measurement of the neutron GDT conditioned upon refraction in the sample. Let us consider this question in more detail. Suppose that a neutron passes through a refractive sample of length L with a refractive index $n(k_0)$. Let us define the medium dispersion law as $k = F(k_0^2)$ and calculate the neutron velocity in the medium $v = L/\tau$,

16

where τ is the time of passage through the sample. Using group time (1) as the latter and taking into account that the phase shift $\Delta\Phi$ can be obviously determined as $\Delta\Phi = kL$, for the velocity in the medium we obtain

$$v = \frac{\hbar}{2m}(F')^{-1},$$

(4)

where m is the neutron mass, and $F' = dF/d(k_o^2)$. Thus, the velocity in the medium depends not only on the refractive index n, but also on the medium dispersion law. From (4) it follows that by demanding fulfillment of $v = nv_0$, we immediately face the requirement $k^2 = k_0^2 + \chi^2$, where χ^2 is an arbitrary constant. Therefore, the relation that was considered as obvious turns out to be valid only for the potential dispersion law. For very slow neutrons, the following dispersion law form is valid:

$$k^2 = k_0^2 - 4\pi\rho b,$$

(5)

where ρ is the number of nuclei per unit volume, and b is the scattering length. Nevertheless, in the case of thermal neutrons, the form of the dispersion law may differ significantly [16].

The result is easily comprehended. Keeping in mind that the nature of the refractive index for any type of waves is associated with interference of primary and secondary waves generated by the scattering by nuclei inside the medium, it is natural to assume that the neutron in the medium is not a true particle, but a quasi-particle with an effective mass $m*$. Supposing that the neutron velocity is $v = \hbar k/m*$, we get the following relation from (4)

$$m* = 2mkF',$$

(6)

and for the potential dispersion law, $m* = m$ is valid. It also should be noted that from the proportionality of the effective mass of the dispersion function derivative, it follows that the mass itself can be negative. In a refractive medium, a negative effective mass can appear in the case of resonant behavior of the scattering amplitude.

References

1. L.A. MacColl, Phys. Rev. V.**40**, 621 (1932).
2. L. Eisenbud, Dissertation, Prinston, June 1948 (unpublished).
3. D. Bohm, in Quantum Theory, Prentice-Hall, New York, 1951. P.257–261.
4. E.P. Wigner, Phys. Rev., V. **98**, 145 (1955).
5. E.H. Hauge, J.A. Støvneng, Rev. Mod. Phys., V.**61**, 917 (1989).
6. R. Landauer, Th. Martin, Rev. Mod. Phys., V.**66**, 217 (1994).
7. A.I. Baz', Sov. J. Nucl. Phys., V.**4**, 182 (1987); Yad. Phys., V. **4**, 252 (1966).
8. V.F. Rubachenko, Sov. J. Nucl. Phys., V.**5**, 48 (1987); Yad. Phys. V. **5**, 895 (1967).
9. Neutron Spin Echo, edited by F. Mezei, Lecture Notes in Physics. Vol. **128**, Springer, Heidelberg, 1980.

10. A.I. Frank, I.V. Bondarenko, A.V. Kozlov, P. Høghøj and G. Ehlers, Physica B, V.**297**, 307 (2001).
11. A.I. Frank, I.Anderson, I.V. Bondarenko, A.V. Kozlov, P. Høghøj and G. Ehlers, Phys. of At. Nuclei, V. **65**, 2009 (2002).
12. A.I. Frank, I.V. Bondarenko, V.V. Vasil'ev, I. Anderson, G. Ehlers, P. Høghøj, JETP Letters, V.**75**, 705 (2002).
13. A.I. Frank, Journal of Physics: Conference Series, V.**528**, 012029 (2014).
14. V.A. Bushuev, A.I. Frank, X-ray optics 2014 (Chernogolovka) 31–33.
15. V.A. Bushuev, A.I. Frank, Physics-Uspechi, V.**61**, 952 (2018).
16. V. F. Sears, Phys. Rep. V.**82**, 1 (1982).

Parity Violation Effects in Capture Process of Slow Neutrons on Lead Nucleus

A.I. Oprea, C. Oprea, Yu.M. Gledenov, P.V. Sedyshev

Frank Laboratory of Neutron Physics (FLNP), Joint Institute for Nuclear Research (JINR), 141980 Dubna, 6 Joliot Curie Street, Moscow Region, Russian Federation

Abstract. In the capture process of slow neutrons by ^{204}Pb nucleus, asymmetry of emitted gamma quanta was evaluated. Using theoretical and experimental data on scattering and capture process of slow neutrons new information about weak matrix element and negative resonance were extracted.

INTRODUCTION

The measured parity breaking effects, in neutrons scattering were the following: spin rotation per unit length of emitted neutrons for initially transversal polarized neutrons (dΦ/dz) and polarization of emitted neutrons of initially longitudinal polarized neutrons (P) [1]. Preliminary results on capture process are published in [2]. Lead nucleus has a few isotopes but only the isotope ^{204}Pb is responsible for parity breaking effects [3]. Relations of definitions of PV effects together with their theoretical expression can be found in [4, 5].

In the capture and scattering process of slow and cold neutrons on Lead nucleus were observed some unexpected large experimental spatial parity violation (PV) effects in comparison with theoretical evaluations. The differences between theoretical and experimental data were explained by the presence of new, unknown negative P-resonance near neutron threshold [3].

In the present work experimental data and theoretical evaluation of neutrons scattering and capture processes of PV effects on ^{204}Pb were analyzed. Possible existence of a negative resonance was confirmed. Matrix element of weak non leptonic interaction was also extracted.

THEORETICAL BACKGROUND

Parity breaking effects were calculated in the frame of the "resonance-resonance" model. According to this approach, PV and asymmetry effects can be observed in the presence of compound nucleus resonances with the same spins and different parities. Parity breaking effects, coming from weak non leptonic interaction between nucleons, in nuclear reactions are going in the presence of strong interaction which is parity conserving. As it is expected that weak interaction is 2–4 order of magnitude lower than strong nuclear interaction and therefore PV effects have very small values (10^{-7}–10^{-4}) which are difficult to measure in experiment. Using nuclear reaction induced by slow neutrons with formation of compound nucleus in the presence of resonance, PV effects are amplified and they can reach even tens of percents values. A comprehensive description of parity breaking effects and their amplification mechanisms can be found in [6, 7].

In the capture process of slow neutrons by ^{204}Pb nucleus, the asymmetry of emitted gamma quanta A_γ, is defined as [3, 4]:

$$A_\nu = \frac{\sigma_{n\gamma}^+ - \sigma_{n\gamma}^-}{\sigma_{n\gamma}^+ + \sigma_{n\gamma}^-}, \tag{1}$$

where: $\sigma_{n\gamma}^+, \sigma_{n\gamma}^-$ are neutron capture cross sections with initial longitudinal polarized neutrons with spins parallel (+) and anti-parallel (-) with the direction of incident neutrons.

Cross sections are evaluated based on the amplitude capture process described in [6,7]. The amplitudes of neutrons capture reaction involving spatial parity breaking process (f_{PV}^{SP}, f_{PV}^{PS}) have the following expression [4, 6, 7]:

$$f_{PV}^{SP}(E_n) \sim W_{SP} \frac{\sqrt{\Gamma_n^S \Gamma_\gamma^P}}{\left[(E-E_S) + i\frac{\Gamma_S}{2}\right]\left[(E-E_P) + i\frac{\Gamma_P}{2}\right]} Exp\left(\varphi_n^S - \varphi_\gamma^P\right), \tag{2}$$

$$f_{PV}^{PS}(E_n) \sim W_{SP} \frac{\sqrt{\Gamma_n^P \Gamma_\gamma^S}}{\left[(E-E_S) + i\frac{\Gamma_S}{2}\right]\left[(E-E_P) + i\frac{\Gamma_P}{2}\right]} Exp\left(\varphi_\lambda^S - \varphi_n^P\right), \tag{3}$$

where W_{SP} is weak non leptonic matrix element. $W_{SP} \sim 10^{-4}$–10^{-2} eV<<1; $E_{S,P}$ is energy of S and P resonances, respectively; Γ_n^S, Γ_n^P are neutron widths corresponding to S and P states of compound nucleus; $\Gamma_\gamma^S, \Gamma_\gamma^P$ are gamma widths in the S and P states; Γ_S, Γ_P are total widths for S and P states, respectively ($\Gamma_S = \Gamma_n^S + \Gamma_\gamma^S + \Gamma_p^S + \Gamma_\alpha^S + ...$, $\Gamma_P = \Gamma_n^P + \Gamma_\gamma^P + \Gamma_p^P + \Gamma_\alpha^P + ...$); φ_n^S, φ_n^P are S and P neutrons phases; $\varphi_\gamma^S, \varphi_\gamma^P$ are S and P gamma phases.

Relation (2) represents the capture of neutrons with orbital momentum l=0 (s-neutron), followed by formation of a compound nucleus in S states. Further, due to weak interactions between nucleons in compound nucleus a gamma quantum is emitted from a P state of compound nucleus. Expression (3) describes the process when neutrons with orbital momentum l=1 (p-neutron) are captured, a compound nucleus in a P state is formed, followed by emission of gamma quanta corresponding to an S state of compound nucleus due to the weak interactions between nucleons.

In comparison with expressions (2) and (3), the amplitudes describing nuclear strong interaction, which are parity conserving (f_{PC}^S, f_{PC}^S) are shown below, [4, 6, 7].

$$f_{PC}^S \sim \frac{\sqrt{\Gamma_n^S \Gamma_\gamma^S}}{(E-E_S) + i\frac{\Gamma_S}{2}}, \qquad f_{PC}^P \sim \frac{\sqrt{\Gamma_n^P \Gamma_\gamma^P}}{(E-E_P) + i\frac{\Gamma_P}{2}} \tag{4}$$

Relations (4) describes the nuclear process which is parity conserving (PC). In the capture process of an s-neutron (or p-neutron), an S (or P) compound nucleus is formed, followed by gamma emission corresponding to S (or P) states of compound nucleus.

For a better understanding of PV and PC phenomena, in the amplitudes from (2–4) expressions, sums of Clebsch-Gordan were not shown. From (2–4) formulas it is obvious that parity breaking and asymmetry effects are coming from the interference of amplitudes described above. Furthermore, theoretical evaluations on other nuclei and reactions like (n,p), (n,n), (n,α) have demonstrated that asymmetry and PV effects can be observed near P

resonances. Also, in the resonances, where the cross sections have maximal values the effects are equal with zero. Between resonances, where the cross sections have small values, the effects can reach maximal values. From these, can be concluded that the measurements of PV effects which are acting in the background of nuclear forces, represents a very difficult and accurate task [2], [4–8].

RESULTS AND DISCUSSIONS

Asymmetry of emitted gamma quanta in $^{204}Pb(n,\gamma)^{205}Pb$ capture reaction from slow and cold neutrons up to 500 eV was evaluated in accordance with relation (1). Cross section, for parallel and anti-parallel spin orientation of incident neutrons relative to their initial direction was calculated applying Flambaum-Sushkov approach [4–8]. Were analyzed also the influence of first 10 resonance of ^{205}Pb compound nucleus and it was concluded that for incident cold and slow neutrons contribution to the PV effects are coming only from the first 2 resonances, an S and P resonance respectively. Energy, spin and parity of S and P states of compound nucleus are respectively: $E_S = -2980$ eV, $J^\Pi = (1/2)^+$ and $E_S = 450$ eV, $J^\Pi = (1/2)^-$ [9]. Taking into account all above, using the two levels approximation in the frame of the formalism of the mixing states of the compound nucleus with the same spins and opposite parities, asymmetry of emitted gamma quanta (A_γ) has the form:

$$A_\gamma = \frac{2}{\sqrt{3}} W_{SP} \lambdabar_n^2 \Gamma_S^n \sqrt{\Gamma_S^\gamma \Gamma_P^\gamma} c_{PNC}(E_n) / ([S][P]) / (\sigma_S^\gamma(E_n) + \sigma_P^\gamma(E_n)), \tag{5}$$

$$c_{PNC}(E_n) = (E_n - E_P) Cos[\Delta\varphi(E_n)] - \frac{\Gamma_P}{2} Sin[\Delta\varphi(E_n)], \tag{5.1}$$

$$[S] = (E - E_S)^2 + \frac{\Gamma_S^2}{4}, \;\; [P] = (E - E_P)^2 + \frac{\Gamma_P^2}{4}, \tag{5.2}$$

$$\sigma_S^\gamma(E_n) = g_S \pi \lambdabar_n^2 \Gamma_n^S \Gamma_\gamma^S [S]^{-1}, \;\; \sigma_P^\gamma(E_n) = g_P \pi \lambdabar_n^2 \Gamma_n^P \Gamma_\gamma^P [P]^{-1}, \tag{5.3}$$

$$g_S = (2J_S + 1)[(2I+1)(2s+1)]^{-1}, \;\; g_P = (2J_P + 1)[(2I+1)(2s+1)]^{-1}, \tag{5.4}$$

where: $\lambdabar_n$ is reduced neutrons wave length; $J_S = J_P = 1/2$ are spins of compound nucleus in S and P states, respectively; $I = 0$ is spin of target nucleus; $s = 1/2$ is neutron spin.
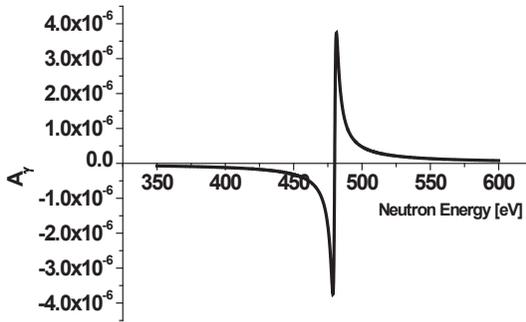
Fig. 1. Energy dependence of A_γ

Neutrons energy dependence of the asymmetry of emitted gamma quanta is represented in Fig. 1.

In the vicinity of P-resonance ($E_P = 480$ eV), A_γ has maximal value and is decreasing quickly faraway from resonance. In the resonance $A_\gamma(E_n = E_P = 480 \text{ eV}) = 0$.

In reference [5] parity breaking effects like polarization of emitted neutrons (P) and neutrons spin rotation ($d\Phi/dz$) in the scattering of cold and slow neutrons were analyzed. Using neutrons resonance parameters from [9] a serious difference between experimental data [1] and theoretical evaluations [5] was observed. Results are shown below.

$$\frac{d\Phi^{theor}}{dz}\left(E_n = 3.27\cdot10^{-3}\,eV\right) = \pm2.41\cdot10^{-8}\,rad/cm- >$$

$$\frac{d\Phi^{exp}}{dz}\left(E_n = 3.27\cdot10^{-3}\,eV\right) = (2.47\pm0.23)\cdot10^{-4}\,rad/cm \tag{6}$$

$$P^{theor}\left(E_n = 1.767\cdot10^{-3}\,eV\right) = \pm1.41\cdot10^{-8} - > P^{exp}\left(E_n = 1.76\cdot10^{-3}\,eV\right) = (0.7\pm0.8)\cdot10^{-6} \tag{7}$$

Due to undetermined phases sign, the $\pm$ sign appears in the expression of theoretical evaluation. The high difference between theoretical and experimental data, in resonant-resonant approach, was explained by the presence of a negative P-resonance near the threshold. Based on qualitative analysis of only polarization data (P), the energy of new P-resonance was suggested to be, $E_P = -16$ eV [3]. It was clear that new data are necessary to be included because in reference [3] the value of weak matrix element W_{SP} was supposed to be of order of 10^{-4} eV.

In [5] the authors added theoretical and experimental data of neutrons spin rotation (see (6) and (7)) and for the first time the energy of P-resonance and the value of weak matrix element were extracted. The obtained results are the following:

$$E_P = -18\,\text{eV}, \qquad W_{SP} = 2.79\cdot10^{-3}\,\text{eV} \tag{8}$$

Results from (8) are obtained by neglecting capture channel in the case P-resonance. In reference [2] gamma asymmetry (A_γ) was measured and cannot by higher than a certain value as shown below:

$$A_\lambda^{exp}\left(3.27\cdot10^{-3}\right) = 5\cdot10^{-7} \tag{9}$$

From here, result that capture data are necessary to be added. Therefore, using expression (5) together with existing measurement (9), scattering theoretical and experimental data of (P) and ($d\Phi/dz$) (see (6), (7)), weak matrix element W_{SP}, energy of P-resonance E_P and gamma width Γ_γ^P were extracted and their values are the following:

$$E_P = -23\,\text{eV}, \ W_{SP} = 3.40\cdot10^{-3}\,\text{eV}, \ \Gamma_\gamma^P = 4.73\cdot10^{-6}\,\text{eV} \tag{10}$$

Considering scattering and capture theoretical evaluations and existing experimental data the hypothesis of the existence of a P-negative resonance near the threshold is once again confirmed. The effect of the presence of the new P-negative resonance is very difficult to observe in the cross section due to the very small value of gamma width (Γ_γ^P) (see (10)).

CONCLUSIONS

Capture and scattering PV process of slow and cold neutrons on ^{204}Pb nucleus were analyzed. Theoretical data of PV process were evaluated in the frame of the model of the mixing states of compound nucleus with the same spin and opposite parities and two levels approximation. From calculated PV effects and existing experimental data the existence of a P-negative resonance near the threshold is confirmed. The values of P-resonance energy, weak matrix element and gamma width were also extracted. Due to the very low values of PV effects their measurements are very difficult and presented data have large absolute errors. For the improvement of future results are necessary new experimental data in a wide energy range which can be obtained at high intensity neutrons sources.

The present work represents a proposal for new PV effects measurements both at basic facilities of FLNP JINR in Dubna and of neutron centers abroad.

REFERENCES

1. B. Heckel, N.F. Ramsey, K. Green, G.L. Greene, R. Gahler, O. Shaerpf, M. Forte, W. Dress, P.D. Miller, R. Golub, J. Byrne, J.M. Pendelbury, Phys. Lett, Vol. **119**B, № 4,5,6 p. 298, 23/30 December 1982.
2. Yu.M. Gledenov, V.V. Nesvizhevsky, P.V. Sedyshev, E.V. Shul'gina, V.A. Vesna, Physics of Atomic Nuclei, Vol. **77**, № 3, p. 316-320, ISSN 1063–7788 (2014).
3. G.A. Lobov, Yadernaya Fizika, Vol. **63**, № 8, p. 1465 (2000) (in Russian).
4. V.E. Bunakov, V.P. Gudkov, Proceedings of XVIth Winter School of B.P. Konstantinovich Institute for Nuclear Physics from Leningrad, p. 34, 1981 (in Russian).
5. A.I. Oprea, C. Oprea, Yu.M. Gledenov, P.V. Sedyshev, Romanian Reports in Physics, Vol. **66**, № 4, p 952–962 (2014).
6. V.V. Flambaum, G.F. Gribakin, Prog. Part. Nucl. Phys. Vol. **35**, p. 423, 1995.
7. V.E. Bunakov, L.B. Pikelner, Progr. Part. Nucl. Phys. Vol. **39**, p. 337–392 (1997).
8. A.I. Oprea, C. Oprea, Yu.M. Gledenov, P.V. Sedyshev, C. Pirvutoiu, D. Vladoiu, Romanian Reports in Physics, ISSN 1221–1451, Vol. **63**, № 2, p. 357–375 (2011).
9. Mughabghab S.F., Divadeenam M., Holden N.E. – Neutron Cross Sections. NY, Academic Press, Vol. **2**, (1981).

The Ion Background in the Radiative Neutron Decay Experiment

Khafizov R.U.[a], Kolesnikov I.A.[a], Nikolenko M.V.[a], Tarnovitsky S.A.[a], Tolokonnikov S.V.[a], Torokhov V.D.[a], Trifonov G.M.[a], Solovei V.A.[a], Kolkhidashvili M.R.[a], Konorov I.V.[b]

[a]*NRC «Kurchatov Institute», Russia*
[b]*Technical University of Munich, Munich, Germany*

khafizov_ru@nrcki.ru

Annotation

This report aims to research the influence of the ionic background on registration of radiative neutron decay events and the measurement of its branching ratio (B.R.). Our methodology is focused on measuring the spectra of triple coincidences of radiative gamma-quantum, beta electron, and recoil proton and double coincidences of beta electron and recoil proton. The peak on the spectrum of triple coincidences shows the number of radiative neutron decays, while the peak on the spectrum of double coincidences shows the number of regular neutron beta-decays. This methodology enabled us to become the first team to measure the branching ratio of radiative neutron decay B.R. = $(3.2 \pm 1.6) \cdot 10^{-3}$ (where C.L. = 99.7% and gamma quanta energy exceeds 35 keV) in 2005 on our old experimental equipment.

We have now prepared a new experiment on radiative neutron decay with the aim of measuring B.R. with a high degree of precision. The precision of branching ratio measurement is determined using the value of the ion background. The spectrum of double coincidences obtained in our experiment shows a fairly significant ion background, the fluctuations of which indicate the precision of measurement for the number of recoil protons. Because the ion background specifically is quite significant, it appears even under super deep vacuum as beta electrons ionize the highly rarified air inside the chamber. The value of ion background very slowly decreases with decreasing density of air inside the equipment. For example, our experimental data lead to the conclusion that the value of the ionic background is significant when compared with the value of the proton peak and on the other hand decreases only by 5–6 times if the pressure within the chamber goes down by two orders of magnitude. Besides, we discovered an additional wide peak on the spectrum of triple coincidences. This peak consists of delayed gamma quanta created during the ionization of rare gas by beta-electrons.

Thus, this experiment allows us to study another important phenomenon, the ionization of rarified gas by beta electrons with emission of gamma quanta. Our last experiment showed that these two phenomena, radiative neutron decay and ionization with gamma quanta emission, are distinguishable in the case of high time resolution and can be studied separately. This is another important result of our last experiment and in this report we mention that the authors of articles registered namely the ionization with gamma radiation events.

This report is dedicated to a discussion of the computer experiment we conducted using the well-known GEANT4 software package. As a result of these calculations, we demonstrated that the value of the ionic background is proportional to the cubic root of the rarefied air density within the equipment, i.e. it changes very smoothly in relation to the pressure within the chamber. Besides, the report presents a comparison of our measurements of double coincidences and triple coincidences, with two other experimental groups.

Introduction

Presently, the characteristics of the ordinary decay mode are measured with precision of tenths of a percentage point. Under these circumstances, the experimental data obtained by different groups of experimentalists can be reconciled only by taking into account the corrections calculated within the framework of the standard theory of electroweak interactions. This means that the experimental research of the ordinary mode of neutron decay have exhausted their usefulness for testing the standard model. To test the theory of electroweak interaction independently, it is necessary to move from the research of the ordinary branch of decay to the next step, namely, to the experimental research of the radiative decay branch.

The radiative decay branch of elementary particles, where an additional particle, a radiative gamma quantum is formed along with the regular decay products, has been discovered for practically all elementary particles. This has been facilitated by the fact that among the rare decay branches the radiative branch is the most intensive, as its value is proportional to the fine structure constant α and is only several percent of the intensity of the regular decay mode (in other words, the relative intensity B.R. of the radiative decay branch has the value of several hundredths of a unit.)

However, for the neutron this decay branch had not been discovered until recently and considered theoretically only [1–4]. Our first attempt to register the radiative neutron decay events was made on intensive cold neutron beam at ILL [5]. But our experiment conducted in 2005 at the FRMII reactor of Munich Technical University became the first experiment to observe this elementary process [6]. We initially identified the events of radiative neutron decay by the triple coincidence, when along with the two regular particles, beta electron and recoil proton, we registered an additional particle, the radiative gamma quantum

$$n \rightarrow p + e^- + \nu + \gamma,$$
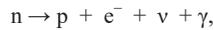
and so could measure the relative intensity of the radiative branch of neutron decay B.R.= $(3.2 \pm 1.6) \cdot 10^{-3}$ (with C.L.= 99.7% and gamma quanta energy over 35 keV; before this experiment we had measured only the upper limit on B.R. at ILL [5]).

The main characteristic of any rare mode of elementary particle decay is its relative intensity, branching ratio (BR). By definition, BR is equal to the ratio between the intensity of the rare decay mode and the intensity of the ordinary mode. In the case of neutron, this intensity ratio can be reduced to the ratio between the number of triple coincidences between the registration of beta-electrons, radiative gamma-quantum and the delayed proton N_T to the number of double coincidences between the registration of the ordinary decay products, beta electron and recoil proton N_D:

$$BR = I(\text{radiative decay}) / I(\text{ordinary decay}) = N(e,p,\gamma) / N(e,p) = N_T / N_D.$$

These two values can be determined only from the analysis of double and triple coincidences spectra, which form corresponding peaks. Identifying these peaks and distinguishing them from the significant background is the central problem in the methodology of BR measurements for neutron radiative decay.

Further, this experimental BR value needs to be compared with the theoretical value, estimated within the framework of the electroweak model. Any difference between these two values would mean that we are observing a deviation from the electroweak interaction theory.

Our group calculated the neutron radiative spectrum in the framework of standard electroweak theory in the following papers [1–4]. The calculated branching ratio for this decay mode as a function of the gamma energy threshold was published in these papers. BR value for the energy region over 35 keV was calculated to be about $2.1 \cdot 10^{-3}$.

It follows that to measure the main characteristic of radiative neutron decay it is necessary to obtain and analyze the spectra of double and triple coincidences. So, it is necessary to consider the main particularity of these spectra – the ion and gamma backgrounds.

Let us consider in detail the question around the value of ion background in the experiment on radiative neutron decay, namely, its value in the spectrum of double coincidences of electron and proton. Theory makes it clear that the number of ions created by an electron that spreads in the media of its path with length of L is equal to $N_{ion} = L/\lambda$. Here, λ is the length of the electron's free path in media with molecular density n. If ionization cross section of media is σ_i, then the length of the free path is inversely proportional to the product of media density to the cross section $\lambda = (n\sigma_i)^{-1}$. On the other hand, if the probability of the one media atom ionizatin is $P(n)$, then the number of ions N_{ion} created when the electron cross the media equals the product of this probability to the total number N of atoms on the electron trajectory length L. This number is equal to the ratio of the trajectory length L to the average distance between nearest atoms of media $\ell = n^{-1/3}$ with density n: $N = L/\ell$. Thus, we arrive at the following chain of equations:

$$N_{ion} = \frac{L}{\lambda} = Ln\sigma_i = P(n)N = P(n)\frac{L}{l} = P(n)Ln^{1/3}.$$

Thus, the classic probability of ion creation per one media atom with density n is equal to the ratio between the two areas – that of ionization cross section σ_i to area $S = n^{-2/3}$, the area per one media atom: $P(n) = \sigma_i/S = \sigma_i \cdot n^{2/3}$.

This formula occurs in the simplest model of a "perfectly black sphere". Introducing a random value, aim distance ρ, leads to the probability of ionization dependent on that aim distance of $P(\rho) = 1$ for all aim distances shorter than the atom radius $a = (\sigma_i/\pi)^{1/2}$ while for greater aim distances probability of ionization is 0 (see Fig. 1).
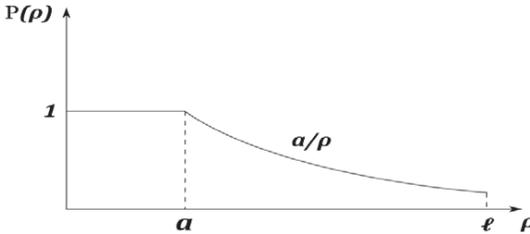
Fig.1. The dependence of the ionization probability on ρ. For the usual model: $P(\rho) = 1$ for $\rho < a$ and $P(\rho) = 0$ for $a < \rho < \ell$; for Coulomb interaction model $P(\rho) = 1$ and $P(\rho) = a/\rho$ for $a < \rho < \ell$.

However, in the case of ionization process in highly rarefied media this simple model becomes inaccurate as it does not take into account Coulomb interaction, which may have a fairly long "Coulomb tail" inversely proportional to the aim distance. In this case, one must consider a more realistic model where probability $P(\rho)$ is not zero, when the electron flies by the atom without touching it, i.e. at aim distances ρ greater than a. So, it is necessary to

consider the long "Coulomb tail" of distribution $P(\rho)$, which falls inversely proportionally to the aim distance (see Fig. 1). Thus, the total ionization cross section will depend on density and have an additional term, inversely proportional to the cubic root of media density n:

$$\sigma_{tot} = \int_0^{2\pi} d\varphi \int_0^a \rho d\rho + \int_0^{2\pi} d\varphi \int_a^l \frac{a}{\rho} \rho d\rho = \pi a^2 + 2\pi a(l-a) = -\pi a^2 + 2\pi al = -\sigma_i + 2(\pi\sigma_i)^{1/2} n^{-1/3}$$

The probability of ionization per one atom will be: $P(n) = \sigma_{tot} \cdot n^{2/3} = -\sigma_i \cdot n^{2/3} + 2(\pi\sigma_i)^{1/2} \cdot n^{1/3}$.

It is evident that in extremely rarified media where $\sigma_i \cdot n^{2/3}$ is significantly below 1, the second member of this formula leads and significantly exceeds the first. Thus, probability of ionization of one atom becomes proportional to the cubic root of density (pressure), i.e. depends on density in a very smooth way. This, in turn, leads to a gradual reducing of the ion background dependency on density and this background cannot be ignored even in highly rarified media. For example, a fall in pressure within the experimental setup of two orders of magnitude leads to a fall in the ionic background equal to the cubic root of pressure, i.e. 4–5 times. Our experiment observed exactly this behavior of ionic background and, as we'll show later in this report, such smooth dependency on density is experimentally demonstrated when measuring spectra of double coincidences obtained by our and emiT groups.

Analysis and comparison of double coincidences spectra

Here let's pause to analyze the spectra of double coincidences between beta-electron and recoil proton, and compare our spectrum with the results obtained by other authors. We have published the diagram of our experimental equipment in the past [5–6, 8]. Here we will simply note that in its sizes our equipment is comparable to the equipment used by the two other groups and the distance between the observed decay zone and the proton detector in our equipment is about 0.5m. The accelerating potential of the electric field is also approximately the same in all three equipment sets, so all three experiments should lead to similarly forms of double and triple coincidences spectra.

Fig.2 demonstrates the summary statistics on double e-p coincidences (coincidences of electron with delayed proton). Fig.2 clearly shows two major peaks: one peak with a maximum in channels 99–100, which is the peak of zero or prompt coincidences [6, 8]. The position of this peak marks the zero time count, namely the time when the electron detector registered the electron. This peak is not physics-related in its nature. Instead, it is a reaction of the detectors and the electronic system to the registration of the beta electron. It is namely the pulse from the electron channel that opens the time windows on spectra Fig.2 for 2.5 μs forward and backwards. The next peak visible in Fig.2 has a maximum in channel 120 and is the peak of e-p coincidences of beta-electron with delayed proton.

An analogous situation was observed in experiments on the measurement of the correlation coefficients by two independent groups at ILL [10] and emiT group at NIST [11], and it was also mentioned at [12]. We would especially like to emphasize the correspondence of our spectrum of double coincidences with an analogous spectrum from the result obtained by the emiT group from NIST [11]. In Fig.3 we present their spectrum and diagram for the registration of the beta electron and the recoil proton. A comparison of our results with the results of the emiT group shows their unquestionable similarity. Moreover, the position of the second proton peak in Fig.3 (emiT group), like in Fig.2 (our result), corresponds well to the simple estimate obtained by dividing the length of a proton trajectory by its average speed.
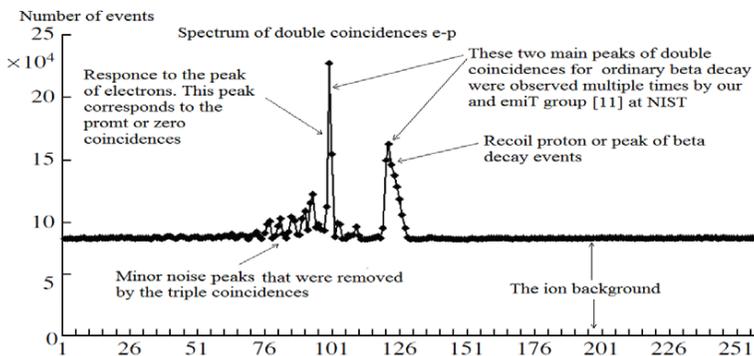
Fig.2. Timing spectrum for e-p coincidences. Each channel corresponds to 25 ns. The peak at channel 99–100 corresponds to the prompt (or zero) coincidences. The coincidences between the decay electrons and delayed recoil protons (e-p coincidences) are contained in the large peak centered at channel 120.

Here we will also note the presence of a significant homogenous ionic background in Fig.2 and Fig.3. However, in both cases this background allows to easily distinguish the neutron decay peak. As we will shortly demonstrate, this ionic background will play a dominant role in the presence of a strong magnetic field and it will become impossible to distinguish events of ordinary neutron decay against it.

Following Avogadro's law, even in the case of a very deep vacuum under pressure of 10^{-6}–10^{-8} mbar, air molecule concentration remains very high. In fact, it is sufficient for beta-electrons produced in neutron decay to create a significantly high ionic background. Here one must note that the probability of ion creation along the trajectory of beta-electron in inverse proportion to the average distance between neighboring ions, i.e. proportional not to the molecule concentration but to the cubic root of this value. From this observation it follows that the value of the ionic background does not significantly depend on the vacuum conditions inside the experimental chamber. In our case, pressure was two orders of magnitude greater than the pressure in the emiT experiment. However, we observed an ionic background of only 4–5 times their background. This estimate is confirmed when one compares the spectra in Fig.2 and Fig.3. Our spectrum, presented in Fig.2, has a 1:1 ratio of the value of e-p coincidences peak and the value of the background. The emiT group (Fig.3) spectrum has a ratio of 4:1 – 5:1, i.e. only 4–5 times our number, that is equal to the cubic root of pressure ratio in both teams' work (see Introduction).

We will present the specific calculations using the GEANT4 package in a separate paper, where we will consider the ionization process in more detail. It is noteworthy that in our case it is impossible to isolate and track individual tracks of electrons ionizing the residual air in the chamber due to their multiple reflections and scattering on the walls of the chamber, the neutron guide and other structural elements of the installation. As shown by concrete calculations, in this case it makes more sense to talk about the steady-state electron density ρ_e inside the chamber and, accordingly, the ion density ρ_i. The density of ions ρ_i is proportional to the density of electrons ρ_e, with the proportionality factor being the probability of the formation of the ion $P(n)$ (see Introduction): $\rho_i = P(n) \cdot \rho_e = 2(\pi\sigma_i)^{1/2} \cdot n^{1/3} \rho_e$. Thus, the ratio of

the ionic background value to the proton peak value also decreases in proportion to the cube root of density or pressure.
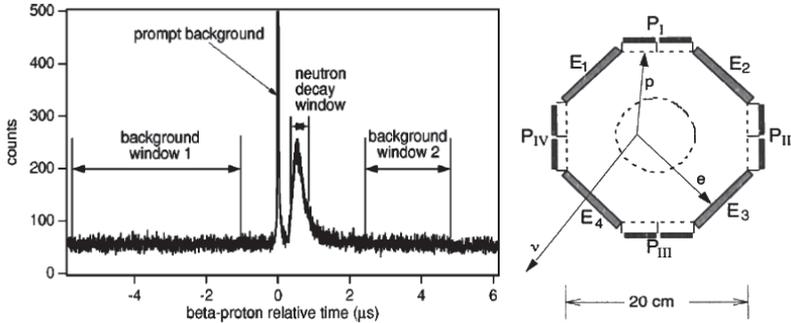
Fig.3. Spectrum of double electron-proton coincidences obtained by emiT Group [11] with two peaks and ion background value comparable to the neutron decay peak; emiT group scheme for registering beta electron and recoil proton.

Fig.2 shows that the total number of events in e-p coincidences peak in our experiment equals $N_D = 3.75 \cdot 10^5$. This value exceeds the value we obtained in our previous experiment conducted on beam PF1 at ILL by two orders of magnitude. It was precisely because of the low statistics volume that we could not identify the events of radiative neutron decay in that experiment and instead defined only the upper B.R. limit [5]. It is very important to note that the peak of double coincidences between electron and the delayed proton is observed against a non-homogenous background (see Fig.2 and Fig.3): besides the homogenous ionic background, which has a value comparable to the value of the e-p coincidences peak, there is an obvious peak in channels 99–100. In essence, this peak is a response peak to the time spectrum of electron registration, which contains just one peak in channels 99–100, signifying the time when the electron detector registered the electron. We will shortly see that the radiative peak of triple coincidences appears against a non-homogenous background with not one, but two response peaks.

The remaining peaks in Fig.2 are small, with just seven peaks distinct from the statistical fluctuations. These occurred because of the noise in the electric circuits of the FRMII neutron guide hall. There are no other physics-related reasons for their occurrence. These peaks appeared and disappeared depending on the time of day, reaching their maxima during the work day and disappearing over the weekends. Such behavior was observed throughout the experiment as we collected statistics. Since the nature of these seven small peaks is in no way related to radiative and ordinary decay, we did not emphasize them in our article.

The comparison conducted demonstrates that the spectra of double coincidences obtained in our experiment completely correspond with the results obtained by the emiT group. Now we will compare these two spectra with the spectrum of double coincidences obtained by the third group. Unfortunately, the authors did not publish the spectrum of double coincidences in their original article [7], instead it was only published this year in paper [13].

Fig.4 displays the spectrum of double coincidences and the diagram of their experimental equipment.
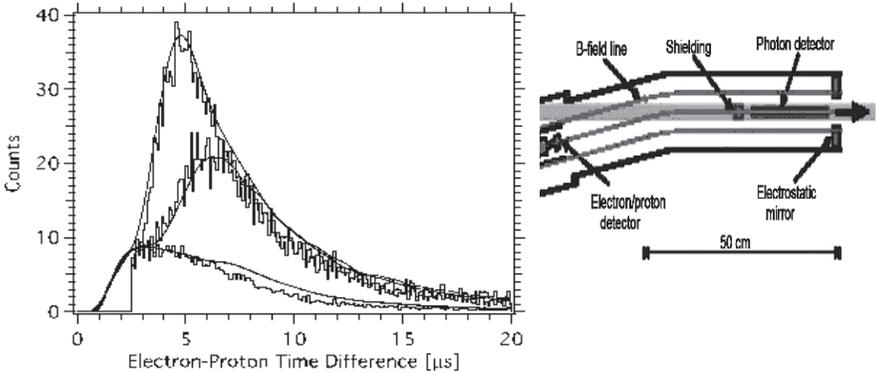
Fig.4. Equipment diagram and the single peak of "electron-proton" coincidences, published in [13]. The lower curve corresponds to 0 volts, the middle curve corresponds to 300 volts and the highest curve corresponds to 500 volts in an electrostatic mirror. The location of the peak's maximum and its significant width differ from our and the emiT results subsequently by one and two orders of magnitude. The location and the width of the peak also deviate by one and two orders of magnitude from the elementary estimates of delay times (see below).

The significant deviation obtained is explained by the fact that the peak in the NIST experiment consists not of beta-decay protons, but rather of ions. The density of gas molecules inside the equipment is proportional to pressure and according to the Avogadro's Law is at the order of 10^7 mol/cm^3 even at the pressure of 10^{-8}–10^{-9} mbar. This is a very significant number, which quite enough for creation the large ionic background in the presence of ionizing radiation. The energy of beta-electrons significantly exceeds the energy of ionization. Besides, the probability of ion creation by electrons is inverse proportional not to volume taken up by one molecule but to the average distance between molecules. It is precisely due to this reason that the ionic background falls proportionally to the cubic root of the pressure and not proportionally to pressure. In the emiT group experiment the pressure was the same as in the NIST experiment, i. so, the ionic background should be the same too. The light ions, together with the beta protons, should have a delay time comparable to 1 μs. The pulses from these particles are simply not visible in the spectrum due to the NIST group's use of combined electron-proton detector (see Figure 5 with the shape of electron and ion pulses). The maximum of the "proton" peak in the NIST experiment, according to the delay times estimations (delay time is proportional to square root of ion mass), falls exactly to the air ions 4–6 μs.

Fig.5 presents the pulse forms on the electron-proton detector. As was pointed out above, the significantly delayed pulses of low amplitude correspond to ion pulses, and the pulses from protons are simply invisible due to a presence of a wide electron pulse of high amplitude. Namely this fact explains the dead zone around zero on the spectrum of electron-ion coincidences in Fig.4.
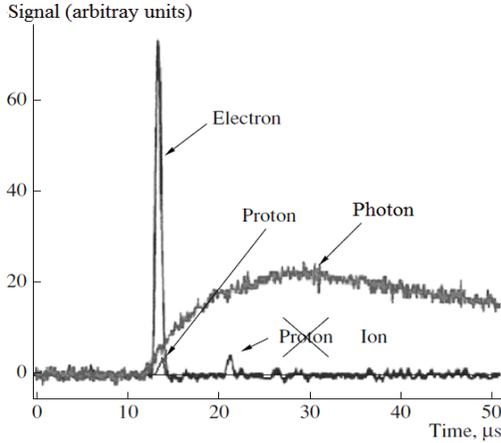
Fig.5. The signal from the decay proton has to be delayed by less than one microsecond, which is why it is located at the base of the electron pulse (see line number 2) and so cannot be registered by the combined electron-proton detector. The pulses that are delayed by longer than 1 microsecond are pulses not from decay protons, as it was indicated in ref. [7], but rather from ions, formed in the decay zone. The line number 1 shows the shape of pulses from the gamma detector.

Analysis and comparison of triple coincidences spectra

In paper [11] the emiT group researched only the ordinary decay mode, thus this comparison is limited to our spectrum of triple coincidences, presented in Fig.5, and the only peak published by the NIST authors in Nature [7], presented in Fig.7. Analysing the double coincidences spectra obtained by our and the emiT groups (both of which present two main peaks) shows that in the spectrum of triple coincidences we should observe not two but three peaks. Namely, along with the sought after radiative peak, the triple e-p-gamma coincidences spectrum should show two (not one!) response peaks to the registration of beta-electrons and the registration of protons. Fig.5 of triple coincidences clearly shows three peaks, and the leftmost peak with the maximum in channel 103 is connected to the peak of the radiative gamma-quanta in question, as this gamma-quantum is registered by the gamma detectors in our equipment before the electron.

It is also important to note that while both teams' double coincidences spectra show the peaks at a distance from each other and easily distinguishable, in the spectrum of the triple coincidences the radiative peak is on the left slope of the response peak to electron registration. This means that we observe the peak of radioactive neutron decay events against a heterogeneous background. At the same time, both response peaks on the spectrum of triple coincidences are significantly wider and located closer to each other than in the original spectrum of double coincidences. As we demonstrate below, one must take into account such spectrum behavior (related to the presence of a response in the electron detector system of data collection) by introducing the non-local response function. Using this well-known

method it is possible to distinguish N_T the number of triple coincidences from the heterogeneous background, arriving at the experimental BR value.
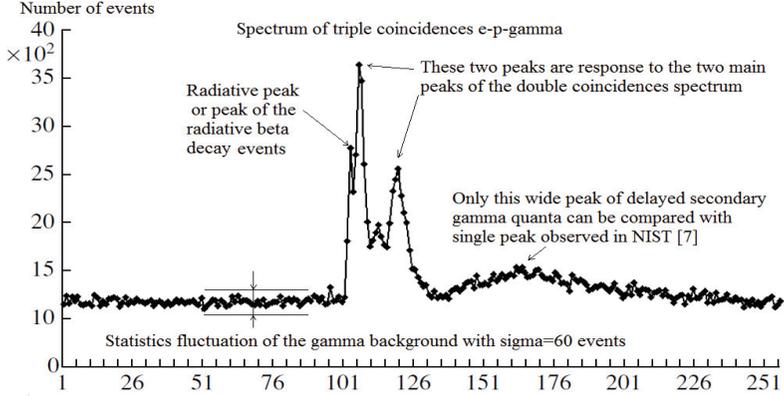
Fig.6. Timing spectrum for triple e-p-g coincidences. Each channel corresponds to 25 ns. In this spectrum, three main peaks in channels 103, 106 and 120 can be distinguished. The leftmost peak in 103 channel among these three main peaks is connected with the peak of radiative decay events.

Comparing Fig.2 and Fig.6, it becomes clear that if we ignore the first leftmost peak with the maximum in channel 103 in Fig. 6, the spectrum of double e-p coincidences will resemble the spectrum of triple e-p-γ coincidences in Fig.2. The peak with the maximum in channel 106 in Fig.6 is connected to the left peak of false coincidences in Fig.2, and the peak with the maximum in channel 120 in Fig.6 is connected to the right peak of e-p coincidences in Fig.2. The emerging picture becomes obvious when one uses a standard procedure, introducing a response function for gamma channel $R_\gamma(t,t')$ [6] , which is also necessary for calculating the number of triple radiative coincidences N_T in radiative peak:

$$S_{out}(t) = \int S_{in}(t') R_\gamma(t,t') dt'$$

Using the method of response function, one can confidently define our double-humped background: the narrow peak with the maximum in channel 106 in Fig.6 is the response to the narrow peak of zero coincidences (by other words this peak is response to beta-electron registration) in channels 99–100 in Fig.2, and the second peak in this double-humped background in Fig.5 is the response to the peak in channels 117–127 in Fig.2 (or this peak is response to proton registration).

It must be noted that in our case we have to use the non-local response function, as the peaks on the original spectrum $S_{in}(t)$ of double coincidences are significantly narrower than those in the spectrum $S_{out}(t)$ of triple coincidences and also are shifted in their relative positions. In this case we use "functional" multiplication, however if we use the local response function, the triple coincidences spectrum is arrived at by simple multiplying the double coincidences spectrum by a number, in which case neither the width of the peaks nor

32

their position change. It is also evident that the local response function approach leads to an erroneous number of triple coincidences N_T and, therefore, the wrong BR value.

When discussing the similarities between the spectra in Fig.2 and Fig.6, it is important to note that the response peak in Fig.6 with a maximum in channel 106 is shifted to the right or delayed in comparison to the peak responding to electron registration in channel 100 in Fig.1. This is due to the fact that in our electron diagram we used a constant fraction discriminator (CFD). CFD has its own delay line and the location of the time-pickoff signal it generates is determined by the method of comparing the fraction of the original signal to the delayed (CFD method [14]). Thus, there is a shift in the first response peak with a maximum in channel 106 in Fig.6 versus the first peak in Fig.2 with the maximum in channel 100. The value of this delay is equal to the front duration of the gamma quantum signal and is on average 150 ns. The CFD method obviously also shifts the radiative peak, but it should be located to the left of the response peak, as is observed in Fig.6.
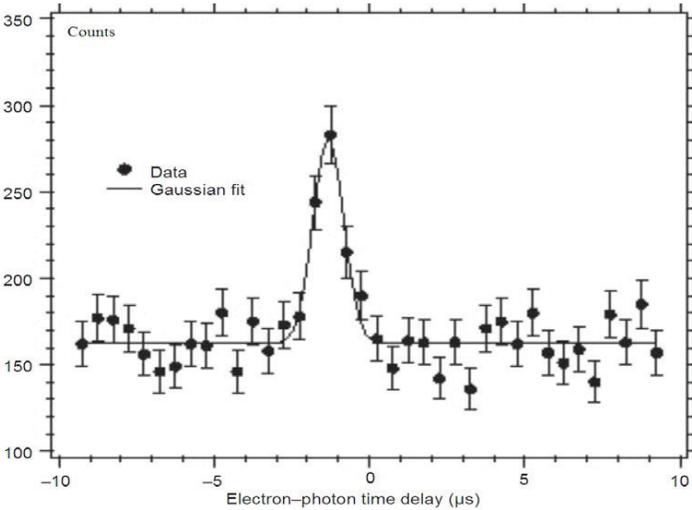
Fig.7. Only peak of "electron-photon" coincidences, shifted to the left of 0 – the time of beta-electron registration – by 1.25 microseconds, published in [7, 11].

As for the wide, almost indistinguishable peak in channel 165 in Fig.6, its influence on the radiative peak in channel 103 is negligible. Its nature is in no way related to the researched phenomenon, so we do not discuss it in our article. This peak is created by the radioactive gamma quanta delayed on average by 1.25 µs and emitted by the radioactive medium within our experimental equipment. The medium is activated by registered beta-electrons. This event of artificial, induced radioactivity has been known for over 100 years and does not have anything in common with the new event of radiative neutron decay which is the subject of current research. As we will demonstrate below, only this 1 microsecond peak and delayed from the registration time by about the same time can be compared to the peak observed by the authors of paper [7] at NIST (see Fig.7). Thus, the authors of this experiment observed not the events of radiative decay but rather the event of artificial radioactivity, already well known in the time of Joliot-Curie.

33

After analyzing the spectra with the help of the non-local response function $R_\gamma(t,t')$ we finalize the average value for the number of radiative neutron decays $N_T = 360$ with a statistics fluctuation of 60 events. B.R. can be expressed as a ratio of N_T to N_D as BR = k (N_T/N_D), where coefficient k = 3.3 is the geometrical factor that we can calculate by using anisotropic emission of radiative gamma-quanta [4]. With the number of observed double e-p coincidences $N_D = 3.75 \cdot 10^5$ and triple e-p-γ coincidences $N_T = 360$, one can deduce the value for radiative decay branching ratio of $(3.2 \pm 1.6) \cdot 10^{-3}$ (99.7 % C.L.) with the threshold gamma energy $\omega = 35$ keV. The average B.R. value we obtained deviates from the standard model, but because of the presence of a significant error (50%) we cannot make any definite conclusions. The measurements must be made with greater precision. According to our estimates, in the future experiment we will be able to make more definite conclusions about deviation from the standard electroweak theory with experimental error less than 10%.

The difference between the NIST experiment and our experiment becomes immediately apparent. First and foremost, it is the time scale: in our spectra, the scale is measured in nanoseconds, while in the other experiment the scale is in microseconds. Besides, we used three types of detectors, each of which registered its own particle: one detector for the electrons, one for the protons, and six identical detectors for the radiative gamma-quanta (see [6]). The duration of the front pulse from the electron and proton detectors is 10 nanoseconds in our experiment and 100 times greater than that in the NIST experiment, in the order of 1 μs. The rise time of gamma signal from our gamma-detectors is on average 150 ns, and from avalanche diode on the NIST equipment greater than 10 μs, besides that the diode pulse arrives with significant noise, which makes the thickness of the front pulse line equal to more than 0.5 μs (see the photon line in Fig.7 from [7]). All of this leads to our factual time resolution being two orders of magnitude better than the resolution achieved in the NIST experiment. However, as the two experiments used equipment which was practically the same in size and smaller than 1 meter, the choice of the time scale is a matter of principle. Given this geometry, it is impossible to get microsecond signal delays from all of the registered charged particles, i.e. electrons and protons. In this light, it is surprising that the peak identified by the authors of the NIST report [7] as the peak of radiative gamma-quanta, is shifted by 1.25 microseconds to the left. The expectation that magnetic fields of several tesla in magnitude delay all electrons and protons, are absolutely ungrounded.

Indeed, the magnetic field cannot change the speed of charged particles. It can only twist a line trajectory into a spiral. The length l of this spiral depends on angle θ between particle velocity and magnetic field direction. In beta decay, electrons can fly out under any angle θ, therefore the magnetic field can increase the time of delay by several orders of magnitude only for a negligible portion of the charged particles. Even this negligible number of particles that flew out at an almost 90 degree angle to the direction of the magnetic field that coincides with the direction of the narrow neutron guide (see Fig.4) will most likely end up on the walls of the neutron guide rather than reach and hit the detector due to the presence of the strong electrostatic field. Because the distance between the point of decay and the detector is about 0.5 meter and electron velocity is comparable with speed of light, the electron time of delay should be less than a microsecond by two orders of magnitude.

Thus, both the 1 microsecond shift and the width of the only peak in Fig.7 in the experiment conducted at NIST, is in sharp contradiction to elementary estimates. We, on the other hand, did not observe any wide peaks before electron registration and our gamma background is very even in this part of the spectrum (see Fig.6). However, when we assume that the NIST experiment authors observed the wide peak, shifted by 1 microsecond, not

before, but after the registration of beta-electrons. In that case, the wide peak on our spectrum in Fig.6 completely corresponds to the wide peak in Fig.7. However, as noted above, density of gas molecules remains high even with the pressure of 10^{-8}–10^{-9} mbar and this residual gas is activated by beta-electrons. The wide peak in our spectrum is formed by the delayed gamma quanta from this induced artificial radioactivity.

Conclusions

The main result of our experiment is the discovery of the radiative peak namely in the location and of the width that we expected. The location and the width of the radiative peak correspond to both estimates and the detailed Monte Carlo simulation of the experiment. Thus, we can identify the events of radiative neutron decay and measure its relative intensity, which was found to be equal B.R. = $(3.2 \pm 1.6) \cdot 10^{-3}$ (with C.L.= 99.7% and gamma quanta energy over 35 keV).

At the same time, the average experimental B.R. value exceeds the theoretical value by 1.5 times. However, due to a significant error we cannot use this result to assert that we observe a deviation from the standard model. Therefore, our most immediate goal is to increase experiment precision, which we can improve by several percent according to estimates.

For last two years we were preparing this new experiment and conducted number of tests for our new electronics. We constructed multichannel generator what can generate the pulses with the same forms as our electron, proton and gamma detectors. During these tests we got the same responses as during our last experiment on real neutron beams at FRMII. It means that all additional peaks on our spectra have no any physics reasons and It proves once more that we were absolute correct when applied the response function method for explaining these peaks as response ones and for developing our experimental spectra.

We created and tested our new electronic system for obtaining experimental spectra. By using this new programmable electronics we can significantly reduce the influence of response peaks on peak with radiative decay events. Now we can get this peak almost isolated from responses. On our estimations all these allow us to reach accuracy for our new experiment about 1%. So, on the base of our new electronics we can confirm or refuse the deviation of our average experimental value of BR from the standard model one.

As concerning the comparison of our experimental results with others we can make the following two main conclusions. The main parameters of our spectrum of double electron-proton coincidences identifying the events of ordinary neutron decay fully coincide with an analogous spectrum published by emiT group in [11].

Unfortunately we cannot say same for another experiment measuring the radiative neutron decay published in [7]. Particularly vexing is the authors' unsubstantiated assertion that they observe their only wide peak of gamma quanta before the registration of beta-electrons. Both the position and the width of this peak are located in sharp contradiction to both the elementary estimates, and the results of our experiment. In the course of our entire experiment we did not observe such a wide peak in the triple coincidences spectrum, located before the arrival of electrons at a huge distance of 1.25 μs. However, it is possible to reconcile our spectra of triple coincidences with the one isolated peak observed at NIST if we assume that at NIST, the gamma-quanta were registered after the beta electrons. Only in this case does the NIST peak almost completely coincide with the peak we observed in the spectra of triple coincidences with the maximum in channel 165, both in terms of the huge delay of 1.25 μs and in terms of its huge width. This peak is created by the delayed secondary

radioactive gamma-quanta, arising from the activation by beta electrons of the media inside experimental chamber, which was the real object of the NIST experimentalists' observation.

Despite the recent disagreements [15], which we consider to be subjective in nature [16], we acknowledge the contribution of our Western colleagues Profs. N. Severijns, O. Zimmer and Drs. H.-F. Wirth, D. Rich to our experiment conducted in 2005. Here it is important to note that the authors of the article published in Nature [7] consciously misled first our Western colleagues and then the physics community at large by insisting that their only wide peak is removed by 1.25 microseconds to the left from the time of electron registration, when in reality this peak was formed by delayed gamma-quanta, emitted by the activated medium inside the experimental equipment, and corresponds to our wide peak with the maximum in channel 165 (refer to Fig.6) [15, 16]**.** The authors would like to thank Profs. D. Dubbers and Drs. T. Soldner, G. Petzoldt and S. Mironov for valuable remarks and discussions. We are also grateful to the administration of the FRMII, especially Profs. K. Schreckenbach and W. Petry for organizing our work. We would especially like to thank RRC President Academician E.P. Velikhov and Prof. V.P. Martem'yanov for their support, without which we would not have been able to conduct this experiment. Financial support for this work was obtained from RFBR (Project N 014-02-00174).

References

1. Gaponov Yu.V., Khafizov R.U., Phys. Lett. B **379** (1996) 7–12.
2. Yu.V. Gaponov, R.U. Khafizov., Radiative neutron beta-decay and experimental neutron anomaly problem. Weak and electromagnetic interactions in nuclei (WEIN '95): proceedings. Edited by H. Ejiri, T. Kishimoto, T. Sato, River Edge, NJ, World Scientific, 1995, 745p.
3. R.U. Khafizov, N. Severijns, About the possibility of conducting an experiment on radiative neutron beta decay Proceedings of VIII International Seminar on Interaction of Neutrons with Nuclei (ISINN-8) Dubna, May 17–20, 2000 (E3-2000-192), 185–195.
4. Khafizov R.U., Physics of Particles and Nuclei, Letters **108** (2001) 45–53.
5. M. Beck, J. Byrne, R.U. Khafizov, et al., JETP Letters **76**, 332 (2002).
6. R.U. Khafizov, N. Severijns, O. Zimmer, et al., JETP Letters **83**, 5 (2006).
7. J.S. Nico, et al., Nature, v. **444** (2006) p. 1059–1062.
8. R.U. Khafizov, N. Severijns et al., Discovery of the neutron radiative decay Proceedings of XIV International Seminar on Interaction of Neutrons with Nuclei (ISINN-14), Dubna, May 24–25, 2006.
9. B.G. Yerozolimsky, Yu.A. Mostovoi, V.P. Fedunin, et al., Yad. Fiz. **28**, 98 (1978); [Sov. J. Nucl. Phys. **28**, 48 (1978)].
10. I.A. Kuznetsov, A.P. Serebrov, I.V. Stepanenko, et al., Phys. Rev. Lett. **75**,794 (1995).
11. L.J. Lising, S.R. Hwang, J.M. Adams, et al., Phys. Rev. C **6**, 055501 (2000).
12. J. Byrne, R.U. Khafizov, Yu.A. Mostovoi, et al., J. Res. Natl. Inst. Stand. Technol. **110**, 415 (2005).
13. R.L. Cooper, T.E. Chupp, M.S. Dewey, et al, Phys. Rev. C **81**, 035503 (2010).
14. T.J. Paulus, IEEE Transactions on Nuclear Science, v.NS-32, no.3, June, p.1242, 1985.
15. N. Severijns, et al., e-print arXiv:nucl-ex/0607023; J. Nico, private communication.
16. R.U. Khafizov, V.A. Solovei, e-print arXiv:nucl-ex/0608038.

DEVELOPMENT OF THE CONCEPT OF NUCLEAR EXCHANGE BETA-FORCES. ON THE POSSIBILITY OF OBTAINING NEUTRON SUBSTANCE IN LABORATORY CONDITIONS

G.B. Ryazantsev[1], I.N. Beckman[1], G.K. Lavrenchenko[2], I.M. Buntseva[1],
S.S. Nedovesov[3]

[1]*Lomonosov Moscow State University, Leninskie Gory, Moscow, Russia, anis-mgu@rambler.ru*
[2]*LLC «Institute of Low Temperature Energy Technology», POB188, Odessa,Ukraine,
lavrenchenko.g.k.@gmail.com*
[3]*Shevchenko National University of Kyiv, Ukraine, pc.remont.tk@gmail.com*

ABSTRACT. In 1932, Heisenberg suggested that the interaction of a neutron with a proton is due to the exchange of an electric charge between these particles [1]. E. Fermi proposed in 1934 the theory of β-radioactivity [2], in which the proton can, under certain conditions, become a neutron and vice versa; at the same time, the electric charge of a heavy particle is changed due to the emission or absorption of two light particles: a neutrino and an electron or positron. The Fermi theory, therefore, contains a certain mechanism for the exchange of electric charge between a proton and a neutron, which was considered by Heisenberg as the basis for the interaction of these particles, and makes possible a theoretical calculation of this interaction, based on data on β decay. The emission and absorption of light particles (electrons, positrons, neutrinos) by heavy particles (protons and neutrons) must be due to the interaction of heavy particles (Heisenberg-Fermi field) in the same way as the emission and absorption of photons is due to the interaction of electric charges (Maxwell's field) . E. Fermi, D.D. Ivanenko and I.E. Tamm arrived at this conclusion independently and almost simultaneously. The calculation of the neutron-proton interaction, based on the Fermi β-decay theory, was carried out by Tamm and his result was very disappointing for ordinary nuclei. The theory of Tamm [3], which he put forward at one time (1934) to explain the mechanism of nuclear forces for ordinary nuclei was not consistent for them. Tamm himself valued his "unsuccessful" theory of nuclear forces more than his Nobel work on Cherenkov radiation.

However, there is reason to believe that the Tamm interaction can be realized precisely for superheavy nuclei (neutron matter) of an appropriate scale (of the order of 200–300 or more femtometers), giving it additional stability. In strongly interacting systems, many virtual particles are present and all kinds of interactions are allowed, resolved by considerations of invariance. V.L. Ginzburg and E.L. Feinberg believed: "... although these beta forces, of course, exist, they do not ensure the stability of the nuclei" [3]. This is true for ordinary nuclei, but is fundamentally changing for super heavyweight. The "original" theory of exchangeable β-nuclear forces Tamm (e - exchange of nucleons), and not only its modification of Hideki Yukawa (π-exchange of nucleons), is still waiting for its recognition and "dominates" in the neutron matter of the Universe, ensuring its stability and wide cosmic distribution, as well as the possibility of obtaining neutron matter in laboratory conditions [4,5].

Introduction

It should be noted that from the very beginning electrons were assigned a significant role in the atomic nucleus. According to E. Rutherford's model before the discovery of the neutron, it was believed that the nuclei consist of protons and electrons. This model was based on two experimental facts: in nuclear reactions with α-particles protons fly out of nuclei, and electrons in radioactive β-decay. In accordance with the classical concepts of the composite system, the nucleus should have seemed to consist of these particles. But on this path there were insurmountable obstacles. To solve these problems, N. Borh even suggested that electrons, entering nuclei, "lose their individuality" and their own moment — spin, and the energy conservation law is satisfied only statistically, i.e. may be violated in individual β-decay acts.

The assumption about the presence in the nucleus of neutral particles with spin 1/2 was already contained in the well-known letter of V. Pauli, where in 1930 he expressed the hypothesis of the existence of a certain neutral particle ejecting from the nucleus along with the β-electron escaping observation energy conservation law in β-decay. But only after the discovery of the neutron was the idea of the possibility of electron production in the process of β decay allowed D.D. Ivanenko suggests that nuclei are composed of protons and neutrons.

Problem of β-nuclear forces

Consider the problem of β-nuclear forces from the standpoint of the theory of β-decay. Immediately after the work of Fermi, I.Ye. Tamm [6] and D.D. Ivanenko [7], it was independently hypothesized that the short-range interaction between a neutron and a proton in the nucleus can occur due to the exchange of an electron-antineutrino pair according to the scheme If we present the Tamm interaction in the form of a Feynman diagram:
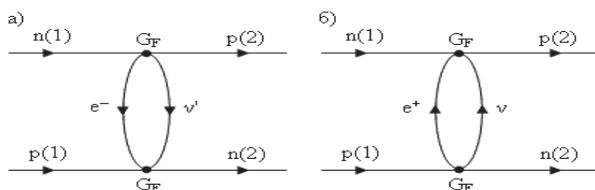
The exchange interaction between the neutron n and the proton p, arising according to the idea of Tamm and Ivanenko due to β-forces.

Neutron n(1), emitting an electron e^- and antineutrino ν ', turns into proton p(2), and proton p(1), absorbing electron and antineutrino - into neutron n(2) (a). The proton p(1), emitting a positron e^+ and a neutrino ν, turns into a neutron n(2), and a neutron n(1), absorbing a pair (e^+ and ν) - into a proton p(2). Gf is a constant characterizing β-forces (b).

The undertaken estimates, based on the experimentally determined β-interaction constant of the Gf, showed, however, that the forces arising between the nucleons due to the exchange β-interactions turn out to be 14–15 orders of magnitude smaller than those needed to hold the nucleons in the atomic nucleus. It would seem that the authors suffered a failure. But the work of Tamm and Ivanenko stimulated the Japanese physicist H. Yukawa, who had alluded to this work, to put forward a new hypothesis. Yukawa suggested that the interaction between the nucleons occurs through the exchange of an unknown previously charged particle, the mass of which he predicted, based on the experimentally known radius of action of nuclear forces.

Nuclear and subatomic physics and weak interaction
Yu.L. Ratis

Institute of power engineering for special applications

Abstract

The formalism allowing to calculate a creation cross-section of the neutrino's exoatom and its decay probability as well as to analyze other exotic electroweak processes without use of heuristic assumptions is constructed. The easiest neutrino's exoatom the "neutroneum" considered in ref. [1] can be interpreted as "the quasi-bound state of a quasi-neutron and a quasi-neutrino". Here and below the prefix "quasi" means that the metastable compound system can be considered as exoatom in which neutrino moves near a neutron. The special property of the neutrino is used for this purpose, namely: the boundary condition "zero at infinity" for the neutrino wave function. This condition is not forbidden if the decay of the neutrino exoatom into the residual atom and the electron is allowed by the energy conservation law. But at the same time the exoatom decay with only neutrino emission is forbidden.

1. Introduction

The base of the theory of neutrino exoatom was developed in [1]. The easiest of them named the "neutroneum" can be interpreted as "the quasi-bound state of the quasi-neutron and the quasi-neutrino" [1]. Here and below the prefix "quasi" means that the metastable compound system can be considered as the exoatom in which the neutrino moves near the neutron. The role of different boundary conditions in physics of nuclear β-processes at the low energies was investigated in [1-2]. It was shown that, at least, for the easiest neutrino exoatom the neutroneum the neutrino confinement in compound system the quasi-neutrino plus the quasi-neutron is not caused by the neutron - neutrino interaction but due to the energy and momentum conservation laws.

We develop below the mathematical formalism for description of the induced exotic electron capture by any atomic nuclei resulting in a creation of the neutrino exoatoms. This approach provides the methodical basis for an analysis of the secondary effects in similar β - processes.

2. Main formalism

Let's consider Hamiltonian describing the exotic electroweak resonances (neutrino exoatom) for interaction of leptons with nucleons:

$$\hat{H} = \hat{H}_0 + \hat{V}_c + \hat{V}_w \tag{2.1}$$

Free Hamiltonian $\hat{H}_0$ in the second quantization representation (SQR) is

$$\hat{H}_0 = \sum_{\lambda_e} \varepsilon_{\lambda_e} \hat{e}^+_{\lambda_e} \hat{e}_{\lambda_e} + \sum_{\lambda_\nu} \varepsilon_{\lambda_\nu} \hat{\nu}^+_{\lambda_\nu} \hat{\nu}_{\lambda_\nu} + \sum_{\lambda_p} \varepsilon_{\lambda_p} \hat{p}^+_{\lambda_p} \hat{p}_{\lambda_p} + \sum_{\lambda_n} \varepsilon_{\lambda_n} \hat{n}^+_{\lambda_n} \hat{n}_{\lambda_n} + \sum_{\lambda_{n_\nu}} \varepsilon_{\lambda_{n_\nu}} \hat{\eta}^+_{\lambda_{n_\nu}} \hat{\eta}_{\lambda_{n_\nu}} \tag{2.2}$$

where $\hat{e}_{\lambda_e}, \hat{\nu}_{\lambda_\nu}, \hat{p}_{\lambda_p}, \hat{n}_{\lambda_n}, \hat{\eta}_{\lambda_{n_\nu}}$ - are the electron, neutrino, proton, neutron and the neutroneum annihilation operators, respectively, and Hermitian conjugate terms are the creation operators for the same particles. Index n_ν here and below means that we deal with the neutroneum.

If the wave functions (WF) of all particles belonging to the continuous spectrum are normalized to δ - function, the sums in (2.2) (and further) are integrals over momentum $\vec{p}_x$ and the sums over the spin projections m_x of the particles:

$$\sum_{\lambda_x} \hat{R}_x = \sum_{\underline{m}_x} \int d\vec{p}_x \hat{R}(\underline{m}_x) \tag{2.3}$$

We postulate that the Hamiltonian of interaction is (See (2.1)):

$$\hat{V} = \hat{V}_c + \hat{V}_w \tag{2.4}$$

and

$$\hat{V}_c = \hat{V}_{ee} + \hat{V}_{pp} + \hat{V}_{ep} \tag{2.5}$$

where $\hat{V}_{ee}$ - Coulomb potential of electron-electron interaction

$$\hat{V}_{ee} = \frac{1}{2} \sum_{\lambda_e^{(1)}, \lambda_e^{(2)}, \lambda_e^{(3)}, \lambda_e^{(4)}} \left\langle \lambda_e^{(1)} \lambda_e^{(2)} \left| V_c \right| \lambda_e^{(3)} \lambda_e^{(4)} \right\rangle \hat{e}_{\lambda_e^{(1)}}^+ e_{\lambda_e^{(2)}}^+ \hat{e}_{\lambda_e^{(4)}} \hat{e}_{\lambda_e^{(3)}} \tag{2.6}$$

$\hat{V}_{pp}$ - Coulomb potential of proton - proton interaction

$$\hat{V}_{pp} = \frac{1}{2} \sum_{\lambda_p^{(1)}, \lambda_p^{(2)}, \lambda_p^{(3)}, \lambda_p^{(4)}} \left\langle \lambda_p^{(1)} \lambda_p^{(2)} \left| V_c \right| \lambda_p^{(3)} \lambda_p^{(4)} \right\rangle \hat{p}_{\lambda_p^{(1)}}^+ \hat{p}_{\lambda_p^{(2)}}^+ \hat{p}_{\lambda_p^{(4)}} \hat{p}_{\lambda_p^{(3)}} \tag{2.7}$$

$\hat{V}_{ep}$ - Coulomb potential of electron - proton interaction:

$$\hat{V}_{ep} = \sum_{\lambda_e, \lambda_p, \lambda_e', \lambda_p'} \left\langle \lambda_e \lambda_p \left| V_c \right| \lambda_e' \lambda_p' \right\rangle \hat{e}_{\lambda_e}^+ \hat{e}_{\lambda_e'} \hat{p}_{\lambda_p}^+ \hat{p}_{\lambda_p'} \tag{2.8}$$

To take into account the contribution of the weak interaction we use formulae

$$\hat{V}_w = \sum_{\lambda_e, \lambda_p, \lambda_{n_\nu}} \left\langle ep \left| V_{n_\nu \to ep} \right| n_\nu \right\rangle \hat{e}_{\lambda_e}^+ \hat{p}_{\lambda_p}^+ \hat{\eta}_{\lambda_{n_\nu}} + \sum_{\lambda_p, \lambda_n, \lambda_{n_\nu}} \left\langle \nu_e n \left| V_{n_\nu \to \iota n} \right| n_\nu \right\rangle \hat{\nu}_{\lambda_\nu}^+ \hat{n}_{\lambda_n}^+ \hat{\eta}_{\lambda_{n_\nu}} + h.c. \tag{2.9}$$

It was shown [1-2] that $(\hbar = c = 1)$

$$\left\langle ep \left| V_{n_\nu \to ep} \right| n_\nu \right\rangle = \frac{G_\partial}{\sqrt{2V^3 V_{eff}^{n_\nu}}} (2\pi)^3 \delta(\vec{k}_{n_\nu} - \vec{k}_p - \vec{k}_e) \hat{S}(j_{n_\nu}, \underline{m}_{n_\nu} | \underline{m}_p, \underline{m}_e). \tag{2.10}$$

where V is the normalizing volume, and the angular factor in (2.10) is equal

$$\hat{S}(j_{n_\nu}, \underline{m}_{n_\nu} | \underline{m}_p, \underline{m}_e) = C_{1/2 \, \underline{m}_p \, 1/2 \, \underline{m}_e}^{j_{n_\nu} \, \underline{m}_{n_\nu}} \phi_{ep}(j_{n_\nu}). \tag{2.11}$$

and

$$\phi_{ep}(j_{n_\nu}) = 1 + 6\lambda(-1)^{j_{n_\nu}} \begin{Bmatrix} 1 & 1/2 & 1/2 \\ j_{n_\nu} & 1/2 & 1/2 \end{Bmatrix} \tag{2.12}$$

The matrix element (2.10) contains wave function in cat-vector $\left| n_\nu \right\rangle$, which by definition is

$$\left| n_\nu \right\rangle = \sum_{\underline{m}_n, \underline{m}_\nu} C_{1/2 \, \underline{m}_n \, 1/2 \, \underline{m}_\nu}^{j_{n_\nu} \, \underline{m}_{n_\nu}} \left| n \right\rangle_{\underline{m}_n} \otimes \left| \nu \right\rangle_{\underline{m}_\nu} \tag{2.13}$$

and the neutrino WF (2.13) satisfies to the boundary condition

$$\lim_{r \to \infty} \left| \nu \right\rangle_{\underline{m}_\nu} = 0 \tag{2.14}$$

According to [1]

$$\begin{cases} \phi_{ep}(0) = 1 + 3\lambda \approx 4.69 \\ \phi_{ep}(1) = 1 - \lambda \approx -0.23 \end{cases} \tag{2.15}$$

46

The operators $\hat{e}_{\lambda_e}, \hat{\nu}_{\lambda_\nu}, \hat{p}_{\lambda_p}, \hat{n}_{\lambda_n}, \hat{\eta}_{\lambda_{n_\nu}}$ satisfy to the standard anti-commutation and commutation rules:

$$\{\hat{e}_{\lambda_e}, \hat{e}^+_{\lambda'_e}\} = \delta_{\lambda\lambda'_e} = \delta(\vec{p}_e - \vec{p}'_e)\delta_{m_e m'_e} \;; \qquad \{\hat{e}_{\lambda_e}, \hat{e}_{\lambda'_e}\} = \{\hat{e}^+_{\lambda_e}, \hat{e}^+_{\lambda'_e}\} = 0 \qquad (2.16)$$

$$\{\hat{\nu}_{\lambda_\nu}, \hat{\nu}^+_{\lambda'_\nu}\} = \delta_{\lambda\lambda'_\nu} = \delta(\vec{p}_\nu - \vec{p}'_\nu)\delta_{\underline{m}_\nu \underline{m}'_\nu} \;; \qquad \{\hat{\nu}_{\lambda_\nu}, \hat{\nu}_{\lambda'_\nu}\} = \{\hat{\nu}^+_{\lambda_\nu}, \hat{\nu}^+_{\lambda'_\nu}\} = 0 \qquad (2.17)$$

$$\{\hat{p}_{\lambda_p}, \hat{p}^+_{\lambda'_p}\} = \delta_{\lambda_p\lambda'_p} = \delta(\vec{p}_p - \vec{p}'_p)\delta_{\underline{m}_p \underline{m}'_p} \;; \qquad \{\hat{p}_{\lambda_p}, \hat{p}_{\lambda'_p}\} = \{\hat{p}^+_{\lambda_p}, \hat{p}^+_{\lambda'_p}\} = 0 \qquad (2.18)$$

$$\{\hat{n}_{\lambda_n}, \hat{n}^+_{\lambda'_n}\} = \delta_{\lambda_n\lambda'_n} = \delta(\vec{p}_n - \vec{p}'_n)\delta_{\underline{m}_n \underline{m}'_n} \;; \qquad \{\hat{n}_{\lambda_n}, \hat{n}_{\lambda'_n}\} = \{\hat{n}^+_{\lambda_n}, \hat{n}^+_{\lambda'_n}\} = 0 \qquad (2.19)$$

$$[\hat{\eta}_{\lambda_{n_\nu}}, \hat{\eta}^+_{\lambda'_{n_\nu}}] = \delta_{\lambda_{n_\nu}\lambda'_{n_\nu}} = \delta(\vec{p}_{n_\nu} - \vec{p}'_{n_\nu})\delta_{j_{n_\nu} j'_{n_\nu}}\delta_{\underline{m}_{n_\nu} \underline{m}'_{n_\nu}} \;; \qquad [\hat{\eta}_{\lambda_{n_\nu}}, \hat{\eta}_{\lambda'}] = [\hat{\eta}^+_{\lambda_{n_\nu}}, \hat{\eta}^+_{\lambda'_{n_\nu}}] = 0 \qquad (2.20)$$

$$[\hat{e}_{\lambda_e}\hat{\eta}^+_{\lambda_{n_\nu}}, \hat{\eta}^+_{\lambda_{n_\nu}}\hat{e}_{\lambda_e}] = [\hat{p}_{\lambda_p}\hat{\eta}^+_{\lambda_{n_\nu}}, \hat{\eta}^+_{\lambda_{n_\nu}}\hat{p}_{\lambda_p}] = 0 \qquad (2.21)$$

$$[\hat{\eta}_{\lambda_{n_\nu}}\hat{e}^+_{\lambda_e}, \hat{e}^+_{\lambda_e}\hat{\eta}_{\lambda_{n_\nu}}] = [\hat{\eta}_{\lambda_{n_\nu}}\hat{p}^+_{\lambda_p}, \hat{p}^+_{\lambda_p}\hat{\eta}_{\lambda_{n_\nu}}] = 0 \qquad (2.22)$$

As in the theory of finite Fermi-systems (TFFS) [3] we use basic functions for given atom. For example, the wave functions of the electron in the Coulomb field of the proton are usual Coulomb functions of discrete and continuous spectrum, i.e., eigen-functions of the Hamiltonian

$$\hat{H}^{(0)}_{ep} = \sum_{\lambda_e}\varepsilon_{\lambda_e}\hat{e}^+_{\lambda_e}\hat{e}_{\lambda_e} + \sum_{\lambda_p}\varepsilon_{\lambda_p}\hat{p}^+_{\lambda_p}\hat{p}_{\lambda_p} + \hat{V}_{ee} + \hat{V}_{pp} + \hat{V}_{ep}. \qquad (2.23)$$

It is obvious that the Hamiltonian (2.23) corresponds to the system of any interacting electrons and protons.

For the free neutrinos we use the plane waves, normalized to unit in volume V, or on δ- function. Transition from one system of normalization to another is carried out by formal substitution of $L \leftrightarrow 2\pi$. All calculations are carried out in $m_l \ll m_N$ approximation. In practice it means that the neutrons, protons and neutroneum considered as infinitely heavy particles in comparison with leptons (the electron and the neutrino).

We use the simplest set of the constants [4]

$$G_\beta \approx 8.76 \cdot 10^{-5} \; MeV \cdot fm^3 = 4.439 \cdot 10^{-7} \; fm^2, \; \lambda = 1.23 . \qquad (2.24)$$

Let's show that the ratios given above satisfy to the compliance principle and can be used to calculate all the properties of heavy neutrino atoms, and, perhaps, neutroneum stars.

3. Perturbation theory and Green's function in the theory of exotic electro-weak processes (TEEP).

The main properties (mass, spin, life-time, the creation cross-section in eH-collisions) of neutrinos exoatom neutroneum established in [1-2]. An obvious lack of works [1-2] is their heuristic character. The self-consistent theory of the creation cross-section, life-time and "effective sizes" of the neutrino exoatom requires a clear understanding the fact that "switch on" of the weak interaction changes all important properties of the hydrogen atom. The system of the eigenfunctions of the standard Coulomb Hamiltonian added by a new function, orthogonal to all eigenfunctions of the non-perturbed Hamiltonian.

Let's consider a problem of the eigenvalues (EV) and the eigenfunctions (EF) of the Hamiltonian $\hat{H}$. As we use SQR then the number of particles in the exoatom is arbitrary. When we have a small parameter, we can use the perturbation theory. In our case the

influence of the weak interaction to the full Hamiltonian is extremely small. According we can use the standard perturbation theory [5].

According to [5] we rewrite our Hamiltonian as:

$$\hat{H} = \hat{H}_0 + \hat{V}(t) \tag{3.1}$$

The Schrödinger equation for the time-dependent WF is:

$$i\hbar \frac{\partial \Psi}{\partial t} = (\hat{H}_0 + \hat{V})\Psi . \tag{3.2}$$

Exact solution Ψ we can write as superposition of EF of non-perturbed Hamiltonian:

$$\Psi = \sum_k a_k(t)\Psi_k^{(0)} \tag{3.3}$$

and

$$\hat{H}_0 \Psi_k^{(0)} = E_k^{(0)} \Psi_k^{(0)} \tag{3.4}$$

The transition probability (Fermi's "golden rule") in the framework of zero order perturbation theory is [5]

$$dw_{fi} = \frac{2\pi}{\hbar} \left| \left\langle \psi_f \left| \hat{V} \right| \psi_i \right\rangle \right| \delta(E_i - E_f) dn_f \tag{3.5}$$

where

$$\Psi(x,t) = \psi(x) \cdot \exp(-iEt / \hbar) \tag{3.6}$$

Similar expression for the first order of the perturbation theory is:

$$dw_{fi} = \frac{2\pi}{\hbar} \left| \left\langle \psi_f \left| \hat{V} \right| \psi_i \right\rangle + \int \frac{\left\langle \psi_f \left| \hat{V} \right| \psi_\nu \right\rangle \left\langle \psi_\nu \left| \hat{V} \right| \psi_i \right\rangle}{E_i - E_\nu + i0} d\nu \right|^2 \delta(E_i - E_f) dn_f \tag{3.7}$$

Let's calculate a decay probability of the exoatom neutroneum.

If the neutroneum WF is normalized to unity in the "box" with volume V, then the decay probability to proton and electron is (see [1-2]):

$$w_{n_\nu \to p + e^-} = \frac{2\pi}{\hbar} \int \frac{V d\vec{p}_e}{(2\pi\hbar)^3} \frac{V d\vec{p}_p}{(2\pi\hbar)^3} \delta(\varepsilon_{n_\nu} - \varepsilon_p - \varepsilon_e) \left\langle \left| \left\langle ep \left| \hat{V}_{ep \leftrightarrow n_\nu} \right| n_\nu \right\rangle \right|^2 \right\rangle , \tag{3.8}$$

where WF of the initial and the final states in SQR are

$$\begin{cases} \left| n_\nu \right\rangle = \eta_{\lambda_{n_\nu}}^+ \left| 0_{l\otimes N} \right\rangle \\ \left| e \right\rangle = \hat{e}_{\lambda_e}^+ \left| 0_l \right\rangle \\ \left| p \right\rangle = \hat{p}_{\lambda_p}^+ \left| 0_N \right\rangle \end{cases} \tag{3.9}$$

where $\left| 0_l \right\rangle$ - the lepton vacuum, $\left| 0_N \right\rangle$ - the nucleon vacuum, and $\left| 0_{l\otimes N} \right\rangle = \left| 0_l \right\rangle \otimes \left| 0_N \right\rangle \equiv \left| 0 \right\rangle$ - direct production of the lepton and the nucleon vacuum, as well as the external square brackets mean averaging over spin projections in the initial state and summation over spin projections in the final state.

As WF of the initial and the final states are defined by (3.9) so only one term "survives" out of all sum (2.9). Therefore according to (3.8) ($\hbar = c = 1$).

$$w_{n_\nu \to p + e^-} = \frac{\phi_{ep}^2 (j_{n_\nu}) G_\beta^2}{8\pi^2 V_{eff}^{n_\nu}} \int d\vec{k}_e \delta(\varepsilon_{n_\nu} - \varepsilon_p - \varepsilon_e) \tag{3.10}$$

is in a full agreement with [1-2].

The problem of a correct calculation of the neutroneum creation cross-section with the perturbation theory is much more difficult. To show it we consider the neutroneum creation reaction in the electron-proton collision.

According to momentum-energy conservation law

$$\left\langle \psi_f \left| \hat{V} \right| \psi_i \right\rangle \sim \delta(\vec{p}_i - \vec{p}_f) \overline{\left\langle \psi_f \left| \hat{V} \right| \psi_i \right\rangle} \tag{3.11}$$

Therefore the neutroneum creation cross-section in ep - collisions (if we take into account the known neutroneum life-time) in the framework of the zero order perturbation theory is [1-2]:

$$\sigma_{ep \to n_\nu} = \frac{2\pi}{\hbar v_e} \left| \left\langle n_\nu \left| \hat{V}_w \right| ep \right\rangle \right|^2 \frac{1}{2\pi} \cdot \frac{\Gamma_{n_\nu}}{(\varepsilon_{ep} - \varepsilon_{n_\nu})^2 + \Gamma_{n_\nu}^2 / 4}. \tag{3.12}$$

The cross-section (3.12) depends on the energy of the incoming electron. The width of the resonant peak Γ_{n_ν} in cross-section (3.12) is extremely small value since we deal with the resonance caused by the weak interaction.

4. A role of the third particle in the initial state

The vanishing width Γ_{n_ν} of a quasi-discrete level permits us to replace the Breit - Wigner formula (3.13) by δ - function $\delta(E_e + E_p - E_{n_\nu})$. It means that the radiationless processes of the neutrino exoatom creation in the free particles collisions are actually forbidden by momentum-energy conservation law.

Thus we have to use (3.7) to calculate the neutroneum creation cross-section. We can do it because the electron WF "tail" is mainly placed inside the nucleus-target (for example, in the proton). Therefore "switch on" of the weak interaction is adiabatic.

According this circumstance the ratio (3.7) we rewrite as:

$$d\sigma_{H(e,e')n_\nu} = \frac{2\pi V}{\hbar v_e} \left| \hat{s} \int \frac{V d\vec{p}_e}{(2\pi\hbar)^3} \frac{V d\vec{p}_p}{(2\pi\hbar)^3} \frac{\left\langle n_\nu \left| \hat{V}_w \right| ep \right\rangle \left\langle epe' \left| \hat{V}_{ee} \right| eH \right\rangle}{E_i - E_{ep} + i0} \right|^2 \delta(E_i - E_f) \frac{V d\vec{p}_{e'}}{(2\pi\hbar)^3} \frac{V d\vec{p}_{n_\nu}}{(2\pi\hbar)^3}$$

$$\tag{4.1}$$

Expression for reaction cross-section $H(e,e')n_\nu$ demands detailed comments.

The neutroneum creation in the gas target was studied in detail [1-2]. From the quantum mechanics point of view formula (4.1) contains the two-particle Green function $\hat{G}_{ep}$:

$$\hat{G}_{ep} \equiv \sum_{e,p} \frac{\left| ep \right\rangle \left\langle ep \right|}{E_i - E_{ep} + i0} = \int \frac{V d\vec{p}_e}{(2\pi\hbar)^3} \frac{V d\vec{p}_p}{(2\pi\hbar)^3} \frac{\left| ep \right\rangle \left\langle ep \right|}{E_i - E_{ep} + i0} \tag{4.2}$$

The sum over e, p includes all eigenfunctions of the Hamiltonian $\hat{H}_c = \hat{H}_0 + \hat{V}_c$:

$$\hat{H}_c \left| ep \right\rangle = E_{ep} \left| ep \right\rangle \tag{4.3}$$

During the derivation (4.2) we have used the fact that the WF of the initial, final and intermediate states are known. For example, WF of the initial state in obvious designations is

$$\left| \psi_i \right\rangle = \left| e \right\rangle \otimes \left| H \right\rangle \equiv \left| eH \right\rangle \tag{4.4}$$

and the hydrogen atom WF is

$$\left| H \right\rangle = \int d\vec{q}\, \varphi_{n l m_l}(\vec{q})\, \hat{e}^{+}_{\vec{q}\, m_s}\, \hat{p}^{+}_{\vec{p}_H - \vec{q}\, m_p}\, \left| 0 \right\rangle \tag{4.5}$$

The main question of the perturbation theory in the framework of TEEP - is the problem of the eigenfunctions of the Hamiltonian

$$\hat{H}_c = \hat{H}_0 + \hat{V}_c \tag{4.6}$$

The set of these WF is incomplete if we deal with the eigenfunctions of the Hamiltonian

$$\hat{H} = \hat{H}_c + \hat{V}_w \tag{4.7}$$

To make the set of two-particle electron-proton eigenfunctions complete, it is necessary to take into account a possibility of the quantum transition $ep \leftrightarrow n_\nu$. As a result the Schrödinger equation is

$$\hat{H}\psi_\lambda = E_\lambda \psi_\lambda \tag{4.8}$$

and the two-particle Green function (4.2) is modified:

$$G_{ep} = \sum_\lambda \frac{\left| \psi_\lambda \right\rangle \left\langle \psi_\lambda \right|}{E - E_\lambda + i\gamma} \tag{4.9}$$

Set $\left| \psi_\lambda \right\rangle$ contains the following basic functions:

1) the functions of a discrete spectrum of the electron in the hydrogen atom;
2) the Coulomb wave functions of a continuous spectrum;
3) the resonant state of neutroneum (state λ_0).

As the matrix element $\left\langle n_\nu \left| \hat{V}_w \right| ep \right\rangle$ is non-equal zero only for the state λ_0, so the contribution into integral (4.1) gives only a pole. This fact was taken into account in [1-2], and in the cross-section the index $\hat{s}$ stresses that the contribution gives only a pole and we have to neglect the contribution of the principal value of the integral into (4.1).

When obtaining the eigenfunctions and the eigenvalues of a Hamiltonian $\hat{H}$ it is necessary to take into account a coupling of the reaction channels: namely, the virtual transition $ep \leftrightarrow \nu n$ and the real transition $ep \leftrightarrow n_\nu$ (in the quarks "language" $eu \leftrightarrow \nu d$ emission of the d - quark at the mass surface).

A small component of the neutroneum WF in the full WF of the ep - pair we can calculate according to [5]

$$\psi_{ep} = \psi_{ep}^{(0)} + \delta\psi_{ep} \tag{4.10}$$

where $\delta\psi_{ep} = c_{n_\nu} \left| n_\nu \right\rangle$.

Above in we use WF normalized in the "box". For the further purposes is more convenient to use δ - function WF normalization. Thus

$$c_{n_\nu} = \int d\vec{k}_{n_\nu} \frac{\left\langle n_\nu \left| \hat{V}_w \right| ep \right\rangle}{E_i - E_f + i0} \tag{4.11}$$

where (see (2.10))

$$\left\langle ep \left| V_{n_\nu, ep} \right| n_\nu \right\rangle = \frac{G_\beta}{\sqrt{2(2\pi)^3 V_{eff}^{n_\nu}}}(2\pi)^3 \delta(\vec{k}_{n_\nu} - \vec{k}_p - \vec{k}_e)\hat{S}(j_{n_\nu}, \underline{m}_{n_\nu} | \underline{m}_p, \underline{m}_e) \tag{4.12}$$

In the plane wave approximation the WF of the particles in the continuous spectrum are:

1) the ep - pair

$$\psi_{ep}^{(0)} = \frac{1}{(2\pi)^3} \exp[i(\vec{k}_e \vec{r}_e + \vec{k}_p \vec{r}_p)] \cdot \chi_{1/2\underline{m}_p}(\vec{s}_p) \chi_{1/2\underline{m}_e}(\vec{s}_e) \qquad (4.13)$$

2) the neutroneum

$$\psi_{n_\nu} = \frac{1}{(2\pi)^{3/2}} \exp(i\vec{k}_{n_\nu} \vec{r}_{n_\nu}) \cdot \chi_{j_{n_\nu} m_{n_\nu}}(\vec{s}_{n_\nu}). \qquad (4.14)$$

We can easy take into account the Coulomb distortions of the WF [4].

The two-particle Green function decomposition includes the singular term c_{n_ν}

$$c_{n_\nu} = \frac{G_\beta \phi_{ep}(j_{n_\nu})}{E_{ep} - E_{n_\nu} + i\gamma} \frac{(2\pi)^{3/2}}{\sqrt{2V_{eff}^{n_\nu}}} \sum_{m_{n_\nu}} C_{1/2\underline{m}_p\, 1/2\underline{m}_e}^{j_{n_\nu} m_{n_\nu}} \qquad (4.15)$$

Therefore the Green function (4.9) has the singular component proportional to the product $\left| n_\nu \right\rangle \left\langle n_\nu \right|$. It means that in the framework of TEEP exists the state, the transition probability to which is equal:

$$\left| c_{n_\nu} \right|^2 = \frac{G_\beta^2 \breve{\phi}_{ep}^2(j_{n_\nu})}{(E_{ep} - E_{n_\nu})^2 + \gamma^2} \frac{(2\pi)^3}{2V_{eff}^{n_\nu}} \sim \delta(E_{ep} - E_{n_\nu}) \qquad (4.16)$$

The energy dependence (4.16) has a δ - function form since the Breit - Wigner resonance is caused by weak interaction, and is extremely narrow. At the same time the ratio (4.16) includes the ratio

$$\gamma \sim \frac{G_\beta^2 \breve{\phi}_{ep}^2(j_{n_\nu})}{V_{eff}^{n_\nu}} \qquad (4.17)$$

Therefore the singular component of the ep - pair Green function is not depended on the weak interaction constant G_β and an effective volume $V_{eff}^{n_\nu}$ of the neutroneum. Exactly thanks to this circumstance in formula (4.1) for the neutroneum creation cross-section only the polar term is survived and there are no the additional factors demanding measurements in special experiments.

Due to the energy-momentum conservation law the electroweak reaction $e + u \rightarrow \nu + d + G$ has a channel with recoil momentum transfer to gluon. At the quarks level of matter the existence of this channel corresponds to the reaction of the induced exotic electron capture, when the neutrino is stopped. It can lead to many the observable secondary effects [6] which are of interest to future investigations.

5. Conclusion
We can sum the results obtain above as follows.
1. The formalism allowing to investigate the exotic electroweak processes by standard methods of quantum mechanics and nuclear physics was developed.
2. The TEEP-results for the main electroweak processes are reproduced by the standard methods of the perturbation theory.

3. It was shown that the new formalism of the theory of the nuclear β- processes at the low energies satisfies to the compliance principle.
4. The correctness of the pole approximation in the TEEP was proved.
5. The base of the general theory of the neutrino atoms is created.
6. The investigations of the secondary effects which accompany the new type of the β-processes, is of huge interest, and still not described in scientific literature.

References

1. Ratis Yu.L. Neutrino's exoatom neutroneum. Hypothesis or reality? Applied physics and mathematics (rus), No. 1, (2017), 28–73.
2. Ratis Yu.L. On a role of boundary conditions in the theory of nuclear β-processes at low energies, New Concepts in Physic chapter of the New Concepts Journal, v. **22,** (2018), 3–19.
3. Migdal A.B. Theory of finite fermi-systems and property of atomic nuclei. M.: Science, 1983, 432 pages.
4. Eisenberg J.M., Greiner W. Nuclear theory, v. **2**, Excitation mechanisms of the nucleus electromagnetic and weak interactions. (rus)-M.: Atomizdat, 1973, 348 pages.
5. Landau L.D., Lifshits E.M., Quantum mechanics. The nonrelativistic theory. Course of theoretical physics. v.**3**, (Science, Moscow, 1989), 768 p.
6. Batkin I.S., Smirnov Yu.G. Secondary effects at nuclear β-decay. PNP journal, JINR, Dubna, v. **11**, No. 6, (1980), 1421–1473.

Neutron Induced Reactions

KNOCK-ON MECHANISM AND PROBABILITY OF ALPHA-CLUSTER FORMATION IN THE (*n,α*) REACTION

B. Batchimeg, G. Khuukhenkhuu, M. Odsuren, J. Munkhsaikhan and Ch. Saikhanbayar

Nuclear Research Center, National University of Mongolia, Ulaanbaatar, Mongolia

Yu.M. Gledenov, E. Sansarbayar and M.V. Sedysheva

Frank laboratory of Neutron Physics, JINR, Dubna, Russia

Guohui Zhang

Institute of Heavy Ion Physics, Peking University, Beijing, China

1. Introduction

Alpha-clustering in nuclei is one of the important subjects for nuclear structure and reaction study [1-5]. The α-clusterization of four nucleons before the emission is usually described by a preformation (or clustering) factor, which is defined as the probability of finding an α-cluster inside the parent nucleus. Consequently, this factor (or probability) should be less than or equal to one. Many attempts for evaluation of the α-cluster formation probability were carried out for a long time using different methods based on various theoretical approaches. For examples, the molecular viewpoints in nuclear structure [4,6–8], one-body model [9,10], preformed α-particle model [11], α-cluster model [12], α-particle occurrence on the surface of a nucleus [13], α-particle formation through the spectroscopic factor [14,15] ratio of the nucleon-nucleon and nucleon-alpha interaction rates [16,17], classical formula for the assault frequency of an α-particle inside a nuclear potential barrier [18,19], cluster formation model [20], density-dependent cluster model [21], binary cluster model [22], exciton model [23] and microscopic cluster model [24,25] were used to study the α-clustering effect. Most of these studies were focused on the α-decay. Several methods were suggested to determine the α-particle formation factor in the (n,α) and (p,α) reactions [10–12, 16,17,23,26]. However, the results of these attempts are not consistent and up to now a common explanation of the α-clustering in a nucleus and an unified method to obtain the α-clustering probability are not available.

Recently, from the unified viewpoint, namely, in the framework of the compound mechanism, using the statistical model we have determined the clustering factors for the resonance ($E_n \leq 5$ keV), intermediate ($E_n \approx 24 - 30$ keV), and fast ($E_n = 2 - 20$ MeV) neutron induced (n,α) reactions [27–30].

In this work we suggest a new method to derive α-clustering probability from the analysis of known experimental data of the fast neutron induced (n,α) reactions and total neutron cross sections for the ^{4}He using the knock-on mechanism. The obtained α-clustering probabilities are compared with our previous results and those determined by other approaches.

2. Method

The method suggested in this work for calculation of the α-clustering probability is based on the knock-on mechanism of nuclear reaction. In this case by analogy of Bohr's postulate of the compound mechanism, we assume that the (n,α) cross section for fast neutrons can be expressed as two stages process:

$$\sigma(n,\alpha) = \Phi_{\alpha} \cdot \sigma_n^{tot}(^4He).\tag{1}$$

Here, the (n,α) cross section is defined as the multiplication of the α-cluster formation probability on the surface of target nucleus, Φ_{α}, and total neutron cross section for the ^{4}He, $\sigma_n^{tot}(^4He)$. From (1) the α-cluster formation probability can be obtained as following:

$$\Phi_{\alpha} = \frac{\sigma(n,\alpha)}{\sigma_n^{tot}(^4He)}.\tag{2}$$

For evaluation of the α-clustering probability, the experimental data of the (n,α) cross sections and total neutron cross sections the ^{4}He were taken from the EXFOR [31] and other references.

3. Results and Discussion

3.1. Light nuclei

Energy dependence of the α-clustering probability obtained by formula (2) for 5 light nuclei of ^{6}Li to ^{20}Ne, for which fast neutron induced (n,α) reaction cross sections are available in the wide energy range, is shown in Fig.1.
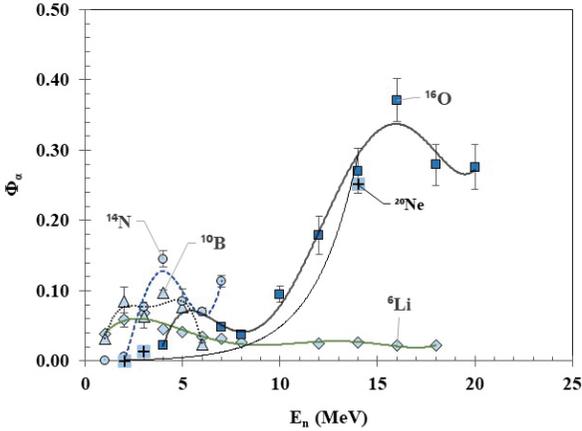
Fig.1. Energy dependence of the α-clustering probability for light nuclei.

The threshold energy calculated by binding energy [32] for some cluster structures of these nuclei is given in Table.1 together with values from Ikeda diagram [8].

Table.1. The threshold energy of some cluster structures for light nuclei

Isotope	Cluster structure	Threshold energy E_{th} (MeV)	
		Calculated values	From Ikeda Diagram [8]
^{6}Li	α+d	1.47	-
	t+t	15.81	-
^{10}B	^{6}Li+α	4.46	-
	d+2α	5.93	-
^{14}N	^{12}C+d	10.27	-
	^{10}B+α	11.61	-
	^{6}Li+2α	16.07	-
^{16}O	^{12}C+α	7.16	7.16
	4α	14.44	14.44
^{20}Ne	^{16}O+α	4.73	4.73
	^{12}C+2α	11.90	11.89
	5α	19.17	19.17

It is seen from Fig.1 that the α-clustering probabilities for given isotopes in the energy range of 1 to 10 MeV are varied not so much and with maximum value of $\Phi_\alpha = 0.145 \pm 0.011$ for the ^{14}N at the neutron energy of 4 MeV. Above 10 MeV the α-clustering probabilities are increased and reached $\Phi_\alpha = 0.371 \pm 0.031$ at $E_n = 16$ MeV and $\Phi_\alpha = 0.251 \pm 0.004$ at $E_n = 14$ MeV for the ^{16}O and ^{20}Ne, respectively. At the same time, the α-cluster formation probability of the ^{6}Li isotope with the lowest α-clusterization threshold energy (see Tab.1) among light nuclei has not the highest value and is varied in the narrow interval of 0.022 to 0.068. This fact shows that the α-clusterization threshold energy is not a single decisive factor in the α-clustering effect for these nuclei.
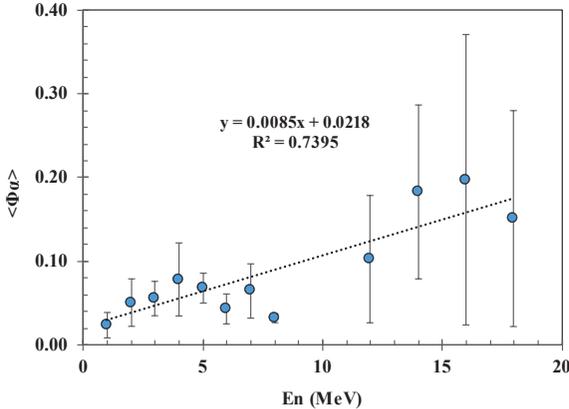
Fig.2. Energy dependence of average α-clustering probability for light target nuclei.

However, essential increasing of the α-clustering probability for the ^{20}Ne and ^{16}O in the energy region of 14 to 16 MeV is perhaps caused by opening the two α-particle ($E_{th} =$

11.90 MeV for ^{20}Ne) and four α-particle (E_{th} = 14.44 MeV for ^{16}O) emission channels for these isotopes. Arithmetic mean values of the α-clustering probability averaged over all light isotopes at each energy point are increased nearly linearly depending on the neutron energy (see Fig.2).

The α-clustering probabilities for odd-odd isotopes ^{6}Li, ^{10}B and ^{14}N at the 1 MeV are decreased depending on the neutron (or proton) number (Fig.3a). At the same time, for these isotopes the α-clustering probabilities become nearly the same at the 3 MeV (Fig.3b) and are linearly increased at the 4 and 5 MeV (Fig.4) depending on the neutron number.

a)   b)
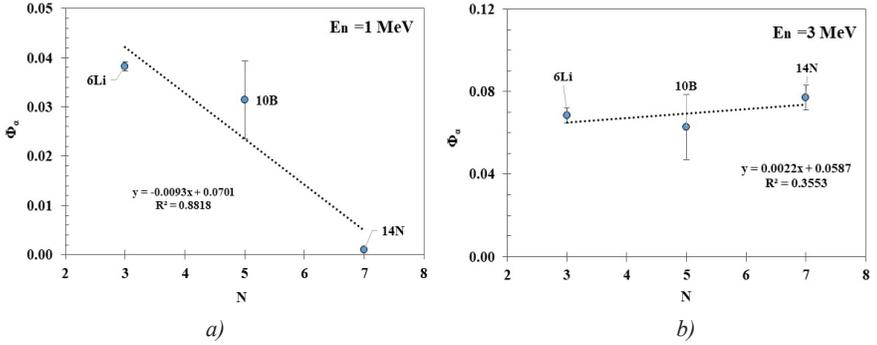
Fig.3. The dependence of the α-clustering probability on neutron number for light odd-odd target nuclei at the 1 MeV (a) and 3 MeV (b).

a)   b)
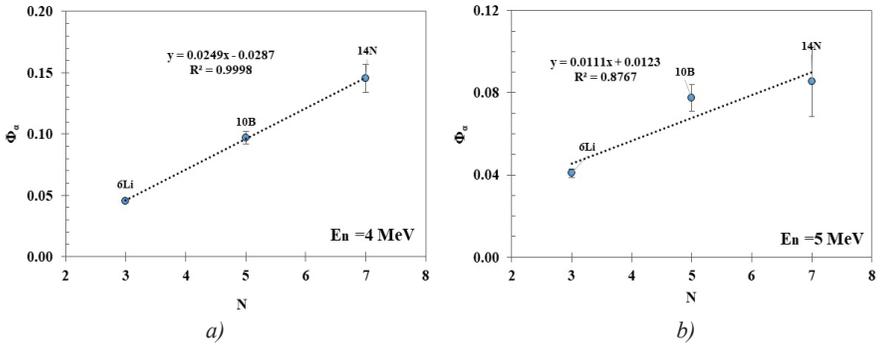
Fig.4. The same as in Fig.3 at the neutron energy 4 MeV (a) and 5 MeV (b).

3.2. Medium mass nuclei

Energy dependence of the α-clustering probability calculated by the formula (2) for 11 medium mass target nuclei is shown in Fig.5.
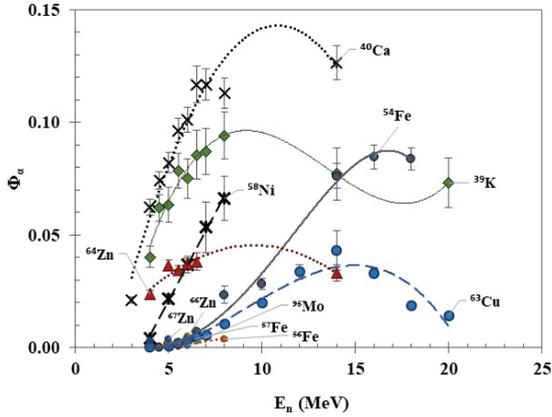
Fig.5. The same as in Fig.1 for medium mass nuclei

Some increasing tendency of the α-clustering probability for all nuclei was observed in the beginning of neutron energy. Among these isotopes the highest α-clustering probability was obtained for the double magic even-even ^{40}Ca. It can be seen that values of the α-clustering probability for the medium mass nuclei are on average lower than those for light nuclei.
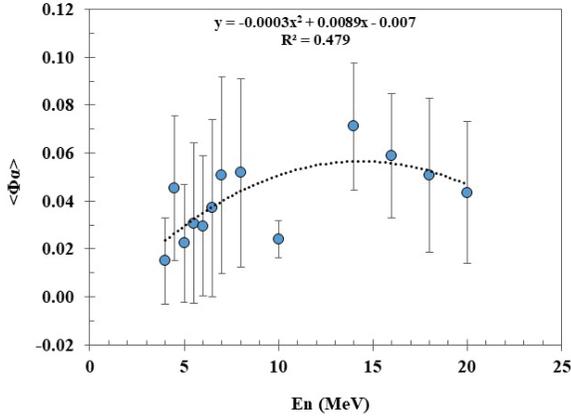
Fig.6. The same as in Fig.2 for medium mass nuclei.

Arithmetic average values of the α-clustering factor at each neutron energy for all medium mass nuclei are increased in the range of 4 to 14 MeV, except value at 10 MeV, after that are decreased, however they have wide dispersions (Fig.6).

3.3. Heavy nuclei

The (n,α) reaction experimental data base for heavy nuclei is very scarce for fast neutrons. In connection with this situation four isotopes of the neodymium and samarium are considered, only, for several MeV energy range. Fig.7 shows that the α-clustering probabilities for these nuclei are increased depending on the neutron energy. In addition, all values of the α-clustering probability for heavy nuclei are considerably lower than one for light and medium mass isotopes.
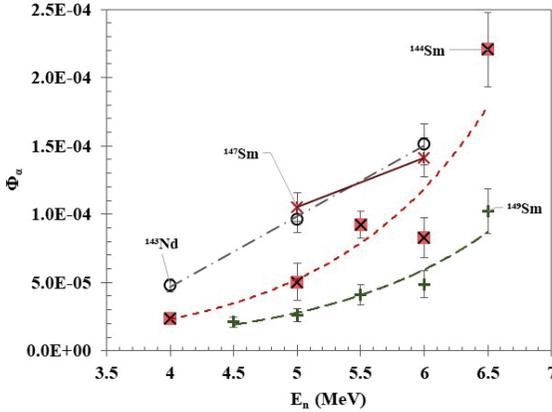
Fig.7. The same as in Fig.1 for heavy nuclei.
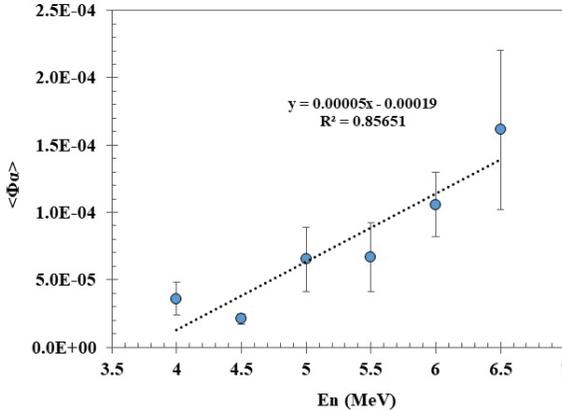
Fig.8. The same as in Fig.2 for heavy nuclei.

The arithmetic average values of the α-clustering probability for heavy nuclei at 4.0, 4.5, 5.0, 5.5, 6.0 and 6.5 MeV are increased linearly depending on the neutron energy (Fig.8).

4. Conclusions

1. The α-clustering probability in the fast neutron induced (n,α) reactions for light, medium mass and heavy nuclei was obtained using the knock-on mechanism.
2. It was seen that the α-clustering probability at the same neutron energy is on average decreased depending on the mass number of the target nuclei.
3. The α-clustering probability for light and heavy nuclei is increased with growth of neutron energy. At the same time, for medium mass nuclei the α-clustering probability is increased in the range of 4 to 14 MeV and from 14 to 20 MeV is decreased.
4. The α-clustering probabilities found in the present work are on average in a satisfactory agreement with our previous results which were obtained in the framework of the statistical model using the comparison method of the (n,α) and (n,p) cross sections [30]. Our present values of the α-clustering probability are lower than those obtained by normalizing of theoretical (n,α) cross sections to experimental ones [27] and using the preformed α-particle model [11].

References

1. P.E.Hodgson, Alpha-clustering in Nuclei, In book: "The Uncertainty Principle and Foundations of Quantum Mechanics". Editors: W.C.Price and S.S.Chissick, Chapter 23, New York, John Wiley, 1977, p.485.
2. K.Wildermuth and Y.C.Tang, An Unified Theory of the Nucleus, Academic Press, Inc. New York, 1977.
3. Clusters in Nuclei, Editor: Christion Beck, vol.**1**, (2010), vol.**2**, (2012) and vol.**3**, (2014), Springer-Verlag, Berlin Heidelberg.
4. W.Von Oertzen, M.Freer and Y.Kanada-En'yo, Physics Reports, v.**432**, 2006, p.43.
5. H.Horiuchi, I.Ikeda and K.Katō, Progress of Theoretical Physics Supplement, N192, 2012, p.1.
6. J.A.Wheeler, Phys. Rev., v.**52**, 1937, p.1083.
7. Structure of Atomic Nuclei, Handbuch der Physik, vol.XXXIX, Edited by S.Flügge, Springer-Verlag, Berlin, 1957.
8. K.Ikeda, N.Takigawa and H.Horiuchi, Supplement of the Prog. Theor. Phys., Extra Number, 1968, p.464.
9. H.A.Bethe, Rev. Mod. Phys., v.**9**, 1937, p.69
10. Yu.P.Popov *et al.*, Sov. J. Nucl. Phys., v.**13**, 1971, p.913.
11. R.Bonetti and L.Milazzo-Colli, Phys. Lett., v.**49**B, 1974, p.17.
12. S.G.Kadmensky and V.I.Furman, Physics of Particles and Nuclei, v.6 (2), 1975, p.469.
13. F.C.Chang, Phys. Rev., vol.**141**, 1966, p.1136
14. I.Tonozuka and A.Arima, Nucl. Phys., v.**323**A, 1979, p.45.
15. W.M.Seif, J.Phys.G: Nucl. Part. Phys., v.**40**, 2013, p.105102.
16. T.Knellwolf and J.Rossel, Helv. Phys. Acta., v.**39**, (1966), p.376.
17. J.I.Hogan, Z.Phys., v.**295** A, 1980, p.169
18. Shuqing Guo *et al.,* Nucl. Phys., v.**934**A, 2015, p.110.
19. G.L.Zhang *et al.,* Nucl. Phys., v.**823**A, 2009, p.16.
20. Saad M.Saleh Ahmed *et al.,* J. Phys. G: Nucl. Part. Phys., v.**40**, 2013, p.065105.
21. Dondong Ni and Zhongzhou Ren, Phys. Rev., v.**82**C, 2010, p.024311.

22. T.T.Ibrahim and S.M.Wyngaardt, J.Phys. G: Nucl. Part. Phys., v.**41**, 2014, p.055111.
23. A.Iwamoto and K.Harada, Phys. Rev., v.**26**C, 1982, p.1821
24. M.Freer *et al.,* Microscopic Clustering in Nuclei, arXiv: 1705.06192v1 [nucl-th] 17 May 2017.
25. Y.C.Tang, Nucl. Phys., v.**463**A, 1987, p.377c.
26. E.Gadioli and P.E.Hodgson, Pre-Equilibrium Nuclear Reactions, Clarendon Press, Oxford, 1992.
27. G.Khuukhenkhuu *et al.,* Proceedings of the XXIV International Seminar on Interaction of Neutrons with Nuclei, JINR, Dubna, 2017, p.166.
28. G.Khuukhenkhuu *et al.,* Proceedings of the XXV International Seminar on Interaction of Neutrons with Nuclei, JINR, Dubna, 2017, p.(in press).
29. G.Khuukhenkhuu *et al.,* Proceedings of the 8th AASPP Workshop on Asian Nuclear Reaction Database Development, INDC(MGL)-0001, IAEA, Vienna, Austria, 2018, p.70.
30. G.Khuukhenkhuu *et al.,* Acta Physica Polonica, v.**49**B, 2018, p.325.
31. http:/www-nds.iaea.org/exfor/exfor.htm
32. A.H.Wapstra and G.Audi, Nucl. Phys., v.**432**A, 1985, p.1.

CROSS SECTIONS OF THE ^{144}Sm(n,a)^{141}Nd REACTION AT 5.5 AND 6.5 MeV

Yu.M. Gledenov[1], M.V. Sedysheva[1], L. Krupa[2,3], E. Sansarbayar[1], G. Khuukhenkhuu[4], Haoyu Jiang[5], Huaiyong Bai[5], Yi Lu[5], Zengqi Cui[5], Jinxiang Chen[5], Guohui Zhang[5]

[1]*Frank Laboratory of Neutron Physics, Joint Institute for Nuclear Research, Dubna 141980, Russia*
[2]*Flerov Laboratory of Nuclear Reactions, Joint Institute for Nuclear Research, Dubna 141980*
[3]*Institute of Experimental and Applied Physics, Czech Technical University in Prague, Horska*
[4]*Nuclear Research Centre, National University of Mongolia, Ulaanbaatar, Mongolia*
[5]*State Key Laboratory of Nuclear Physics and Technology, Institute of Heavy Ion Physics, Peking University, Beijing 100871, China*

ABSTRACT

The ^{144}Sm(n,α)^{141}Nd cross sections were measured at E_n = 5.5 and 6.5 MeV. The experiments were performed at the 4.5 MV Van de Graaff Accelerator of Peking University. A twin-gridded ionization chamber was used as the detector, and back-to-back ^{144}Sm$_2$O$_3$ samples were mounted on its common cathode. The mono-energetic neutrons were generated using energetic deuteron beam from the accelerator to bombard a deuterium gas target. The relative neutron flux was monitored using a BF$_3$ long counter. The absolute neutron flux was calibrated using a ^{238}U standard sample. The present results are compared with existing measurements and evaluations.

I. INTRODUCTION

^{144}Sm, a stable isotope of samarium (natural abundance 3.08%), is the fission product in nuclear reactors. The study of ^{144}Sm(n,α)^{141}Nd reaction is important in nuclear engineering applications. Besides, measurements of this cross section could enhance our understanding in nuclear physics. For example, in nuclear astrophysics, the (n,α) cross sections of samarium could be used in the calculations of reaction rates which are significant in the analysis of explosive nucleosynthesis [1]. However, the measurements are quite scanty for this reaction. For neutron energies from 4 to 7 MeV, there is no measurement except our results in 2016 because of the small cross section of this reaction and the low intensity of the neutron flux [2]. For other neutron energy region, only three measurements exist around 14 MeV, and there are three-times differences among them [3-5]. Thus, the ^{144}Sm(n,α)^{141}Nd reaction cross section differs by more than one orders of magnitude among different evaluated nuclear data libraries [6]. So, accurate measurements are demanded to clarify exciting discrepancies among different libraries and address application needs.

For samarium isotopes, we have measured the cross sections of the ^{144}Sm(n,α)^{141}Nd at E_n = 4.0, 5.0 and 6.0 MeV [2], the ^{147}Sm(n,α)^{144}Nd reaction at E_n = 5.0 and 6.0 MeV [7], and the ^{149}Sm(n,α)^{146}Nd reaction at E_n = 4.5, 5.0, 5.5, 6.0 and 6.5 MeV [8,9]. In the present work, we measured the ^{144}Sm(n,α)^{141}Nd reactions at E_n = 5.5 and 6.5 MeV.

II. DETAILS OF EXPERIMENTS

The experiments were performed at the 4.5-MV Van de Graaff accelerator of Peking University, China. The experimental apparatus, which is shown in Fig.1, consists of three main parts: the neutron source, the charged particle detector (with samples inside) and the neutron flux monitor.

1– Cathode; 2– Grid; 3– Anode; 4– Shield
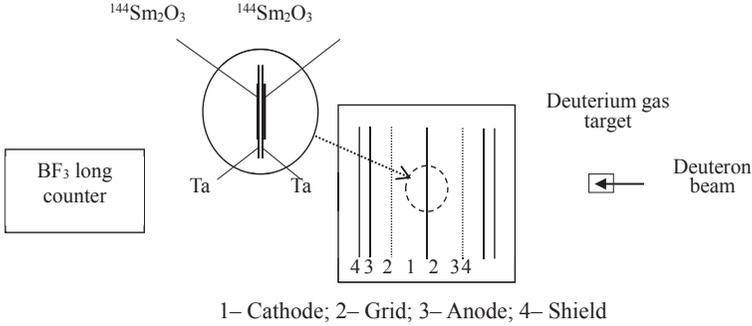
Fig. 1. Experimental setup.

The mono-energetic neutrons were generated using energetic deuteron beam from the accelerator to bombard a deuterium gas target. For neutron energies of 5.5 and 6.5 MeV, the corresponding neutron energy spreads (1σ) were 0.14 and 0.10 MeV, respectively [9]. The beam current was about 2.0 μA throughout the measurement.

The α-particle detector is a twin gridded ionization chamber (GIC) with a common cathode, and its structure can be found in Ref. [10]. The distance from the cathode to the grid was 61 mm, from grid to anode was 15 mm, and from the position of samples to the near end of the gas target cell was 15.25 cm. Working gas of the GIC was Kr +2.83% CO_2, and the pressure is 2.02 atm for the α-particles to be stopped before reaching the grids. High voltages applied on the cathodes and anodes were -2600 V and 1300 V (the grids electrodes were grounded) which allowed complete collection of electrons from the ionization tracks.

A sample changer was set at the common cathode of the ionization chamber with five sample positions, and back-to-back double samples can be placed at each of them. The sample positions could be changed without opening the GIC. Each $^{144}Sm_2O_3$ sample was prepared on the 0.1mm thick tantalum backing. Two back-to-back $^{144}Sm_2O_3$ samples were mounted on the common cathode so that forward ($0° \sim 90°$) and backward ($90° \sim 180°$) emitted α-particles can be detected simultaneously. Data of the samples are listed in Table 1, and the number of ^{144}Sm atoms in the samples was determined by weighing the samples. Besides, two back-to-back tantalum films 0.1 mm in thickness were mounted on another sample position for background measurements. In addition, two compound α-sources were back-to-back placed at one of the sample positions for energy calibration and adjustment of the data acquisition system.

For the total ^{144}Sm$(n,\alpha)^{141}$Nd cross sections, good agreements are achieved between present measurements and theoretical calculations using Talys-1.9. However, for the forward/backward ratios, the calculated results could not reproduce the experimental data. At the MeV region, ^{144}Sm$(n,\alpha)^{141}$Nd cross sections have large forward/backward ratios. For samarium isotopes, the forward/backward ratios are generally bigger than those from the model calculations, and this phenomena were also confirmed by other measurements [2, 7–9]. The contribution of non-statistical effects might lead to these deviations between the measured results and the model calculations.

The sources of uncertainty and their magnitudes are listed in Table IV. The uncertainty was calculated by the error propagation formula. Major source of uncertainty was the detection efficiency of α-particles for both $E_n = 5.5$ and 6.5 MeV. Around the neutron energy of 6.5 MeV, the cross sections of the ^{238}U(n, f) reaction change rapidly as the neutron energy increases, and it would lead to big uncertainty of fission counts in the determination of the absolute neutron flux. So, the neutron energy spreads would be another major source of uncertainty at $E_n = 6.5$ MeV.

At the 6.5 MeV neutron energy point, because we did not measure the background, the background of $E_n = 5.5$ MeV was used for the subtraction. Due to the difference of neutron energy, the error caused by background uncertainty was considered. We increased the background counts of $E_n = 5.5$ MeV by 100%, and recalculated the ^{144}Sm$(n, \alpha)^{141}$Nd reaction cross section at 6.5 MeV neutron energy point. The error was obtained by comparing the new cross section with the original one.

TABLE IV. Sources of uncertainty and their magnitudes.

Sources of uncertainty	Magnitude (%)	
	5.5 MeV	6.5 MeV
Statistical error of α-particles (N_α)	3.45[a] 5.60[b]	3.49[a] 6.50[b]
Valid-event-area of α-sources events (N_α)	0.47[a] 0.70[b]	0.15[a] 1.03[b]
Detection efficiency of α-particles (ε_α)	6.16[a] 11.82[b]	5.13[a] 9.49[b]
Background reduction ($N_{\alpha back}$)	1.41[a] 3.68[b]	0.87[a] 3.88[b]
Background uncertainty ($N_{\alpha back}$)	Only for 6.5 MeV	3.09[a] 17.82[b]
Neutron energy spreads (N_f)	0.80	6.87
Statistical error of fission events (N_f)	0.45	0.54
Detection efficiency for fission fragment (ε_f)	5.11	5.03
Numbers of ^{238}U nucleus (N_{238U})	0.45	0.45
^{238}U (n, f) cross sections (σ_f)	0.70	0.70
Normalization of the BF$_3$ counts (N_{BF_3})	3.30	9.65
Numbers of ^{144}Sm nucleus (N_{samp})	1.00	1.00
Total	9.1	15.1

[a] For the forward results of the ^{144}Sm$(n, \alpha)^{141}$Nd reaction
[b] For the backward results of the ^{144}Sm$(n, \alpha)^{141}$Nd reaction
(The symbols in the parentheses refer to the quantities in Eqs. (1) and (2), N_{BF_3} refers to the counts of the BF$_3$ counter.)

Results of the present experiments are compared with existing measurements, evaluations, and Talys-1.9 calculations (ldmodel 4, $1.012r_V$) as shown in Fig. 6. In both magnitude and tendency, there are order of magnitude differences among different evaluation libraries in the MeV region. Our experiment results are closer to the data of TENDL-2015 libraries [18]. The Talys-1.9 calculations agree with our present measurements as well as the Alford's and Luo's results in the 14 MeV region. However, the present experiment results are higher than our measurements in 2016, therefore further measurements in the MeV region are necessary to clarify the discrepancies among different libraries and experiments.
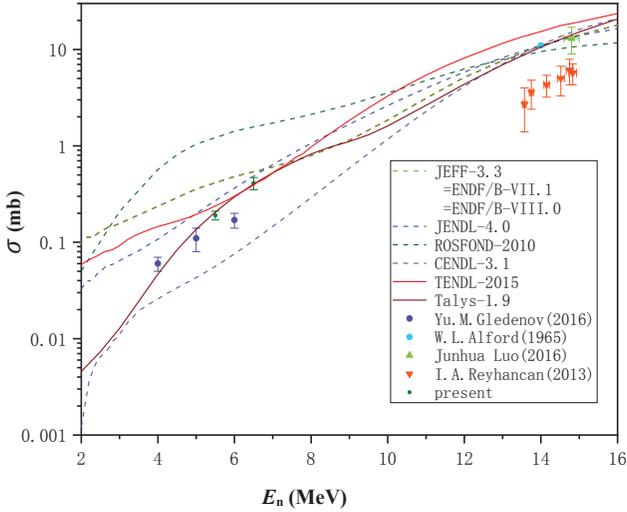
Fig. 6. Present cross sections of the $^{144}Sm(n,\alpha)^{141}Nd$ reaction compared with existing measurements, evaluations and Talys-1.9 calculations (ldmodel 4, $1.012r_V$).

IV. CONCLUSIONS

In the present work, cross sections of the $^{144}Sm(n,\alpha)^{141}Nd$ reaction were measured at 5.5 and 6.5 MeV neutron energy points. There are very large discrepancies among different evaluation libraries, and our results are closer to the data of TENDL-2015 library. Theoretical analyses using Talys-1.9 code was performed, and agreement was achieved between present measurements and calculations. The present results are higher than our measurements in 2016, and further experiments in the MeV region are necessary to clarify the discrepancies among different libraries and measurements.

ACKNOWLEDGEMENTS

REFERENCES

[1]   Yu.M. Gledenov, P.E. Koehler, J. Andrzejewski, and K.H. Guber, Phys. Rev. C **62**, 042801(R) (2000).

[2]   Gledenov Yury, Zhang Guohui, Gonchigdorj Khuukhenkhuu, Sedysheva Milana, Krupa Lubos, Enkhbold Sansarbayar, Chuprakov Igor, Wang Zhimin, Fan Xiao, Zhang Luyu, and Bai Huaiyong, EPJ Web of Conferences **146**, 11033 (2017).

[3]   I. A. Reyhancan, A. Durusoy, Nuclear Science and Engineering, **174**, 202 (2013).

[4]   W.L. Alford, R.D. Koehler, Bulletin of the American Physical Society, **10**, 260 (1965).

[5]   Luo J., Wu C., Jiang L., Long H., Radiochimica Acta, **104**, 523 (2016).

[6]   ENDF: Evaluated Nuclear Data File, Database Version of 2018-02-13, https://www-nds.iaea.org/exfor/endf.htm.

[7]   Yu.M. Gledenov, M.V. Sedysheva, V.A. Stolupin, Guohui Zhang, Jiaguo Zhang, Hao Wu, Jiaming Liu, Jinxiang Chen, G. Khuukhenkhuu, P.E. Koehler, and P.J. Szalanski , Physical Review C, **80**, 044602 (2009).

[8]   Yu.M. Gledenov, Guohui Zhang, G. Khuukhenkhuu, M.V. Sedysheva, P.J. Szalanski , P.E. Koehler, Jiaming Liu, Hao Wu, Xiang Liu, and Jinxiang Chen, Physical Review C, **82**, 014601 (2010).

[9]   Guohui Zhang, Yu.M. Gledenov, G. Khuukhenkhuu, M.V. Sedysheva, P.J. Szalanski, P.E. Koehler, Yu.N. Voronov, J. Liu, X. Liu, J. Han, and J. Chen, Physical Review Letters, **107**, 252502 (2011).

[10] X. Zhang, Z. Chen, Y. Chen, J. Yuan, G. Tang, G. Zhang, J. Chen, Y. M. Gledenov, G. Khuukhenkhuu, and M. Sedysheva, Physical Review C **61**, 054607 (2000).

[11] Guohui Zhang, Hao Wu, Jiaguo Zhang, Jiaming Liu, Yu.M. Gledenov, M.V. Sedysheva, G. Khuukhenkhuu, and P.J. Szalanski, Eur. Phys. J. A, **43**, 1 (2010).

[12] Pronyaev V., Simakov S., Marcinkevicius B., University of Leeds, **158**, 80 (2015).

[13] Yu.M. Gledenov, M.V. Sedysheva, V.A. Stolupin, Guohui Zhang, Jinhua Han, Zhimin Wang, Xiao Fan, Xiang Liu, Jinxiang Chen, G. Khuukhenkhuu, and P.J. Szalanski , Physical Review C, **89**, 064607 (2014).

[14] J.F. Ziegler, SRIM-2013, http://www.srim.org/#SRIM.

[15] A.J. Koning, S. Hilaire, and M.C. Duijvestijn, TALYS-1.9, http://www.talys.eu/.

[16] K.-H. Schmidt, B. Jurado, C. Amouroux and C. Schmitt, Nuclear Data Sheets **131**, 107 (2016).

[17] Haiyong Bai, Haoyu Jiang, Yi Lu, Zengqi Cui, Jinxiang Chen, Guohui Zhang, "Determined of the ^{238}U nucleus number and simulation of neutron induced fission energy spectrum" (to be published).

[18] A.J. Koning, D. Rochman, J. Kopecky, J. Ch. Sublet, E. Bauge, S. Hilaire, P. Romain, B. Morillon, H. Duarte, S. van der Marck, S. Pomp, H. Sjostrand, R. Forrest, H. Henriksson, O. Cabellos, S. Goriely J. Leppanen, H. Leeb, A. Plompen and R. Mills, "TENDL-2015: TALYS-based evaluated nuclear data library", https://tendl.web.psi.ch/tendl_2015/tendl2015.html.

ALPHA-CLUSTERING IN SLOW AND FAST NEUTRON INDUCED (n,α) REACTIONS

G. Khuukhenkhuu[1], M. Odsuren[1,2], J. Munkhsaikhan[1], B. Batchimeg[1], Yu.M. Gledenov[3], E. Sansarbayar[1,3], and M.V. Sedysheva[3]

[1]*Nuclear Research Center, National University of Mongolia, Ulaanbaatar, Mongolia*

[2]*School of Engineering and Applied Sciences, National University of Mongolia, Ulaanbaatar, Mongolia*

[3]*Frank Laboratory of Neutron Physics, JINR, Dubna, Russia*

1. INTRODUCTION

Alpha-particle clustering in nuclei is one of the important subjects for understanding of α-decay, α-particle transfer and emission reactions, and nuclear structure [1]. The α-clustering effect was investigated for long time by many authors (see, for example, [2–17]) who used different theoretical approaches to this problem.

In order to evaluate the α-particle formation probability for nucleus Bethe first assumed [2] to use the emission probability of neutron with the same energy. This hypothesis was considered by Popov *et al.* [3−5] using the experimental data of (n,α) reactions for resonance neutrons and found a ratio of the reduced average neutron-width to the alpha-width in the range of 2.5÷8.0.

In the framework of the pre-compound mechanism Bonetti and Milazzo-Colli suggested [6] the preformed α-particle model which was used in analysis of experimental data for α-decay, (n,α) and (p,α) reactions. From such analyses the α-particle preformation probability was found to be $\phi_\alpha = 0.7 \div 0.01$. Tonozuka and Arima [7] obtained a ratio of the calculated reduced α-width to the observed value and estimated surface α-clustering in the α-decay for ^{212}Po. It was shown that the surface α-clustering effect produces a tremendous enhancement of the α-decay widths of the ^{212}Po.

In the framework of the pre-equilibrium approach to the nuclear reactions with complex particle emission Hogan calculated [8] the rates of nucleon-nucleon and nucleon-alpha interactions in nuclear matter and obtained the α-particle preformation factor $\phi_\alpha = 0.075 \div 0.4$.

A rough estimate of the probability of occurrence of an α-cluster in a nuclear surface was made by Chang [9,10] using the ratio of volume of the surface region to the volume of the nucleus. The probability of occurrence of the α-cluster in a surface of ^{212}Po was $6.2 \cdot 10^{-4}$. Knellwolf and Rossel obtained [11] the α-particle preformation probability in the compound nucleus ^{41}Ca to be 0.57 by comparison of (n,α) and (n,p) cross sections for the same neutron energy.

Using the exciton model Iwamoto and Harada suggested [12] a method to calculate the α-particle formation factor from the overlap integral between the wave functions of the α-particle and four nucleons. In this method the excitons are formed from not only particles above the Fermi level but from nucleons below, also. They gave the relative α-particle formation factors normalized to unity as a function of the α-particle energy.

Zhang, Royer and Li using the semiclassical approach to frequency of the α-cluster motion inside daughter nucleus obtained [13,14] the α-particle preformation probability for α-

decay of some heavy nuclei to be 0.0065÷0.244. Kadmensky and Furman developed [15] the α-cluster model and obtained the surface α-clustering probabilities $7 \cdot 10^{-4}$, $3 \cdot 10^{-5}$ and $8 \cdot 10^{-7}$ for favoured, semifavoured and unfavoured α-transitions, respectively. Because of the large binding energy of a free α-particle, it can be presumed that the α-cluster is a rather stable substructure particularly in light nuclei [16]. Two body α+ α and three body α+ α+ n cluster structures of the ^{8}Be and ^{9}Be, respectively, were, for example, studied [17,18] and the relative probabilities of such configurations were obtained. However, serious difficulties occur in the theoretical calculation of the absolute α-clustering probability.

So, from the above mentioned approaches to the α-clustering problem it is seen that up to now a common opinion to explain the α-clustering effect and an unified method to obtain the α-clustering probability there are no.

In this work, we from the unified view point, namely, in the framework of the statistical model evaluated the α-clustering factor for slow and fast neutron induced (n,α) reactions. Our results are compared with values of the α-clustering probability which were obtained by other authors.

2. FORMULAE

2.1. Slow Neutron Induced (n,α) Reaction Formulae

2.1.1. *Resonance Neutron Induced (n,α) Reaction*

Using the statistical model and taking into account the α-clustering in the surface of the compound nucleus the Weisskopf's formula [19] for the average α-width of level can be written in the following form:

$$< \Gamma_\alpha(J) > = \frac{D(J)}{2\pi} T_\alpha(l) \phi_\alpha, \tag{1}$$

where $D(J)$ is the average level spacing for given J; T_α is the transmission factor of α-particle through potential barrier of the daughter nucleus; ϕ_α is the α-clustering factor. From (1) the α-clustering factor is given by

$$\phi_\alpha = 2\pi \frac{< \Gamma_\alpha(J) >}{D(J) T_\alpha(l)}. \tag{2}$$

To simplify calculations we neglect the angular momentum dependence of the transmission factor. Then the formula (2) can be rewritten as following:

$$\phi_\alpha = 2\pi \frac{< \Gamma_\alpha(J) >}{D(J) T_\alpha}. \tag{3}$$

Here the average level spacing for given J, $D(J)$, is expressed by

$$D(J) = \frac{D_0}{g(J)}, \tag{4}$$

where D_0 is the observed level spacing for s-resonances; $g(J)$ is the spin factor:

$$g(J) = \frac{2J+1}{2(2I+1)}. \tag{5}$$

Here J is the compound nucleus spin; I is the target nucleus spin.

It is possible to calculate by using the formula (3) the α-clustering factor for resonance neutron induced (n,α) reaction.

2.1.2. Intermediate Neutron Induced (n,α) Reaction

In the framework of the statistical model an averaged (n,α) cross section by analogy with (n,γ) reaction is given by [20,21]:

$$< \sigma(n,\alpha) >= 2\pi^2 \lambda_n^2 \sum_l \sum_J \frac{g(J)}{D(J)} \frac{<\Gamma_n(J,l)><\Gamma_\alpha(J,l)>}{<\Gamma(J,l)>} F_l . \tag{6}$$

Here: λ_n is the wave length of the incident neutron divided by 2π:

$$\lambda_n^2 = 2.07 \cdot 10^{-22} \frac{cm^2}{E_n(keV)}; \tag{7}$$

E_n is the incident neutron energy; $<\Gamma_n(J,l)>$, $<\Gamma_\alpha(J,l)>$ and $<\Gamma(J,l)>$ are the average neutron, alpha and total level widths;

F_l is the level width fluctuation factor which is occurred in the range of 0.6÷1.0.

The average total level width can be expressed as

$$< \Gamma(J,l) >=< \Gamma_n(J,l) > + < \Gamma_\gamma(J,l) > + < \Gamma_\alpha(J,l) > +... \tag{8}$$

In most cases for intermediate neutrons can be assumed $\Gamma_n >> \Gamma_\gamma >> \Gamma_\alpha$. So, the total level width is given by

$$< \Gamma(J,l) >\approx< \Gamma_n(J,l) > . \tag{9}$$

From (1), (6) and (9) can be gotten

$$< \sigma(n,\alpha) >\approx \pi \lambda_n^2 \sum_l \sum_J g(J) T_\alpha(l) \phi_\alpha F_l . \tag{10}$$

If we neglect the angular momentum and spin dependences of the total (n,α) cross section averaged over the wide neutron energy range and assume $F_l \approx 1$ can obtain from (10) following simple formula for α-clustering factor:

$$\phi_\alpha \approx \frac{< \sigma(n,\alpha) >}{\pi \lambda_n^2 T_\alpha} . \tag{11}$$

This formula can be utilized to calculate the α-clustering factor using the averaged experimental (n,α) cross section.

2.2. Alpha-Clustering in Fast Neutron Induced (n,α) Reaction

By analogy with formula (11) the proton clustering factor can be written in the following form:

$$\phi_p \approx \frac{<\sigma(n,p)>}{\pi\hbar_n^2 T_p} \tag{12}$$

From formulas (11) and (12) can be obtained following ratio:

$$\frac{\phi_\alpha}{\phi_p} \approx \frac{<\sigma(n,\alpha)>}{<\sigma(n,p)>} \cdot \frac{T_p}{T_\alpha}. \tag{13}$$

If we assume $\phi_p = 1$ the α-clustering factor for (n,α) reaction induced by quasimonoenergetic fast neutrons is expressed as following:

$$\phi_\alpha \approx \frac{\sigma(n,\alpha)T_p}{\sigma(n,p)T_\alpha}. \tag{14}$$

The α-clustering factor in (14) is defined as the relative probability of interaction of an incident neutron with an α-cluster to that with proton.

The transmission factors T_α and T_p in the formulas (3), (11) and (14) are calculated by Rasmussen's formula [22,23].

3. RESULTS AND DISCUSSION

3.1. Alpha-Clustering in the Slow Neutron Induced (n,α) Reaction

3.1.1. Alpha-clustering for Resonance Neutron Induced (n,α) Reaction

Table 1. Experimental data and results of our calculations for resonance neutrons

Target Isotopes	Γ_α(exp) (μeV) [5]	D_o (eV) [24]	T_α	ϕ_α
[64]Zn	12	2940	8.63E-08	0.30
[67]Zn	580±340	367	2.75E-05	0.21
[95]Mo	26±18	81	1.58E-06	0.53
[123]Te	7.3±3.7 (3.0±2.0)*	25.1	2.32E-07	1.97 (0.81)*
[143]Nd	21±8	37.6	4.12E-06	0.37
[145]Nd	0.32±0.19	17.8	1.41E-07	0.35
[147]Sm	2.3±0.6	5.7	4.67E-06	0.24
[149]Sm	0.21±0.06	2.2	5.12E-07	0.52

*) Previous data [25]

The formula (3) is utilized for some isotopes to estimate the α-clustering factor for the (n,α) reaction induced by resonance neutrons. Experimental data of the average α-widths were taken from Ref. [5]. Average level spacing for s-resonances [24] was used in this calculations. The transmission factors were calculated, as mentioned above, by Rasmussen's formula for zero angular momentum $l_\alpha=0$. Values of the experimental data and results of our calculations for some isotopes are given in Table 1.

3.1.2. Alpha-Clustering in the Intermediate Neutron Induced (n,α) Reaction

The formula (11) is used to estimate the α-clustering factor for 24÷30 keV neutron induced (n,α) reactions. Experimental data of the (n,α) cross sections were taken from Ref. [5]. Values of the experimental averaged (n,α) cross sections for 24 or 30 keV neutrons and results of our calculations for α-clustering factor are given in Table 2.

Table 2. Experimental (n,α) cross sections and results of our calculations for 24÷30 keV neutrons

Target nuclei	E_n (keV)	$\sigma(n,\alpha)$ (μbarn)	T_α ($l_\alpha=0$)	ϕ_α by formula (11)
Mo-95	30	20±4	1.75E-06	0.53
Te-123	24	2.8±0.7	2.48E-07	0.52
Nd-143	30	20±3	4.5E-06	0.20
Sm-147	30	28±5	5.14E-06	0.25

In the case of slow neutrons from Tables 1 and 2 can be obtained following common results for α-clustering factors (see Table.3)

Table 3. Alpha-clustering factors for slow neutron induced (n,α) reactions

Target Nuclei	ϕ_α for resonance neutrons	ϕ_α for intermediate neutrons
Mo-95	0.53	0.53
Te-123	1.97 (0.81)[*]	0.52
Nd-143	0.37	0.20
Sm-147	0.24	0.25

3.2. Alpha –Clustering in (n,α) Reaction Induced by 4÷6 MeV Neutrons

The formula (14) is used to estimate the α-clustering factor for the (n,α) reaction induced by 4÷6 MeV neutrons where experimental (n,α) and (n,p) cross sections simultaneously there are for the same isotopes [26]. The experimental data and results of our calculations are given in Table.4.

Table 4. Experimental data and results of our calculations for 4÷6 MeV neutrons

E_n (MeV)	Target Nuclei	Reaction	$Q_{(n,p/\alpha)}$ (MeV)	$E_{p/\alpha}$ (MeV)	$\sigma_{(n,p/\alpha)}$ (mbarn)	$T_{p/\alpha}$	ϕ_α by formula (14)	$\overline{\phi}_\alpha$
4	^{40}Ca	(n,α)	1.748	5.18	156.4	0.282	0.29	0.0655
		(n,p)	-0.529	3.38	300	0.161		
	^{54}Fe	(n,α)	0.841	4.49	0.76	5.32E-4	0.02	
		(n,p)	0.088	4.01	276	0.0041		
	^{58}Ni	(n,α)	2.89	6.43	13.4	0.056	0.0024	
		(n,p)	0.395	4.32	352.4	0.0035		
	^{63}Cu	(n,α)	1.715	5.36	0.281	0.0015	0.013	
		(n,p)	0.716	4.64	74.8	0.0053		
	^{64}Zn	(n,α)	3.867	7.38	59.6	0.162	0.0022	
		(n,p)	0.208	4.14	132.9	8E-4		
4.5	^{39}K	(n,α)	1.363	5.28	145	0.78	0.19	0.19
		(n,p)	0.217	4.6	280	0.292		
5	^{41}K	(n,α)	-0.111	4.42	3.4	0.123	0.04	0.0232
		(n,p)	-1.71	3.21	14.1	0.0206		
	^{54}Fe	(n,α)	0.841	5.42	2	0.014	0.013	
		(n,p)	0.088	4.99	406.1	0.038		
	^{58}Ni	(n,α)	2.89	7.36	47.4	0.382	0.0073	
		(n,p)	0.395	5.3	509	0.0302		
	^{59}Co	(n,α)	0.320	4.96	0.13	0.0017	0.037	
		(n,p)	-0.783	4.15	8.1	0.004		
	^{63}Cu	(n,α)	1.715	6.29	1.69	0.0247	0.037	
		(n,p)	0.716	5.62	73.22	0.0396		
	^{64}Zn	(n,α)	3.867	8.32	79.1	0.841	0.0051	
		(n,p)	0.208	5.12	181	0.0099		
6	^{41}K	(n,α)	-0.111	5.32	7.5	0.92	0.08	0.0656
		(n,p)	-1.71	4.19	16.8	0.165		
	^{54}Fe	(n,α)	0.841	6.35	8	0.147	0.02	
		(n,p)	0.088	5.97	465	0.177		
	^{55}Mn	(n,α)	-0.626	4.99	0.5	0.0089	0.097	
		(n,p)	-1.806	4.12	5.65	0.0099		
	^{59}Co	(n,α)	0.320	5.9	1.09	0.0315	0.085	
		(n,p)	-0.783	5.13	14.52	0.0357		
	^{63}Cu	(n,α)	1.715	7.24	5.01	0.21	0.046	
		(n,p)	0.716	6.61	88.7	0.172		

3.3. Discussion

It is seen from Tables 1 and 2 that the α-clustering factors for the (n,α) reactions induced by resonance and intermediate neutrons are varied in the range of 0.20 to 0.53 for all isotopes except ^{123}Te. As to ^{123}Te-target nucleus new value $\Gamma_\alpha^{exp} = 7.3 \pm 3.7$ μeV gives the

α-clustering factor $\phi_\alpha = 1.97$ which is not possible to be $\phi_\alpha > 1$. At the same time from the previous datum $\Gamma_\alpha^{exp} = 3.0 \pm 2.0$ for the ^{123}Te(n,α)^{120}Sn reaction the α-clustering factor was found to be $\phi_\alpha = 0.81$ (see Table 1) that is plausible.

Also, Table 3 shows that the α-clustering factors for each given isotopes are almost the same on resonance and intermediate neutrons.

In the case of fast neutrons (E_n=4÷6 MeV) the α-clustering factors are varied from 0.0022 to 0.29 (see Table 4). It is not seen from here an energy regular dependence of the α-clustering factor for considered isotopes. In the energy range of 4 to 6 MeV common arithmetic average value of the $\overline{\phi}_\alpha$, which obtained at each neutron energy point, can be found to be $<\phi_\alpha> = 0.086$.

This value of $<\phi_\alpha> = 0.086$ can be compared with our previous results of $\phi_\alpha = 0.22 \div 0.28$ at the same neutron energy range of E_n=4÷6 MeV [27]. It can be seen that our present results for α-clustering factor are a little less than previous ones, although main conception of the two approaches is very similar and methods of calculation are different.

In addition, it should be noted that our present results of the α-clustering factor $\phi_\alpha = 0.20 \div 0.53$ for slow neutrons are close to our previous ones $\phi_\alpha = 0.22 \div 0.28$ for fast neutrons. So, in future more detailed consideration of these facts is needed.

Our values of the α-clustering factor obtained in this work are satisfactorily in agreement with results of Popov *et al.* [3÷5], Bonetti and Milazzo-Colli [6], Hogan [8], and Knellwolf and Rossel [11].

4.   CONCLUSION

1. The α-clustering factors for (n,α) reactions induced by slow (resonance and intermediate) and fast neutrons were obtained for some isotopes using the statistical model of nuclear reactions.

2. In the case of slow neutrons the α-clustering factors are varied in the range of 0.20 to 0.53. At the same time the α-clustering factors for fast neutron induced (n,α) reaction were found in the range of 0.0022 to 0.29.

3. The present arithmetic average value $<\phi_\alpha> = 0.086$ for neutron energy E_n= 4÷6 MeV is a little less than our previous results of the α-clustering factor $\phi_\alpha = 0.22 \div 0.28$ for the same neutron energy range. At the same time the present values of the α-clustering factor $\phi_\alpha = 0.20 \div 0.53$ for slow neutrons are close to our previous ones of $\phi_\alpha = 0.22 \div 0.28$ for fast neutrons.

4. Our values of the α-clustering factor for slow and fast neutron induced (n,α) reactions on an average are satisfactorily in agreement with most of evaluations which obtained by other authors using the different approaches to this problem.

References
1. P.E. Hodgson, Alpha-clustering in Nuclei, Chapter 23, In book: "The Uncertainty Principle and Foundations of Quantum Mechanics". Editors: W.C. Price and S.S. Chissick, New York: John Wiley, 1977, p.485.
2. H.A. Bethe, Rev. Mod. Phys., v.**9**, N2, 1937, p.69.
3. Yu.P. Popov, M. Przytula, K.G. Rodionov *et al*., Jour. Nucl. Phys., v.**13**, N5, 1971, p.913, (in Russian).
4. Yu.P. Popov and V.I. Furman, In book: III School of Neutron Physics (Lectures), April 19-30, 1978, Alushta, D3-11787, JINR, Dubna, p.390, (in Russian).
5. N.P. Balabanov, V.A. Vtyurin, Yu.M. Gledenov and Yu.P. Popov, Physics of Elementary Particles and Atomic Nuclei, v.**21**, N2, 1990, p.131.
6. R. Bonetti and L. Milazzo-Colli, Phys. Lett., v.**49** B, N1, 1974, p.17.
7. I. Tonozuka and A. Arima, Nucl. Phys., v.**323** A, 1979, p.45.
8. J.I. Hogan, Z. Phys., v.**295** A, N2, 1980, p.169.
9. F.C. Chang, Phys. Rev., vol.**141**, N3, 1966, p.1136.
10. F.C. Chang, Phys. Rev., vol.**155**, N4, 1967, p.1299.
11. T. Knellwolf and J. Rossel, Helv. Phys. Acta., v.**39**, N4, (1966), p.376.
12. A. Iwamoto and K. Harada, Phys. Rev., v.**26** C, N5, 1982, p.1821.
13. H.F. Zhang and G. Royer, Phys. Rev., v.**77** C, N5, 2008, p.054318.
14. H.F. Zhang, G. Royer and J.Q. Li, Phys. Rev., v.**84** C, N2, 2011, p.027303.
15. S.G. Kadmensky and V.I. Furman, Physics of Elementary Particles and Atomic Nuclei, v.**6**, part.2, 1975, p.469, (in Russian).
16. K. Wildermuth and Y.C. Tang, A Unified Theory of the Nucleus, Academic Press, Inc. New York, 1977.
17. Yu. Kikuchi, M. Odsuren, T. Myo and K. Kato, Phys. Rev., vol.**93** C, N5, 2016, p.054605.
18. M. Odsuren, K. Kato, M. Aikawa and T. Myo, Phys. Rev., vol.**89** C, N3, 2014, p.034322.
19. J.M. Blatt and V.F. Weisskopf, Theoretical Nuclear Physics, New York, John Wiley and Sons, 1952.
20. A.M. Lane and J.E. Lynn, The Proceedings of the Physical Society, Section A, vol.**70**, part.8, N452 A, 1957, p.557.
21. Yu.P. Popov, V.I. Salatskij and G. Khuukhenkhuu, Jour. Nucl. Phys., vol.**32**, N4, (10), 1980, p.459.
22. J.O. Rasmussen, Phys. Rev., v.**113**, N6, 1959, p.1593.
23. T. Delgersaikhan, G. Khuukhenkhuu, M. Odsuren and J. Munkhsaikhan, Scientific Transactions of the National University of Mongolia: Physics, N362 (17), 2012, p.158.
24. S.F. Mughabghab. Atlas of Neutron Resonances, 5-th Edition Elsevier, 2006, Amsterdam.
25. Yu.P. Popov, (n,α) Reaction on Resonance Neutrons, JINR, 3-8747, 1975, Dubna (in Russian).
26. https://www-nds.iaea.org/exfor/exfor.htm
27. G. Khuukhenkhuu, J. Munkhsaikhan, M. Odsuren *et al.,* Mongolian Journal of Physics, Issue 2, 2016, p.507.

STUDY OF 14.1 MeV NEUTRONS INELASTIC SCATTERING ON IRON

Fedorov N.A.[1,2*], Tretyakova T.Yu.[3], Kopatch Yu.N.[1], Bystritsky V.M.[1], Grozdanov D.N.[1,4], Aliyev F.A.[1,5], Ruskov I.N.[4], Skoy V.R.[1], Dabylova S.[1], Gorelikov A.V.[2], Hramco C.[1,6], Kumar A.[7], Gandhi A.[7], Wang D.[8], Bogolyubov E.P.[9], Yurkov D.I.[9], and TANGRA collaboration

[1]*Joint Institute for Nuclear Research (JINR), Dubna, Russia*
[2]*Faculty of Physics, Lomonosov Moscow State University (MSU), Moscow, Russia*
[3]*Skobeltsyn Institute of Nuclear Physics (SINP), MSU, Moscow, Russia*
[4]*Institute for Nuclear Research and Nuclear Energy (INRNE), Bulgarian Academy of Sciences (BAS), Sofia, Bulgaria*
[5]*Institute of Geology and Geophysics (IGG), Baku, Azerbaijan*
[6]*Institute of Chemistry, Academy of Science of Moldova, Chisinau, Republic of Moldova*
[7]*Banaras Hindu University, Varanasi, India*
[8]*Xi'an Jiao Tong University, Xi'an, China*
[9]*All-Russia Research Institute of Automatics (VNIIA), Moscow, Russia*

Abstract

The angular distributions of gamma-rays from the inelastic scattering (INS) of 14.1 MeV neutrons on iron (Fe) are investigated with Tagged Neutron Method (TNM). The anisotropy of γ-rays emitted during the INS-process was measured, using an improved TANGRA (TAgged Neutron and Gamma RAys) setup. The setup's configuration and the digital method of data processing provide a possibility to significantly improve the spatial resolution of gamma-ray detection system and, on the other hand, to increase the precision of obtained gamma-ray angular distributions data. Detailed γ-spectrum for (*n,n'*) reaction was obtained and γ-ray angular distribution was measured for 847 keV and 1238 keV γ-transitions.

Keywords: Iron (Fe), Fast neutrons; Tagged neutrons and gamma rays; TANGRA

* Corresponding author: N.A. Fedorov
Tel. + 7-496-216-3131; Fax: +7-496-216-5085; Email: na.fedorov@physics.msu.ru.

1. Introduction

The present work was undertaken with the aim to study the angular distributions of gamma rays following inelastic scattering of 14.1 MeV neutrons with various nuclei. The precise measurement of the γ-ray yields and n-γ correlations at large (>165º) and small (< 45º) angles are very important for formulation of correct assumptions about the neutron inelastic scattering mechanism, because the theoretical description of the angular correlations in these areas is very sensitive to the neutron-nucleus interaction parameters and depends on the theoretical model features. Moreover, precise information about the γ-ray angular distributions is necessary for fast elemental analysis of compound chemical substances, because one has to take into account the dependence of the γ-ray intensity on the angle between the direction of the neutron beam and the γ-detector. The existing database on the angular distributions of γ-rays emitted during the neutron inelastic scattering process contains contradictory information and quite scattered values at large and small angles. The tagged neutron method is based on registration of the 3.5-MeV α-particle from the reaction:

$$d + t \rightarrow n + \alpha \qquad (1)$$

The α-particle has practically the opposite direction of flight relative to the direction of the neutron emission. The energy of the neutron is 14.1 MeV. The α-particles are registered in coincidence with the pulses from the characteristic nuclear γ-radiation, emitted during the neutron-induced reaction on the nuclei A in the sample.

$$A(n,x)B^* \xrightarrow{\quad \gamma \quad} B \qquad (2)$$

So, it is possible to reconstruct the neutron flight direction by fixing the α-particle emission angle, i.e. to "tag" the neutron. Practically, the position-sensitive α-detector, embedded in the neutron generator, does the "tagging" of the neutrons. The α-γ coincidences allows one significantly decrease number of the background events in the γ−spectra.

This paper is dedicated to the investigation of the neutron inelastic scattering reaction on iron. The ^{56}Fe is an important structural material for nuclear engineering and nuclear physics research applications. There were a lot of experiments made on iron in the past with neutron energies from 1 up to 14 MeV to investigate inelastic scattering process, but most of them didn't consider γ-quanta angular distributions. Recently, a high-resolution measurement of the inelastic scattering cross-section was done at the nELBE neutron ToF-facility in the energy range from about 0.1 up to 10 MeV, It was shown that angular distribution coefficients have a strong energy dependence [10]. In this work we measured γ-quanta angular distributions with 14.1 MeV incident neutrons.

2. Experiment

The scheme of TANGRA-setup for studying the fast neutron scattering reactions is shown in Fig. 1. The neutron generator ING-27 is used as a neutron source. The neutrons are produced in the reaction (1), induced by the continuous deuteron beam with kinetic energy of 80–100 keV, focused on a tritium-enriched target. The products of this reaction are a 14.1 MeV neutron and 3.52 MeV α-particle. The maximal intensity of the "tagged" neutron flux in 4π-geometry is 5×10^7 c^{-1}. The α-particles are registered by a 64-pixel α-detector with pixel dimensions of 6×6 mm^2. The α-detector is located at a distance of ~ 10 cm from the tritium-enriched target.

The γ-quanta emitted in the neutron inelastic scattering are registered by a "Romasha" system, consisted of 18 BGO-scintillator γ-detectors placed around the sample with ~14° step. The background events are separated by using the Time-of-Flight (ToF) method. The "start" of the measurement time duration is given by the signal from the αγ-detector and the "stop" – by the signal from the α -detector. The difference in speed between the neutron and the photon provides the possibility to separate the γ-rays from the neutrons. For data acquisition a personal computer with two ADCM-16 boards was used [2].

The profiles of the tagged neutron beams were measured prior to the experiment, using a position-sensitive silicon charged particle detector (profilometer) [3]. This information is used for adjusting the neutron generator beams and for sample's sizes optimization. The experimental data analysis procedure is discussed in detail in our previous paper [1].

The sample used was a 4×4×4 cm^3 Al-container filled with natural iron powder.
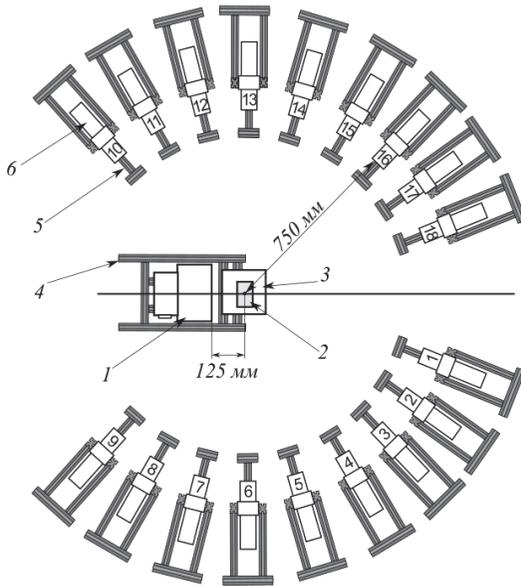
Fig. 1. Scheme of the TANGRA setup in the reaction plane: *1* – portable neutron generator ING-27, *2* – sample at the center of "Romasha" γ-ray registration system, *3* – sample holder, *4* – generator support , *5* – γ-ray detector holder, *6* – BGO γ-ray detector. The "tagged" neutron beam direction is indicated by horizontal plain line.

3. Optimization of sample's sizes and correction factor calculation

Sizes of the irradiated sample were chosen from two contradictory criteria: the sample's sizes must allow us to use as many tagged beams as possible, but, on the other hand, the self-absorption γ-quanta inside the sample must not significantly change the observed γ-quanta angular distribution.

We used Geant4 Monte-Carlo simulation to estimate the influence of the γ-quanta and neutrons absorption inside the sample. The simulation results showed that the optimal sample shape has a square section in the detector plane. To calculate the influence of the sample on the observed angular distribution, the predefined in Geant4 was changed to isotropic. The difference between the angular distributions for different pixels on the same vertical strip was found to be insignificant, so, we decided to use all 8 pixels on the vertical strip, and the height of all samples was set equal to 14 cm.

The example of Geant4-calculation based data correction procedure is illustrated in Fig. 2. The simulated areas of the full energy absorption peaks for each "strip-detector" combination were calculated and normalized per average photopeak area of each strip. In Fig. 2(a) the calculated correction factor C^i is presented. After that, the obtained experimental angular distribution W^i_{exp}, which is shown in Fig. 2(b), was divided by the correction factor:

$$W^i_{corrected} = \frac{W^i_{exp}}{C^i}$$

(3)

Here index i is the detector's number in Fig. 2. The example of corrected experimental data is presented in Fig. 2(d), with approximation by series of Legendre polynomials and renormalization per coefficient A (Eq. 3):

$$W(\theta) = A\left(1 + \sum_{k=2,4..}^{2J} a_k P_k(\cos\theta)\right),$$

(4)

where a_k are expansion coefficients, J is γ-transition multipolarity.
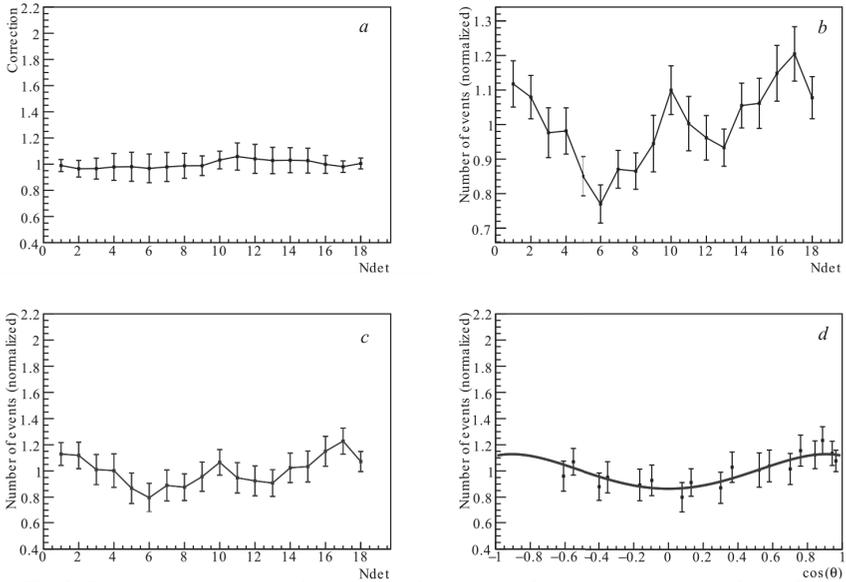

Fig. 2. Data processing example: calculated correction factor (a), experimental angular distribution (b), corrected experimental data (c), corrected angular distribution (d).

4. Results

In this experimental session we used HPGe γ-spectrometer to obtain high-resolution γ-spectrum. We can distinguish at least 46 γ-transitions generated from ^{56}Fe(n,n′), ^{56}Fe(n,2n′) reactions. Their parameters and references to other experiments in which the same γ-lines were observed are presented in the Table 1.

Table 1. Parameters of the γ-transitions observed in this work.

E_γ, keV[12]	Reaction	E_{in},keV	JP_{in}	E_{fin}, keV	JP_{fin}	Reference
477.2	(n,2n′)	1408	7/2–	931.3	5/2–	[5]
846.8	(n,n′)	846.8	2+	0	0+	[5],,[7],[9],[11]
931.3	(n,2n′)	931.3	5/2–	0	3/2–	[5] ,[6]
955.8	(n,n′)	4401.3	2+	3445.3	3+	[9]
1037.9	(n,n′)	3123.0	4+	2085.1	4+	[5],[9],[11]
1175.2	(n,n′)	4298.2	4+	3123	4+	[9]
1238.3	(n,n′)	2085.1	4+	846.8	2+	[5],[7],[9],[11]
1303	(n,n′)	3388.6	6+	2085.1	4+	[5],[11]
1312	(n,n′)	4683.04	3+	3370	2+	[5]
1335.4	(n,n′)	4458.4	4+	3123	4+	[9]
1360.3	(n,n′)	3445.4	3+	2598.5	2+	[9]
1408.4	(n,2n′)	1408.4	7/2–	0	3/2–	[5]
1579.5	(n,n′)	4539.5	1+,2+	2960	2+	[9]
1669.9	(n,n′)	3755.6	6+	2085.1	4+	[5],[9],[11]
1771.5	(n,n′)	3856.5	3+	2085.1	4+	[9],[11]
1810.8	(n,n′)	2657.6	2+	846.8	2+	[5],[9],[11]
1852.4	(n,n′)	4509.6	3–	2657.6	2+	[9]
1881.9	(n,n′)	4539.5	1+,2+	2657.6	2+	[9]
1918	(n,n′)	4878	2+	2960	2+	[9]
1963.9	(n,n′)	4048.9	3+	2085.1	4+	[9]
2015.2	(n,n′)	4100.3	4+	2085.1	4+	[9]
2034.9	(n,n′)	4119.9	3+	2085.1	4+	[5],[9]
2094.9	(n,n′)	2941.7	0+	846.8	2+	[9],[11]
2113.2	(n,n′)	2960.0	2+	846.8	2+	[5],[9],[11]
2212.9	(n,n′)	4298.1	4+	2085.1	4+	[9]
2273.2	(n,n′)	3120.1	1+	846.8	2+	[9],[11]
2373.2	(n,n′)	4458.4	4+	2085.1	4+	[9]
2424.9	(n,n′)	4509.6	3–	2085.1	4+	[9]
2460.3	(n,n′)	5402.3		2491.5	0+	[9]
2468.9	(n,n′)	4554.8	4+	2085.1	4+	[9]
2523.4	(n,n′)	3370	2+	846.8	2+	[9],[11]
2573	(n,n′)	4660.0	3+,4+	2085.1	4+	[9]
2598.6	(n,n′)	3445.3	3+	846.8	2+	[9],[11]
2601	(n,n′)	3448.4	1+	846.8	2+	[9],[11]
2657.6	(n,n′)	2657.6	2+	0	0+	[9]
2753	(n,n′)	3600	2+	846.8	2+	[9]
2759	(n,n′)	3605	2+	846.8	2+	[9],[11]
2983	(n,n′)	3829.8	2+	846.8	2+	[9],[11]
3009.7	(n,n′)	3856.5	3+	846.8	2+	[9]
3064	(n,n′)	5149.5	2+	2085.1	4+	[9]
3202.03	(n,n′)	4048.8	3+	846.8	2+	[9]

3253.7	(n,n')	4100.4	3+	846.8	2+	[9]
3448	(n,n')	3448.4	1+	0	0+	[9]
3548	(n,n')	4395.0	3+	846.8	2+	[9]
3600	(n,n')	3600	2+	0	0+	[9]
3663.6	(n,n')	4509.6	3–	846.8	2+	[9]

The most detailed spectrum is obtained in paper [9]: 82 γ-transitions correlated with reaction ^{56}Fe(n,n′) are described and their intensities are measured. In our γ spectrum we can identify γ-lines with intensities higher than 0.4% only, due to the high background radiation level generated from the inelastic scattering of neutrons in the shielding and construction elements of the experimental setup. The registered γ-ray spectrum for Fe is shown in Fig. 3.
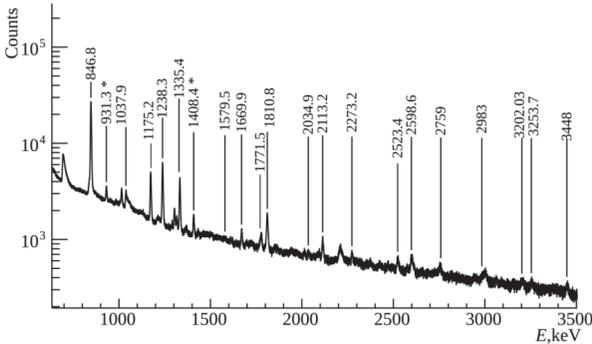

Fig. 3. Gamma-spectrum for Fe (HPGe). Energies of the most intensive γ-transitions E_γ (in keV) from reactions ^{56}Fe(n,n′),(n,2n′) are signed. Lines generated by reaction (n,2n′) are marked with an asterisk.
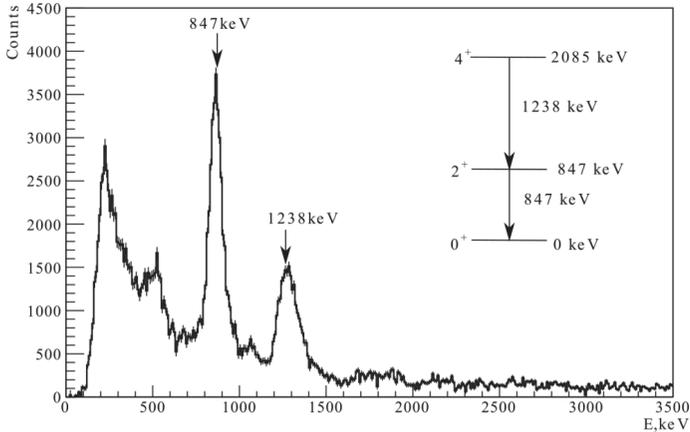

Fig. 4. Gamma-spectrum for iron, obtained by "Romasha" BGO γ-detector system.

During the last series of experiments with TANGRA setup, the γ-quanta angular distributions for Fe have been measured using the "Romasha" γ-spectrometer system. In Fig. 4 the γ-spectrum obtained by the BGO γ-detectors is presented.

We measured γ-quanta angular distributions for two the most intensive γ-transitions: 847 keV and 1238 keV that correspond to excitation of 847 keV(2^+) and 2085 keV(4^+) levels. Measured γ-quanta angular distributions and their approximations are shown in the Fig. 5. The coefficients of the Legendre polynomial approximation are presented in Table.2 in comparison with experimental results from papers [6–8].
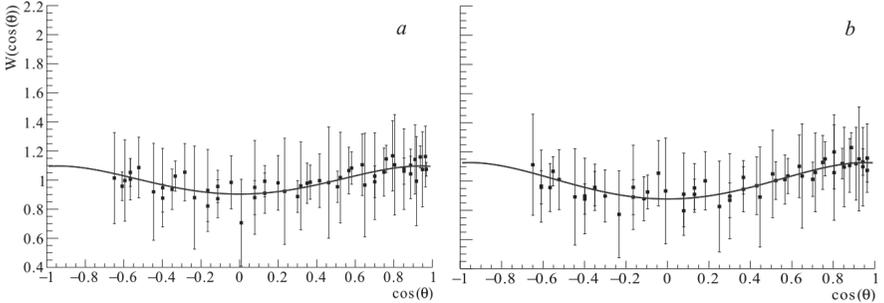

Fig. 5. The angular distributions of the γ-quanta from 14.1 MeV neutron inelastic scattering on ^{56}Fe: 847 keV (a), 1238 keV (b).

Table 2. Legandre polynomial approximation coefficients for the γ-quanta angular distributions obtained in this work in comparison with previous measurements.

E_γ, keV	a_2	a_4	Reference
846.8	0.15 ± 0.04	−0.06 ± 0.05	this work
	0.21 ± 0.05	0.07 ± 0.03	[6]
	0.36	0.38	[7]
	0.09	0.1	[8]
1238.3	0.19 ± 0.04	−0.07 ± 0.06	this work
	0.32 ± 0.08	0.16 ± 0.08	[6]
	0.37	−0.23	[7]
	0.14	−0.1	[8]

The discrepancy between results of different experiments is not significant, except the results from paper [7]. The obtained values correspond to the main trends of the energy dependences of the angular distribution coefficients obtained in the work [10]: for 846.8 keV γ-transition a_2-value is clearly positive and a_4 is mainly negative in the range of initial neutron energies between 0.1 and 7 MeV. Above 2 MeV the angular distribution flattens out. For the 1238.3 keV γ-ray angular distribution positive a_2 and negative a_4 in the same neutron energy range are observed.

Conclusion

Using TANGRA facility and the tagged neutron method we studied the inelastic scattering of 14.1 MeV neutrons on the iron. The most important advantage of the setup used in all the experiments is that we succeed to cover a wide range of angles with a big number of points, in which the registration of γ-quanta was simultaneously carried out.

References

1. D.N. Grozdanov, N.A. Fedorov, V.M. Bystritski, Yu.N. Kopach, I.N. Ruskov, V.R. Skoy, T.Yu. Tretyakova, N.I. Zamyatin, D. Wang, F.A. Aliev, C. Hramco, A. Gandhi, A. Kumar, S. Dabylova, E.P. Bogolubov, Yu.N. Barmakov, Measurement of Angular Distributions of Gamma Rays from the Inelastic Scattering of 14.1-MeV Neutrons by Carbon and Oxygen Nuclei, Phys. of At. Nucl., v. **5**, 588 (2018).
2. «AFI electronics,». Available: http://afi.jinr.ru.
3. N. Zamyatin, V. Bystritsky, Y. Kopach, F. Aliyev, D. Grozdanov, N. Fedorov, C. Hramko, I. Ruskov, V. Skoy, V. Slepnev, D. Wang и E. Zubarev, Neutron beam profilometer on the base of double-sided silicon strip detectors, Nucl. Instr. and Meth. A, v. **898** , 46 (2018).
4. N. Fedorov, T. Tretyakova, D. Grozdanov, V. Bystritsky, Y. Kopach, I. Ruskov, V. Skoy, I. Zamyatin, D. Wang, F. Aliev, C. Hramko, A. Kumar, A. Gandi, S. Dabylova, D. Yurkov, and Yu. Barmakov, Investigation of the neutron inelastic scattering on 27Al, Phys. of At. Nuclei, in press.
5. S. Simakov, A. Pavlik, A. Vonach и S. Hlavac, Status of experimental and evaluated discrete γ-ray production at En=14.5 MeV, INDC(CPP)-0413, Vienna: IAEA NUCLEAR DATA SECTION, 1998.
6. A.P. Dyagterev, Yu.E. Kozyr, G.A. Prokopec, Angular distribution of gamma-quanta from 14,6-MeV neutron interaction with 56Fe and 23Na nuclei, "Neutron Physics" (Proc. Of IV All-Union Conf. on Neutr. Physics, Kiev. 18–22 Apr. 1977), Moscow, CNIIautomatinform, v. **2**, p. 57, 1977.
7. U. Abbondanno, R. Giacomich, M. Lagonegro, G. Paul, Gamma Rays Resulting from Nonelastic Processes of 14.2 MeV Neutrons with Sodium, Magnesium, Silicon, Sulfur, Titanium, Chromium and Iron, J. Nucl. Energ., v. **27**, 227 (1973).
8. J. Lachkar, J. Sigaud, Y. Patin, G. Haouat., Nucl. Sci. Eng., v. **55**, 168 (1974).
9. J. Lachkar, J. Sigaud, Y. Patin, G. Haouat, Etude des niveaux de 56Fe excites par parles reactions (p, p'γ) et (n, n'γ), Nucl. Phys. A, v. **222**, 333 (1974).
10. R. Beyer , M. Dietz, D. Bemmerer et.al., Eur. Phys. J. A, v. **54**, 58 (2018).
11. R. Beyer, R. Schwengner, R. Hannaske, A.R. Junghans, Nucl. Phys. A, v. **927**, 41 (2014).
12. H. Junde, H. Su, Y. Dong., Nucl. Data Sheets, v. **112**, 1513 (2011).

Feasibility Analysis of Unfolding Fast Neutron Spectrum by Using (n, n'γ) Reaction

Li Xuesong, Yu Gongshuo, Jiang Wengang, Xie Feng

Northwest Institute of Nuclear Technology, Xi'an 710024, Shaanxi, China

Abstract: Multi-nuclide neutron activation method is usually used to unfolding the fast neutron spectrum. This method has the limitation of the number of candidate nuclides for the reaction cross section, products' decay characters etc. In this paper, a novel approach was proposed to break the limitation, which can employ a large number of γ rays emitting from the given (n, n'γ) reactions. Considering the number of isotopes and the (n, n'γ) cross sections, Mg, As, Mn, V, Br, Rb, Y, Nb, Rh, Sb, I, Pr, Ho, Gd, Sm, Nd, Pd and Ru were selected as the candidate target elements. By grouping some of these elements, it is easy to find dozens of γ rays from their (n, n'γ) reactions to unfold the fast neutron spectrum. Two target composing mode were supposed in this paper. The multi-γ-ray mode seemed better than the multi-nuclide-mode. Vertical experiment mode was suggested.

1 Introduction

Multi-nuclide neutron activation and flying-time methods are the main approaches to get the fast neutron spectrum[1, 2]. Flying-time method can be used to directly measure the neutron spectrum. But high time-resolution is needed for the high energy neutrons. And if the neutron flux is small, much time will be needed to accumulate enough counts. So flying-time method has its limitation. For multi-nuclide neutron activation method, researchers must get enough neutron activation channels. However, up to now, the number of the practicable neutron activations does not exceed twenty-five. Furthermore, those candidate nuclides can't be used at one time in one experiment. Then the neutron spectrum can't be unfolded finely in this condition, sometimes even can't be unfolded. So the limitation of this method is obvious.

Inelastic scattering reaction (n, n'γ) is an important energy-threshold reaction channel among all of the (n, X) reactions between neutron and nucleus. In the reaction process, nucleus will be activated to a high energy state. Mono-energy γ-ray will be emitted from the excited nucleus. So each high energy state of the nucleus is equivalent a selected nuclide in multi-nuclide neutron activation method. In 1997，Fehrenbacher G. etc. used the 692 keV γ-ray produced in ^{72}Ge (n, n'γ) in HPGe detector to unfolding the neutron spectrum of ^{252}Cf and got a preliminary result[3]. In 2013, A. Oberstedt etc. measured two γ-rays produced in Br(n, n'γ) in LaBr$_3$:Ce detector and got the coarse neutron spectrum of ^{252}Cf[4]. In 2014, A. Ebran etc. in CEA measured the efficiencies of five γ-rays produced in (n, n'γ) of La and Br in LaBr$_3$:Ce detector and the fast neutron detection efficiency relative to 306 keV γ-ray from Br(n, n'γ) was determined up to 0.5%[5]. So it is obvious that this method has a good sensitivity of neutron which is suitable for unfolding the spectrum of low neutron flux.

Up to now, it is the preliminary stage for the usage of (n, n'γ) in unfolding neutron spectrum.

Non-Statistical and Asymmetry Effects in Fast Neutrons Reactions

A.I. Oprea, C. Oprea, P.V. Sedyshev, Yu.M. Gledenov, M.V. Sedysheva

Frank Laboratory of Nuclear Research, JINR, 141980 Dubna, Russia

Abstract. Cross sections and strength functions in neutron reactions on ^{147}Sm were evaluated from slow and resonance neutrons up to MeV region. For their description the neutron resonance parameters, transmission coefficients for exit channels and the Hauser-Feshbach formalism were included. The theoretical evaluations are performed by using Talys free software and author's computer programs. The obtained cross sections and strength functions are compared with experimental data in order to explain possible non- statistical effects reported previously by some authors on the distributions of alpha widths.

INTRODUCTION

Fast neutrons reactions with emission of charged particles like protons and alpha particles are of interest for fundamental and applicative researches. For fundamental investigations, nuclear processes induced by fast neutrons provide new data on nuclear reactions mechanisms, structure of atomic nuclei, parameters of optical potential, levels density and spacing. Related to applicative studies fast neutrons processes are important for material sciences, nuclear technologies, neutrons activations analysis, tagged neutrons method, astrophysics, etc. [1, 2].

Fast neutrons reactions on medium and heavy nuclei are investigated for a long time in LNF JINR, Dubna, and became traditional due to accumulated experience, human resource and existence of necessary devices and facilities [3].

In the present work ^{147}Sm$(n,\alpha)^{144}$Nd process induced by fast neutrons was investigated in a wide incident neutrons energy range starting from keV's region up to 20 MeV. Cross sections, asymmetry effects and alpha strength functions were evaluated using own and dedicated computer codes. Asymmetry effects and strength functions results are qualitatively explained considering changing of radius and parameters of potential in entrance and emergent channels respectively.

THEORETICAL BACKGROUND

The (n,α) reaction on ^{147}Sm nucleus with neutrons energy from keV up to 20 MeV can be described in the frame of statistical model of nuclear reactions and therefore cross sections are obtained applying the Hauser-Feshbach approach. In this case cross section has the form [4]:

$$\sigma_{n\alpha} = g\pi\hat{\lambda}_n^2 \frac{T_n T_\alpha}{\sum_c T_c} W_{n\alpha},$$

(1)

where T is transmission coefficient; g is statistical factor; $\hat{\lambda}_n$ is reduced neutron wavelength; $W_{n\alpha}$ is width fluctuation correction factor.

Transmission coefficients were evaluated using quantum mechanical approach based on reflection factor [5, 6]. Sum on the denominator is over all open energetic possible channels together with momentum and spin conservations. Width fluctuation correction factor, $W_{n\alpha}$, was evaluated using Moldauer approach [7, 8].

In the fast neutrons energy range direct and pre-equilibrium mechanisms give their contribution to the cross section also. For this reason Talys codes were used. This freeware soft, working mainly under Linux is dedicated to nuclear reactions and structure of atomic nuclei calculations. In Talys are implemented compound, direct and pre-equilibrium nuclear reaction mechanisms together with nuclear data of optical potential, nuclear density and levels spacing for a large number of nuclei and isotopes [9].

Another physical parameter of interest is the strength functions. Strength functions, as function of energy (E), momentum (J) and parity (Π), are related to transmission coefficients by a proportional factor and they are defined as [10]:

$$S(E,J,\Pi) = \frac{T(E,J,\Pi)}{2\pi}. \tag{2}$$

RESULTS AND DISCUSSIONS

For the evaluation of ^{147}Sm(n,α)^{144}Nd cross section starting from 0.5 keV up to 500 keV Hauser-Feshbach formalism were used. It was realized a computer program which calculates transmission coefficients using quantum mechanical approach and were considered all open channels. In this energy range were considered only compound processes. Experimental results from [10] were described very well. Results are shown in Fig. 1.
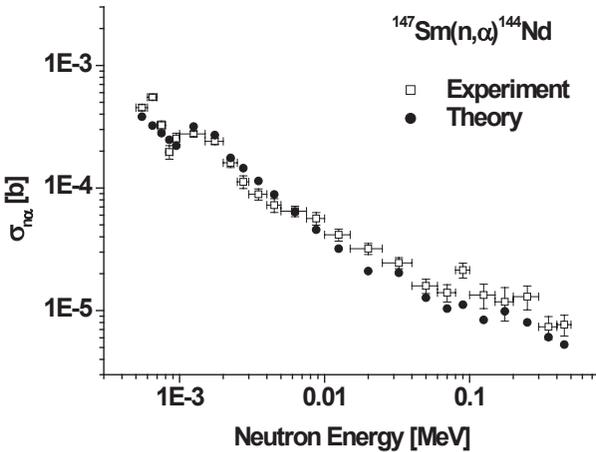

Fig. 1. Theoretical and experimental cross sections of ^{147}Sm(n,α)^{144}Nd reaction.

In the evaluation it was taken a rectangular optical potential, $U = V + I \cdot W$, with real and imaginary part in the incident and emergent channels. Radius channel has the usual expression $R = R_0 \cdot A^{1/3}$ [fm] ($R_0 = 1.45$ fm, A is atomic mass). At 1 keV, in the alpha channel, real part of optical potential was $V_\alpha = 225$ MeV and imaginary part, $W_\alpha = 0.15$ MeV. With the increasing of the energy, up to 450 keV, in order to describe experimental data, V_α was also increased slowly with about 15%. Calculations result that the experimental data are not so sensible to parameters of optical potential and channel radius in entrance channel.

For neutrons energy interval from 0.45 MeV up to 20 MeV cross sections were calculated with the help of Talys. In comparison with our soft (results from Fig. 1) in Talys the optical potential is of Wood-Saxon form, with real and imaginary part, with the following components: volume, surface and spin-orbital [9]. Also, in the Talys calculations, compound, direct and pre-equilibrium mechanisms were enabled together with discrete and continuum states of residual nuclei. Results are shown in Fig. 2 a) and b).
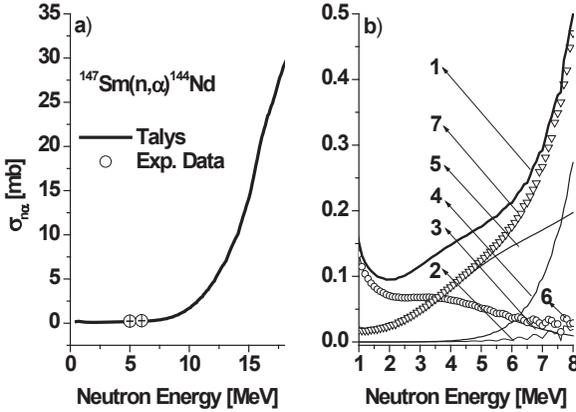

Fig. 2. Fast neutrons cross sections of ^{147}Sm(n,α)^{144}Nd reaction. a) Comparison of Talys evaluations and experimental data (2 points – 5 and 6 MeV). b) Contribution to the cross section of direct and compound processes together with discrete and continuum states of residual nucleus. 1– total (n,α) cross section (1 = 2 + 3 + 4 + 5 = 6 + 7); 2 – Discrete states + Direct processes; 3– Discrete + Compound; 4 – Continuum + Direct; 5 – Continuum + Compound; 6 – Discrete + Direct + Compound; 7 – Continuum + Direct + Compound.

In Fig.2a theoretical evaluations are compared with experimental data obtained by us at 5 and 6 MeV respectively and a very good agreement was obtained. Up to 7–8 MeV compound processes are dominant. Lower than 1 MeV discrete states are dominant but with the increasing of incident energy continuum states become more important and higher than 8 MeV discrete states can be neglected (see Fig. 2b).

The above analysis it is important because at 5 and 6 MeV a forward–backward effect (FB) was observed [11]. FB effect is defined as the ratio of all registered forward and backward events, $S_{FB} = A_F/A_B$, where $A_{F,B}$ is:

$$A_F(E_n) = 2\pi \int_0^{\pi/2} \phi_n(E_n)\sigma_{n\alpha}(E_n,\theta)\sin(\theta)d\theta, \; A_B(E_n) = 2\pi \int_{\pi/2}^{\pi} \phi_n(E_n)\sigma_{n\alpha}(E_n,\theta)\sin(\theta)d\theta, \quad (3)$$

where θ is polar angle; $\sigma_{n\alpha}(E_n, \theta)$ is differential cross section of (n,α)-reaction; $\phi_v(E_n)$ is neutrons incident flux.

Using (n,α) differential cross sections, relation (3), neglecting the loss of alpha particles in the target (tin target) and a neutron flux proportional with $1/E_n^{0.9}$ the FB effect for 5 and 6 MeV was calculated. Results are given in Table 1.

Table 1. ^{147}Sm(n,α)^{144}Nd cross section with evaluated and experimental FB effect

E_n [MeV] [I]	Direct [mb] Talys		Compound [mb] Talys		Total Talys [mb] [VI]	S_{FB} Talys [VII]	S_{FB} Exp [VIII]
	Discr [II]	Cont [III]	Discr [IV]	Cont [V]			
5	0.00097	0.00787	0.05023	0.11627	0.1754	1.0122±0.0096	1.65±0.165
6	0.00248	0.02951	0.03379	0.14606	0.2118	1.0436±0.0127	2.54±0.254

In Table 1, columns II, III, IV and V are the cross sections for 5 and 6 MeV with the contribution of direct and compound processes related to discrete and continuum states of the residual nuclei calculated with Talys. Column VI is the sum of column II to V and these theoretical values are in good agreement with experimental data. From Table 1 results that the direct processes are not dominant at 5 and 6 MeV but they will become important at higher energies quite quickly. Considering these facts the experimental FB effects from column VIII are to large in comparison with theoretical evaluations (column VII) and they can not come from direct processes as suggested by authors of [11] naming them as non-statistical effects. This discrepancy can be explained taking into account that at fast neutrons energies many emergent channels with participation of alpha particles are open. Further the measurements were done with a double gridded ionization chamber and the resolution of registered alpha particles is of order of 200 keV which also could influence the final results of experiments.
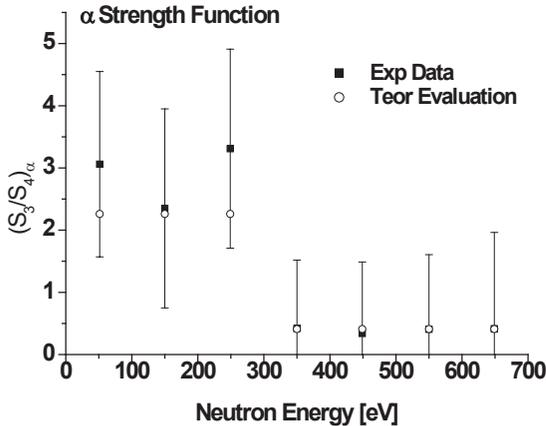

Fig. 3. Alpha strength function. Theory and experiment.

In the resonance region of ^{147}Sm(n,α) reaction, ratios of alpha strength functions, S_3/S_4, corresponding to the spin of compound nucleus $J = 3, 4$ where measured [10]. It was expected

that alpha strength ratios to be constant with energy (as predicted by theory) but around 300 eV the ratio is abruptly decreasing. Experimental data on alpha strength ratios from [10] are compared with our theoretical evaluations (see Fig. 3). In [10] the decreasing was explained once again by the presence of non-statistical effects. In the given spin channel of the compound nucleus the averaged strength function was calculated as sum of transmission coefficients considering spin and momentum conservation. Calculations were realized with our soft, taking into account all possible channels and rectangular optical potential with real and imaginary part $U = V + I \cdot W = 225$ MeV $+ I \cdot 0.15$ MeV. The agreement between theoretical and experimental data was obtained by varying the radius of alpha channels with about +20%. According to theory a very low component of direct processes can exist in principle in the resonance region but this cannot explain the ratio decreasing. Another explanation can come also from the fact that in the hundreds of eV energy range there are present other channels including alpha particles. Furthermore experimental data have large errors which are coming from the low values of the cross sections (of order of 0.01 b) combined with high background.

CONCLUSIONS

Cross sections and angular distributions of ^{147}Sm(n,α)^{144}Nd reaction were calculated in a wide energy range, from 0.5 keV up to 20 MeV using own computer codes and Talys software. Also, FB effect for 5 and 6 MeV together with alpha strength ratios in the resonance region were evaluated. Cross sections, FB effect and alpha strength function ratios were compared with experimental data. In the case of (n,α) cross sections a good agreement between theory and experiment was obtained and the contribution of different nuclear reaction mechanisms given by discrete and continuum states of residual nuclei was also extracted. Differences between experimental and theoretical FB effect and alpha strength function ratios was explained mainly by the presence of other open channels involving alpha particles concurring with investigated (n,α) one because it was demonstrated that the direct component is low in comparison with compound processes for the mentioned incident neutrons energy values.

The present researches are realized in the frame of fast neutrons induced reactions nuclear data program from FLNP JINR, Dubna, developed at Electrostatic Generator EG-5 and IREN, the neutrons source facility.

REFERENCES

1. C. Oprea, A.I. Oprea, XXVth International Seminar of the Interaction of Neutrons with Nuclei (ISINN25), Proceedings of the Seminar, ISBN 978-5-9530-0485-5, JINR Dubna Publishing House, Dubna, May 22–26, p. 105 (2017).
2. M. Salvatore, I. Slessarev, A. Tchistiakov, Nucl. Sci. Eng. **130**, p. 309 (1998).

3. G. Khuukhenkhuua, Yu.M. Gledenov, M.V. Sedysheva, M.Odsuren, J. Munkhsaikhan, T. Delgersaikhan, Letters to Physics of Elementary Particles and Atomic Nuclei, v. **11**, No. 6, p. 1159 (2014).
4. W. Hauser, H. Feshbach, Phys. Rev. **87**, vol. 2, p. 366 (1952).
5. A. Foderaro, The Element of Neutrons Interaction Theory, MIT Press, ISBN 9780262561600 (1971).
6. A.I. Oprea, C. Oprea, C. Pirvutoiu, D. Vladoiu, Romanian Reports in Physics, vol. **63**, 1, p. 107 (2011).
7. P.A. Moldauer, Phys. Rev., v. **157**, 4, p. 907 (1967).
8. P.A. Moldauer, Rev. Mod. Phys., v. **36**, p. 1079 (1964).
9. A.J. Koning, S. Hilaire and M.C. Duijvestijn, .TALYS-1.0., Proceedings of the International Conference on Nuclear Data for Science and Technology, April 22–27, 2007, Nice, France, editors O.Bersillon, F.Gunsing, E.Bauge, R.Jacqmin, S.Leray, EDP Sciences, 211 (2008).
10. P.E. Koehler, Yu.M. Gledenov, T. Rauscher, S. Frolich, Phys. Rev. C **69**, 015803 (2004).
11. Yu.M. Gledenov, M.V. Sedysheva, V.A. Stolupin, Guohui Zhang, Jiaguo Zhang, Hao Wu, Jiaming Liu, Jinxiang Chen, G. Khuukhenkhuu, P. E. Koehler, P. J. Szalanski, Phys. Rev. C **80**, 044602 (2009).

Nuclear Structure, Nuclear Data

A RELIABILITY OF THE RESULTS OF A STUDY OF THE NUCLEAR SUPERFLUIDITY AND HIDDEN PARAMETERS OF THE GAMMA DECAY OF THE COMPOUND STATE

Vu D.C.[1,4], Sukhovoj A.M.[1], Mitsyna L.V.[1], Nguyen X.N.[2], Pham D.K.[3], Nguyen N.A.[2]

[1]*Joint Institute for Nuclear Research, Dubna, 141980, Russia*
[2]*Dalat Nuclear Research Institute, Vietnam Atomic Energy Institute, Hanoi, Vietnam*
[3]*Hanoi University of Science and Technology, 1 Dai Co Viet, Hanoi city, Vietnam*
[4]*Vietnam Academy of Science and Technology Institute of Physics, Hanoi, Vietnam*

An analysis of the intensities of the two-step cascades (TSC) of reaction products emitted sequentially is now the only possibility of a study of an interaction between Fermi- and Bose-states in an excited nucleus, at least, up to the binding energy of the last nucleon. To obtain reliable information about this interaction, it is necessary to recognize sources of the process distortion. In the present work we attempted a difficult task to evaluate the hidden parameters influence on the required parameters.

1. INTRODUCTION

At small excitation energy, in a nucleus the levels of different types can be excited. In even-even deformed nucleus, for example, quasi-particle and vibrational levels as well as rotational bands have been observed. When the excitation energy grows, the nuclear levels appear, the wave functions of which contain components of all types [1,2]. It is caused by a fragmentation of nuclear states in the gamma-decay process. So at the nuclear excitation energies E_{ex} above some MeV, in the nucleus there are no, in pure form, quasi-particle, vibrational and rotational nuclear levels.

A common defect of a majority of modern nuclear models is an incorrect representation of the excited nucleus as a purely fermion system. The only realistic model of the level density, which takes into account the boson excitations [3] in the nucleus, postulates an existence a phase transition at $E_{ex} \geq B_n$ (B_n is the neutron binding energy). But this model does not explain a real process of nuclear transition to the superfluid state. So, for a practical investigation of the interaction between Fermi- and Boson-systems, the models for the excited nucleus and its cascade decay (as far as possible, including nucleon products of nuclear reaction) are needed.

2. A POSSIBILITY OF EXPERIMENTAL INVESTIGATION OF THE NUCLEAR SUPERFLUIDITY

To detect the effects connected with the nuclear superfluidity, it is necessary to determine [4] the level density ρ and the partial widths Γ of emission of the products at the decay of high-excited nuclear levels (above 5–10 MeV). At that, the ρ and Γ values must be defined in the whole energy region (from the nuclear compound-state up to the ground state). As there are no modern spectrometers to determine the parameters of all nuclear levels, so the experiment must provide the accuracy, at least, of a few tens of percent. Such accuracy is just enough to determine the ρ and Γ values in the required energy region as it corresponds to real

large coefficients of transfer of errors of the experimental spectra and cross sections to errors of desired gamma-decay parameters.

As shown in [5 - 7], in order to get reliable information about the superfluid phase of the nuclear matter it is necessary to obtain the level density up to E_{ex} not less than $4\Delta_0$ (Δ_0 is the pairing energy of the last nucleon in the nucleus) with an acceptable accuracy. The level density g of quasi-particle levels near Fermi-surface is about 10 MeV^{-1}, whereas the excitation energy of known phonon bands is of order 1 MeV^{-1}. Thus, the only possibility of experimental identification of the boson levels is a feature of the energy dependence of their density, which decreases at a growth of the partial widths of emission products of the nuclear reaction.

It should be noted that the level density and the partial widths of emission are included in the measured spectra and cross sections of reactions as $\rho \times \Gamma$ product. It means that any experiment, in which the coincidence method is not used, may be mathematically presented by only one equation with two (or even more) unknown values. In other words, whatever ρ and Γ values (from zero up to infinity) can ensure an accurate description of the cross sections and spectra.

For experiments, which use the coincidence method for recording of the set of the parameters (intensities of gamma transitions and energies of all excited levels), a situation is more favorable. The energies of both of initial level of TSC and of its final level are determined by the experimental conditions, as well as the intensities of two cascade quanta. The uncertainty of the extracted ρ and Γ parameters was essentially decreased, if to separate carefully the intensity $I_{\gamma\gamma}(E_1)$ of primary transitions of the TSC from its total intensity $I_{\gamma\gamma}(E_1,E_2)$ (E_1 is energy of primary cascade quantum, E_2 is energy of secondary quantum).

Each of experimental spectra of two coincided gamma-quanta is a superposition of two mirror-symmetrical distributions. If the set of resolved pairs of peaks of the cascades are big enough, using information about their energies, we can determine the intensity of the cascades as a function of only primary transitions with a good accuracy. An inevitable distortion of a shape of the $I_{\gamma\gamma}(E_1)$ distribution due to inaccurate accounting [5] of a contribution of unresolved transitions can be minimized with statistics increase. Our analysis of the experimental TSC intensities, for 44 nuclei of the mass region $28 \leq A \leq 200$ [6 – 10], unambiguously showed that at TSC recording with a statistics of $\sim$ 4000 events (and more) in a summary peak, this distortion has no effect on the errors of extracted parameters and can be neglected. In all our experiments, three of quarters of all investigated nuclei had a minimal required statistics, and it was some times more for the rest of nuclei (in the case of ^{172}Yb, for example, the percentage of resolved TSC to the ground state was 70%).

The method [11, 12] of decomposition of experimental spectrum into two required distributions $I_{\gamma\gamma}(E_1)$ and $I_{\gamma\gamma}(E_2)$ was firstly realized in Dubna.

3. THE METHOD FOR A STUDY OF THE GAMMA DECAY

For the first time, the method for simultaneous determination ρ and Γ values from measured intensities $I_{\gamma\gamma}(E_1)$ of the two-step cascades at radiative capture of the thermal neutrons by stable target nuclei was proposed in Dubna [13, 14]. In the experiments the intensities $I_{\gamma\gamma}$ to a group of low-lying levels of a target nucleus were measured, when the high-lying compound state decays and the TSC quanta were recorded by two Ge-detectors, as coincidences. At that, the interval of spins, parities and the partial widths of excited levels, density of which must be determined for evaluation of the nuclear entropy [3], are limited by selection rules on multipolarity.

Our method allows us to get unique information about gamma decay of any nuclei [5, 6]. The intensity distributions $I_{\gamma\gamma}(E_1)$, derived using the procedure [13] were approximated by fitted parameters $p_1,p_2..$ and $q_1,q_2..$ of suitable functions $\rho(E_{ex}) = \varphi(p_1,p_2,...)$ and $\Gamma(E_1) = \psi(q_1,q_2..)$. A choice of the models, which define the hypothetical $\rho(E_{ex})$ and $\Gamma(E_1)$ functions with an optimal number of fitted parameters, is very important, as it is just a source of the systematics error of the analysis.

A cascade decay of a neutron resonance (or any compound-state) λ occurs through the intermediate levels i to the final levels f. The part of primary transitions $I_{\gamma\gamma}(E_1)$ for any small energy interval ΔE_j of cascades is expressed by an equation:

$$I_{\gamma\gamma}(E_1) = \sum_{\lambda,f}\sum_i \frac{\Gamma_{\lambda i}}{\Gamma_\lambda}\frac{\Gamma_{if}}{\Gamma_i} = \sum_{\lambda,f}\sum_j \frac{\Gamma_{\lambda j}}{<\Gamma_{\lambda j}>M_{\lambda j}}n_j\frac{\Gamma_{jf}}{<\Gamma_{jf}>m_{jf}}. \tag{1}$$

A sum of the partial widths $\Sigma_j\Gamma_{\lambda j}$ of primary transitions to $M_{\lambda j}$ intermediate levels is $<\Gamma_{\lambda j}>M_{\lambda j}$, and a sum $\Sigma_j\Gamma_{jf}$ for secondary transitions to m_{jf} final levels is $<\Gamma_{jf}>m_{jf}$, inasmuch as $<\Gamma_{\lambda j}> = \Sigma_j\Gamma_{\lambda j}/M_{\lambda j}$ and $<\Gamma_{jf}> = \Sigma_j\Gamma_{jf}/m_{jf}$. In a small energy interval ΔE_j a sum of intermediate levels is $n_j = \rho\Delta E_j$.

One can see that in the equation (1) for any i and f levels of TSC there are two independent parts:
1) $I_1 = \rho\times\Gamma/\sum(\rho\times\Gamma)$ distribution of the spectrum of primary gamma-transitions and
2) $I_2 = \Gamma/\sum(\rho\times\Gamma)$ distribution of branching coefficients.

At that, anti-correlation between ρ and Γ values in I_1 distribution is absolute (100%), but correlation between I_1 and I_2 distributions is practically absent (of course, by a condition that a probability of emission of secondary gamma quantum to f levels does not depend on a probability of gamma transition between the levels λ and i). As in $I_{\gamma\gamma}(E_1)$ distribution the correlation between the ρ and Γ values becomes weaker, it limits an area and increases the precision of possible solutions of equation (1).

Correlation coefficients are different for products of type $\rho\times\Gamma$ as well as $\rho\times\rho$ and $\Gamma\times\Gamma$ (for various energies of gamma-transitions and excitation energies). But as correlation coefficients between the spectrum I_1 of primary transitions and branching coefficients I_2 are almost zero, this fact provides a possibility to avoid the fatal errors at analysis. A high statistics allowed us to obtain $I_{\gamma\gamma}(E_1)$ distributions carefully enough (with a required accuracy of several tens of percent in any energy bins).So we can evaluate the errors $\Delta\rho$ and $\Delta\Gamma$ for a majority of obtained values [6, 7, 10] by several tens of percent at $\Delta I_{\gamma\gamma}$ error of about 1%. How $\Delta I_{\gamma\gamma}$ connects with $\Delta\rho$ and $\Delta\Gamma$ at any step of iteration process of solving the system (1) by Monte-Carlo method, one can see in detail in [5–10].

In order to get a reliable data by the method of analysis of TSC intensities, the following representations about the required $\rho(E_{ex})$ and $\Gamma(E_1)$ functions are absolutely necessary:
1) the number of quasi-particles begins to grow from zero (for even-even and odd-odd nuclei) or from unity (for even-odd and odd-even nuclei) at an increase of E_{ex} (as in the model [2,15], for example);
2) the levels of collective type must appear at the breaking of each Cooper pair (as in the model [4], for example);
3) the dependences of the radiative widths of the dipole transitions on the excitation energy can be nonmonotonical functions [16].

4. EVALUATION OF AN INFLUENCE OF HIDDEN PARAMETERS ON THE ANALYSIS RESULTS

As was already said, a necessity of simultaneous fitting of the parameters included in the intensity $I_{\gamma\gamma}$ distribution is evident due to the strong correlation between the $\rho(E_{ex})$ and $\Gamma(E_1)$ functions. The first step to solve this difficult problem was done in Dubna. There are no yet both the experiments on a study of an interaction between nuclear Fermi- and Bose-states, which can really compete with our data, and the modern models to describe this process with some degree of certainty. For now, our purpose is to determine and evaluate factors, which exert strong influence on the investigated process, when comparing different variants of our empirical model.

At approximation of $I_{\gamma\gamma}(E_1)$ intensities, the fitting of the parameters of the $\rho(E_{ex})$ and $\Gamma(E_1)$ functions is practically unambiguous in a wide region of required values. The best fits have usually a small scatter for the iteration processes with different vectors of initial values. Nevertheless, a correctness of $\rho(E_{ex})$ and $\Gamma(E_1)$ energy dependences in used models (and phenomenological representations) cannot be determined in the framework of the experiment. The most probable $\rho(E_{ex})$ and $\Gamma(E_1)$ functions can be chosen only analyzing different alternative models.

As the required $\rho(E_{ex})$ and $\Gamma(E_1)$ functions can be obtained only from indirect experiment, hidden parameters of the decay process (the breaking thresholds of the Cooper pairs of nucleons, local peaks in the energy dependence of the radiative widths, etc.) represent as serious problem. So it is very important to describe reliably the nuclear properties in the points of breaking the Cooper pairs.

In a base of our experimental data, the fact is established that in these points there are breaks in the energy dependence of the nuclear level density as well as distinctive local changes in the dependences of the radiative widths on the excitation energy. At that, our results won't be in a contradiction with smoothness of the evaporating cross sections, if there are increases in the partial widths (or radiative strength functions) in the points of the Cooper pairs' breaking. This effect can be rather confirmed by pygmy-resonance, which was discovered in many nuclei [17]. It should be noted that pygmy-resonyance take place not in all nuclei. But if to take into account that pygmy-resonance strength varies for different nuclei, whereas its center coincides well with the breaking point of the second Cooper pair, and the level densities of different nuclei noticeably vary in the points of Cooper pairs' breaking [6, 7, 8], then our experiments could explain the pygmi-resonance specific.

For a local intensification of the partial widths, an additional fitted coefficient M was introduced to their expressions [9]. The maximal value of the intensification was at $M = \rho_{fg}/\rho_{exp}$, where ρ_{fg} is the highest possible density of quasi-particle levels and ρ_{exp} is the level density, which provides an accurate description of experimental intensity distribution. In order to evaluate the probable increasing of the radiative strength functions, the parameter M varied at solving of the system of equations (1).

In order to investigate an interconnection between stepwise changes in the energy dependence of the nuclear level density and changes of the intensities of gamma transitions, four nuclei with different nucleon parities (^{172}Yb, ^{176,177}Lu and ^{193}Os) [6, 7] were analyzed. At that, the TSC intensities for these nuclei were fitted with an additional parameter M. The results of the analysis are presented in Figs.1–4.

An inability to describe $I_{\gamma\gamma}(E_1)$ distribution with help of $\rho(E_{ex})$ function calculated using Fermi-gas model is evident in Fig. 1. One can see also in Fig. 1 that the changes in the radiative strength functions (at various M) not lead to a noticeable modification of the

approximated TSC intensity, whereas a mutual scatter of ρ and Γ became significantly bigger in the presence of M in the fittings (see Figs. 2, 3).
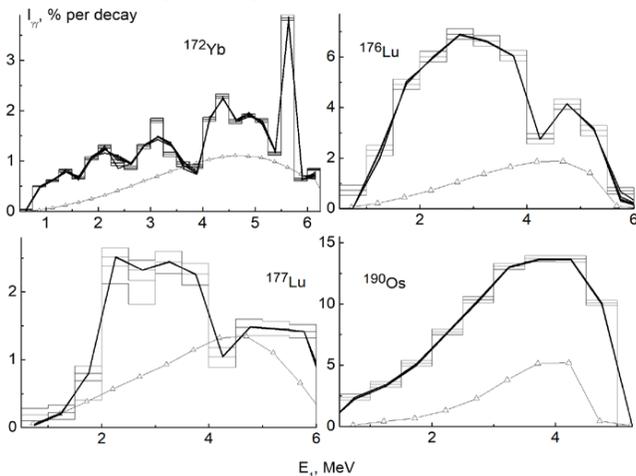

Fig. 1. The intensity distribution $I_{\gamma\gamma}(E_1)$ of primary transitions of TSC for ^{172}Yb, ^{176}Lu, ^{177}Lu and ^{193}Os nuclei. The broken solid line is the best fit; histogram is a total intensity of TSC in energy intervals with width of 0.5 MeV (0.25 MeV for ^{172}Yb); triangles is calculation using the models [18,19] with a constant value for $M1$-strength functions.
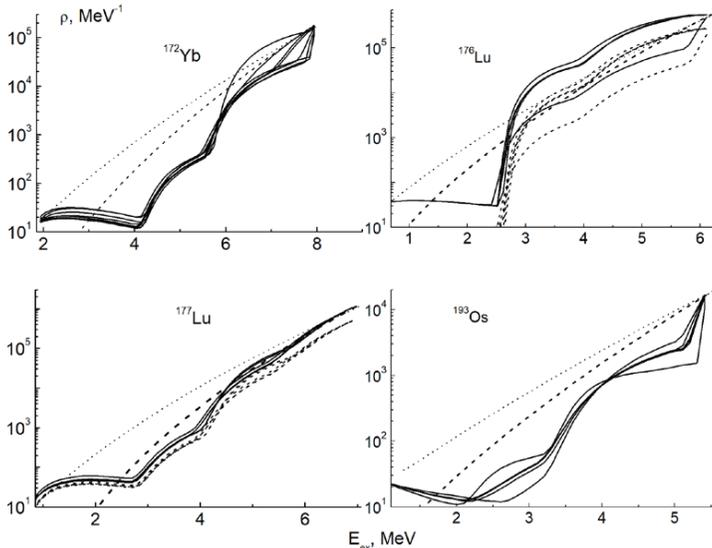

Fig. 2. The level density dependences on the excitation energy for TSC of ^{172}Yb, ^{176}Lu, ^{177}Lu and ^{193}Os nuclei. Solid lines are the best fits; dashed and dotted are level densities calculated using the Fermi-gas model with and without taking into account the shell inhomogenities of single-partial spectrum, correspondingly.
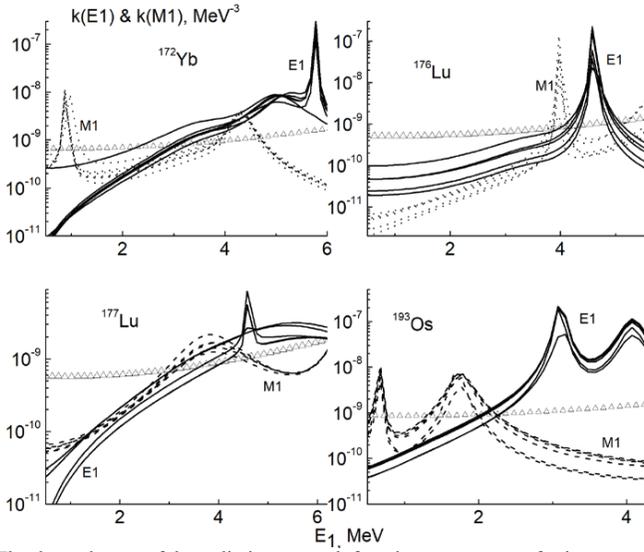
Fig. 3. The dependences of the radiative strength functions on energy of primary transitions of TSC ^{172}Yb, ^{176}Lu, ^{177}Lu and ^{193}Os nuclei. Solid lines – E1-transitions; dashed lines – M1-transitions.
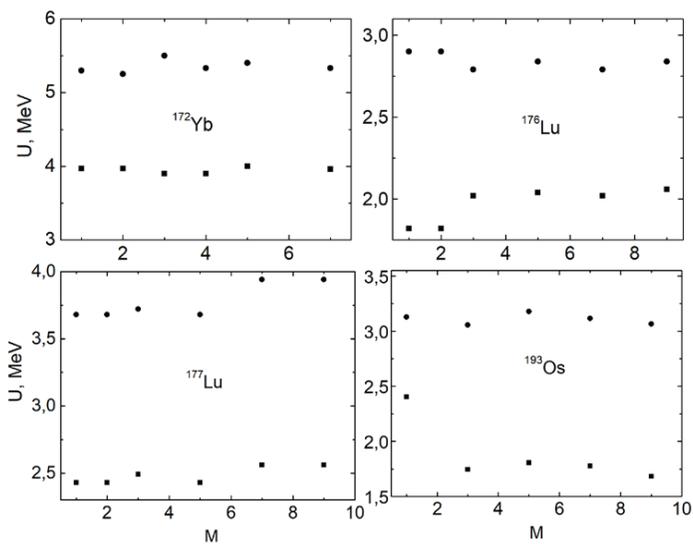

Fig.4. The breaking thresholds of the Cooper pairs of nucleons in ^{172}Yb, ^{176}Lu, ^{177}Lu and ^{193}Os nuclei at various M values. Points are the breaking thresholds U_2 for the second Cooper pairs; squares are the thresholds U_3 for the third pairs.

For ^{172}Yb and ^{193}Os the intense increase in the strength functions is observed at $E_{ex} \sim B_n$. At that, intensity description becomes more precise at the energies lower than the breaking threshold for the second Cooper pair (at $E_1 \leq 1–2$ MeV). Incidentally, in these nuclei the point of the fourth Cooper pair almost coincides with B_n (and in some nuclei just at this energy the phase transition to the Fermi-system is predicted [3]).

The most probable values of the breaking thresholds of the second and the third Cooper pairs at different parameters M are shown in Fig. 4. From their small scatter follows that a change of the intensity of emitted gamma-quanta weakly influences the positions of points of the Cooper pairs' breaking, but the observed intensity of gamma-transitions from the breaking point, at that, essentially changes for different nuclei and at various energies.

5. CONCLUSION

For the cascades measured with a small background and coincidence statistics high enough, the shape of $I_{\gamma\gamma}(E_1)$ distribution can be determined [11] with an sufficient uncertainty (of about several percent) to unambiguously determine nuclear parameters.

One can accept that experimental errors of the total sum $I_{\gamma\gamma}(E_1,E_1)$ are the same as the errors of the intense primary transition (5–10% per decay), which are used for normalization of the absolute values of the cascades. Such accuracy guarantees a reliable determination of the parameters of the cascade gamma-decay (including the breaking thresholds for Cooper pairs) even at improper representation of $\Gamma(E_1)$ function.

Errors of the obtained $\rho(E_{ex})$ and $\Gamma(E_1)$ functions, which are describe the $I_{\gamma\gamma}(E_1)$ distribution with such accuracy, are mainly conditioned by an inaccuracy of their representations used by the empirical model [5].

When analyzing in the framework of the Dubna method, the $I_{\gamma\gamma}(E_1)$ intensities were described for 44 nuclei of the mass region of $28 \leq A \leq 200$, and a realistic picture of interaction between Fermi- and Bose-states in the nucleus, below the neutron binding energy, was firstly obtained.

The experiments were carried out in Dubna, Riga, Rzhezh and Dalat. Now a group from Belgrad began the experiment at the reactors in Munich and Budapest.

REFERENCES

1. V.G. Soloviev, Sov. J. Phys. Part. Nucl., **3** (1972) 390.
2. Reference Input Parameter Library RIPL-2, Handbook for calculations of nuclear reaction data, IAEA-TECDOC (2002).
3. A.V. Ignatyuk, G. N. Smirenkin, A. S. Tishin, Sov. J. Nucl. Phys., 21, **255**(1975).
4. A.V. Ignatyuk, Report INDC-233(L), IAEA (Vienna, 1985).
5. A.M. Sukhovoj, Phys. Atom. Nucl. **78**, 230 (2015).
6. A.M. Sukhovoj, L.V. Mitsyna, N. Jovancevich, Phys. Atom. Nucl. **79**, 313 (2016).
7. D.C. Vu et al., Phys. Atom. Nucl. **80,** 237(2017).
8. N.A. Nguyen et al., JINR preprint E3-2017-72, Dubna, JINR, 2017.
9. N. Jovancevich, A.M. Sukhovoj, W.I. Furman, and V.A. Khitrov, in *Proceedings of XX International Seminar on Interaction of Neutrons with Nuclei, Dubna, May 2012,* Preprint № E3-2013-22 (Dubna, 2013), p. 157; http://isinn.jinr.ru/past-isinns.html.

10. L.V. Mitsyna, A.M. Sukhovoj, in *Proceedings of XXII International Seminar on Interaction of Neutrons with Nuclei, Dubna, May 2014,* Preprint № E3-2015-13 (Dubna, 2015), p. 245; http://isinn.jinr.ru/past-isinns.html.
11. S.T. Boneva et al., Sov. J. Part. Nucl. **22**, 232 (1991).
12. A.M. Sukhovoj, V.A. Khitrov, Instrum. Exp. Tech., **27**, 1071 (1984).[Instrum. Exp. Fiz., **27,** 1017(1984)].
13. S.T. Boneva, A.M. Sukhovoj, V.A. Khitrov, and A.V. Voinov, Nucl. Phys. **589**, 293(1995).
14. Yu.P. Popov et al., Izv. Acad. Nauk SSSR, Ser, Fiz., **48**, 1830(1984).
15. V.M. Strutinsky, in *Proceedings of the International Congress on Nuclear Physics, Paris, France, 1958*, p. 617.
16. E.V. Vasilieva, A.M. Sukhovoj, V.A.Khitrov, Phys. At. Nucl. 64, 153(2001).
17. D. Bohle et al., Phys. Lett. **137B**, 27(1984).
18. W. Dilg, W. Schantl, H. Vonach, and M. Uhl, Nucl. Phys. A **217**, 269(1973).
19. S.G. Kadmenskij, V.P. Markushev and W.I. Furman, Sov. J. Nucl. Phys. **37,** 165 (1983).

What Is Possible to Find out about the Dipole Photon Strength Function from Study of Resonance Neutron Radiative Capture by ^{195}Pt Nucleus Measured in DANCE Experiment

N. Simbirtseva[1,2] , F. Bečvář[3], R.F. Casten[4,5] , A. Couture[6], W. Furman[1], M. Krtička[3], S. Valenta[3]

[1]*Joint Institute for Nuclear Research, RU-141980 Dubna, Russia*
[2]*Institute of Nuclear Physics, Almaty, 050032, the Republic of Kazakhstan*
[3]*Charles University in Prague, CZ-180 00 Prague 8, Czech Republic*
[4]*Yale University, Wright Lab, New Haven, CT 06520 USA*
[5]*Michigan State University, FRIB, E Lansing, MI 48824 USA*
[6]*Los Alamos National Laboratory, P.O. Box 1663, Los Alamos, New Mexico 87545, USA*

Abstract

The ^{195}Pt(n,γ)^{196}Pt reaction was measured with the multi-detector array DANCE (Detector for Advanced Neutron Capture Experiments) consisting of 160 BaF$_2$ scintillation detectors at the resonance neutron beam of the Los Alamos Neutron Science Center. The multi-step cascade γ-ray spectra from individual neutron resonances were prepared and compared with predictions based on different photon strength function models. The simulated spectra were obtained by the DICEBOX statistical model code in combination with the GEANT4-based simulation of the detector response. From a comparison of the experimental and simulated spectra for multiplicities m=2–7 a piece of new information on the photon strength functions of ^{196}Pt was derived.

Introduction

The neutron radiative capture plays an important role in the process of nucleosynthesis as well as in the dynamics of nuclear reactors and ADS. The correct and reliable description of (n,γ)-reaction requires detailed understanding of the cascade γ-decay of highly excited nuclear states. This in turn needs information on the photon strength functions (PSFs) and the level density (LD). Due to the extremely complicated structure of highly excited nuclear states mainly a statistical approach can serve as a basis for the analysis of related experimental data and their theoretical analysis. During past decades many phenomenological information on PSF and LD was obtained using various experimental methods and related data analyzes [1–10].

At excitation energy near and below the neutron binding energy B$_n$ the main contribution into PSF comes from E1 and M1 strengths and for discrete excitations near the ground state from the E2 strength too. The E1 part of PSF is mainly given by the giant dipole resonance (GDR) but some additional structures such as the pygmy resonances and scissors modes can play an essential role.

An existence and the global features of the GDR were proved and studied in many experimental and theoretical investigations but the PSF properties near and below B$_n$ are under the question. Data from several different experimental techniques [7–9] indicate a presence of resonance-like structures in the PSF at E$_γ$ ~ 4–8 MeV in several A ~ 190–200

nuclei. Unfortunately, previously used experimental methods did not usually allow to determine unambiguously the detailed characteristics of these resonances.

Beside that at low $E_\gamma \leq 2$ MeV two effects violating the traditional GDR picture were observed. The first one [10,11] is a possible temperature dependence of the GDR width that leads to a non-zero value of the E1 strength when E_γ goes to zero. The second one [2–4] is the sharp increase of the E1 PSF for $E_\gamma \leq 2$ MeV observed in many nuclei (although not as heavy as Pt) from Oslo-type experiments [12]. Additional experimental approaches need to clear out the PSF properties at these very low E_γ. One of them – analysis of multi-step cascade (MSC) spectra – exploits coincidence γ-ray spectra measured with detector system DANCE [13,14] in combination of the resonance neutron beam of the Los Alamos LANSCE neutron spallation source [15]. Analysis and first results of the decay properties of [196]Pt with this method is a subject of this contribution.

Experiment

The experimental MSC spectra were obtained at the neutron spallation source LANSCE using the detector array DANCE. The pulsed 800 MeV H^{−} beam from the LANSCE linear accelerator was injected into the proton storage ring after being stripped to H^{+} by a thin foil. The average current was 100 μA. The pulsed beam was then extracted with a repetition rate of 20 Hz and struck a tungsten spallation target. The resulting fast neutrons were moderated in the upper-tier water moderator and sent to flight path 14 at the Manuel Lujan Jr. Neutron Scattering Center. The DANCE detector array is installed at 20 m on this flight path.

The DANCE spectrometer [13,14] is designed for studying neutron capture cross sections on small samples. It consists of 160 BaF_2 scintillation crystals surrounding a sample and subtending a solid angle of near 4π. A [6]LiH shell about 6 cm thick is placed between the sample and the BaF_2 crystals to reduce the scattered neutron flux striking the crystals. The remaining background from scattered neutrons interacting with the BaF_2 crystals is subtracted in the off-line analysis. Besides the BaF_2 crystals, the DANCE setup includes four additional detectors that are used to monitor the neutron flux.

Data analysis and simulation procedure

The acquisition system of the DANCE array allows obtaining spectra of deposited energy sums from individual events [16] from well-resolved (s-wave) neutron resonances using the time-of-flight technique. These spectra, sorted according to detected multiplicity are shown in Fig. 1. They consist of a prominent peak (Q-value peak) in vicinity of the neutron binding energy B_n and a long tail down to low sum energy. The events in the peak deposited all the energy emitted by γ rays in the detector array while events at the low energy tail correspond to γ-cascades for which a part of the emitted energy escaped detection.

From γ cascades that deposited energy sum in the vicinity of B_n, specifically between 7 and 8 MeV, we constructed so-called MSC spectra [16]. They are for a few resonances presented in Fig. 2. The spectra are normalized to the same area in all shown multiplicities. In total we were able to extract MSC spectra from 5 and 11 resonances with $J^\pi = 0^-$ and 1^-, respectively. As a result of expected Porter-Thomas fluctuations of individual transitions intensities the spectra are not identical but sometimes substantially differ, especially for low multiplicities m. For comparison presented below we have made an unweighted average of these spectra for resonances with given spin.

Experimental MSC spectra were compared with predictions of simulations based on different models of PSFs and LD. The predictions were obtained with help of the statistical model code DICEBOX [17], which was used for simulation of the cascades starting at isolated resonances with given spin and parity, with subsequent modelling of the response of the DANCE array to these cascades with a code based on the GEANT4 package [18]. In the DICEBOX code complete information on properties of low-lying levels in ^{196}Pt was taken from available experimental data [19] below excitation energy of 1.88 MeV. Experimental data indicate that the information is not complete above this energy. At higher energies the levels and individual transitions were generated using the PSFs for different transitions types (E1, M1 and E2) and LD models. The code allows to treat correctly expected fluctuations in positions of levels as well as Porter-Tomas fluctuations of transition intensities via concept of different nuclear realizations [17].

So far, we have tested a consistency of experimental spectra with predictions for a few PSFs models. These models were based mainly on widely-used models, such as those available in the RIPL-3 database, or were inspired by available experimental data [7–9].
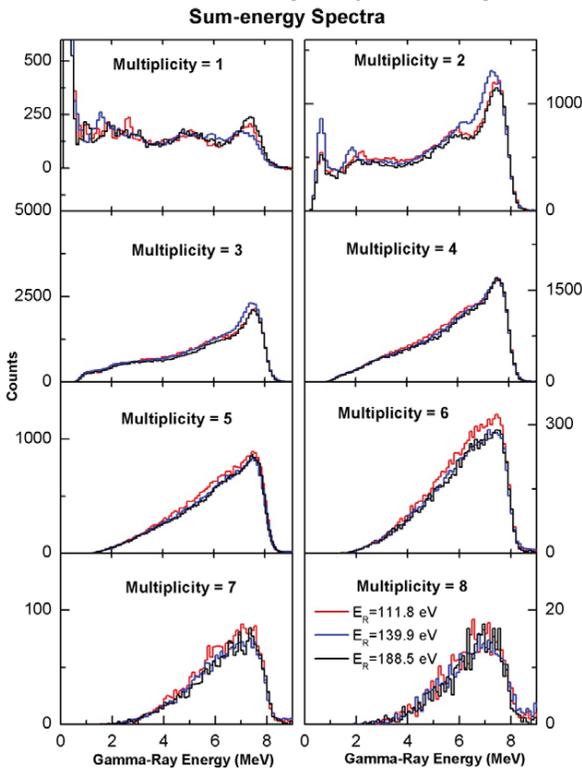

Fig. 1. Examples of the spectra of deposited energy sums for the neutron resonances with $J^{\pi} = 1^{-}$. Spectra for resonances with neutron energies $E_n = 111.8$ eV, 139.9 eV, and 188.5 eV are shown.
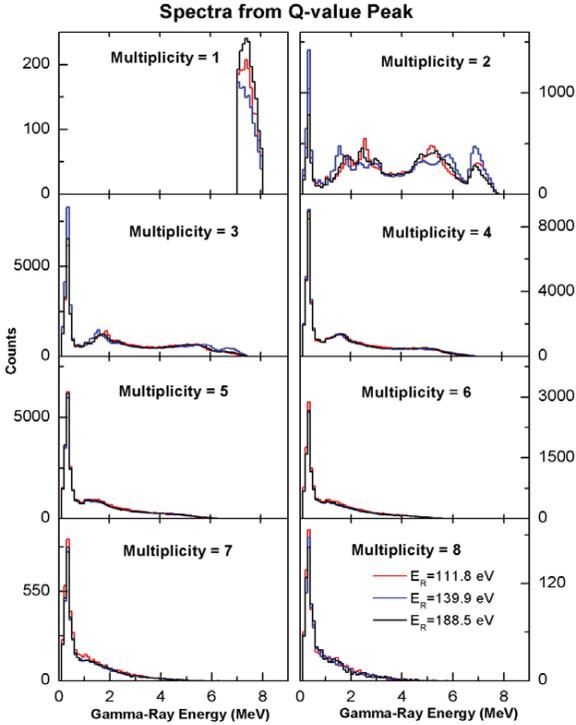
Fig. 2. Examples of multi-step γ-cascade spectra for some neutron resonances with $J^\pi = 1^-$. Only events depositing energy in the Q-value peak between 7 and 8 MeV were used for construction of the MSC spectra. Resonance energies are indicated in the legend.

Results and discussion

Simulations with PSFs that do not contain any resonance structure near $E_\gamma \sim 5.6$ MeV were found to be unable to reproduce the shape of the MSC spectra. As a result our data confirm a presence of a resonance-like structure at these energies. Postulation of the resonance structure near this energy significantly improves the agreement between simulated and experimental spectra. A very good reproduction of experiment was obtained with a model based on experimental data from Oslo experiment [8] that is shown in Fig. 3. The comparison of experimental MSC spectra with the predictions with this model is shown in Fig. 4 for s-wave resonances with both spins $J^\pi = 0^-$ and 1^-. The experimental data averaged over all measured neutron resonances are shown as lines while the gray corridors correspond to predictions. The corridor characterizes the fluctuations of spectra from different nuclear realizations and corresponds to the average +/– one standard deviation.

116

In reality, data from this experiment (similarly to any available experimental data [7–9]) is not available for at $E_\gamma < 2$ MeV. An extrapolation for these energies is thus required. A reasonable reproduction of MSC spectra requires PSF which is not very far from a constant value for $E_\gamma < 2$–2.5 MeV. Predictions with PSFs models having either a zero limit or a limit higher than about 2×10^{-8} MeV^{-3} for $E_\gamma = 0$ are unable to correctly predict the MSC spectra.

We have also found that the predicted spectra are sensitive to parity dependence of the LD, at least for excitation energies below about 3 MeV. A parity dependence can be expected as there are only a few negative parity levels below about 2 MeV known in ^{196}Pt. The simulations with some parity dependence introduced below about 3 MeV seem to describe the experimental MSC spectra better than simulation with the same number of positive- and negative-parity levels at all energies.

The comparison also indicates that the M1 strength, at least for $E_\gamma \sim 3$–4 MeV, is not negligible but our sensitivity to different E1/M1 composition at $E_\gamma > 4$ MeV seems to be partly limited.
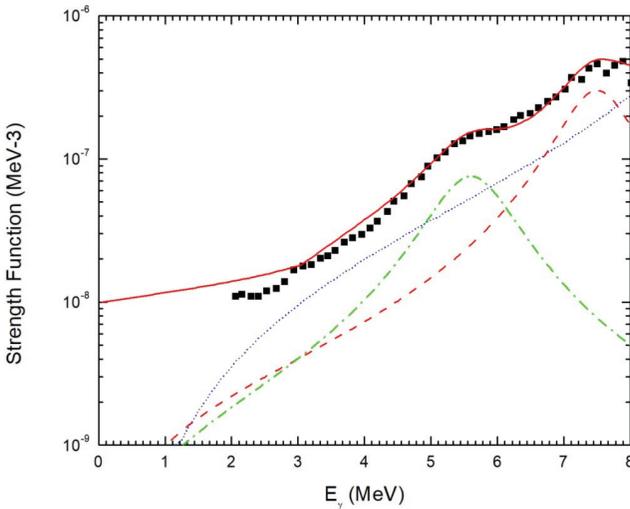

Fig. 3. The PSFs (lines) used in simulations presented in Fig. 4 together with PSF from [8] (black squares). Sum of used E1 and M1 PSFs (full line) consists of a GDR tail (based on QRPA calculations as published in [8] – dotted line), two resonance structures (dash and dot-and-dash lines) and a tail toward low E_γ (not shown).

Conclusion

The multi-step cascade spectra from several neutron resonances formed in the ^{195}Pt(n,γ)^{196}Pt reaction were measured with the DANCE detector array at the Los Alamos Neutron Science Center. Comparison of these spectra with their counterparts obtained from simulations based on different models of photon strength functions and level density confirms

presence of a resonance structure in the PSF near 5.6 MeV and a non-zero limit of PSF for very low energies.
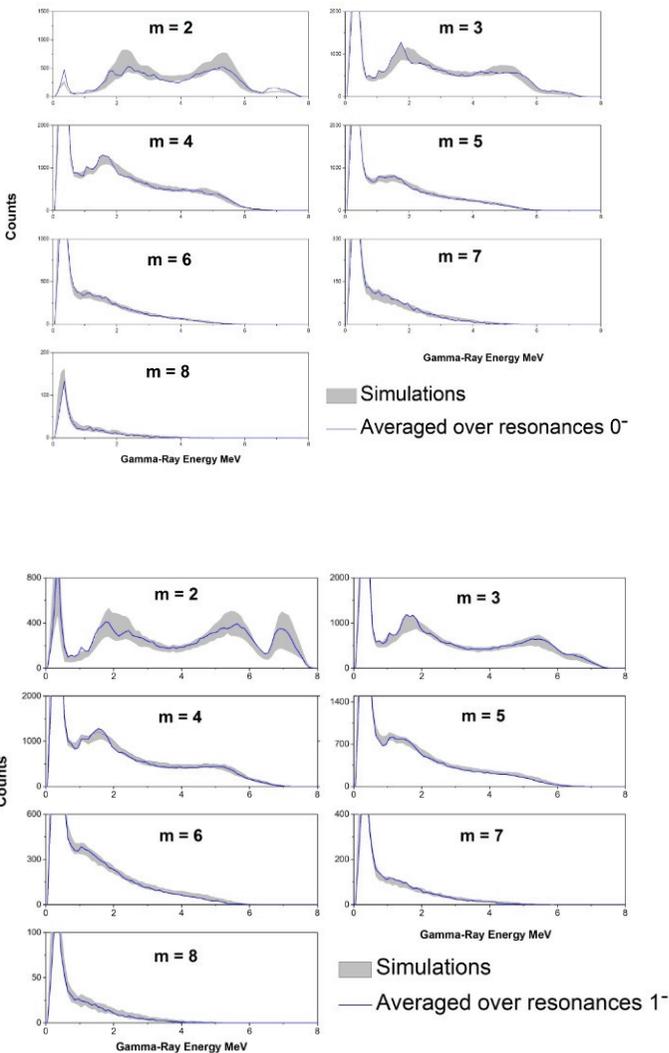

Fig.4. Comparison of the simulated MSC spectra (gray region) and experimental ones (lines) averaged over all measured neutron resonances coming from radiative neutron capture on ^{193}Pt. The upper and lower panels correspond to spectra from $J^{\pi} = 0^-$ and 1^- resonances.

References

1. A. Schiller *et al.*, Nucl. Instrum. Methods Phys., A **447**, 498 (2000).
2. A. Voinov *et al.*, Phys. Rev. Lett., **93**, 142504 (2004).
3. A. Larsen *et al.*, Phys. Rev., C**73**, 064301 (2006).
4. M. Guttormsen *et al.*, Phys. Rev., C**71**, 044307 (2005).
5. M. Krticka, F. Becvar, I. Tomandl *et al.*, Phys. Rev., C**77**, 054319 (2008).
6. S.A. Sheets, U. Agvaanluvsan, J.A. Becker *et al.*, Phys. Rev., C**79**, 024301 (2009).
7. R. Massarczyk, G. Schramm, *et al.*, Phys. Rev., C**87**, 044306 (2013).
8. F. Giacoppo, F.L. Bello Garrote, *et al.*, EPJ Web of Conferences **93**, 01039 (2015).
9. G.A. Bartholomew *et al.*, Adv.in Nucl. Phys., **7**, 229 (1973).
10. W.I. Furman, K. Niedzwidziuk, Yu.P. Popov, *et al.*, Phys. Lett., B**44**, 465 (1973).
11. S.G. Kadmensky, V. P. Markushev and W.I. Furman, Yad. Fiz., **37**, 277(1983); Sov. J. Nucl. Phys., **37**, 165 (1983).
12. A.Simon *et al.*, Phys. Rev., C **93**, 034303 (2016).
13. M. Heil *et al.*, Nucl. Instrum. Methods Phys. Res., A **459**, 229 (2001).
14. R. Reifarth *et al.*, Nucl. Instrum. Methods Phys. Res., A **459**, 229 (2001).
15. P. W. Lisowski *et al.*, Nucl. Sci. Eng., **106**, 208 (1990).
16. S. Valenta *et al.*, Phys. Rev., C**96**, 054315 (2017).
17. F. Becvar, Nucl. Instrum. Methods Phys. Res., Sect., A **417**, 434 (1998).
18. M. Jandel *et al.*, Nucl. Instrum. Methods Phys. Res.,B **261**,1117 (2007).
19. National Nuclear Data Center On-Line Data Service for the ENSDF database, URL: http://www.nndc.bnl.gov/ensdf/

Nuclear Analytical Methods in the Life Sciences

5. Conclusions

The presence of Pd in one of the samples was proved and its content was determined. Further improvement of the experimental conditions will increase the sensitivity of this method and may allow performing elemental prompt-gamma resonance neutron capture analysis of bigger samples and more complex substances.

References

1. IREN Facility, http://flnph.jinr.ru/ru/facilities/iren.
2. I. Ruskov, Yu.N. Kopach, V.R. Skoy, et al., "A multi-detector NaI(Tl) gamma-ray spectrometry system for investigation of neutron induced capture and fission reactions", Phys. Proc. **59**, 107–113 (2014).
3. N.V. Bazhazhina, Yu.D. Mareev, L.B. Pikelner, et al., "Analysis of element and isotope composition of samples by neutron spectroscopy at the IREN facility", Phys. Part. Nucl. Lett. **12**, 578 (2015).

Application of Neutron Resonance Capture Analysis for Determination of Isotope Composition of Fibula from Podbolotyevsky Burial Ground (10th Century AD)

S.T. Mazhen[1,2], S.B. Borzakov[1], A.M. Ergashov[1,2], Yu.D. Mareev[1], P.V. Sedyshev[1],
N.V. Simbirtseva[1,2], V.N. Shvetsov[1], I.A. Saprykina[3], O.V. Zelentsova[3]

[1]Frank Laboratory of Neutron Physics, Joint Institute for Nuclear Research, Dubna, Russia
[2]Institute of Nuclear Physics, Almaty, 050032, the Republic of Kazakhstan
[3]Institute of Archaeology Russian Academy of Sciences, Moscow, Russia

ABSTRACT

Neutron resonance capture analysis is based on the registration of neutron resonances in radiative capture. One of the main advantages of this method is nondestructive property. The investigations were carried out at the Intense Resonance Neutron source (IREN) in Frank laboratory of Neutron Physics. The gamma-quanta liquid scintillator detector was used at this experiment. The analyzed sample, in our case it was fibula, was provided by the Institute of Archeology of the Russian Academy of Sciences. The Viking Age fibula was found in the grave of the Podbolotyevsky burial ground, which was belonged to the Finno-Ugric tribe of Murom. This burial ground dates from the VIII-IX centuries.

1. INTRODUCTION

The method of Neutron Resonance Capture Analysis (NRCA) is currently being developed in the Frank Laboratory of Neutron Physics for the purpose of the element composition determination of our samples [1]. The method is based on the use of a pulsed neutron source and time-of-flight technology [2]. Multi-sectional liquid scintillator detector (210 liters) was used for the registration prompt gamma-quanta and was created at FLNP JINR [3].

The low-lying resonance parameters were determined for almost all stable nuclei to date [4, 5]. Furthermore, the set of energies and parameters of this resonance do not completely coincide for any isotopes pair. Consequently, the elemental and isotopic composition of sample can be defined by means of energy peak position of resonances. Also, if you know area under the resonances, you can calculate the number of the element or isotope's nuclei.

This analysis was carried out for the material which was transferred by the Institute of Archeology RAS. The provided sample fibula (Fig. 1) was found during excavations in the Podbolotyevsky burial ground in the Vladimir Region. The archaeological funeral monument was found at the end of the 20th century. The experts have found nearly 7000 artifacts, from jewelry to weaponry during 3 years. There are hundreds of the Finno-Ugric tribe of Murom graves that lived downstream River Oka from the 10th century and were engaged in hunting, crafts and agriculture. Scientists have studied 181 graves over the past three years and 20 more are studied to date. Elemental and isotopic composition of fibula can be interested for the territory identification where the fibula was made.
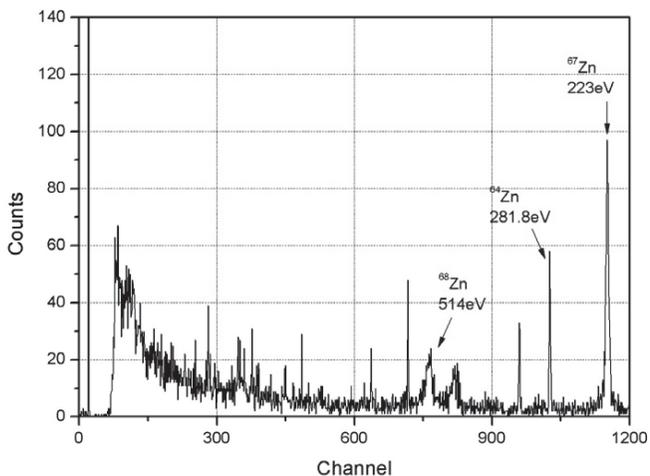
Fig. 4. The time-of-flight spectrum of reactions (n,γ) of a standard zinc sample.
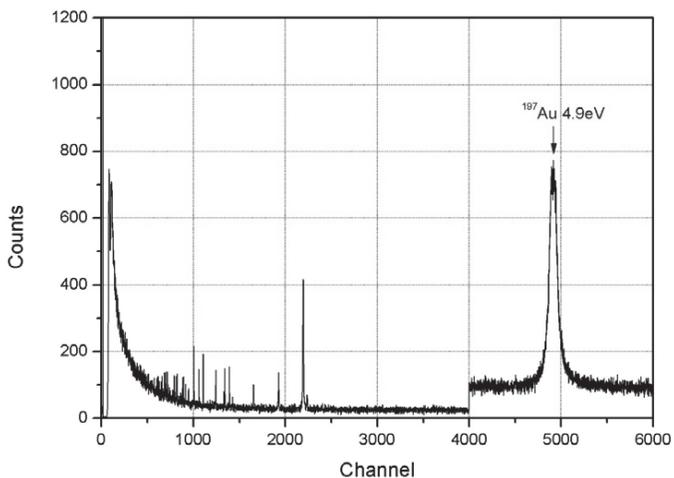

Fig. 5. The time-of-flight spectrum of reactions (n,γ) of a standard gold sample.

3. DATA ANALYSIS AND RESULTS

Three resonances of zinc, two resonances of copper and one resonance of gold were selected during the analysis of the experimental data. The sum of the detector counts in resonance is expressed by the formula:

$$\sum N = f(E_0) \cdot S \cdot t \cdot \varepsilon_\gamma \cdot \frac{\Gamma_\gamma}{\Gamma} A. \tag{2}$$

Here, $f(E_0)$ is the neutron flux density at the resonance energy E_0, S – the sample area, t – measuring time, ε_γ – the detection efficiency of the detector radiative capture, $\Gamma\gamma$, Γ – the radiative and total resonance widths.

$$A = \int_{-\infty}^{+\infty} [1 - T(E)] \, dE \tag{3}$$

is resonance area on the transmission curve.

$$T(E) = e^{-n\sigma(E)} \tag{4}$$

is the energy dependence of the neutron transmission by the sample; $\sigma(E)$ – the total cross section at this energy with Doppler broadening, n – the number of isotope nuclei per unit area. The value A was determined from experimental data for investigated sample by the formula:

$$A_x = \frac{\sum N_x \cdot M_s \cdot S_s}{\sum N_s \cdot M_x \cdot S_x} \cdot A_s. \tag{5}$$

Here, $\sum N_x$, $\sum N_s$ are counts under the resonance peak of the investigated and standard samples, S_x, S_s – the areas of the investigated and standard samples. M_x, M_s – the numbers of monitor counts during the measurement of the investigated and of standard samples.

The value A_s was calculated by means of well-known parameters of resonances for the standard sample, the value n_x was determined from the value of A_x for the investigated sample. The values of $\sigma(E)$ and A were numerically determined by using the algorithm which was described in [6]. This procedure is schematically shown in (Fig. 6). The analysis results are presented in the Table 1.
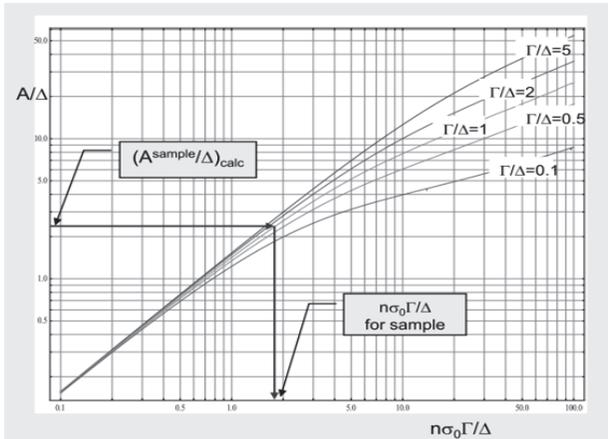

Fig. 6. The dependence of A value on number of nuclei and resonance parameters [6].

Table 1. The results of measurements with the fibula

№	Element	Mass, g	Weight, %
1	Au	0.0171±0.0027	0.85±0.14
2	Cu	13.5±1.5	67.8±7.5
3	Zn	1.06±0.39	5.3±2.0

4. CONCLUSION

This paper presents the results of investigation of the fibula which was found in the Podbolotyevsky burial ground (VIII-IX centuries). The elemental and isotopic composition of the sample was determined by the neutron resonance analysis method. The mass of fibula was 19.9 g. The mass of zinc, determined by resonances is equal to 1.06 ± 0.39 g. The fibula was probably made on the Old Russian territory by the assumption of experts from the Institute of Archeology of the Russian Academy of Sciences. These conclusions are based on following fact: these kinds of artifacts usually have a small zinc portion in the composition - no more than 10%. However, 27% of the fibula material remains unidentified. We think that it might be lead. The detection efficiency of a gamma-ray detector in radiative capture of neutrons by lead isotopes is rather low, and during such short time of statistics collection, lead resonances still do not exceed the background.

REFERENCES

1. N.V. Bazhazhina, Yu.D. Mareev, L.B. Pikelner, P.V. Sedyshev, V.N. Shvetsov. Analysis of element and isotope composition of samples by neutron spectroscopy at the IREN facility. Physics of Particles and Nuclei Letters, **12** (2015), 578–583.
2. O.V. Belikov, A.V. Belozerov, Yu. Becher, Yu. Bulycheva, A.A. Fateev, A.A. Galt, A.S. Kayukov, A.R. Krylov, V.V. Kobetz, P.V. Logachev, A.S. Medvedko, I.N. Meshkov, V.F. Minashkin, V.M. Pavlov, V.A. Petrov, V.G. Pyataev, A.D. Rogov, P.V. Sedyshev, V.G. Shabratov, V.A. Shvec, V.N. Shvetsov, A.V. Skrypnik, A.P. Sumbaev, A.V. Ufimtsev, V.N. Zamrij. Physical start-up of the first stage of IREN facility. Journal of Physics: Conf. Ser., **205** (2010), 012053.
3. H. Maletsky, L.B. Pikelner, K.G. Rodionov, I.M. Salamatin, E.I. Sharapov. Detector of neutrons and gamma rays for work in the field of neutron spectroscopy. Communication of JINR 13-6609 (Dubna, JINR, 1972) 1–15 (in Russian).
4. S.F. Mughabghab. Neutron Gross Sections, Neutron Resonance Parameters and Thermal Gross Sections. Academic Press, New York, 1984.
5. S.I. Sukhoruchkin, Z.N. Soroko, V.V. Deriglazov. Low Energy Neutron Physics. Landolt-Bornstein.V. I/16B, Berlin: Springer Verlag, 1998.
6. V.N. Efimov, I.I. Shelontsev. Calculation for graphs of determining the parameters of neutron resonances by the transmission method. Communications of the JINR P-641 (Dubna, 1961) 1–19 (in Russian).

Neutron Activation Analysis in Study of Features of Accumulation of Microelements in Coastal Aquatic Ecosystems

P.S. Nekhoroshkov, A.V. Kravtsova, M.V. Frontasyeva

Frank Laboratory of Neutron Physics, Joint Institute for Nuclear Research, Russian Federation
p.nekhoroshkov@gmail.com

Introduction

Coastal aquatic ecosystems exist under constant anthropogenic pressure nowadays. It includes industrial, agricultural and recreational type of impacts. Any coastal area is a complex of biotic and abiotic objects, which are connected by elemental fluxes in one environmental system. For analysis of ecological state, we should assess the levels of elemental concentrations and ranges of accumulations. After analysis we could create the recommendations for purposes of ecological, industrial and residential management.

Neutron activation analysis (NAA) with the parameters of irradiation at the reactor IBR-2 fits well for accurate determination (at ppm, ppb levels) of 36 elements (Na, Mg, Al, Cl, K, Ca, Sc, Ti, V, Cr, Mn, Fe, Co, Ni, Cu, Zn, As, Se, Br, Rb, Sr, Mo, Sb, I, Cs, Ba, La, Ce, Sm, Tb, Yb, Hf, Ta, Au Th and U) in marine organisms and substrate. The quantity of elements is connected with detection limits and minimal presence (at background areas) of element in objects, thus the list of elements can be expanded up to 46. It will be described in the next studies.

The aim of the study was to assess the levels of accumulation of microelements in model coastal aquatic ecosystems at the different component of the environment. Model coastal aquatic ecosystems usually include several types of major organisms on the specific substrates (milieus), which can reflect the major type of the anthropogenic pollution. In the study the phytoplankton, molluscs, seaweeds (macroalgae) were used as biomonitoring organisms on the different shallow water areas. This objects, reflecting the main chemical anthropogenic fluxes in the water area, accumulated major of trace and other microelements, which can be derived from sources of pollution and natural unstudied sources. Besides that the main accumulation processes in the organisms can be different depending on the physiological processes and lifeforms of organisms. For our study, the phytoplankton is a basic member of the trophic chain as well as the seaweeds, which can produce the primary biomass by using the photosynthesis. Then the molluscs as primary filtrators and first stage consuments can reflect the intensity of the elemental fluxes in system of resuspended sediments and primary producers. In addition, the molluscs and seaweeds can accumulate the elements during 1-4 years of lifetimes in comparison with the several days in phytoplankton.

The key task of the study was to evaluate ranges of concentrations of elements corresponded to different marine objects to create the "reference" values for future biomonitoring analysis by using NAA.

Material and Methods

The samples were collected during different projects and studies during 2013, 2015 and 2016 years. To juxtapose the ranges and maximal concentrations among the main organisms from the selected coastal zones we were analyzed 50 samples of phytoplankton, 100 samples of seaweeds (*Cystoseira sp.*) from the Black Sea water areas and 20 samples of soft tissue of molluscs (*Mytilus galloprovincialis*) from the South African coastal model zone (Saldanha Bay). The last one was in good agreement with the reference data for the Black sea molluscs (except the terrigenous elements) (Pantelica et al., 2005). The data was check for reproducibility of the maximal values. The outliers were excluded from the analysis to diminish the influence of the casual cases events. Data for phytoplankton and seaweeds was compared with reference data for plankton (from field studies and from SRMs data) in the previous study (Nekhoroshkov et al., 2014, Kravtsova et al., 2014).

Neutron activation analysis was used as a main technique for determination of contents of microelements in different objects, which were collected in the coastal aquatic ecosystems. The specific parameters of determination are presented in the **Table 1**.

Table 1. Features of elemental determination by using NAA and standard reference materials (SRMs)

Element	Isotope	Gamma line, keV	Half-life	Technique of analysis	Deviation (Certified/Determined), %	SRM	Organi-zation
Na	^{24}Na	1368.6	14.7 h	2	19.8	2709	NIST
Mg	^{27}Mg	1014.4	9.5 min	1	0.3	1547	NIST
Al	^{28}Al	1779	2.2 min	1	0.2	1632c	NIST
Cl	^{38}Cl	2167.7	37.2 min	1	7.2	1575a	NIST
K	^{42}K	1524.6	12.4 h	2	9.4	2709	NIST
Ca	^{49}Ca	3084.4	8.7 min	1	14.4	1515	NIST
Sc	^{46}Sc	889.2	83.8 d	3	4	1633c	NIST
Ti	^{51}Ti	320	5.8 min	1	7.4	1633b	NIST
V	^{52}V	1434.1	3.8 min	1	1	1633b	NIST
Cr	^{51}Cr	320.1	27.7 d	3	1	1633c	NIST
Mn	^{56}Mn	1810.7	2.6 h	1	0.2	1575a	NIST
Fe	^{59}Fe	1099.2	44.5 d	3	5.3	667	IRMM
Co	^{58}Co	810.8	70.9 d	3	1.8	2709	NIST
Ni	^{60}Co	1332.5	5.2 y	3	3.4	2709	NIST
Cu	^{66}Cu	1039	5.1 min	1	1	2710	NIST
Zn	^{65}Zn	1116	244.0 d	3	3.2	2709	NIST
As	^{76}As	559.1	26.3 h	2	37.4	1633c	NIST
Se	^{75}Se	264.7	119.8 d	3	18.6	1633c	NIST
Br	^{82}Br	776.5	35.3 h	2	0	667	IRMM
Rb	^{86}Rb	1076.6	18.6 d	3	9.3	1633c	NIST
Sr	^{85}Sr	514	64.8 d	3	5.6	2709	NIST
Mo	^{99}Mo	140.5	65.9 h	2	0	2709	NIST
Sb	^{124}Sb	1691	60.2 d	3	7	1633c	NIST
I	^{128}I	442.9	25.0 min	1	22.6	1547	NIST
Cs	^{134}Cs	795.8	2.1 y	3	4.6	1633c	NIST
Ba	^{131}Ba	496.8	11.8 d	2	11.3	1633c	NIST
La	^{140}La	1596.5	40.2h	2	4.8	1633c	NIST

Ce	^{141}Ce	145.4	32.5 d	3	1.4	667	IRMM
Sm	^{153}Sm	103.2	46.8h	2	0.4	667	IRMM
Tb	^{160}Tb	879.4	72.3 d	3	5.1	1633c	NIST
Yb	^{169}Yb	198	32 d	3	3.4	1633c	NIST
Hf	^{181}Hf	482	42.4 d	3	11.7	2709	NIST
Ta	^{182}Ta	1221.4	114.4 d	3	4.9	1633c	NIST
Au	^{198}Au	411.8	2.7 d	2	43	2709	NIST
Th	^{233}Pa	312	27 d	3	0.6	667	IRMM
U	^{239}Np	228.2	2.4 d	2	1	1633c	NIST

1: conventional NAA, measured 15 min after 3 min of irradiation and ~3 min of decay;
2: epithermal NAA, measured 30 min after 4 days of irradiation and ~3 days of decay;
3: epithermal NAA, measured 90 min after 4 days of irradiation and ~22 days of decay.

Deviation (in %) corresponded to differences between certified and determined concentrations at the final stage of the neutron activation analysis. In the case of 0 % (Br, Mo and In) the element was determined by using one standard without comparative analysis between others SRMs. This statement concerns also the elements with high deviation (As, Se, I and Au). The concentrations of such elements were given and used in analysis as indicative forms.
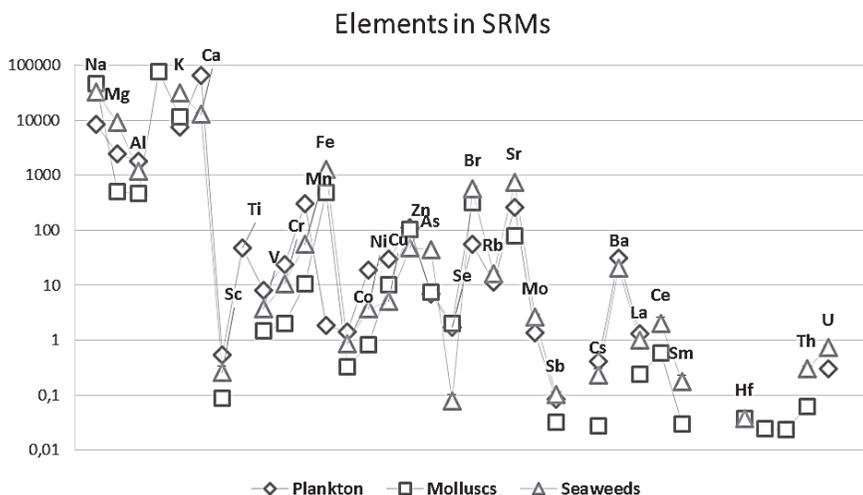

Fig. 1. Certified and indicative concentrations of elements (ppm) in different objects of coastal ecosystems from standard reference materials BCR 414 (plankton >125 um), NIST 2974 (*Mytilus edulis*) and IAEA 140 (*Fucus sp.*).

Results

The concentrations of 36 elements were determined for all kind of samples. For comparison, the same values were analyzed among standard reference materials (**Fig. 1**). Uncertainties (depends on element) for plankton SRM BCR 414 were 1-20 %, molluscs SRM NIST 2974 – 0.1-18.1%, Seaweeds SRM IAEA 140 – 2.1-30.0 %.

Table 2. Maximal concentrations of elements in different kind of objects

Objects Specification Element	Plankton >115 μm Reference data[1]	Phytoplankton >35 μm		Molluscs Mussels *Mytilus galloprovincialis*		Seaweeds Brown algae *Cystoseira sp.*	
	Max	Max	%	Max	%	Max	%
Na	64000	4200	1.5	16000	19.8	26600	5.3
Mg	-	2200	2.9	2234	0.3	12100	14
Al	-	13000	0.8	80	0.2	560	32.4
Cl	-	10000	1.8	31500	9.4	73300	17.7
K	17000	3900	1.5	10320	14.4	62000	6.5
Ca	19000	97000	3.2	1470	4	34100	27
Sc	0.45	2.3	30	0.03	7.4	0.2	4.5
Ti	400	870	7.5	-		-	
V	4	23	2.2	1	1	2	24.6
Cr	620	33	1	0.7	1	-	
Mn	80	190	3.2	4.512	0.2	55	31.1
Fe	2460	8600	1	150	5.3	720	1.9
Co	1.5	2.4	1.5	0.2	1.8	0.8	25.6
Ni	6	17	1.2	0.65	3.4	6.08	9.9
Cu	142	200	6.1	9.6	1	-	
Zn	386	280	1	150	3.2	80	20
As	17	4.9	1.3	8	37.4	55	13
Se	0.6	0.4	1.7	4.3	18.6		
Br	2000	180	2.1	210	0	370	32.2
Rb	7	22	8.5	4	9.3	22	8.2
Sr	130	120	1.3	30	5.6	1400	3.2
Mo	0.3	4	30	0.6	0	-	
Sb	3.2	1.4	1.8	0.03	7	0.1	10
I	139	50	0.6	7.0	22.6	230	8.2
Cs	0.6	1.4	4.1	0.04	4.6	0.06	50
Ba	47	71	3.8	1	11.3	68	2.2
La	1.2	5	4.8	0.1		-	
Ce	2.6	20	30	0.2		-	
Sm	0.16	0.7	30	-		0.05	40
Tb	0.22	0.12	30	0.004		-	
Yb	0.13	0.4	30	-		-	
Hf	0.11	0.8	30	-		-	
Ta	0.06	0.13	30	0.001		-	
Au	-	0.02	30	0.002	43	0.07	57.1
Th	0.29	2	2.9	0.03	0.6	-	
U		0.5	4.1	0.18	1	0.8	12.5

[1]Reference data of plankton from Leonova et al, 2013.
Underlined values demonstrate the maximal values among objects

Data of concentrations in plankton (in Fig. 1 and in Table 2) were presented for comparison with phytoplankton because the main parameter of such samples is a fraction size, because a lot of different type of plankton organisms can be collected at the same sample. Maximal concentrations among analyzed standards were distinguished:

- In plankton (SRM BCR 414 fraction >125 um): Al, Ca, Sc, Ti, V, Cr, Mn, Co, Ni, Cu, Zn, Cs, La.
- In molluscs (SRM NIST 2974 Mytilus edulis): Na, Se
- In seaweeds (SRM IAEA 140 Fucus sp.): Mg, K, Fe, As, Mo, Br, Sr, Sb

The maximal concentrations among different objects of coastal organisms:

- Phytoplankton (>35 um): Al, Ca, Sc, Ti, V, Cr, Mn, Fe, Co, Ni, Cu, Sb, Cs
- Molluscs (*Mytilus galloprovincialis*, soft tissue): Zn, Se
- Seaweeds (*Cystoseira sp.*): Na, Mg, Cl, K, As, Br, Sr, I

Discussions

Almost all elements for each group, which were presented in the high concentrations in SRMs (**Fig. 1**), were corresponded to groups, which were emphasized (**Table 2**). Exception concerning with:

- Fe, Sb in phytoplankton were in higher amounts in real field samples due to additional sources of enrichment
- Zn in molluscs in higher real concentrations can be influenced by hydrological changes in water masses and specificity of hyrgochemical structure of the coastal water in studied zone of the Saldanha Bay
- Na, Cl, I can accumulated in higher amounts due to natural presence in dissolved and suspended particles of salts derived from marine milieu and can deviate around a certified values in a higher or lower side.

Phytoplankton includes small cells which are suspended in a water masses and can adsorb any mineral and organic mollecules. That is the reason why they accumulate a microelements related to mineral (terrigenous) component of the suspended bottom sediments. In addition, the river flows contain the high concentrations of biogenic elements (mainly N, P, Si), which can be attracted feature of water area for develop of community. At the same time they can accumulate the microelements of terrigenous (f. e. Al, Ca, Sc, Ti, …, Cs, La) and anthropogenic origin (depends on the sources: f. e. V, Co, Ni, Cu, Zn) which presented in suspended forms in bottom sediments.

Thus, zooplankton and phytoplankton accumulated in high amounts the elements, which connected and derived from resuspended sediments and other mineral particles from coastal river flows. In the biomonitoring studies, the important task should be analysis of terrigenous component by using specific equations (Nekhoroshkov et al., 2017).

Phytoplankton and zooplankton usually differ by fractions, lifetime, speed of accumulation. Besides that, the plankton in general includes high amounts of mineral suspension and zooplankton organisms. Molluscs feed on phytoplanktonic cells and can adsorb the mineral suspension directly from the water. However, the inner self-cleaning processes during lifetime can regulate the highest concentration of pollutants including such elements as V, Cr, Mn, Fe, Cu, Zn, As, Mo etc.

Key features of groups of macro and microelements in comparison analysis:

- o Elements had a terrigenous origin, accumulated at low level in bottom sediments, reached higher values in phytoplankton and seaweeds, molluscs (Al, Ti, Sc, Th, U, REE et al.). To this group can be added such elements as K, Ca, V, Cr, Co, Ni, Rb, Mo, Sb, Cs, Ba, Au), should take into consideration hydrological state
- o Elements accumulated to equal levels depending on ratio between suspended and dissolved forms and anthropogenic affects (Cr, Co, Ni, Zn, As, Mo et al.)
- o Elements can be accumulated in the higher amounts than presented in this study due to additional intake from sources of pollution (V, Cr, Co, Ni, Cu, Zn, As, Br, Se, Mo, Sb)

Such elemental values can be used as reference for juxtaposing of real field concentrations and in comparison biomonitoring study. Moreover, such values can be recommended as threshold for routine analysis in the verification procedure and identifying the traces of pollution. In the case of source of constant pollution the concentrations of elements in studied organisms should be analyzed by groups to emphasize typical connections.

Conclusions

According to the aim and task the list of microelements were considered. The groups of elements were installed by using comparative analysis: Phytoplankton Al, Ca, Sc, Ti, V, Cr, Mn, Co, Ni, Cu, Zn, Cs, La. In molluscs: Na, Se. Seaweeds: Mg, Cl, K, As, Br, Sr, I, Fe, Mo. The maximal concentrations of elements, which were given in the study, can be used in the future biomonitoring studies as reference values, such elemental groups should be carefully analyzed separately.

References

1. Pantelica A.I., Salagean M.N., Georgescu I.I. Thirty-year experience in applying neutron activation for analysis of mineral and biological samples from the Romanian sector of the Danube River and the Black Sea. *Ovidius University Annals of Chemistry*. 2005. Vol. **16**, # 1–4, pp. 1–8.
2. Kravtsova, A., Milchakova, N., & Frontasyeva, M. Elemental accumulation in the Black Sea brown algae Cystoseira studied by neutron activation analysis. *Ecological Chemistry and Engineering S*, 2014, **21**(1), pp. 9–23.
3. Kravtsova, Alexandra V., Nataliya A. Milchakova, and Marina V. Frontasyeva. Levels, spatial variation and compartmentalization of trace elements in brown algae Cystoseira from marine protected areas of Crimea (Black Sea). *Marine pollution bulletin.* 2015. Vol. **97**, 1–2, Pp: 548–554.
4. Nekhoroshkov P. S., Kravtsova A. V., Frontasyeva M. V., Tokarev Y. N. Neutron activation analysis and scanning electron microscopy of phytoplankton in the coastal zone of Crimea (the Black Sea). *American Journal of Analytical Chemistry*. 2014. Vol. **5**(5), pp. 323–334.
5. Nekhoroshkov P. S, Frontasyeva M. V., Tokarev Y. N. Variability of concentration of microelements in phytoplankton communities in coastal zone of the Sevastopol city (Crimea) and its features. *Ecology of Urban Areas*. 2017. Vol. **4**. Pp. 37–48.
6. Leonova, G.A., Bobrov, V.A., Bogush, A.A. and Bychinskii, V.A., 2013. Concentration of chemical elements by zooplankton of the White Sea. *Oceanology*, **53**(1), pp.54–70.

Neutron Activation Analysis at IREN and IBR-2 Facilities

S.B. Borzakov[1,2], A.Yu. Dmitriev[1], C. Hramco[1], G.K. Kanagatova[1,2,3]

[1]*Frank Laboratory of Neutron Physics*, *Joint Institute for Nuclear Research, Dubna, Russia*
[2]*Dubna State University, Dubna, Russia*
[3]*The Institute of Nuclear Physics, Almaty, Kazakhstan*

Abstract

The installation for neutron activation analysis (NAA) at the IREN facility, which consists of HPGe detector, a sample changer, chemical equipment, and control software, is described. Some results obtained by the NAA method, which have been carried out at IREN and IBR-2 facilities are presented. The neutron spectrum obtained at these facilities has big part of resonance neutrons. A program was developed for the calculation of effective resonance integrals, which takes into account the real spectrum of resonance neutrons, as well as the thermal motion of atoms and the absorption of neutrons in the sample. The flux densities for thermal and resonance neutrons have been determined.

Introduction

Neutron activation analysis (NAA) is a method for determining the elemental composition of a substance, based on measuring the characteristics of radiation emitted by radioactive nuclei that appear after neutron irradiation. The first activation of various elements by neutrons was observed by E. Fermi in 1934. G. de Heversey and H. Levi in 1936 first applied this phenomenon to determine the content of elements in the samples. At present, neutron activation analysis is widely used in geology, ecology, archeology and other fields of research [1]. The main process of interaction of neutrons with nuclei, leading to the formation of unstable nuclei, is radiation capture, that is, the capture of neutrons followed by the emission of gamma quanta. NAA allows us to determine the content of more than 40 elements with high sensitivity.

Neutron sources in FLNP and installation for activation analysis

IREN (Intensive Source of Resonance Neutrons) consists of linear electron accelerator and a tungsten target (4 cm diameter and 10 cm height), surrounded by a moderator. Electrons enter the target, lose energy and emit bremsstrahlung quanta in a wide range of energies. The number of emitted gamma rays decreases with increasing energy. The maximum energy of gamma rays is equal to the kinetic energy of the electrons. The neutrons are created as a result of the reactions (γ, n), $(\gamma, 2n)$, etc. The average energy of the emitted neutrons is 1 MeV. To obtain neutrons of lower energies, the target is surrounded by a moderator. The water is used as moderator, which also cools the target. The moderator is a cylinder with a diameter of 15 cm. Neutrons pass in it a distance of the order of 5 cm [2].

Table 1. The calculated values of the effective resonance integrals

Nuclide	Number of resonances	Resonance integral, b [5]	Effective resonance integral, b	
			$\alpha = 0$	$\alpha = 0.1$
^{197}Au	24	1550 ± 28	1577	1849
^{94}Zr	18	0.23 ± 0.01	0.30	0.78
^{97}Zr	18	5.3 ± 0.3	6.43	19.5
^{63}Cu	24	4.97 ± 0.08	4.95	9.52

The first term describes contribution from thermal cross-section tail (according to $1/v$ low). The second term describes the contribution of resonances. $\sigma_0 = \frac{4\pi}{k^2} g_J \frac{\Gamma_n}{\Gamma}$ is the total capture cross-section where $E = E_{ri}$, E_{ri} – resonance energy, Γ_n – neutron width, Γ_γ – radiative width, $\Gamma = \Gamma_n + \Gamma_\gamma$ is total width, g_J is the statistical factor and k is neutron impulse. The factors G_i depend on sample thickness and temperature. $\sigma_{n\gamma} = \sigma_0 \cdot \frac{\Gamma_\gamma}{\Gamma} \psi(\theta, x)$, where function $\psi(\theta,x)$ describes the thermal motion of atoms, $x = \frac{2(E-E_r)}{\Gamma}$, $\theta = \frac{\Gamma}{\Delta}$. $\Delta = \sqrt{\frac{4E_r k_B T}{A}}$ is the Doppler width. The Padé approximation has been used to calculate the $\psi(\theta,x)$ function [7]. Resonance parameters were taken from [8].

The calculations show the big difference (up to tens of percent) between calculated values and known from literature ones. The calculated values have been used for accurate determination of the neutron flux density and for calculations of concentrations of elements by the absolute method.

Conclusions

As a result of the measurements, the following neutron flux density values were obtained at the IREN facility:

$$\Phi_{th}=1{,}0 \cdot 10^8 \text{ n/(cm}^2 \cdot \text{s) and } \Phi_{res}=1{,}1 \cdot 10^7 \text{ n/(cm}^2 \cdot \text{s).}$$

In our laboratory, the method of activation analysis was used to study ecological samples from Egypt [9] and for investigations of archeological samples – bracelets and fragments of human remains from the burials of the Moscow Kremlin [10].

References

1. Z.R. Alfassi, "Instrumental Multi-Element Chemical Analysis", Kluwer Academic Publishers: Dordrecht, the Netherlands, 1998.
2. Belikov O.V. et al., "Physical start-up of the first stage of IREN facility", ISINN-17, Dubna, Russia, May 27–30, 2009, Proceedings, Dubna, 2010; http://isinn.jinr.ru/proceedings/isinn-17/pdf/Shvetsov.pdf

3. S.S. Pavlov, A.Yu. Dmitriev, M.V. Frontasyeva, "An automation system for neutron activation analysis at the reactor IBR-2, Frank Laboratory of Neutron Physics, Joint Institute for Nuclear Research, Dubna, Russia", J. Radioanal. Nucl. Chem., V. **309** (1). PP. 27–38, 2016; http://link.springer.com/article/10.1007/s10967-016-4864-8.

4. E.P. Shabalin, F.U. Verkhoglyadov, M.V. Bulavin, F.D. Rogov, E.N. Kulagin, S.A. Kulikov, "Spectrum and the neutron flux density in the irradiation channel of beam No.3 of the IBR-2 reactor", Part. Nucl. Lett. 2015, V. **12**, No. 2 (1993), p. 505–516.

5. T.S. Belanova, A.V. Ignatyuk, A.B. Paschenko, V.I. Plyaskin, "Radiative Neutron Capture", Handbook, M., Energoatomizdat, 1986.

6. http://nucleardata.nuclear.lu.se/toi/radSearch.asp

7. S.B. Borzakov, "Calculation of Effective Resonance Integrals", ISINN-20, Alushta, Ukraine, May 21–26, 2012, Proceedings, JINR, Dubna, 2013.

8. S.I. Sukhoruchkin et al., "Tables of Neutron Resonance Parameters", Landolt-Bornstein, Num. Data and Functional Relationships in Science and Technology, Group I, V. **16**, subvolume B, ed. H. Schopper, Springer, 1998.

9. M.S. Hamada et al., "Assessment of air pollution in vicinity of phosphate fertilizer plant in Abu-Zabal city, Egipt, using vegetation epithermal neutron activation analysis", ISINN-25, Dubna, Russia, May 22–26, 2017, Proceedings, Dubna, 2018.

10. T.D. Panova, A.Yu. Dmitriev, S.B. Borzakov, C. Hramco, "Qualitative and Quantitative Analysis of Arsenic and Mercury in Human Remains of the XVI–XVII Centuries from the Moscow Kremlin Necropolises by Neutron Activation Analysis at the IREN Facility and the IBR-2 Reactor of FLNP JINR", PEPAN Letters, v.**15**, # 1(213), p. 117–124, 2018.

Neutron Sources
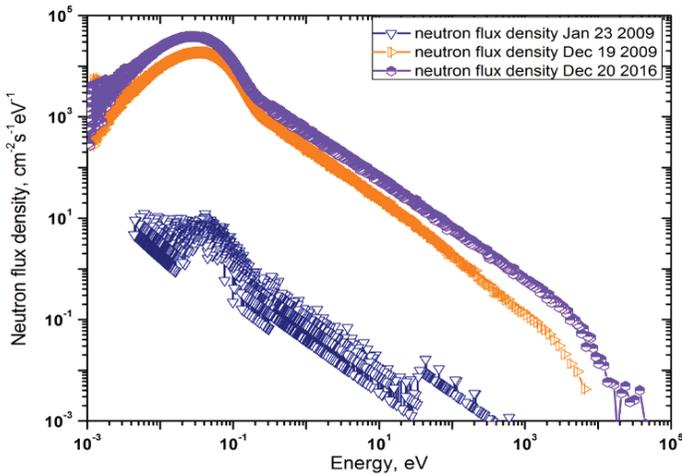
Fig.11. Spectra of neutron flux density from IREN obtained during development of the facility.
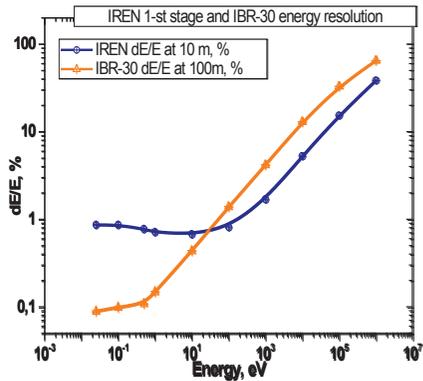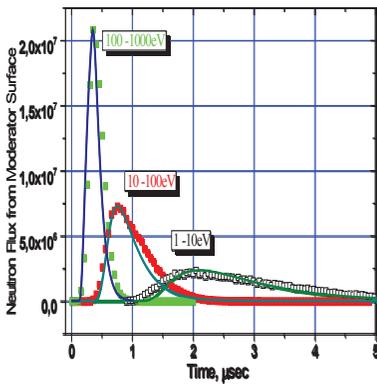
Fig.12. IREN vs IBR-30.

Fig.13 shows an experimental comparison of the energy resolutions of IREN and IBR-30. Measurements were made on the flight base 60 m with Ta(n,γ) sample. It is seen that the width of the resonances in the region up to 20 eV are approximately equal, but higher energy it is much better for IREN facility.

But this is one of the first measurements. Now the neutron flux at IREN is about 5 times more.
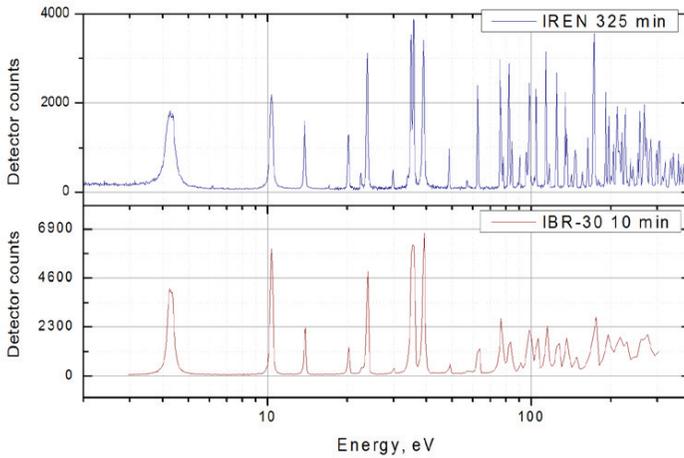
Fig.13. Energy resolution IREN vs IBR-30.

The scientific program at the IREN facility includes research:
- symmetries violation in neutron induced reactions;
- neutron induced fission;
- neutron fundamental properties;
- nuclear structure;
- nuclear data;
- resonance capture and transmission analysis.

Due to the fact that IREN facility has not yet reached the design parameters, now we conduct preliminary experiments, tests of new equipment and perform some applied research.

Preliminary experiments to assess the possibility of studying the fission physics in neutron resonances are carried out (Fig.14).

The measurements were carried out on the flight base 10 m. As the detector an ionization fission chamber was used. The target was the uranium-235.

The ionization chamber was organized so, that it was possible to register both binary fission (signals from the cathode in the interval A1-A2) and ternary fission – 2 fission fragments + alpha particle (alpha particles with high energy passed through the thin foil of the electrode A2 and were registered by the anode A3).

Also new detector system on neutron beams is being tested.

«Romashka" is a mobile, easily tunable, multi-detector system with the scintillator detectors. The system allows to register both time of flight and energy spectra, to analyze pileaps, multiplicity of coincidences, dead time and other parameters which are necessary for the correct determination of neutron cross sections and neutron resonance parameters. The graph (Fig.15) shows the dependence of the output of (n, γ)-reaction from tantalum sample on neutron energy, obtained by measurements on the flight base of 30 m.
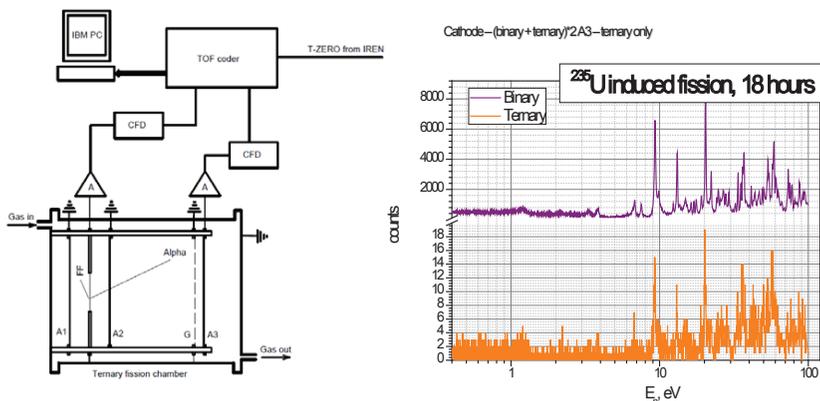
Fig.14. Investigation of fission in neutron resonances.
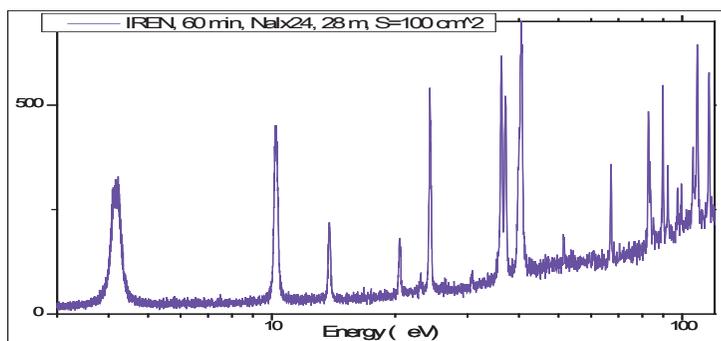
Fig. 15. Tests of new detector systems on neutron beams. The multi-detector system "Romashka-IREN".

At the IREN facility the effects of neutrons and gamma rays on plastic scintillators used in the CMS experiment at CERN was studied.

The experience of three years of operation of the hadron calorimeter showed an unexpectedly large decrease in the light output of plastic detectors. It was concluded that not all the factors of radioactive radiation influence on scintillators were taken into account. To address this issue, four types of plastic scintillators were studied. The maximum irradiation time is 30 days. The value of light output of samples of different shapes after irradiation was compared with the value of light output before irradiation. The results obtained showed no substantial effect of rate of irradiation on the light output.

In the CMS experiment, there is a large amount of bronze between scintillators. Therefore, the effect of the additional induced radioactivity emitted by the radioisotopes resulting from the neutron irradiation of bronze was studied. To do this, two identical SCSN-81 scintillators were irradiated at the same distance from the IREN target. But behind one of them there was a disk made of bronze. Measurements of light output showed that there is a substantial contribution from induced activity. The results of the measurements confirmed the results of the calculation using the program FLUKA. Thus,

the reason for reducing the light output of the hadron calorimeter scintillators was found out.

Another example of applied work is the use of neutron resonance analysis for non-destructive determination of the elemental composition of various samples.

Last year, at IREN facility experiments to determine the elemental composition of a number of archaeological artifacts were conducted. Neutron resonance capture analysis - NRCA was used in the studies. A large liquid scintillator detector was used as a γ-quantum detector.

In Frank Laboratory neutron activation analysis three samples of human remains from necropolis of the Moscow Kremlin (Fig.16) was conducted. The samples were the rib and hair of Queen Anastasia, who was the first wife of king Ivan 4, as well as the rib of Knyaz Dmitry, who was the son of Tsar Ivan 4.

The samples were irradiated at two facilities – IREN and IBR-2 reactor. The induced activity spectra of the irradiated samples were measured using a germanium detector. The mass fractions of arsenic, mercury and some other elements were determined by relative and absolute methods. The obtained values confirmed the fact of mercury poisoning of Queen Anastasia. Increased mercury content was found in the bone remains of Knyaz Dmitry.

Sample 1.

Sample 2.

Sample 3.

Spectrum of the Sample 1.

Spectrum of the Sample 3.
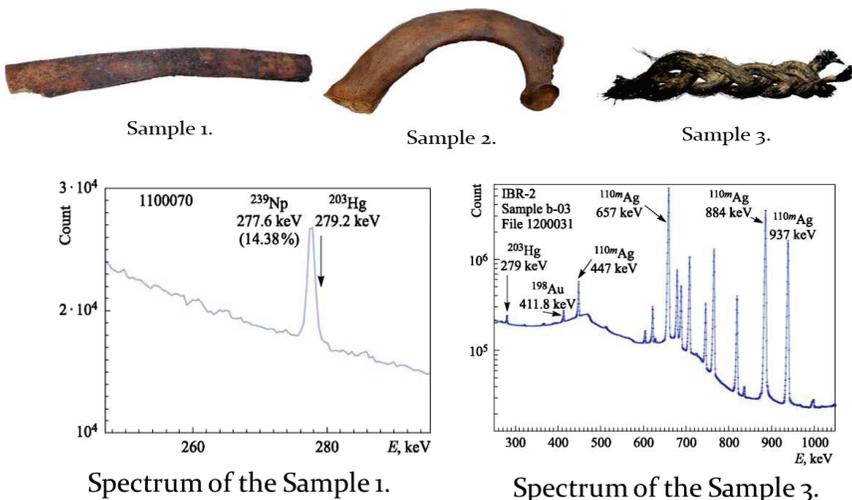
Sample №	Arsenic (As)		Mercury (Hg)	
	Mass fraction, mg/kg	Relative error, %	Mass fraction, mg/kg	Relative error, %
1	0.19	30	0.36	19.1
2	0.23	30	0.2	29.5
3	1.18	18.3	46.6	2.5

Fig.16. Analysis of arsenic and mercury in human remains of the 16th – 17th centuries at IBR-2 reactor and IREN facility.

References

1. Janeva N.B., Grigoriev Yu.V., Gundorin N.A., Lukyanov A.A., Kopatch Yu.N., Koyumdjieva N.T., Pikelner L.B., Ruskov I.N., Shvetsov V.N., Sedyshev P.V., Zeinalov Sh., Future neutron data activity on the neutron source IREN, Proc Int. Conf. on Nuclear Measurements, Evaluations and Applications-NEMEA-6, Krakow, 25–28 Oct 2010, France: OECD-NEA; 2011, p.153. www.oecd-nea.org/science/wpec/nemea6/, www.oecd-nea.org/science/wpec/nemea6/NEMEA6_web.pdf.
2. Enik T.E., Likhachev A.N., Mitsyna L.V., Popov A.B., Salamatin I.M., Sirotin A.P. In: Neutron spectroscopy, nuclear structure, related topics. XXI Int. Seminar on Interaction of neutron with nuclei. Alushta, Ukraine, May 20 – 25, 2013, JINR E3-2014-13, 2014, p. 227.
3. IREN Facility http://flnp.jinr.ru/35/.
4. CMS HCAL Collaboration.” Design, Performance, and Calibration of CMS Hadron Endcap Calorimeters”, CMS-NOTE-2008-010, 32 p.
5. G.G. Bunatian, V.G. Nikolenko, A.B. Popov, JINR Communications, E6-2009-182, Dubna (2009).

TOF METHOD MEASUREMENTS AT INR SPALLATION
NEUTRON SOURCE RADEX

Djilkibaev R.M., Khliustin D.V., Vasilev I.A.

Institute for Nuclear Research, Russian Academy of Sciences, Moscow, Russia

Abstract. Installation INES based on pulsed spallation neutron source RADEX has been developed at INR RAS, Moscow, Russia. INES is designed for investigations of neutron cross sections for reactor fuel and construction material alloys. INES uses 50 meter spectrometer base, which together with 500 ns proton beam duration of accelerator makes possible to measure group total and group capture cross sections of researched materials. Cross sections are experimentally observed and measured with corresponding block-effect and Doppler-effect values, with automatic averaging of resonance structure of all isotopes, available in alloy. Measured results are used for calibration of calculation codes, which are used in the process of design and certification of nuclear reactor cores and their biological radiation protection shields.

Installation INES uses four Helium-3 detectors as beam intensity monitors, four Helium-3 detectors as transmittance functions detectors and 8-sectional liquid (n,γ) detector which scintillator's volume is 40 liters.

During year 2017 new fast 16-channel data acquisition system was developed, tested and employed. It uses modern electronic element base, has 100 nanosecond time step in 16-channel mode and 50 nanosecond step in 8-channel mode. This data acquisition system is designed to work in multiplicity mode, which provides good separation between effect and background during capture (n,γ) and fission (n,f) cross sections measurements. At beam frequency 50 Hz, statistics is being collected into 200000 channel histogram. Exact spectrum and cross sections measurements will enable more exact calculations of fast breeder reactor cores characteristics, including critical mass and breeding ratio.

1. Introduction

One of the most important tasks, for which INR RAS proton linac was designed and built, were TOF measurements to provide fast neutron reactors program by exact neutron group cross sections data. Powerful linac with one-turn beam extraction storage ring for high intensity, and long TOF bases for high $\left(\frac{\Delta t}{L}\right)$ parameter were designed. Target reloading machine allows to change proton beam target making modeling of the reactor's core and measure corresponding neutron spectrum.

Project parameters of the proton linac of INR Russian Academy of Sciences are: proton energy 600 MeV, pulsed current 50 mA, frequency 100 Hz, maximum pulse duration 100 (200) mks; They provide average current 0.5 (1.0) mA, mean beam power 300 (600) kW, neutron yield into angle $4\pi \sim 10^{17}$ neutrons per sec.

Corresponding to the technical project, linac is equipped by the storage ring which has project parameters: beam aperture 200 mm, circle length $2\pi R = 102.8$ meters, proton cycling period 430 nanoseconds at 600 MeV. Maximum pulse current, allowed by space charge is 10 Amperes at 600 MeV, it corresponds to maximum pulse intensity $2.3 \cdot 10^{13}$ protons in each pulse at 100 Hz and average neutron flux with W target in short pulses at 100 Hz, up to

2.5· 10^{16} n/s. Storage ring now is under construction. Significant part of its radiation sustainable equipment is already manufactured.

2. Accuracy requirements

Requirements for accuracy of group neutron cross sections for many types of reactors are determined by share of delayed neutrons of employed fissile nuclide and shown in table 1.

Table 1

Reactor fuel composition	U^{235}	U^{233}	Pu^{239}	BN-1200 nitride fuel
Desirable accuracy of criticality coefficient calculation ($\Delta K/K$), %	0.6	0.2	0.2	0.42

Diffusion one-group approximation gives expression for critical radius

$$R_{crit} = \frac{\pi}{\sqrt{3(K_{inf}-1)\Sigma_a \Sigma_{tr}}} - \frac{0.71}{\Sigma_{tr}} \qquad (1)$$

And expression for critical mass

$$M_{crit} \sim R_{crit}^3 \sim (\Sigma_a \Sigma_{tr})^{\frac{3}{2}} \sim (\sigma_a \sigma_s)^{\frac{3}{2}} \qquad (2)$$

Accuracy of neutron cross sections must provide exactness of critical mass prediction $\left|\frac{(M_{calc}-M_{measured})}{M_{measured}}\right|$ better then value, which corresponds to maximum allowed $\left(\frac{\Delta K}{K}\right)$ value.

Accuracy of TOF transmittance method for measurements of total cross sections for one channel of data acquisition system is defined by expressions:

$$N(x) = N_0 \exp(-n x \sigma_{total}),$$
$$T = \frac{N_x}{N_0},$$
$$\sigma_{total} = \left(\frac{1}{nx}\right) ln\left(\frac{1}{T}\right),$$
$$\frac{(\delta \sigma_{total})}{(\sigma_{total})} = \left(\frac{1}{\sqrt{N_0}}\right)\left(\sqrt{\frac{1+T}{T}}\right)\left(\frac{1}{ln\left(\frac{1}{T}\right)}\right). \qquad (3)$$

For total cross section accuracy 0.2% it's necessary to accumulate statistics ~1000000 counts in each histogram channel. Coefficient which depends on pattern thickness is shown on fig.1.

Achieved accuracy of fast breeder reactors criticality predictions $\frac{\Delta K}{K}$ is shown in table 2.

Table 2. Accuracy of existing nuclear data and their calculation codes

Neutron constant system	MCNP	ABBN-78	ABBN-93
$\frac{\Delta K}{K}$, %	2	2	0.5
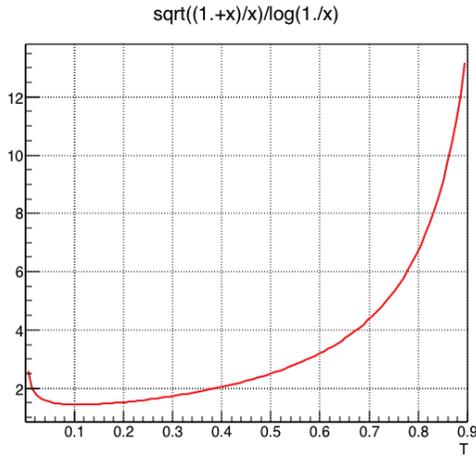
Fig.1: Coefficient proportional to pattern thickness.

During fact neutron moderation, number of scatterings between energies E_0 and E is

$$N_{scatterings} = \left(\frac{1}{\xi}\right)\ln\left(\frac{E_0}{E}\right),\qquad(4)$$

$$\text{where } \left(\frac{1}{\xi}\right) \approx \frac{A}{2} + \frac{1}{3} + \frac{1}{18A}.$$

If E_0=14 MeV and E=0.0253 eV, for substance like Li_6D we find that 28 energy groups in ABBN-78 are enough.

Due to presence in the core of fast breeder reactor such medium atomic mass nuclides like Na, Fe, Cr, Ni, Ti, in neutron group cross section constants ABBN-93 were chosen 299 groups. In our measurements we are working to fit ABBN-93 requirements.

Energy resolution of TOF spectrometer as function of $(\Delta t/L)$ parameter is shown in table 3. Here, $\Delta E = 2.77 \cdot 10^{-5} \cdot E^{3/2} \cdot (\Delta t/L)$, Δt – nanoseconds, L – meters, E – eV.

Table 3

$\Delta t, \left(\frac{ns}{m}\right)$	$\Delta E, eV$						
	E=10 eV	E=100 eV	E=1 KeV	E=10 KeV	E=100 KeV	E=1 MeV	E=10 MeV
100	0.09	2.8	88	2800	88000	2800000	88E6
500	0.04	1.4	44	1400	44000	1400000	44E6
10	0.009	0.28	8.8	280	8800	280000	8.8E6
5	**0.004**	**0.14**	**4.4**	**140**	**4400**	**140000**	**4.4E6**
1	0.0009	0.028	0.88	28	880	28000	880000
0.5	0.0004	0.014	0.44	14	440	14000	440000
0.1	0.00009	0.028	0.088	2.8	88	2800	88000

Value 5 ns/m, which is marked in table 3 by thick line, corresponds to our measurements on installation INES.

Influence of Doppler-effect and cross sections self-shielding of multi-isotope compounds on reactor criticality and other parameters on example of one-group diffusion theory

$$D\Delta\Phi - \Sigma_a\Phi + \upsilon\,\Sigma_f\Phi = 0 \,, \tag{5}$$

$$D\Delta\Phi + (\eta - 1)\,\Sigma_a\Phi = 0, \tag{6}$$

thus we get differential equation with Laplasian and buckling parameter

$$\Delta\Phi + (\eta - 1)\left(\frac{\Sigma_a}{D}\right)\Phi = 0 \tag{7}$$

or the same equation in ordinary form

$$\Delta\Phi + \left(\frac{\eta - 1}{L^2 + \tau}\right)\Phi = 0, \tag{4}$$

where D – diffusion coefficient, Φ – neutron flux, Σ_a – macroscopic absorption cross section, τ – Fermi's age of neutron flux, L^2 – square of diffusion's length.

Lower resonance levels have mainly neutron capture properties. Doppler-effect and internal block-effect influence on value of Σ_a and are measured by gamma-detectors. Upper resonance levels are mainly scattering neutrons without absorption them. At the same time Doppler-effect and multi-isotope alloy's interference of resonance levels influence on value D. Thus, leakage from fast neutron reactor's core into reflector also changes at different temperatures and dilutions. This effect if researched by transmission functions measurements in TOF experiments. Both first and second effects are able to change effective L^2 and τ.

In TOF experiments transmission and self-indication functions must be measured in unresolved resonance area that is possible using multiplicity coincidence method.

It's necessary to mention that into one energy group of ABBN-93 many histogram channels are coming, so as energy width of one group grows in high energy region as shown in table 4.

Compared to resonance structure measurements, where energy level's width Γ_γ is approximately constant in wide energy range and is about 0.1 eV for heavy nucleus, group cross sections measurements allow to measure up to higher upper energy level using the same TOF spectrometer with the same energy resolution ($\Delta t/L$) measured in nanoseconds per meter. It is also important that number of counts per channel, in expression for accuracy of measurements, corresponds not to single data acquisition system channel, but to energy group where present many histogram channels.

Table 4. Group energy width, eV, of the ABBN-78 neutron constants

	Energy width ΔE, eV of group number N						
	E=10 eV	E=100 eV	E=1 KeV	E=10 KeV	E=100 KeV	E=1 MeV	E=10 MeV
Group's number	21	18	15	12	9	6	1
Width	11.5	115	1150	11500	115000	600000	3500000

At the same time, capture cross sections measurements must be done in the energy area of unresolved resonances using multiplicity coincidence method, which gives an opportunity to distinguish effect and background.

3. Experimental installation INES

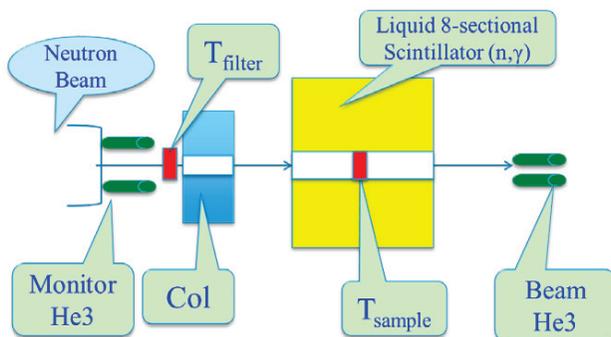Installation INES is shown on fig.2.

Fig. 2: Installation INES.

Corresponding to fig. 2, neutron beam arrives from the left side in the evacuated neutron guide. Four monitor He-3 counters are in beam. After that, patterns-filters like Mn-55 are installed, and beam is collimated for liquid scintillator detector's aperture. Measured isotope plate is installed to the center of the scintillator tank. From the right side, before beam capture, four He-3 counters are installed to measure total cross section.

During the described our measurements, pure patterns of Gold Au-197 and Tantalum Ta-181 were used. In figs.3 and 4 we can see the best world data taken from BNL. For Ta-181 we can see resolved resonances area up to neutron energy 2500 eV.

In the figure 5 our INR measurements of Ta-181 are shown. On 'X'-axis is histogram channel number, on 'Y'-axis number of counts.

During measurements of Au-197 and Ta-181, proton linac was working with parameters: proton energy 209 MeV, pulsed current 10 mA, pulse width 1 mks, frequency 50 Hz. Installation INES was installed on 50 meter TOF base of spallation pulsed neutron source RADEX.

In fig. 6, work with experimental histogram is shown. Experimental spectral histograms can be transformed into cross section curves by main two methods. Below few hundreds eV for heavy atoms with high resonance level densities, where ΔE of spectrometer resolution function is smaller than Γ_γ which is about 0.1 eV, the method of form can be used. At higher neutron energies in the resolved area it's necessary to use method of square areas.

Program for resonance parameters definition automatically calculates: background level as function of neutrons energy on experimental histogram like fig.7, energy of the center of resonance area, width of resonance on half-altitude, area of the resonance.

In fig. 8 we can see action of Mn-55 filner: in its 336 eV resonance area, all counts are background. Observing this effect makes possible to calculate the background component as energy's function and extract it from the spectra.
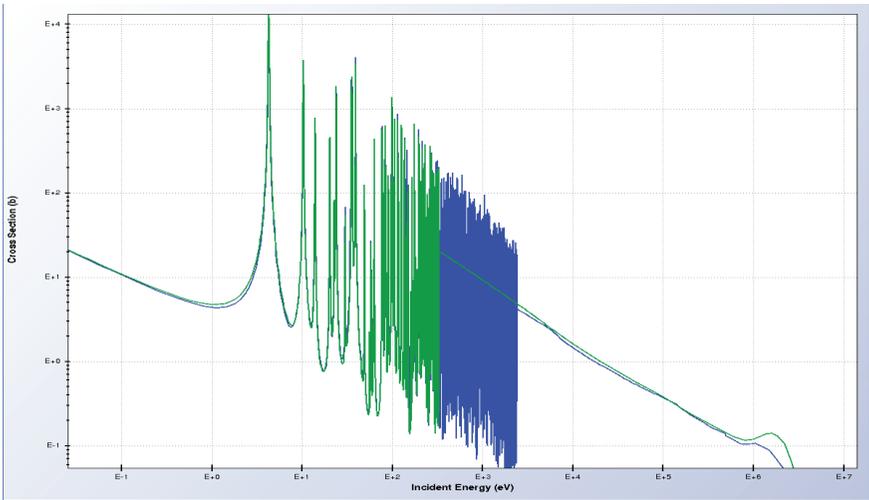
Fig. 3: The best world data for Ta-181 capture cross section in wide energy region.
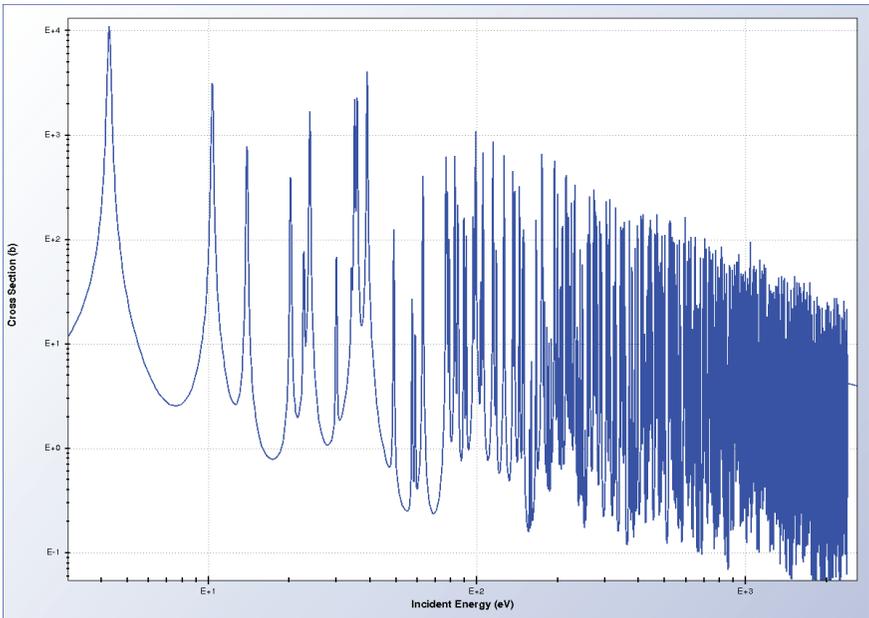
Fig. 4: Ta-181 capture cross section area of the resolved resonances, up to 2500 eV.
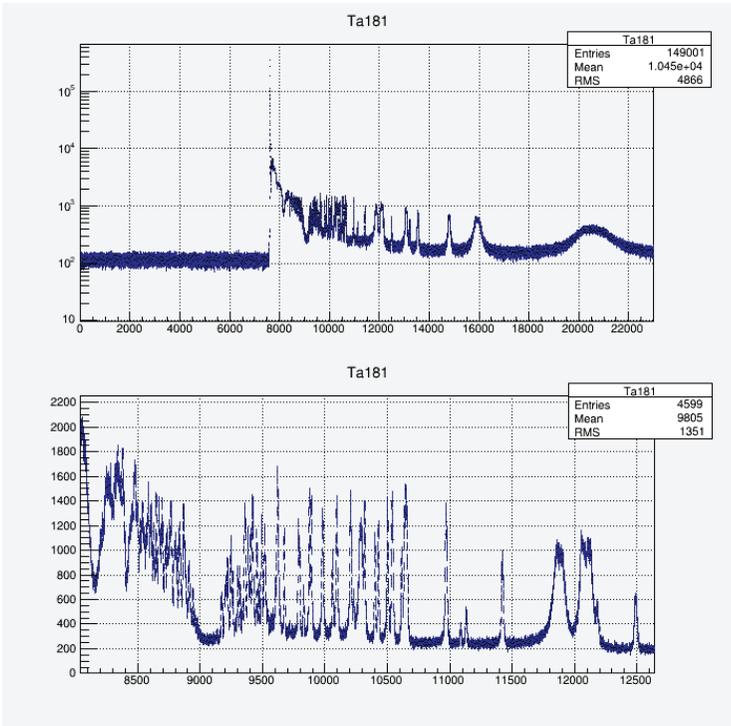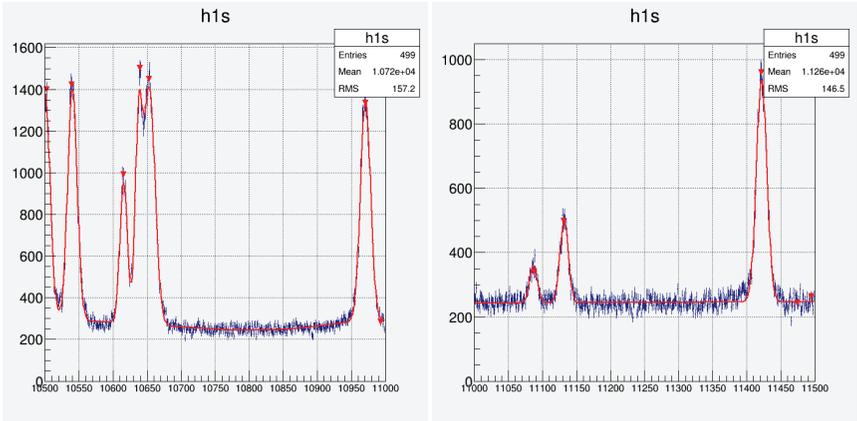
Fig. 5: Ta-181 capture cross section.

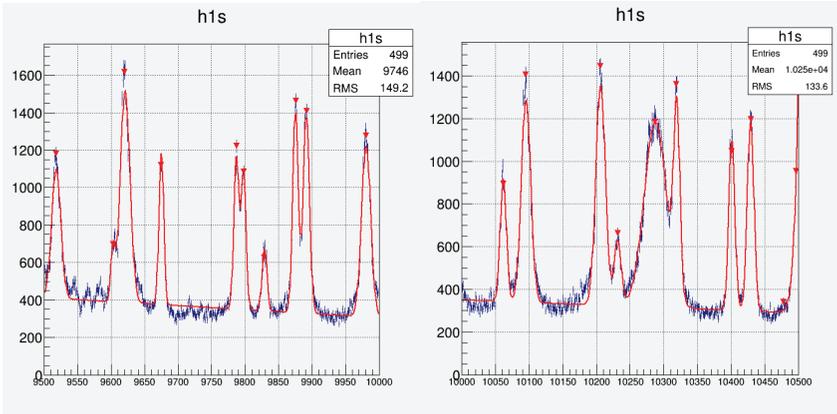Fig. 6: Separation of effect from background.
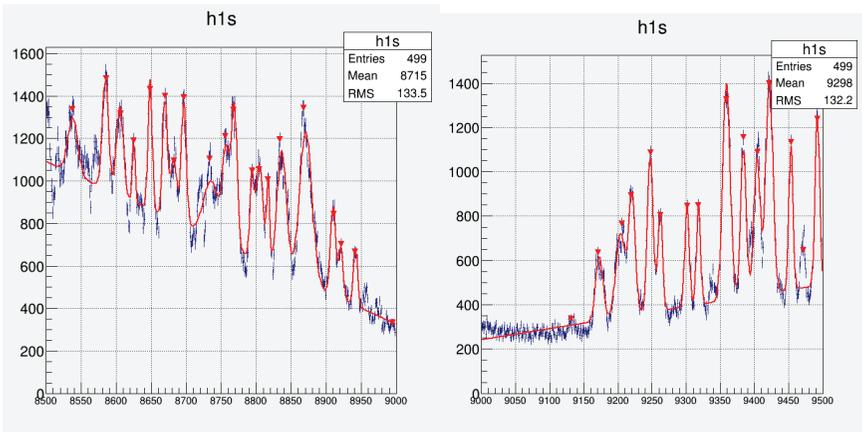
164

Fig. 7: Ta-181 capture experimental spectra.

Fig. 8: Ta-181 spectrum between channels number 8500 and 9500.

At energies upper then few hundreds eV, in the case of heavy nuclides with most dense energy level system and the smallest intervals between resonances, spectrometer resolution function's value is much larger then energy width Γ_γ with doppler-effect. Due to this, experimental histogram gives us Gauss resonance parameters. When we know them, using another program for each resonance we transform the curve into the cross section curve descripted by Breit-Wigner parameters.

Unresolved area is illustrated by fig. 9. Also it's necessary to mention, that researched pattern inside the detector becomes radioactive during measurements.
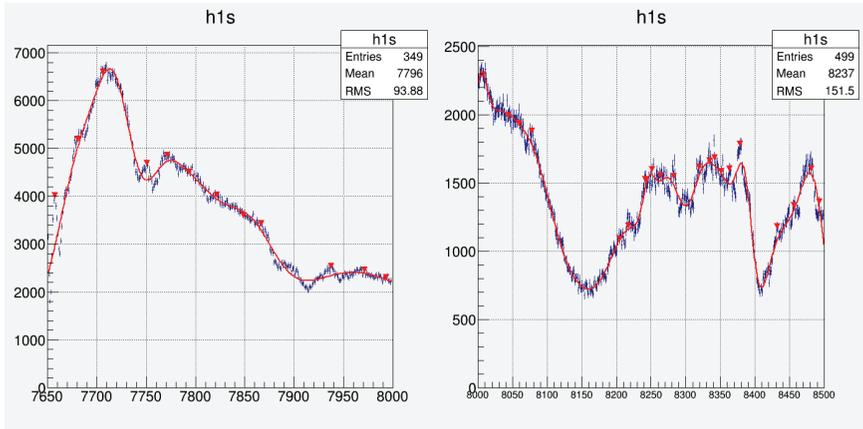
Fig. 9: Ta-181 unresolved capture resonance area after the proton beam flash.

Isotope	D_0, eV	Isotope (A+1)	T(1/2) of (A+1)
Ta-181	1.13	Ta-182m2	15.8 minutes
In-115	1.9	In-116m1	54 minutes
Au-197	1.15	Au-198	2.7 days
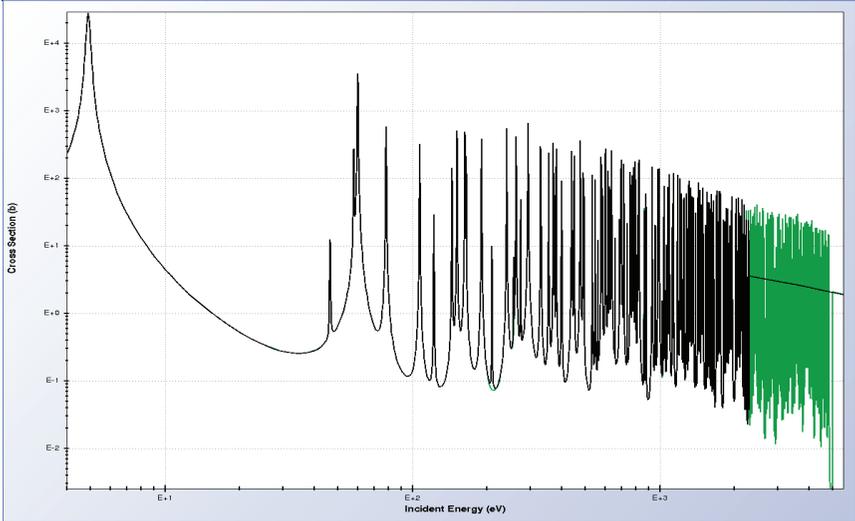
Fig. 10. Capture cross section of Au-197.

In fig.10 we can see, that in $Au^{197}(n,\gamma)$ cross section, up to 5000 eV resonances are resolved in BNL data base.

In fig. 14 scintillator signals after pre-amplifier are shown. They are around 60 nanoseconds at half-altitude.

New 16-channel multiplicity data acquisition system was tested at first using Co-60 gamma source and Cf-252 spontaneous fission neutron source, than it was tested on pulsed beam.

During turning, high sustainability to radio frequency transients was achieved. After turning and testing, 16-channel multiplicity system was used in measurements at TOF base 50 meters during accelerator's work with proton bean duration 500 ns.

TOF histograms of Ta-181, In-115, and Au-197 were successfully measured using 40 liter liquid scintillator gamma detector, four He-3 counters SNM-18 as neutron beam monitors and four He-3 neutron counters SNM-17 as transmission detectors.

5. Conclusion

Installation INES has properties, high enough for measurements of total and capture cross sections of reactor and construction materials in energy groups of ABBN-78 and ABBN-93 neutron constants, which are used for core criticality calculations during construction of fast breeder reactors BN-800 and BN-1200.

Internal block-effects for reactor alloys and radiation shield materials resonance cross section structure, also as Doppler-effect, can be measured. Measurements can be done both for separated isotopes of natural multi-isotope mixtures, and for multi-isotope mixtures of many chemical elements like stainless steel.

During the nearest future we plan to measure new reactor alloys group cross sections, including burning absorber reactor materials for isotope separation quality control. Also measurements of total and capture cross sections of separated isotopes, measurements at different thicknesses and temperatures in ABBN-93 energy group intervals.

Proton linac shows good progress. Operation with proton energy up to 423 MeV compared with increase of linac pulse proton current to 16 mA is planned for 2019 nearest years.

TOF measurements with 300 nanosecond proton beam are planned for 2019. Also frequency 100 Hz achievement is in progress. TOF stations at 250 meters and at 500 meters are discussed. Proton storage ring is under construction.

THE FEASIBILITY STUDY OF CSNS BACK-N USING FOR TEMPERATURE MEASUREMENT BY RESONANCE NEUTRONS

Zhaohui Song[1], Yicheng Yi[1], Yi Lu[1,2], Xianpeng Zhang[1]

[1]State Key Laboratory of Intense Pulsed Radiation Simulation and Effect, Northwest Institute of Nuclear Technology, 710024, Xi'an, China

[2]State Key Laboratory of Nuclear Physics and Technology, Institute of Heavy Ion Physics, Peking University, 100871, Beijing, China

szh197107@126.com

Abstract: The temperature measurement using neutron resonance spectrum can be used for temperature measurement of shockwave, but a pulsed white neutron source with high intensity is needed. The back-streaming white neutron beam line (Back-n) of the China Spallation Neutron Source (CSNS) was built and started running since the beginning of 2018. The white neutron source can provide neutrons from 1eV up to hundreds of MeV by impinging 1.6 GeV protons onto a thick tungsten target. There are two experimental halls along the Back-n beam line which respectively has a flight path of ~55 meters (Hall 1) and ~76 meters (Hall 2). The resonance sample (such as ^{181}Ta) was placed at Hall 1 and measured the neutron transmission spectrum at Hall 2. The neutron transmission spectrum through the resonance sample was simulated by MCNP. The 4.28 eV and 10.36 eV resonance drop of ^{181}Ta can be seen from the transmission spectrum. CSNS Back-n may be applied for temperature measurement by neutron resonance spectrum in the future.

Key words: Temperature measurement, Resonance neutron, CSNS Back-n, Monte Carlo simulation

Introduction

The Doppler broadening of the lower energy neutron absorption resonances of some metals, such as natural hafnium, tantalum, iridium and rhenium, have been studied for the purpose of measuring temperature in remote or isolated environments[1-3]. This new method of temperature measurement using neutron resonance spectrum can be also applied to some experimental studies of dynamic system, such as detonation, explosion, shock, and so on.

In order to apply this method, a pulsed neutron source which has plenty of low energy neutrons with high intensity is needed. The back-streaming white neutron beam line (Back-n) of the China Spallation Neutron Source (CSNS) was built and started running since the beginning of 2018. The white neutron source can provide neutrons from 1eV up to hundreds of MeV by impinging 1.6 GeV protons onto a thick tungsten target[4].

The feasibility of CSNS Back-n beam line using for temperature measurement by resonance neutron will be discussed in this paper.

Principle

It is proposed that the sample temperature be determined from transmission data by a methodology which directly appeals to the equations of the governing physics rather than

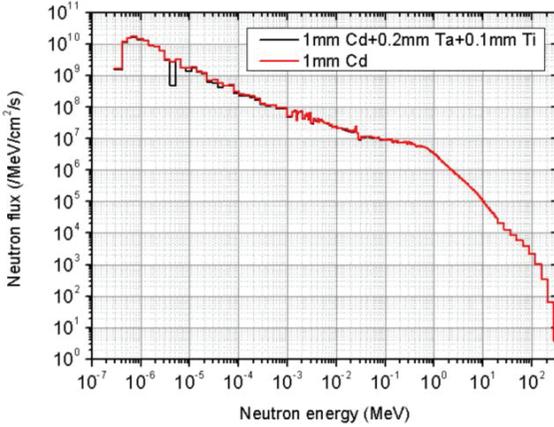neutron energy spectrum is provided by Dr. H.T. Jing[9], shown as Figure 3.

Figure 3. Neutron spectrum of CSNS back-n

The neutron intensities spectra after the neutrons passed through the sample were recorded according to different temperatures. The results are shown as Figure 4.
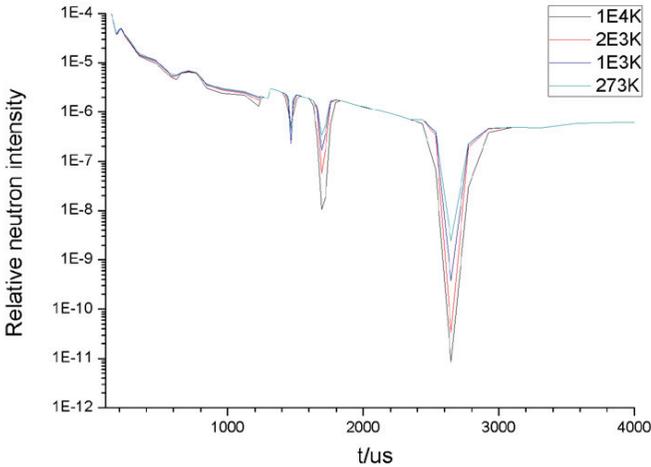

Figure 4. Neutron transmission spectrum at Hall 2

The 4.28 eV and 10.36 eV resonance drops of Ta-181 can be seen clearly from the transmission spectrum. The width of the absorption peak could be obtained and it was broaden when the temperature was changed to a higher temperature.

We can use TOF methods to measure the Doppler Broadening at Hall 2 by fast timing technique. The current neutron beam of CSNS Back-n can be used for stable temperature measurement by using neutron resonance spectrum; but for a dynamic system, the intensity of low energy neutron for single pulse is not enough high.

Discussion

1. On the one hand, the effective cross-section of the sample is important to this method. Different models and assumptions may give different results. On the other hand, the calculation results of this work may have a relative bigger uncertainty because the input neutron energy spectrum must be corrected by measured results.

2. A ^{6}Li glass scintillation detector with flat energy response for low neutron energy neutrons is planning to use. Fission chamber with SiC detector is also a good choice. An appropriate sample is also important.

3. In order to escape from gamma flash and high energy neutrons, the gating photomultiplier is recommended. The signal from another fast scintillation detector which monitors the gamma flash can be used as a triggered signal for the gating photomultiplier.

References

1. Hu Chunming, Tong Jianfei, Yu Chaoju, Temperature Measurement in Dynamic System Using Neutron Resonance Spectroscopy, Nuclear Electronics & Detection Technology, Vol.**31**, No.6(2011) 595–598. (in Chinese).

2. H.J. Stone, M.G. Tuckers, Y. Le Godec, et al. Nucl. Instr. and Meth. A**547** (2005) 601–615.

3. J.E. Lynn, W.J. Trela, Nucl. Instr. and Meth. B**192** (2002) 318–330.

4. The CSNS Back-n Collaboration. Back-n white neutron facility for nuclear data measurements at CSNS. http://doi.org/10.1088/1748-0221/12/07/P07022

5. G. Breit, E. Wigner, Phys. Rev. 49 (1936) 519.

6. L.Y. Zhang, H.T. Jing, J.Y. Tang, et al. Applied Radiation and Isotopes 132 (2018) 212–221.

7. R.E. MacFARLANE and D.W.MUIR. NJOY99.0 Code System for Producing Pointwise and Multigroup Neutron and Photon Cross Sections from ENDF/B Data. PSR-480/NJOY99.0, Los Alamos National Laboratory.

8. Gokham Yesilyurt, William R. Martin. Nucl. Sci. and Eng.**171** (2012) 239–257.

9. H.T. Jing, J.Y. Tang, H.Q. Tang, et al. Nucl. Instr. and Meth. A**621** (2010) 91–96.

The Optimization of Shielding Structure in Neutron-Gamma Well Logging Instrument

Lei Song[1], Baolong Ma[2], Sheng Wang[2]*

[1]School of Automation Engineering, University of Electronic Science and Technology of China, Chengdu, Sichuan Province China,
[2]School of Nuclear Science and Technology, Xi'an Jiaotong University, Xi'an, Shaanxi Province, China

Abstract

Neutron-gamma well logging instrument was widely used in well logging processing. The D-D controlled neutron generator, which produced 2.45 MeV neutrons, was used as the neutron source in the logging instrument. However, one part of the 2.45 MeV neutrons will directly reach the detector of the logging instrument and deposited energy in it. Thus the secondary photons will be arose and made adverse effect on the measurement accuracy of the instrument. A shielding structure, which was between the neutron source and detector, can reduce the effect caused by the radiation particles. However it is hard to design an efficient shielding structure.

This study was aimed to design the shielding structure of the well logging instrument. The shape of the shielding structure was set as a cylinder and its length was fixed as 10 cm. The MCNP code was invoked by the Genetic Algorithm to optimize the shielding structure from 7 shielding materials.

Two shielding structures were obtained by the optimizing program. The first structure was with three layers, gadolinium oxide-polyethylene-lead and each length of the layers was 5.2 cm, 1.3 cm and 3.5 cm, respectively; the other structure was with four layers, boron carbide- polyethylene- boron carbide-lead and each length of the layers was 1.0 cm, 0.9 cm, 4.6 cm, 3.5 cm, respectively. The results showed that, the optimized shielding structures can effectively reduce the deposited energy in the detector.

Keywords : Shielding structure, Optimization, Neutron-gamma well logging instrument, D-D Neutron source

1. Introduction

Radiation shielding is an important part of nuclear facilities. It can limit the radiation damage to the people and device around the nuclear facilities[1–3]. Many issues, such as volume, length, weight, price and shielding effectiveness will be considered when designing new shielding structure.

Neutron-gamma (N-G) well logging instrument is widely used in the well logging process because of its accuracy measurement. It contains several parts, such as neutron source, detector, shielding structure and electronic device. The neutron source will generate the neutron during the logging period. These neutron will interact with the stratum's elements which surrounding the instrument. As the result, the specific gamma rays will be emitted. After that, the detectors within the logging instrument will detect and analyze the gamma

rays' signal. Finally, the component of the stratum was obtained.

However, the neutron source will evenly release neutron into surrounding area. Part of the neutron will directly go into the detector. These neutron and their secondary particles will deposit energy in the detector. As the result, the errors may occur during the logging process. A shielding structure, which was between the neutron source and detector, can relieve this problem[4]. Unfortunately, the space in the N-G well logging instrument is limited. Only a small room can be used for shielding structure. Thus, it is a challenge to design the shielding structure in the limited space, especially for the multilayer shielding structure.

Many optimization techniques, such as genetic algorithm, linear programming, sequential quadratic programming and transmission matrix method can be used for designing the shielding structure[5–9]. Several excellent shielding materials which can be used in reactor and accelerator have presented in the studies. These studies demonstrated that it was a good way to design the shielding structure by optimization algorithms.

However, in these studies, the most important constraint condition is that the absorb dose at a certain distance should below than a threshold. The optimization parameters of the shielding material, such as the weight, volume, shape and price must follow this condition. The situation is different in the well logging instrument. Because of the limitation of the instrument's space, the volume and the shape of the shielding structure is fixed. Therefore, the primary constraint condition of optimizing the shielding structure in well logging instrument is that the shape of the structure is fixed. Based on this condition, the aim of this study is minimizing the deposited energy in the detector while the shape of detector is fixed. The procedure of this study is shown as below:

First, simplify the structure of the D-G well logging device and construct the simulating model which can be calculated by MCNP software;

Second, optimize the shielding structure by genetic algorithm and MCNP calculation;

Third, obtained the optimized shielding structure which with different number of layers.

2. Methodology

2.1 Modeling of N-G well logging instrument

The structure of the N-G well logging instrument is shown in Fig.1. There are several devices in N-G well logging instrument, such as neutron source, shielding structure, detector, electronic device, iron tube and so on. This study aims to develop a novel shielding structure of the instrument. Thus the simulating model should contain at least three parts, the neutron source, shielding structure and detector. The rest of the device is not necessary and can be ignored in the simulating model. In the commercial well logging instrument, the neutron source, shielding structure and detector are coaxial. Their simulating model also should be coaxial.

A miniaturized controlled neutron generator was used in the N-G well logging instrument. 2.45 MeV neutron was produced by D-D fusion. The formula of fusion reaction is show as below:

$$^2_1D + {}^2_1D \rightarrow {}^3He + n \qquad (1)$$

The shape of the neutron source can be simplified as a cylinder which diameter is 2.5 cm and height is 10 cm. Although neutron will evenly emitted into surrounding area, only neutron that directly fly to the detector may influence on the logging result. Thus direction of emitted neutron was set as one direction, faced to the detector. And this direction also defined as an axial positive direction.
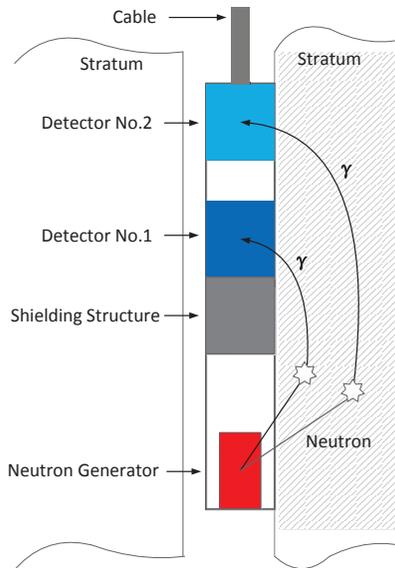
Fig. 1. The structure of D-G well logging instrument.

The distance between neutron source and shielding structure was 50 cm. The space which will insert the shielding structure was a cylinder. The diameter and the length of the cylinder were 5 cm and 10 cm, respectively. Because, in this study, the shielding structure was multilayer, the first layer of the structure was defined as the one which close to the neutron source. Then the second layer and so on. There were two types of shielding structure, the one with 3 layers and 4 layers.
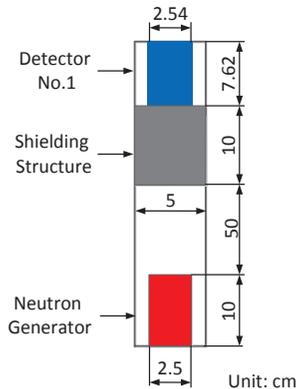
Fig. 2. The simulating model of the well logging instrument.

A cylinder sodium iodide detector was constructed in the model. The diameter and the length of the cylinder were 2.54 cm and 7.62 cm. It was close to the shielding structure. The simulating model was shown in Fig.2.

2.2 Forms of the shielding material

In this study, a D-D fusion neutron generator was used in the N-G well logging instrument. The 2.45 MeV neutron will interact with the elements of shielding structure. These interactions include elastic scattering, inelastic scattering and radiation capture. The gamma rays with different energy will be emitted after the reactions. Thus, the shielding structure should prevent both neutron and gamma ray reach the detector. For this purpose, the shielding structure should at least contain 3 parts:

1st part should promptly reduce the neutron energy. Mostly, the materials with high inelastic scattering cross section, such as iron and tungsten will be used;

2nd part can efficiently absorb the low-energy neutron and polyethylene (PE), lead-boron polyethylene (PB202), boron carbide (B_4C), gadolinium oxide (Ga_2O_3) will be selected;

3rd part will be used to prevent gamma rays. Tungsten, lead, such metal with high density are the good options.

Based on this information, a form of the shielding material can be established. The data of the selected material was shown in Table 1.

Table 1 Data of the shielding material

Name	component / wt%	density/g•cm^{-3}
Iron	Fe: 100	7.86
Tungsten	W: 100	19.35
PE	H: 14.3, C: 85.7	0.95
PB202	H: 0.0271, B: 0.0077, O: 0.1652, Pb: 0.8	3.42
B_4C	B: 76.9, C: 23.1	2.52
Ga_2O_3	O: 27.3, Ga: 72.7	7.407
Lead	Pb: 100	11.344

2.3 Optimal design of the shielding structure by genetic algorithm

The genetic algorithm (GA), which is based on natural selection, is widely used for solving optimization problems. It works on a population of individuals, and repeatedly modifies the potential solutions relying on bio-inspired operators such as mutation, crossover and selection. Over successive generations, the population "evolves" toward an optimal solution. In this study, a GA program developed by Andrew Chipperfield and Peter Fleming was selected for optimization. It has excellent global search capabilities and optimization efficiency.

There were two kind of parameters should be considered in this designing problem, length of each layer within the shielding structure and its material. The optional shielding materials were shown in Table 1. It can be easily invoked by the GA algorithm. The length of each layer should follow two constraint conditions:

1) The range of each layer's length should be from 0 cm to 10 cm;

2) Total length of shielding structure is 10 cm.

Based on the 1) condition, the expectation value of each layer was 5 cm. If the GA

algorithm directly generated each length of layers l_i, the expectation value of total length will reach to $5 \cdot n$ cm, where n the number of shielding layers. Therefore, total length of shielding structure will beyond 10cm. To solve this problem, GA algorithm generated several percentages p_i of total length instead of the length of layers l_i. The range of p_i was from 0 to 1. The proportion of each layer can be calculated by the binary tree method. Every proportion of layer can be obtained by multiplying several percentage p_i. The calculating process was shown in Fig.3.
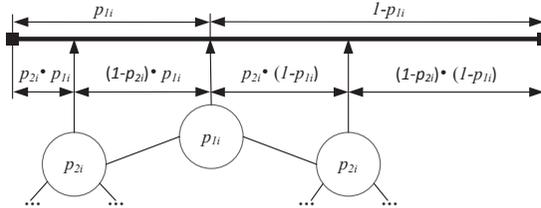
Fig. 3. The calculation process of each layer's proportion. Thick line is the total length of the shielding structure. It can be divided by several proportions.

When the neutron and gamma ray reached the detector, they will deposit energy into the detector and the light will be emitted. This light will be used for analyzing the stratum's element. Part of the neutron and their secondary particles will directly go into the detector and they also deposited energy into the detector. We named this part of deposited energy as direct deposited energy. Thus, the error will be occurred during the well logging process. The shielding structure can limit this error. It means that the objective function of this optimization was minimized the direct deposited energy E_d. The objective function was shown below:

$$f(x) = \min(E_d(x)) \tag{2}$$

After the shielding structure had been generated, MCNP software will be invoked to calculate the direct deposited energy. In this study, calculations to design the optimal shielding were performed using the MCNP6 code and the ENDF/B-VI cross section set. Mode n p was used. The flow chart of the optimization program was shown in Fig.4.
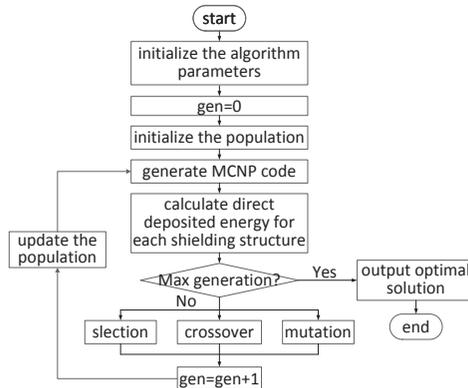

Fig.4. The optimization program algorithm.

3. Result

In order to find the optimal shielding structure, the domain constraint of each variable was set at 0–1 (the total thickness was set at 0–10 cm), the population size was set at 70 according to the number of variables, the gap between generations was set at 0.9, and the number of generations was set at 80 after several trials.

By running the program, two types of shielding structures presented were obtained, as presented in Table 2.

Table 2 Optimized shielding structures

Number of shielding layer	Material	Length of layer/ cm	Deposited energy / MeV•g^{-1}
3	Ga$_2$O$_3$	5.2	1.242×10^{-5}
	PB202	1.3	
	Pb	3.5	
4	B$_4$C	1.0	0.917×10^{-5}
	PE	0.9	
	B$_4$C	4.6	
	Pb	3.5	

As mentioned above, shield 2.45 MeV neutron need three major steps: moderating neutron, absorbing neutron and absorbing gamma ray. The optimized shielding structures followed this principle. The whole shielding structure can be separated into two parts: neutron shielding domain and gamma shielding domain. The neutron shielding domain arranged at the front layers. Neutron moderation and absorbing materials were set in this area. The gamma shielding domain located at the last layer. It can protect detector from the secondary gamma rays.

Comparing with two types of shielding structures, four layers structure specified and modified the neutron shielding domain and the direct deposited energy was lower than three layers structure. This result shows that: 1) shield neutron can reduce the direct deposited energy in the detector and 2) specified neutron shielding structure is more efficient than the single layer structure.

4. Conclusion

Thus far, the method to optimize multilayer shielding structure of the N-G well logging instrument was established employing genetic algorithms and MCNP code. The optimization factors and objective function were presented as well. The optimized shielding structures with three and four layers have presented in this study. The direct deposited energy can be reduced by specified and modified the neutron shielding domain.

However, this study was focused on the well logging instrument with D-D neutron generator. The neutron energy was only 2.45 MeV. It is noted that the D-T neutron generator also employed in the N-G well logging instrument. D-T neutron generator has higher neutron yield and the neutron energy is over 14MeV. Thus, the shielding structure in the D-T N-G well logging instrument can be designed in future work.

References

1. Wielopolski, L., Mitra, S., Doron, O. Non-carbon-based compact shadow shielding for 14 MeV neutrons. J. Radioanal. Nucl. Chem. 2007, 276, 179–182.
2. Hu, G., Hu, H., Wang, S., Han, H., Otake, Y., Pan, Z., Taketani, A., Ota, H., Hashiguchi, T., Yan, M. New shielding material development for compact accelerator-driven neutron source. Aip Adv. 2017, 7, 324–341.
3. Bayat E., Afarideh H., Davani F.A., et al. A quality survey on different shielding configurations of gamma ray detector used with a portable PGNAA system [J]. Radiation Physics & Chemistry, 2016, 120:7–11.
4. Rasoulinejad M., Izadi N.R., Ghal-Eh N. A simple well-logging tool using boron-lined sodium iodide scintillators and a ^{241}Am-Be neutron source [J]. Radiat. Prot. Dosimetry, 2012, 151(3):580–585.
5. Hu, H., Wang, Q., Qin, J., Wu, Y., Zhang, T., Xie, Z., Jiang, X., Zhang, G., Xu, H., Zheng, X., Zhang, J., Liu, W., Li, Z., Zhang, B., Li, L., Song, Z., Ouyang, X., Zhu, J., Zhao, Y., Mi, X., Dong, Z., Li, C., Jiang, Z., Zhan, Y. Study on composite material for shielding mixed neutron and gamma -rays. IEEE Trans. Nucl. Sci. 2008, 55, 2376–2384.
6. Kebwaro, J.M., Zhao, Y., He, C. Design and optimization of HPLWR high pressure turbine gamma ray shield. Nucl. Eng. Des. 2015, 284, 293–299.
7. Leech, W.D., Rohach, A.F. Weight optimization of reactor shielding using transmission matrix methods. Nucl. Eng. Des. 1972. 22, 167–169.
8. Tunes, M.A., de Oliveira, C.R.E., Schon, C.G. Multi-objective optimization of a compact pressurized water nuclear reactor computational model for biological shielding design using innovative materials. Nucl. Eng. Des. 2017,313, 20–28.
9. Ma B., Otake Y., Wang S., et al. Shielding design of a target station and radiation dose level investigation of proton linac for a compact accelerator-driven neutron source applied at industrial sites. [J]. Applied Radiation & Isotopes, 2018, 137:129.

EXPERIMENTAL STUDY OF SYNERGISTIC EFFECTS OF NEUTRON AND GAMMA RAY IRRADIATION ON LINEAR REGULATOR

X.M. Jin[*], Y. Liu, S.C. Yang, C.H. Wang, X.Y. Bai, W. Chen

State Key Laboratory of Intense Pulsed Radiation Simulation and Effect, Northwest Institute of Nuclear Technology, 710024, Xi'an, China

Abstract: Synergistic effects of linear regulator in mixed neutron and gamma ray irradiation environment are studied. The electrical tests of the linear regulator were performed in three irradiation environments: neutron, gamma ray, combined irradiation of neutron and gamma ray. Comparison of the output voltage and the power current of the linear regulator in these three radiation environments is presented. The experiment results show that single neutron radiation induces no degradation and synergistic effects of neutron and gamma ray are related with the operational modes of the linear regulator. For off-load mode, the output voltage of the linear regulator exhibits identical TID degradation in the mixed neutron and gamma ray radiation environment with that in single gamma ray radiation environment. However, for on-load mode, the output voltage of the linear regulator increases slightly in combined neutron and gamma ray irradiation environment and decreases significantly in single gamma ray radiation environment. Bias configurations of the transistors inside the linear regulator vary at different operational modes and have considerable impact on the synergistic effects of neutron and gamma ray.

Keywords: linear regulator, neutron, gamma ray, synergistic effect

I. Introduction

Linear regulators are widely used in space applications, and can offers excellent ac performance with very low ground current. High power-supply rejection ratio, low noise, fast start-up, and outstanding line and load transient response are provided while consuming a very low ground current. In electronic systems, a linear regulator provides a stable dc output voltage over a wide range of load currents and input voltage variations. Although the main disadvantage of a linear regulator is its low efficiency, it is widely used in various electronic systems in space applications. However, linear regulators have been found to be very sensitive to radiation effects, especially total ionizing dose (TID) effects and displacement damage. The radiation responses for a linear regulator may range from transient output perturbations to permanent circuit failure depending on its technology process and topology [1–4].

To study the radiation hardness for a linear regulator, the estimation of the sensitivity to radiation is a mandatory step to get an insight about the impact of radiation on its electrical parameters and functions. In radiation ground accelerated tests, TID effect is usually decoupled from displacement damage, assuming these two effects are independent. However, this assumption may neglect the interaction between different radiation effects and would lead to a misestimate of radiation tolerance. Many literatures have reported that some electronic devices exhibit synergistic effects under mixed

neutron and gamma ray exposure [5-7].

In this paper, synergistic effects of neutron and gamma ray are studied on a linear regulator using fabricated by an advanced BiCMOS fabrication process. MOS transistors inside the linear regulator are very sensitive to gamma ray-induced TID effects [8, 9], while bipolar junction transistors are very sensitive to neutron-induced displacement damage [10]. In mixed neutron and gamma ray exposure, the degradations for both MOS and bipolar junction transistors will lead to synergistic effects on the output voltage and current of the linear regulator. Interestingly, the experimental measures also show that the synergistic effects strongly depend on its load conditions.

II. Test description

Device under test is TPS79333DDCR manufactured by Texas Instruments. The input voltage is adjustable from 2.7 up to 6.5 V. In the experimental testing the input voltage of the linear regulator was fixed to be 6 V, and the output voltage was 3.3 V before radiation. The schematic of the testing system is shown in Fig. 1. The EN terminal is an output enable signal which is connected to the input voltage. The NR terminal is a noise reduction signal and is floating during the measurement. Two operational modes of the device are tested. In the off-load state, the output is floating. In the on-load state, the electrical impedance is a resistor of 100 Ω.
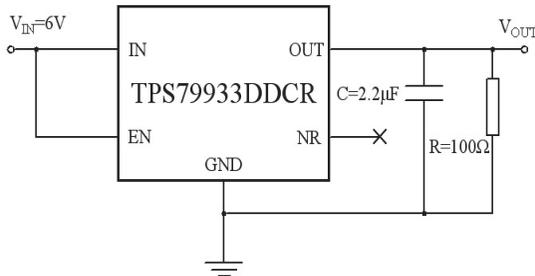
Fig. 1. Schematic of the test system.

The output voltage and the power supply current are tested in neutron radiation, gamma ray radiation and mixed neutron and gamma ray radiation environments. In each radiation environment, two samples are measured for each operational mode. The irradiation experiments were carried out at room temperature in Northwest Institute of Nuclear Technology, China. The information for all the radiation experiments is shown in table 1. The gamma ray exposure was performed using a Co-60 irradiator with a dose rate of 0.2 Gy(Si)/s. Neutron exposure and synergistic irradiation of neutron and gamma ray were performed using nuclear reactor in different states. The ratio of neutron flux and gamma dose rate (n/γ) is 7.7×10^{11} n/(cm^2·Gy(Si)) in the neutron irradiation environment and 5.4×10^{10} n/(cm^2·Gy(Si)) in the synergistic irradiation environment. The neutron energy ranges from 3.6×10^{-3} eV up to 20 MeV and the neutron spectrum is shown in Fig. 2. The neutron fluence is given as 1 MeV equivalent fluence. In the higher n/γ irradiation the neutron radiation effect dominates, so the TID effect induced by parasitic gamma ray can be ignored.

Table 1. The radiation parameters in the experiments

Radiation field	Neutron fluence rate (n/cm^2/s)	Gamma ray dose rate (Gy(Si)/s)	Total neutron fluence (n/cm^2)	Total gamma ray dose (Gy(Si))
Gamma ray	0	0.2	0	1.85×10^3
Neutron	2.7×10^{10}	3.5×10^{-2}	1.0×10^{14}	1.29×10^2
Mixed neutron and gamma	6.5×10^9	0.12	1.0×10^{14}	1.85×10^3
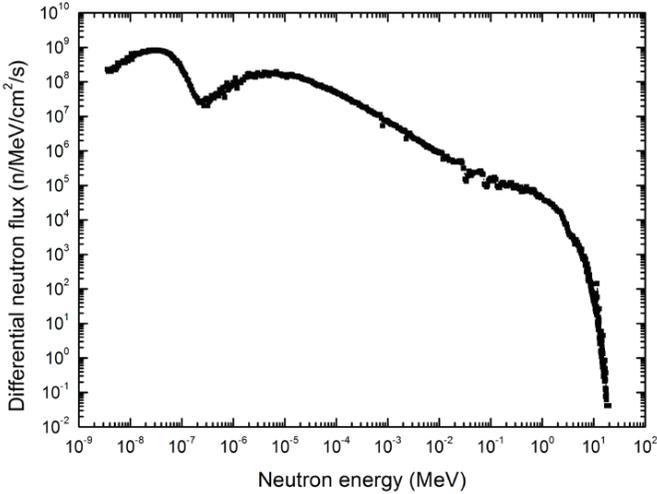
Fig. 2. Differential neutron flux at XAPR.

III. Experimental results

As shown in Fig. 3, for on-load state with 100 Ω, the output voltage shows almost no degradation in single neutron radiation. The single gamma ray radiation first induces a slight increase from 3.3 V at 5.55×10^2 Gy(Si) to 3.4 V at 9.25×10^2 Gy(Si) and then a significant decrease to 0 V at 1.85×10^3 Gy(Si) for the output voltage. However, the output voltage under mixed neutron and gamma ray radiation kept constant up to 3×10^{13} n/cm^2 and increased from 3.3 V at 3×10^{13} n/cm^2 to 4.0 V at 1×10^{14} n/cm^2. Single gamma ray radiation induces a significant decrease of output voltage, while single neutron radiation has almost no obvious impact on the output voltage. However, mixed neutron and gamma ray radiation cause a slight increase on the output voltage.

Similarly, as shown in Fig. 4, the power supply current shows no degradation in the single neutron radiation. In the single gamma ray radiation, the power supply current first increases slightly from 3.5×10^{-2} A at 1.85×10^2 Gy(Si) to 4×10^{-2} A at 9.25×10^2 Gy(Si) and then decreases greatly to 6×10^{-3} A at 1.85×10^3 Gy(Si). In the mixed neutron and gamma ray radiation, the power supply current increases slightly from 3×10^{-2} A to 4×10^{-2} A. The synergistic effects for the power supply current are consistent with that for the output voltage. The linear regulator exhibits strong synergistic effects induced by

mixed neutron and gamma ray for on-load operational mode, indicating the opposite trend due to the TID effects caused by single gamma ray.
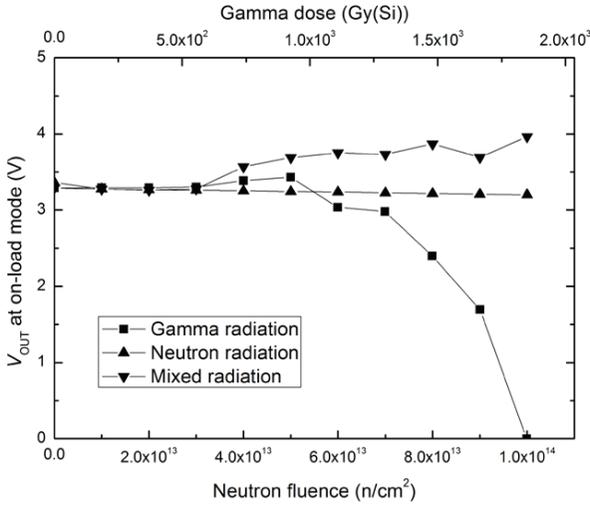

Fig. 3. Degradation of the output voltage in different radiation environments for on-load state.
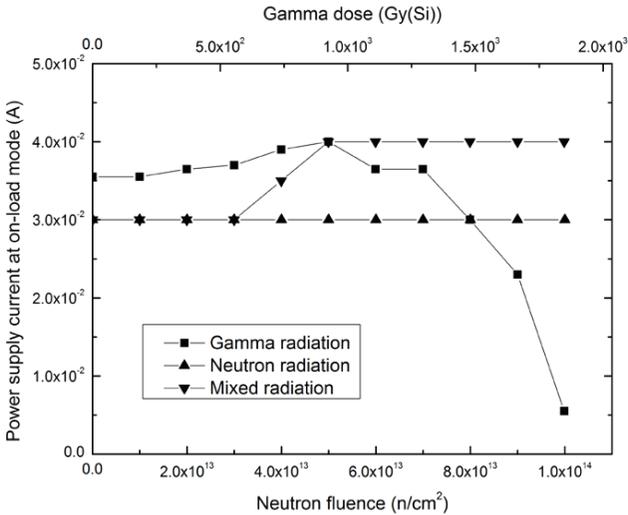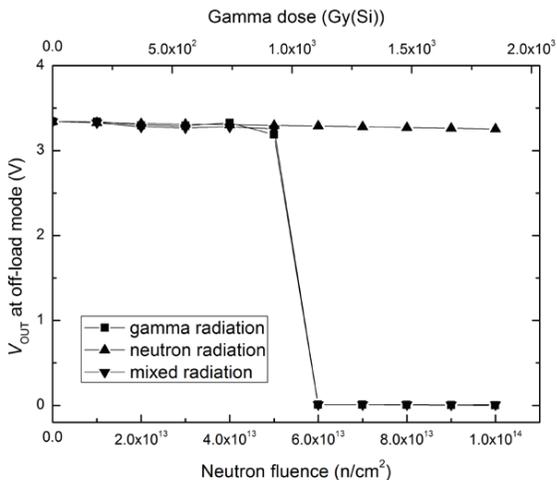

Fig. 4. Degradation of the power supply current in different radiation environments for on-load state.

For off-load state, the output voltage holds steady in single neutron radiation. However, the output voltage decreases from 3.2 V at 9.25×10^2 Gy(Si) to 8×10^{-3} V at 1.11×10^3 Gy(Si) in single gamma ray

radiation and mixed neutron and gamma ray radiation, as shown in Fig. 5. The power supply current increases from 1×10^{-3} A to 5×10^{-3} A during single gamma ray radiation. However, in neutron and mixed neutron and gamma ray radiation, the power supply current remains unchanged, as shown in Fig. 6. The radiation effects induced by mixed neutron and gamma ray are due to the TID effects induced by gamma ray component. Furthermore, the neutron radiation, to some extent, contributes to the restrain of the increase of the power supply current.

Fig. 5. Degradation of the output voltage in different radiation environments for off-load state.
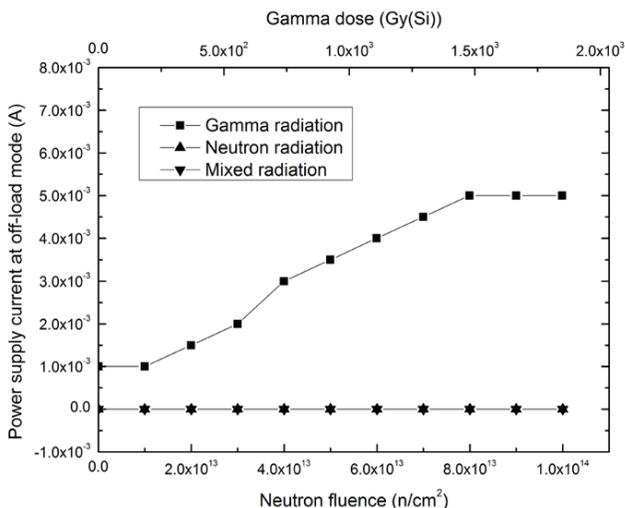
Fig. 6. Degradation of the power supply current in different radiation environments for off-load state.

186

IV. Discussion

The linear regulator includes both MOS and bipolar transistors, which are sensitive to gamma ray and neutron respectively. The degradation between them has coupling effects in the circuit. Fig. 7 shows the linear regulator topology. It is composed of two MOS transistors, one operational amplifier, or gate, thermal shutdown, overshoot detect and some resistances.
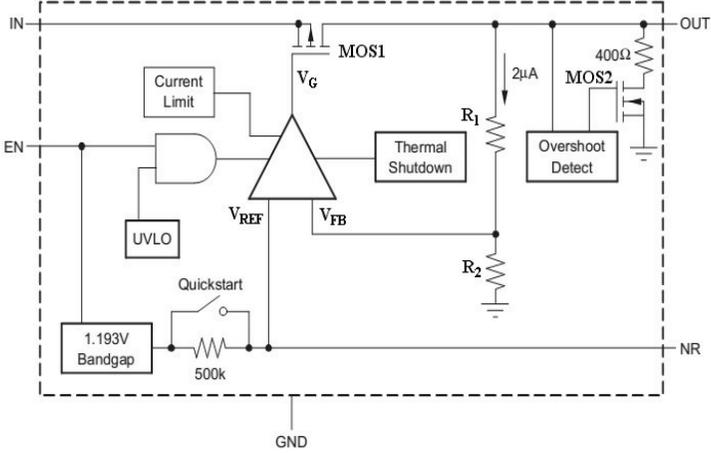
Fig. 7. Functional block diagram of the device.

The linear regulator utilizes a feedback circuit to regulate the output voltage. The operation mechanism is expressed as the following equations.

$$V_{\mathrm{G}} = A \cdot (V_{\mathrm{FB}} - V_{\mathrm{REF}}) \tag{1}$$

$$V_{\mathrm{FB}} = \frac{R_1}{R_1 + R_2} V_{\mathrm{OUT}} \tag{2}$$

Here V_{G} is the gate-control voltage of MOS1, A is the voltage gain of the operational amplifier, V_{FB} is the voltage at the feedback point, V_{REF} is the standard reference voltage of the linear regulator, R_1 and R_2 are the corresponding resistances in the linear regulator, and V_{OUT} is the output voltage of the linear regulator.

Gamma ray-induced TID effects lead to negative shift of the threshold voltage for both MOS1 and MOS2. MOS1 is a p-channel MOS transistor, so the decrease of its transconductance due to the TID effects reduces the conductivity from input voltage terminal to output voltage terminal. On the contrary, MOS2 is an n-channel MOS transistor, so the increase of its transconductance due to the TID effects increases the conductivity from the output voltage terminal to the ground terminal. Therefore, the output voltage decreases due to the increasing TID. However, the variation of the power supply current of the linear regulator depends on the degradation of the two transistors. The degradation of MOS1 induces the decrease of the power supply current, while the degradation of MOS2 leads to the

increase of the power supply current. For the off-load mode, the gate voltage of MOS1 is higher than that for the on-load mode and exhibits severer degradation.

Neutron-induced displacement damage mainly reduces the voltage gain of the operational amplifier, leading to the subsequent increase of the power supply current and the output voltage due to the decrease of gate voltage of MOS1. On the other hand, neutron radiation reduces the concentration of majority carriers, leading to the subsequent decrease of the power supply current and the output voltage. Under single neutron radiation, both the output voltage and the power supply current exhibit no significant variation due to these two competitive factors. However, under mixed neutron and gamma ray radiation, for the on-load mode, the decrease effect of voltage gain of the operational amplifier induced by neutron dominates and leads to the slight increase of the output voltage and the power supply current. For the off-load mode, the TID effects of MOS1 induced by gamma ray dominates due to its worst-case bias condition and leads to the synergistic effects of the linear regulator exhibit almost the same as TID effects. Therefore, synergistic effects strongly depend on the load conditions which have a great impact on the degradation degree due to different bias conditions.

V. Conclusion

Radiation effects on the linear regulator exhibit a strong dependence with its operational modes. The synergistic effects of mixed neutron and gamma ray are observed for the on-load state. For off-load state, the radiation effects in mixed neutron and gamma ray are caused by the TID effects due to single gamma ray radiation. Gamma ray induces the shift of threshold voltage and degradation of series resistance in MOS transistors, while neutron induces the decrease of the current gain in bipolar transistors. The circuit with BiCMOS technology is very likely to exhibit synergistic effects of mixed neutron and gamma ray, due to coupling effects between the MOS and bipolar transistors. This innovative mechanism may cause a significant problem for the radiation hardness.

References

1. A. T. Kelly, P. C. Adell, A. F. Witulski, W. T. Holman, R. D. Schrimpf, and V. Pouget, "Total dose and single event transients in linear voltage regulators," *IEEE Trans. Nucl. Sci.*, vol. **54**, no. 4, pp 1327–1334, 2007.
2. P. C. Adell, R. D. Schrimpf, W. T. Holman, J. Todd, S. Caveriviere, and K. F. Galloway, "Total dose effects in linear voltage regulators," *IEEE Trans. Nucl. Sci.*, vol. **51**, pp. 3816–3821, 2004.
3. P. C. Adell, R. D. Schrimpf, H. J. Barnaby, R. Marec, C. Chatry, P. Calvel, C. Barillot, and O. Mion, "Analysis of single-event transients in analog circuits," *IEEE Trans. Nucl. Sci.*, vol. **47**, pp. 2616–2623, 2000.
4. R. L. Pease, L. M. Cohn, D. M. Fleetwood, M. A. Gehlhausen, T. L. Turflinger, D. B. Brown, and A. H. Johnston, "A proposed hardness assurance test methodology for bipolar linear circuits and devices in a space ionizing radiation environment," *IEEE Trans. Nucl. Sci.*, vol. **44**, pp. 1981–1988, 1997.

5. J. L. Gorelick, R. Ladbury, and L. K anchawa, "The effects of neutron irradiation on gamma sensitivity of linear integrated circuits," *IEEE Trans. Nucl. Sci.*, vol. **51**, no. 6, pp 3679-3585, 2004.

6. P. J. Mcmarr, M. E. Nelson, H. Hughes, and K. J. Delikat, "14-MeV neutron and Co[60] gamma testing of a power MOSFET optocoupler," *IEEE Trans. Nucl. Sci.*, vol. **50**, no. 6, pp 2030–2037, 2003.

7. D. R. Ball, R. D. Schrimpf, and H. J. Barnaby, "Separation of ionizing and displacement damage using gate-controlled lateral PNP bipolar transistors," *IEEE Trans. Nucl. Sci.*, vol. **49**, no. 6, pp 3185–3190, 2002.

8. J. R. Schwank, M. R. Shaneyfelt, D. M. Fleetwood, J. A. Felix, P. E. Dodd, P. Paillet, and V. F. Cavrois, "Radiation effects in MOS oxides," *IEEE Trans. Nucl. Sci.*, vol. **55**, no. 4, pp 1833–1853, 2008.

9. T. R. Oldham, and F. B. Mclean, "Total ionizing dose effects in MOS oxides and devices," *IEEE Trans. Nucl. Sci.*, vol. **50**, no. 3, pp 483–499, 2003.

10. J. R. Srour, C. J. Marshall and P. W. Marshall, "Review of displacement damage effects in silicon devices," *IEEE Trans. Nucl. Sci.*, vol. **50**, no. 3, pp 653–670, 2003.

Calculations,
Methodical Aspects

The gained results allow to confirm that the IBR-2 experimental beamline №3 may be used as a field for producing medical radioisotopes ^{99m}Tc, ^{99}Mo and ^{131}I. The obtained effective experience and positive results of the experiment can be used for implementing experiments on the production of rather wide range of radioisotopes on the IBR-2 reactor as well.

References

1. Seth. A. Hoedl and W. Derek Updegraff, The Production of Medical Isotopes without Nuclear Reactors or Uranium Enrichment. Science and Global Security, 2015, Volume **23**, pp. 121–153.
2. Isotopes. Properties. Producing. Appliance. Red. V.U. Baranova. M. Phys. Math. Lit., Vol. **2**, 2005, p. 389–412 (in Russian).
3. Gerasimov A.S., Kiselev G.V., Lantsov M.N., Producing of ^{99}Mo in nuclear reactors. Atomic Energy Journal. Vol. **67**, № 1, 1989, p.104–108.
4. Markina M., Stariznyi V., Breger A., Energy distribution of gamma radiation of products of fission of ^{235}U with small time of irradiation. Atomic Energy Journal., 1979, Vol. **46**, № 6, p.411.
5. Verkhogliadov A., et al., Irradiation facility at the IBR-2 reactor for the investigation of material radiation hardness. Nucl. Inst. and Meth.B, 2015, Vol. **343**. – pp. 26–29.
6. E. Shabalin, et al., The spectrum and density of neutron flux in the irradiation beamline №3 of the IBR-2 reactor. Physics of particles and nuclei letters, 2015, Vol. **12**, №2. pp. 336–343.
7. M. Bulavin, S. Kulikov, Current experiments at the irradiation facility of the IBR-2 reactor. Journal of Physics: Conference Series 1021 (2018) 012041, p. 1–4.

Determination of the Number of ^{232}Th Nuclei in the Sample Using Small Solid Angle Method

Haoyu Jiang, Huaiyong Bai, Yi Lu, Zengqi Cui, Jinxiang Chen, Guohui Zhang*

State Key Laboratory of Nuclear Physics and Technology, Institute of Heavy Ion Physics, Peking University, Beijing 100871, China

Yu. M. Gledenov, M. V. Sedysheva

Frank Laboratory of Neutron Physics, Joint Institute for Nuclear Research, Dubna 141980, Russia

G. Khuukhenkhuu

Nuclear Research Centre, National University of Mongolia, Ulaanbaatar, Mongolia

ABSTRACT

The ^{232}Th(n, f) cross-section data from EXFOR library were collected and analyzed, which show that the measurement results using mono-energetic neutron sources are obviously higher than those using white neutron sources. In order to clarify the existing discrepancies, accurate ^{232}Th(n, f) cross-section measurements are being planned. The ^{232}Th(OH)$_4$ foil sample was prepared. A small solid angle device was designed and installed by which the number of ^{232}Th nuclei in the sample was determined.

I. INTRODUCTION

^{232}Th, the most stable isotope of thorium (natural abundance ~100%), is a fissionable nucleus which plays an important role in the Th-U fuel cycle [1,2]. The study of the ^{232}Th (n, f) reaction is important in nuclear engineering applications [3-5]. Besides, measurements of this cross section could enhance our understanding in nuclear physics. For example, the special structure of the ^{232}Th(n, f) cross sections called the "thorium anomaly" effect could be explained by triple-humped barriers of ^{232}Th [6,7].

However, comparing with other fissile nuclei, such as ^{238}U or ^{235}U, existing measurements of ^{232}Th are much fewer for the (n, f) reaction. Besides, there is a systematic difference between the measurement results using mono-energetic neutron sources and those using white neutron sources in the MeV region. The experimental cross sections from 1.5 to 15 MeV taken from EXFOR library are shown in Fig. 1 [8]. Due to the update of experimental techniques and apparatus, only the data after 1970s were collected and analyzed. In order to show the overall trend of the experimental data more clearly, error bars were omitted, and the data points are connected with straight lines.

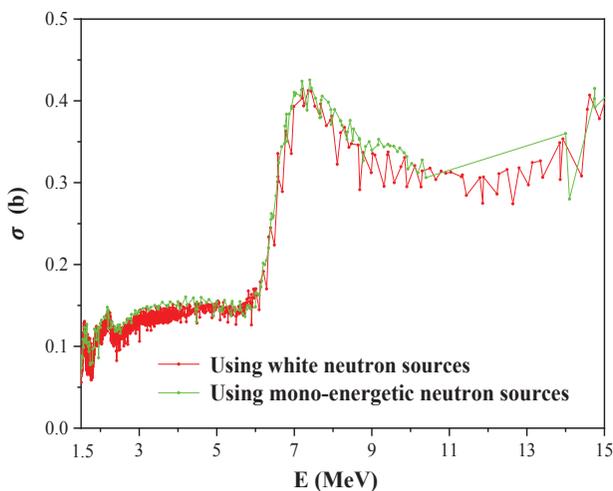* Corresponding author: guohuizhang@pku.edu.cn

Fig. 1 (Color online) Experimental cross sections of the ^{232}Th(n, f) reaction from 1.5 to 15.0 MeV using white neutron sources and mono-energetic neutron sources. The results were taken from EXFOR library (after 1970s).

From Fig. 1, one could see that the measurement results using mono-energetic neutron sources are obviously higher than those using white neutron sources. The results using mono-energetic neutron sources was 5.47% higher than those using white neutron sources on average, and the percentage was up to 8.16% for 2.0 MeV < E_n < 4.0 MeV. So, in order to clarify the existing discrepancies, accurate ^{232}Th(n, f) cross-section measurements are being planned.
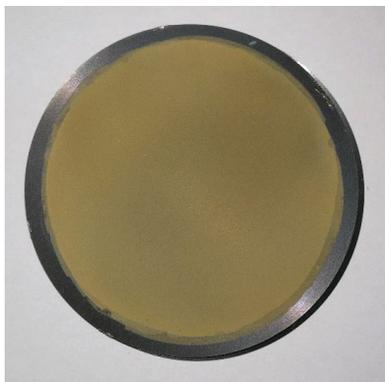
Fig. 2 (Color online) Picture of the ^{232}Th(OH)$_4$ sample.

A ^{232}Th(OH)$_4$ foil sample with tantalum backing was prepared by Joint Institute for Nuclear Research in Dubna, and picture of which is shown in Fig. 2. The diameter of the sample is 44.0 mm. Determination of the number of ^{232}Th nuclei is the indispensable step for ^{232}Th(n, f) cross-section measurements. For the α-radioactive material, α-spectrometry is a common technique of nucleus number determination. The decay chain of ^{232}Th is presented in Fig. 3.
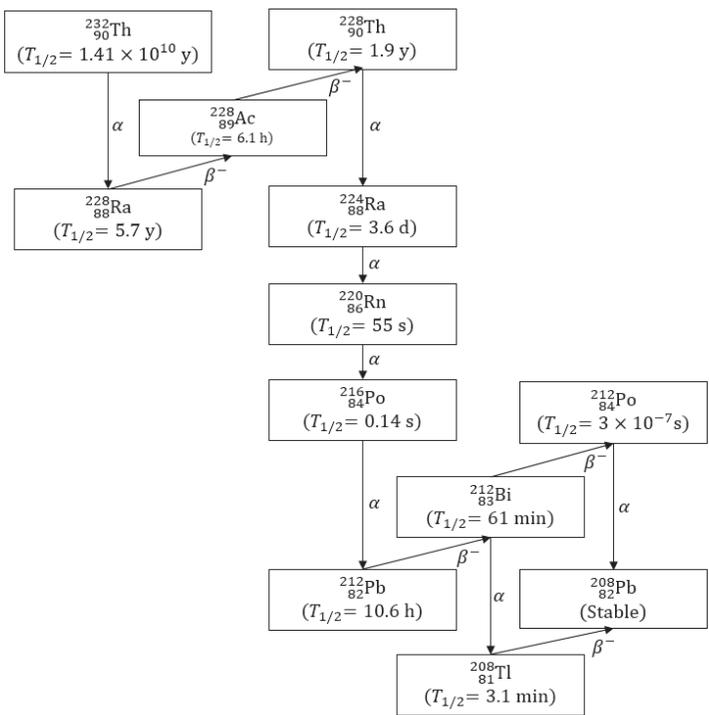
Fig. 3 The decay chain of ^{232}Th.

With regard to α counters, the grid ionization chamber (GIC) has a wide range of applications because of the big detection efficiency (~50%). However, both the limited energy resolution and the peak tailing effect restrict its usage [9]. A typical ^{232}Th α spectrum measured by GIC is shown in Fig. 4. The strong asymmetry and tailing of the peaks can be observed from the spectrum. The big tailing of α peaks from the daughter nuclides of ^{232}Th would introduce significant error when determining the counts of the α peak from ^{232}Th. So, other techniques should be used instead of the GIC method.

III. RESULTS

The measured energy spectra of α particles are shown in Fig. 7, from which, one could notice that the background is quiet weak. However, the tailing of the peaks from the daughter nuclides would increase the total counts of the ^{232}Th peak. An exponential function was used to fit the tailing and then subtracted from the ^{232}Th peak region. The proportion of the fitting counts to the total ^{232}Th peak counts is 4.81%. One fifth of the fitting counts in the region is taken as the uncertainty from the fitting method.
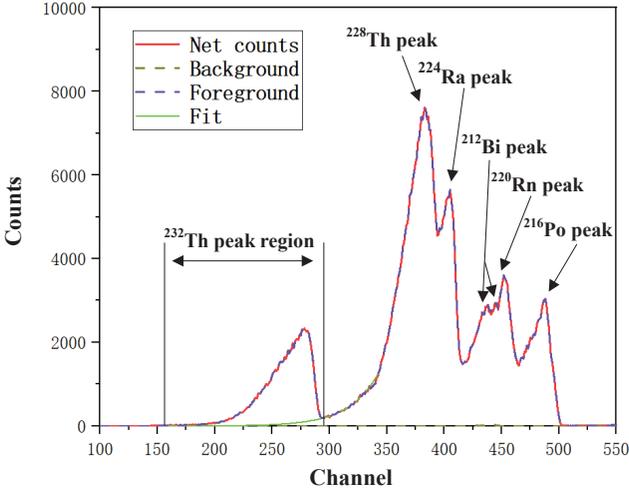
Fig. 7 (Color online) Spectra from measurements.

The number of ^{232}Th nuclei N can be calculated from the following equation:

$$N = \frac{n_{\text{fore}} - n_{\text{fit}} - n_{\text{back}} \times \frac{t_{\text{fore}}}{t_{\text{back}}}}{t_{\text{fore}} \times \varepsilon \times \lambda}, \tag{1}$$

where n_{fore} and n_{back} are foreground counts and background counts in the ^{232}Th peak region. n_{fit} is the fitting counts in the ^{232}Th peak region. t_{fore} and t_{back} are the durations of foreground and background measurements. ε is the detection efficiency of the small solid angle device calculated through Monte Carlo simulation (back-scattering of α particles was taken into account, and the proportion of the back-scattering α particles to the total α particles is 0.4%), and the value of ε is 0.002460 in the present measurement. λ is the α decay constant of ^{232}Th. From equation (1), the calculated the number ^{232}Th of nuclei is 1.86×10^{19}.

Sources of the error for ε are the uncertainties of geometry (0.75%), Monte Carlo

simulation (0.32%), and unevenness of the sample edge (0.30%). Sources of the error for n_{fore} include the uncertainties of ^{232}Th peak region determination (0.19%) and the statistical error (0.35%). Taken from one fifth of the fitting counts, the uncertainty of n_{fit} is 0.96%. The uncertainty of λ is 0.40% [11]. Magnitudes of other sources of errors are so small that they can be ignored. Thus, the total uncertainty of the number of ^{232}Th nuclei is 1.41%.

IV. CONCLUSIONS

In the present work, the ^{232}Th(n, f) cross-section data from EXFOR library were collected and analyzed, and it is found that the measurement results using mono-energetic neutron sources are obviously higher than those using white neutron sources. A ^{232}Th(OH)$_4$ foil sample was prepared for the ^{232}Th(n, f) cross-section measurements. In order to determine the ^{232}Th nucleus number in the sample, a small solid angle device was designed and installed. The experiment was conducted, and the measured the number of ^{232}Th nuclei is $1.86 \times 10^{19}(1 \pm 1.41\%)$.

REFERENCES

[1] J. Meija, T. B. Coplen, M. Berglund, W. A. Brand, P. D. Bièvre, M. Gröning, N. E. Holden, J. Irrgeher, R. D. Loss, T. Walczyk and T. Prohask, Pure Appl. Chem. **88**, 265 (2016).

[2] Wikipedia, Thorium, https://en.wikipedia.org/wiki/Thorium.

[3] International Atomic Energy Agency, "IAEA-TECDOC-1349 Potential of thorium-based fuel cycles to constrain plutonium and to reduce the long-lived waste toxicity", Vienna, April 2003.

[4] International Atomic Energy Agency, "IAEA-TECDOC-1450 Thorium Fuel Cycle – Potential Benefits and Challenges", Vienna, May 2005.

[5] M. Jiang, H. Xu, Z. Dai, Bulletin of the Chinese Academy of Sciences, **27**, 366 (2012).

[6] S. Bjornholm and J. E. Lynn, Rev. Mod. Phys. **52**, 725 (1980).

[7] J. Blons, C. Mazur, D. Paya, M. Ribrag, and H. Weigmann, Nucl. Phys. **A414**, 1 (1984).

[8] Experimental Nuclear Reaction Data (EXFOR), Database Version of 2018-04-11, http://www.nndc.bnl.gov/exfor/exfor.htm.

[9] E. GARCIA-TORAÑO, Appl. Radiat. Isot. **64**, 1273 (2006).

[10] E. García-Toraño, T. Durán Ramiro, C. Burgos and M. Begoñaa Ahedo, Appl. Radiat. Isot. **66**, 881 (2008).

[11] ENDF: Evaluated Nuclear Data File, Database Version of 2018-02-13, https://www-nds.iaea.org/exfor/endf.htm.

Estimation of the Neutron Generation from Gas Puff Z-Pinch on Qiangguang Facility

Liangping Wang, Peitian Cong, Xinjun Zhang, Jinhai Zhang, Mo Li

State Key Laboratory of Intense Pulsed Radiation Simulation and Effect (Northwest Institute of Nuclear Technology), Xi'an, 710024, China

Abstract. Z-pinch using a deuterium gas-puff load has been validated as a plasma neutron source (PNS) on many accelerators such as Saturn, Z, Angara-5 and S-300. The experimental results on these accelerators show that the production of the neutron can be scaled as $Y_n \propto I_m^4$, where Y_n is the yield and I_m is the peak current of the accelerator, no matter what mechanism is eventually determined to be responsible for generating fusion neutrons. The neutron production on Qiangguang generator (1.5 MA, 100 ns) is analytically estimated that approximately 4×10^{10} D-D neutrons would be produced, among which the thermonuclear neutrons are only 7×10^7. The gas puff construction used on Qiangguang is introduced and the optimum line mass of the D_2 gas is given. The results show that the optimum line mass is approximately 50 μg/cm for Qiangguang's driving current. The mass density distribution obtained with the classical ballistic-transport model demonstrates that the gas puff forms a hollow gas shell with the length of 2 cm. For D_2 to produce a gas flow with the line mass 50 μg/cm, the firing time of Qiangguang changes to 250 μs and the absolute pressure of the chamber increases to 4.2 atm.

I. INTRODUCTION

Z-pinches can be used not only as a powerful X-ray radiation[1-3] source, but also a very powerful plasma neutron source (PNS)[4-6], which can be applied to radiation material science, detector calibration, nuclear medicine and illicit material detection. In fact using the deuterium Z-pinch plasmas to generate fusion neutrons is not a new idea. The main purpose of the Z-pinch researches on last century is looking for controlled thermonuclear fusion neutrons however it was soon found the observed neutrons were not produced by thermonuclear fusion but beam-target reaction[7]. In recent years with the rapid development of the gas puff load the Z-pinch plasma has become the most powerful neutron source with the record of 4×10^{13} on Z (15 MA, 100 ns) facility[8]. Velikovich has induced that half of the neutron yield on Z is produced by thermonuclear fusion and the others come from beam-target mechanism, and he also predicted that the neutrons would be all produced by thermonuclear fusion when the current of the accelerator is big than 26 MA[4]. These inspiring results evoke again the researchers' interesting in inertial controlled fusion through Z-pinch and a new concept is proposed as the magnetized liner inertial fusion (MAGLIF)[9,10].

In the present paper, The D-D neutron yield by a D_2 gas puff on Qiangguang is predicted through analytical estimation as well as the scaling relationship given by neutron yields on other generators; this is done in Section II. The construction of the gas puff load is shown in Section III, and in this section the optimum line mass of the gas puff is also obtained by analyzed the Krypton pinch experimental results performed before. In Section IV the density profile of the gas flow is obtained by the classical Ballistic-Transport model and Section V will give a brief summary.

II. ESTIMATION OF THE D-D NEUTRONS YIELD ON QIANGGUANG GENERATOR

Qiangguang[11] is a facility that includes a linear transformer driver (LTD), an intermediate storage, a pulse compression line, a pulse output line and a vacuum chamber. The facility will send a pulse with 2 MV to the vacuum chamber and the typical load current has a peak of 1.5 MA with the rise time of about 100~120 ns.

A. Estimates of the thermal D-D neutron yield

The thermonuclear neutron yield Y from stagnated Z-pinch plasma is estimated as[4]

$$Y_n = \frac{1}{4} n_i^2 \langle \sigma \upsilon \rangle \pi R^2 l \tau , \tag{1}$$

where $n_i = \mu / (\pi R^2 m_D)$ is the deuterium ion number density in the pinch plasma (μ is the line mass of the load, m_D is the mass of the deuterium ion), R and l are the compressed pinch radius and length, respectively, $\langle \sigma \upsilon \rangle$ is the average ion-temperature-dependent rate of the DD fusion reaction, τ is the confinement time of the dense pinch, and the factor 1/4 is the product of the factor 1/2, introduced because the colliding ions are identical, and the branching ration 1/2 between D+D→He³+n and D+D→T+p, of which only the former produces a neutron.

First we estimate the parameters of the stagnated pinch plasma. The outer diameter of the gas puff used on Qiangguang is 20 mm, and therefore the final radius of the stagnated column R=1 mm given the 10-fold radial compression of the pinch. For the line mass of the gas puff load μ=50 μg/cm the ion number density for the stagnated plasma column $n_i \approx 5 \times 10^{20}$ cm⁻³. The energy imparted to the plasma during the implosion phase can be valued as

$$E = \frac{1}{2} \int I^2 dL \cong \alpha I_m^2 (MA) \ln \frac{R_0}{R} \text{kJ/cm} . \tag{2}$$

Here, R_0 is the initial outer radius of the gas puff, α is the dimensionless factor accounting for the current pulse shape and for Qiangguang's current the typical value of α is 0.7,[12] and I_m is the peak current. Substituting into (2) the compression ratio we find $E \approx 4\text{kJ/cm}$. Neglecting the radiation losses from deuterium, the temperature of the plasma from the energy balance can be expressed as

$$\frac{3}{2} n_i (T_i + T_e) \times \pi R^2 = E \tag{3}$$

Taking R=1 mm, $n_i \approx 4 \times 10^{20}$ cm⁻³, and $E \approx 4\text{kJ/cm}$ in (3) we get $(T + T_e)$ = 1.3 keV. The ion-electron temperature equilibration time for the deuterium is $\tau_{ei} \approx 2 \times 10^{12} T_e^{3/2} (\text{keV}) / n_i$ and for the density $n_i \approx 4 \times 10^{20}$ it is 3 ns for T_e= 0.7 keV. The confinement time is estimated as $\tau = R/V$ where V is the implosion velocity, for μ= 50 μg/cm and $E \approx 4\text{kJ/cm}$ the velocity is ~4 × 10⁷cm/s. Given R=1 mm and $V = 4 \times 10^7$cm/s we get τ ~3 ns, which means the ion-electron equilibration time is compared to the confinement time and the temperature equilibration nearly arrives between electrons and ions, so the temperature of the ion on Qiangguang's experiments is below 1 keV.

When the temperature of the deuterium ion is 1 keV the total D-D fusion reaction $\langle \sigma \upsilon \rangle$ averaged over the Maxwellian distribution of ions is $7 \times 10^{-23} \mathrm{cm}^3/\mathrm{s}$. Substituting these values of the parameters into the formula (1) we can obtain an estimation for the thermal neutron yield on Qiangguang is 7×10^7. According to (1), the neutron yield scales as $n_i^2 \propto \mu^2$. From the Z-pinch implosion physics the line mass of the load scales as current squared $\mu \propto I_m^2$, which implies the yield from the thermonuclear $Y_n \propto I_m^4$.

B. Estimates for beam-target neutron yield

Now consider the alternative mechanism of fusion neutron production in Z-pinch plasma, the beam-target mechanism, which is mainly responsible for neutrons produced by the lower current driving Z-pinch plasma below 7 MA according to Velikovich's calculation[4].

The distance traveled by an average beam ion with energy E_b before it produces a neutron in the fusion reaction with a target ion is

$$l_{bf} = \frac{1}{\sigma(E_b) n_i} . \tag{4}$$

For the ions with the energy $E_b = 100$ keV we can obtain the length $l_{bf} = 1.5$ km with the parameters $n_i \approx 4 \times 10^{20}$ and $\sigma(E_b) = 1.7 \times 10^{-26} \mathrm{cm}^2$ [13], while the maximum distance that a beam ion can travel inside the pinch plasma in the axial direction is the length of the pinch l. So, to produce one neutron l_{bf}/l fast ions is needed in the deuterium beam. For the load with $l = 2$ cm the number of fast ions is 75 thousand.

Because most of the neutrons are produced by the beams during the time τ while the pinch remains confined near the axis, we can express the beam current needed to produce the neutron yield Y_n as

$$I_b = Y_n \frac{l_{bf}}{l} \frac{e}{\tau} = \frac{\pi R^2 m_D e Y_n}{\sigma(E_b) \mu l \tau} . \tag{5}$$

Using this formula we can estimate the upper limit of the neutron yield supposing that all the load current is carried by the accelerated ions. For Qiangguang's current 1.5 MA the limiting yield is 5×10^{11}.

It is obvious that not all the load current flow through the accelerated ions. The experiments on S-300 facility[14] show that the D-D neutron yield is about 6×10^{10} under the driving current 1.6 MA, which means that the beam current is 180 kA by formula (5) with the parameters on S-300 ($\mu = 20 \, \mu g/cm$, $R = 1$ mm, $l = 2$ cm, and $E_b = 150$ keV), and the beam current occupies 11% of the total load current. Assuming that the percent is almost the same for Qiangguang and S-300, we estimate that the D-D neutron yield produced by the beam-target mechanism is about 5×10^{10} for Qiangguang facility.

The energy coupled to the accelerated ions is expressed as

$$W_b = \frac{\pi m_D E_b Y_n R^2}{\sigma(E_b) \mu l} . \tag{6}$$

For the parameters of the experiment on S-300, we obtain $W_b = 140$ J, while the magnetic energy coupled to the Z-pinch plasma during the implosion phase is 10 kJ, this means an

efficiency of 1.4% for the magnetic energy converting into fast ions. Given the same efficiency for Qiangguang we can also obtain an estimate of neutron yield for Qiangguang. Substituting $\mu = 50\,\mu g/cm$, $R=1$ mm, $l = 2$ cm, and $E_b = 150$ keV into the formula (6) we obtain the neutron yield is 4×10^{10}. From formula (6) it can be seen that $Y_n \propto \mu W_b$, which implies that the yield scales as $Y_n \propto I_m^4$ with $\mu \propto I_m^2$ and $W_b \propto I_m^2$.

Formulas (5) and (6) give different neutron yield estimations, 4×10^{10} and 9×10^{10} respectively, and it is difficult to say which value is more accurate by now. For a conservative estimate we select 4×10^{10} as the neutron yield from the beam-target mechanism on Qiangguang.

III. THE CONSTRUCTION AND THE OPTIMUM LINE MASS OF THE GAS PUFF

A kind of annular-shell gas puff adopted on Qiangguang[15] is shown in Fig.3. The throat has a 0.25 mm-width in radial direction and its area 18 mm^2. The outer and the inner radius of the gas exit are 9 mm and 7.5 mm respectively.
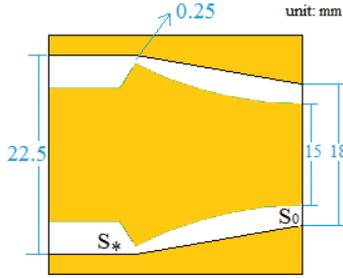
Fig.1. The sketch of the gas puff on Qiangguang (unit: mm).

Based on the aerodynamic analysis we can know that the line mass of the gas-puff is directly proportional to the product of the gas pressure P in the chamber, the atomic weight A, and the area of the throat S_*. The relation is expressed as[16]

$$\mu = kPAS_* . \tag{7}$$

Here k is the scaling factor.

From the snow-plow model the implosion time t_{imp} of the gas puff is expressed as[17]

$$t_{imp} = C_t \frac{\mu^{1/2} R_0}{I_m}, \tag{8}$$

Where R_0 is the initial radius, I_m is the peak current, C_t is a constant related to the shape of the current waveform. The line mass deduced from formula (8) is expressed as

$$\mu = C_m \left[\frac{t_{imp}(us) I_m(MA)}{\langle R \rangle (cm)} \right]^2 \mu g/cm , \tag{9}$$

Where <R> is the average radius of the shell[17]

$$\langle R\rangle = \int n(r)r^2 dr \bigg/ \int n(r)r\,dr = \frac{2R_O}{3}\frac{1-\left(R_I/R_O\right)^3}{1-\left(R_I/R_O\right)^2}, \tag{10}$$

R_I and R_O are the inner and the outer radius of the gas puff. For $R_I = 7.5$ mm and $R_O = 9$ mm the average radius $<R>$ is 8.3 mm by formula (10). C_m is a constant which is related to the shape of the current and the width of the gas shell $\Delta = R_O - R_I$. Mosher given the expression of the constant C_m in reference [17] as the following formula

$$C_m = 10^3\left[12+1.3\frac{\Delta}{R_O}+10\left(\frac{t_c}{t_{imp}}\right)+8\left(\frac{t_c}{t_{imp}}\right)^3\right]^{-2}, \tag{11}$$

where t_c is the rising time of the current. For most of the gas-puff Z-pinch experiments on Qianguang the ratios t_c/t_{imp} are 0.8~0.9, and the corresponding values of C_m are 1.66 ~ 1.35.

The optimum line mass of the gas puff can be deduced from the krypton experiments that had been performed on Qiangguang.

Table 1. Results of 15 shots of Kr experiments.

Shot	load current (MA)	t_c (ns)	t_{imp} (ns)	line mass (μg/cm)
03081	1.4	90	100	36.5
03082	1.4	88	101	39.6
03083	1.5	97	113	58.5
03084	1.5	95	110	54.8
03086	1.5	92	101	41.7
03087	1.4	100	120	60.6
03089	1.4	96	106	40.5
03091	1.4	110	136	81.9
03092	1.5	94	110	55.9
03093	1.4	88	101	39.6
03094	1.5	94	110	55.9
03095	1.4	90	105	44.1
03096	1.5	92	110	58.1
03098	1.5	97	115	62.5
03099	1.5	97	124	82.5

The line-mass data calculated by the formula (9) for fifteen shots of Kr Z-pinch are listed in the Table 1, as well as the load current, the rising time of the current and the implosion time. We take the average line mass of the fifteen shots as the optimum line mass which is 50 μg/cm.

IV. THE PROFILES OF THE GAS DENSITY

The density profiles can be determined by the classic ballistic-transport model (BFM)[18]. The BFM treats the gas flow as emerging from a thin annulus with a Gaussian distribution in angle about the nozzle tilt angle, and this distribution is the propagated forward ballistically along the axial direction of the nozzle. The BTM is illustrated as the following formula[18]

$$n(r,z) = \frac{N}{\pi \delta^2} \exp\left[-\frac{r^2 + (R_C - z\theta_t)^2}{\delta^2}\right] I_0 \left[\frac{2r(R_C - z\theta_t)}{\delta^2}\right] \qquad (12)$$

where $\delta(z) = (z + z_0)\theta_d$, z is the distance from the nozzle, z_0 is the gas-source offset from the nozzle plane, θ_d is the divergence angle of gas escaping from the nozzle, θ_t is the nozzle tilt angle, N is the line density, R_C is the nozzle radius and I_0 is the Bessel function. The parameters θ_t and R_C can be determined from the nozzle geometry while θ_d and z_0 are chosen to simultaneously provide the best fit to the measured density profile. For Qiangguang's gas puff the parameters are set as $\theta_d \approx 11°$, $\theta_t \approx 0.17$rad, $z_0 = 5$ mm, $R_C = 8.3$ mm, and $N = 4 \times 10^{17} / \text{cm}$, respectively.

The calculated density contour lines for axis distance z in the range from 0 to 4 cm are shown in Fig. 2. The gas density in the main district is $10^{16} \sim 10^{17}/\text{cm}^3$, which two orders of magnitude lower than that of the gas at normal pressure and room temperature. Gas flowing from the nozzle forms a hollow shell within the length 2 cm and will assembles on the axis to form a solid column when the length is beyond 2 cm, so the anode of the gas puff should be assembled on the position z = 2 cm.
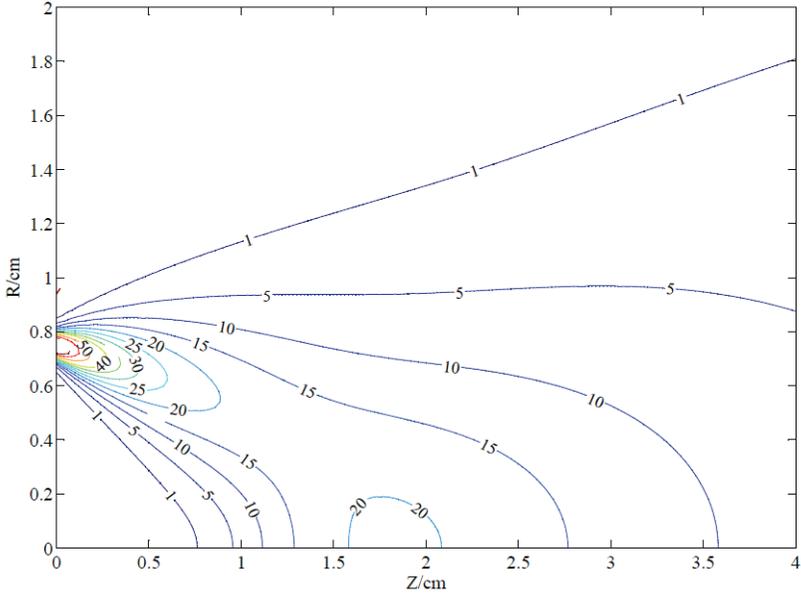
Fig. 2. The contour line of the gas density (the unit for the number density is 10^{16} cm^{-3}).

As mentioned above, the optimum line mass 50 μg/cm is obtained from the data of the Kr Z-pinch experiments, where the gas pressure of the chamber is 2.5 atm (absolute pressure). This means by the formula (7) that the chamber pressure is nearly 50 atm in the D$_2$

experiments if other conditions are the same while the mass of the krypton atomic is nearly 20 times that of the D_2 molecule. Obviously, it is too difficult to keep the chamber from gas leakage in such a high pressure. In fact the line mass in the gas puff z-pinch experiments can be adjusted by changing the firing time of the generator. For the Kr experiments on Qiangguang the generator is fired 60 μs after the breakdown signal of the pin located in the anode of the gas puff, while the krypton gas flow from the nozzle achieves the quasi steady state after ~250 μs when the line mass is 600 μg/cm or so[19]. The line mass for D_2 will arrive 50 μg/cm when the delay time is adjusted to 250μs and the chamber pressure is 4.2 atm.

V. SUMMARY

In conclusion, we have estimated the D-D neutron yield on Qiangguang generator. Nearly 4×10^{10} D-D neutrons will be produced from the beam-target mechanism, while the thermonuclear neutrons are only 7×10^{7}. The means the percent of the thermonuclear neutron is less than 1% of the total neutron yield. The optimum lines mass is 50 μg/cm analyzed from the krypton experimental data on Qiangguang and the corresponding density profile is illustrated by the classical ballistic- transport model. The density profile shows that a hollow gas shell is formed whose length is not beyond 2 cm. This result may imply that the interval between the nozzle and the anode net should be not beyond 2cm. For D_2 to produce a gas flow with the line mass 50 μg/cm the firing time of Qiangguang is needed to adjust to 250 μs and the absolute pressure of the chamber is increased to 4.2 atm.

References

1. C.A. Coverdale, B. Jones, D.J. Ampleford, J. Chittenden, C. Jennings, J.W. Thornhill, J.P. Apruzese, R.W. Clark, K.G. Whitney, A. Dasgupta, J. Davis, J. Guiliani, P.D. Le Pell, C. Deeney, D.B. Sinars, M.E. Cuneo. High Energy Density Physics, **6**(1), 143–152 (2010).
2. C. Deeney, M.R. Douglas, R.B. Spielman, T.J. Nash, D.L. Peterson, P. L' Eplattenier, G.A. Chandler, J.F. Seamen, K.W. Struve. Phys. Rev. Lett. **81**(22), 4883–4886 (1998).
3. R.B. Spielman, C. Deeney, G.A. Chandler, M.R. Douglas, D.L. Fehl, M.K. Matzen, D.H. McDaniel, T.J. Nash, J.L. Porter, T.W.L. Sanford, J.F. Seamen, W.A. Stygar, K.W. Struve, S.P. Breeze, J.S. McGurn, J.A. Torres, D.M. Zagar, T.L. Gilliland, D.O. Jobe, J.L. Mckenney, R.C. Mock, M. Vargas, and T. Wagoner . Physics of Plasmas, **5**(5), 2105–2111 (1998).
4. A.L. Velikovich, R.W. Clark, J. Davis, Y.K. Chong, C. Deeney, C.A. Coverdale, C.L. Ruiz,   G.W. Cooper, A.J. Nelson, J. Franklin, and L.I. Rudakov. Physics of Plasmas, **14**(2), 022701 (2007).
5. V.V. Vikhrev and V.D. Korolev. Plasma Physics Reports, **33**(5), 357–380 (2007).

6. C.A. Coverdale, C. Deeney, A.L. Velikovich, J. Davis, R.W. Clark, Y.K. Chong, J. Chittenden, S. Chantrenne, C.L. Ruiz, G.W. Cooper, A.J. Nelson, J. Franklin, P.D. Le Pell, J.P. Apruzese, J. Levine, and J. Banister, Physics of Plasmas, **14**(5), 056309 (2007).

7. O.A. Anderson, W.R. Baker, S.A. Colgate, H.P. Furth, J. Ise, Jr., R.V. Pyle, and R.E. Wright, Phys. Rev. **109**, 612 (1958).

8. C.A. Coverdale, C. Deeney, A.L. Velikovich, R.W. Clark, Y.K. Chong, J. Davis, J. Chittenden, C.L. Ruiz, G.W. Cooper, A.J. Nelson, J.P. Apruzese, J. Levine, J. Banister, and N. Qi. Physics of Plasmas, **14**(2)**,** 022706 (2007).

9. A.B. Sefkow, S.A. Slutz, J.M. Koning, M.M. Marinak, K.J. Peterson, D.B. Sinars, and R.A. Vesey. Physics of Plasmas, **21**(7), 072711 (2014).

10. S.A. Slutz, W.A. Stygar, M.R. Gomez, K.J. Peterson, A.B. Sefkow, D.B. Sinars, R.A. Vesey,   E.M. Campbell, and R. Betti. Physics of Plasmas, **23**(2)**,** 022702 (2016).

11. Wang Liangping, Guo Ning, Han Juan, Wu Jian, Li Mo, Wei Fuli, and Qiuaici. IEEE Transactions on Plasma Science, **40**(2), 511–518 (2012).

12. Wang Liangping, Li Mo, Han Juanjuan, Wu Jian, Guo Ning, and Qiu Aici. Physics of Plasmas, **21**(6), 062706 (2014).

13. J.L. Giuliani. IEEE Transactions on Plasma Science, **43**(8), 2385–2453 (2015).

14. D. Klir, J. Kravarik, P. Kubes, K. Rezac, J. Cikhardt, E .Litseva1, T. Hyhlik, S.S. Ananev, Y.L. Bakshaev, V. A. Bryzgunov, A.S. Chernenko, Y.G. Kalinin, E.D. Kazakov, V.D. Korolev, G.I. Ustroev, A.A. Zelenin, L. Juha, J. Krasa, A. Velyhan, L. Vysin, J. Sonsky, and I.V. Volobuev. Plasma Physics and Controlled Fusion, **52**(6), 065013 (2010).

15. Wang Liangping, Qiu Aici, Kuai Bin, Cong Peitian, Guo Ning. High Power Laser and Particle Beams, **17**(2), 295–298 (2005).

16. Zhou Guangjun and Yan Zongyi. Fluid Dynamics [M]. Beijing: Higher Education Press, 2003.

17. D. Mosher, R.J. Commisso, and B.V. Webel. 12th IEEE international pulsed power conference. 1078–1081 (1999).

18. J.W. Schumer, D. Mosher, B. Moosman, B.V. Weber, R.J. Commisso, Niansheng Qi, J. Schein, and M. Krishnan, IEEE Transactions on Plasma Science, **30**(2), 488–497 (2002).

19. Zhang Xinjun. A Study of measuring line mass density of Gas-Puff Z-Pinch Load by interferometry (Master Thesis). Northwest Institute of Nuclear Technology, Xi'an, Shannxi, China, (2003).

The Influence of Power Chip's Neutron Radiation Effect on Nanometer SRAM's Data Status

J.L. Li, S.C. Yang, C. Qi, Y. Liu, X.M. Jin, C.H. Wang

State Key Laboratory of Intense Pulsed Radiation Simulation and Effect, Northwest Institute of Nuclear Technology, P. O. Box 69-10, 710024, Xi'an, China

Abstract

This paper compares the differences of neutron radiation effect when SRAM is powered by power chip or DC power. The experiment result shows that before the neutron fluence reaches up to 9.2×10^{12} cm^{-2}, the main factor that causing SRAM upset is neutron induced single event effect whether SRAMs are powered by power chip or DC power. When the total neutron fluence is beyond 9.2×10^{12} cm^{-2}, the power chip can't function well and output regularly and then the SRAM which is powered by power chip will upset drastically due to the breakdown of supply voltage. This is because of the displacement damage of power chip caused by neutrons. However, for SRAM which is powered by DC power, even though the total neutron fluence is beyond 9.2×10^{12} cm^{-2}, neutron induced single event effect is still the main reason that causing it upset.

Keywords: Displacement damage; neutron induced single event effect; power chip; DC power supply; SRAM

1. Introduction

With the development of semiconductor technology, the semiconductor device has higher integration level, better performance and lower power dissipation. SRAM (SRAM: Static Random Access Memory) is widely used in electronic systems as cache due to its fast access speed. It can be used in digital processing device, information processing device and automatic control equipment. SRAM lost its all data when the power breakdown as SRAM is volatile memory. Hence, to investigate the influence of power chip's neutron radiation effect on SRAM's data status is of great important. When SRAM work in neutron radiation environment, its function will be influenced by the neutron radiation effect[1-3].

To investigate the difference of neutron radiation effect when the SRAM powered by DC power or power chip, we divided SRAMs into two groups that one group is powered by power chip and the other is powered by DC power. After neutron irradiation experiment, we obtained the failure mode of two groups of SRAMs that corresponds to two different neutron radiation effects. The difference and the mechanism of two neutron radiation effects are analyzed.

2. Experimental details

To investigate the neutron radiation effect of two groups of SRAMs, we carried out experiment using Xi'an pulse reactor (XAPR). During experiment, the operated power of XAPR is 500 kW with the neutron flux is 2.67×10^{10} cm^{-2}·s^{-1} and the neutron/gamma ray ratio (n/γ ratio) is 7.7×10^{9} cm^{-2}·rad(Si)$^{-1}$.

The device under test is the 130 nm SRAM designed by ISSI whose type is IS62WV1288DBLL. And its nominal working voltage is from 2.3 V to 3.6 V. Fig.1 shows the functional schematic of IS62WV1288DBLL. A0-A16 are address pins and I/O 0-I/O 7 are data pins. CS1 and CS2 are used to input chip selected signal. OE is used to control output function and WE is used to control read and write functions. Its total capacity is 1 Mbits with 128 K (128×1024) addresses and each addresses has 8 bits.
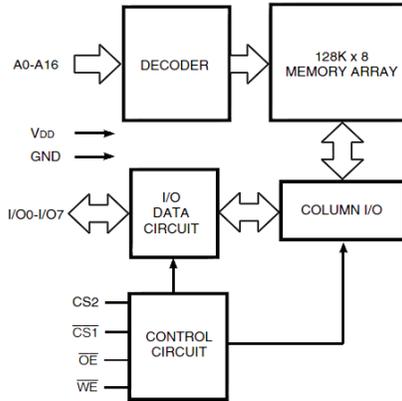

Fig. 1. Functional schematic of IS62WV1288DBLL.

The power chip we choose is designed by TI whose type is LM2576T-3.3. It is a step down power supply management which is monolithic integrated. The input voltage is from 6 V to 40 V, and the output is constant voltage of 3.3 V. It can provide the drive current up to 3A. Fig. 2 shows the functional schematic of LM2576T-3.3. It is integrated with frequency compensation and fixed frequency generator and the switching frequency is 52 kHz.
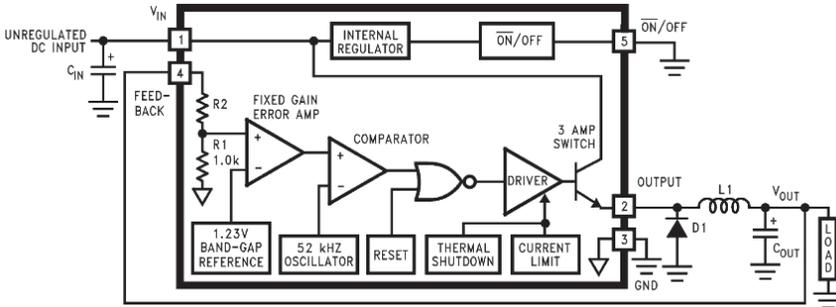
Fig. 2. Functional schematic of LM2576T-3.3.

SRAMs were weld on the irradiation board as its storage data was measured through the connection of test board and irradiation board by flat cable. The irradiation board was designed including four SRAMs (1#, 2#, 3#, 4#) and one power chip which is shown in Fig. 3. SRAMs were divided into two

groups, 1# and 3# were powered with 3.3 V input voltage by power chip and the power chip was powered with 7 V input voltage by DC power. 2# and 4# were powered by DC power through long cable about 20 meters.

During experiment, the orientation of the incident neutrons was vertical with respect to the front surface of the tested SRAMs. All the SRAMs were under static testing. Loading up a uniform byte pattern 55 (hex) before irradiation and then scanning each of them every five seconds for upset errors in sequential logic address during neutron irradiation. For a single scan of each SRAM device, the logic states of all the memory cells in the tested SRAM device were monitored within three seconds for a single scan. The test system compared the data of two read-back cycle dynamically to get the upset status of SRAM.

1#	2#
3#	4#
Power Supply by Power Chip	Power Supply by DC Power
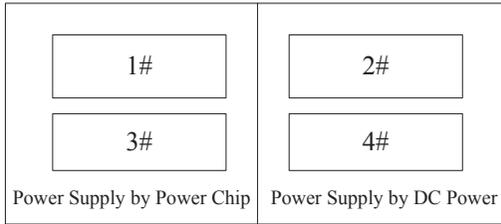
Fig. 3. Schematic diagram of irradiation board.

3. Experimental results and discussion

3.1 The power chip's neutron radiation effect

During neutron radiation experiment, we have monitored the change of power chip's output voiltage. Fig. 4 shows the variation of power chip's output voltage with neutron fluence. With the accumulation of neutron fluence, the output voltage decreased steadily. The output voltage changed from 3.3 V to 3.2 V as the neutron fluence changed from 0 cm^{-2} to 9.2×10^{12} cm^{-2} and the failing range is about 3%. However, when the neutron fluence is beyond 9.2×10^{12} cm^{-2}, the output voltage decreased dramatically. And the output voltage is 0.1 V until the neutron fulence is up to 1.0×10^{13} cm^{-2}. From Fig. 4 we can conclude that there is a threshold of neutron fluence making the power chip fail to work. And the threshold is about 9.2×10^{12} cm^{-2}.

The displacement damage effect was the main reason that causing the power chip failed to work [4]. It is caused by non-ionizing energy deposition which can be called as displacement energy deposition. A large number of displaced atoms are generated in semiconductor material through displacement energy deposited by neutrons. And then results in a large number of defects of all kinds. The degradation of semiconductor device's performance is relative to the number and the types of defects. And the displacement damage effect is permanent. Hence, if the neutron fluence of power chip is up to 9.2×10^{12} cm^{-2}, it can't work normal again.
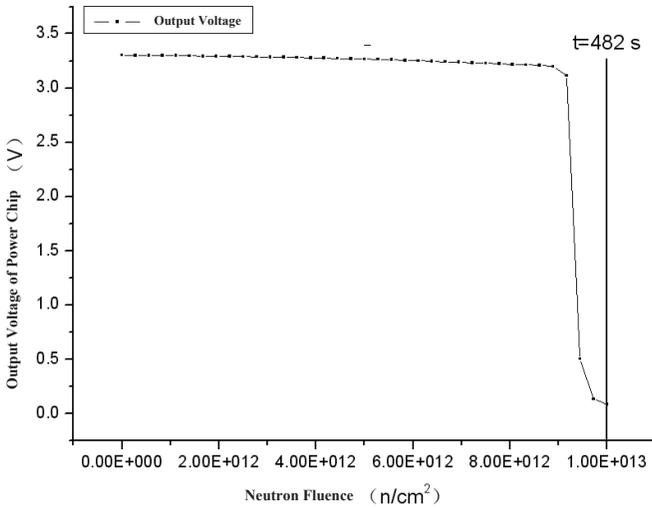
Fig. 4. The variation of power chip's output voltage with neutron fluence.

### 3.2 The neutron radiation effect of SRAM powered by different power supply

As mentioned before, we divided the SRAM into two groups, one group (1# and 3 # SRAM) were powered by power chip and the other group (2# and 4# SRAM) were powered by DC power as shown in Fig. 3. We test the upset number of SRAM during neutron radiation and the test curve of SRAM's upset number over time (neutron fluence) is shown in Fig. 5. Fig. 5(1) gives the whole process of reactor's operation including power increasing, power decreasing and steady state as Fig. 5(2) just gives the steady state of reactor. From Fig. 5(1) we can see that before the neutron fluence reach to 9.2×10^{12} cm^{-2}, the upset number of all the SRAMs increase linearly with time. When the neutron fluence is beyond 9.2×10^{12} cm^{-2}, the upset numbers of 1# and 3# SRAM which is powered by power chip increase drastically to about 0.5 Mbits. However, the tendency of upset numbers' variation of 2# and 4# SRAM which is powered by DC power does not change.

As 1# and 3# SRAM's maximum upset number is about 0.5 Mbits, it is exactly half of the capacity of IS62WV1288DBLL. Combined with the output voltage of power chip, we can draw the conclusion that the vast upset number was caused by the breakdown of power chip when the neutron fluence is beyond 9.2×10^{12} cm^{-2}, which making the memory cell of SRAM lost its stored information. And during the test process, the data of SRAM's memory cell is random hence the total upset number is half of the total capacity. Therefore, the failure of 1# and 3# SRAM when the neutron fluence is beyond 9.2×10^{12} cm^{-2} is mainly because the displacement damage effect of power chip.

It is shown in Fig. 5(2) that before the neutron fluence reaches to 9.2×10^{12} cm^{-2}. The slope of the upset number verse time increases with the increasing of reactor's power. And when the reactor operated in steady state, the slope does not change again. The upset cross section of SRAMs in
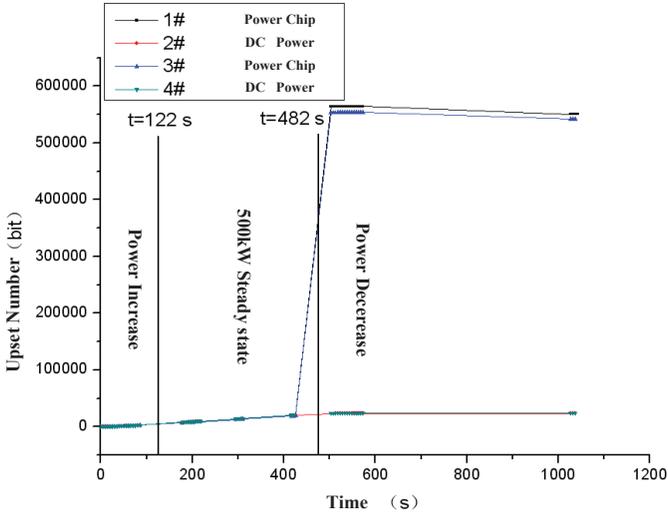
(1)
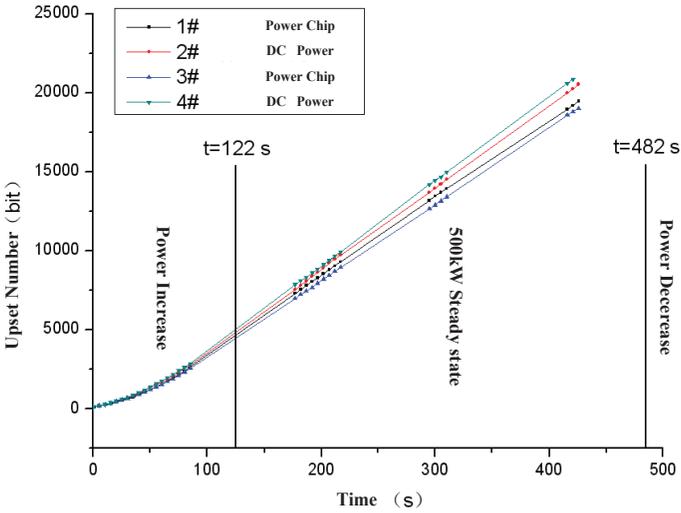
(2)

Fig. 5. The test curve of SRAM's upset number over time (neutron fluence). (1) The whole process of reactor's operation. (2) Operation of reactor's steady state.

reactor's steady state is equal to the slope of zero-crossing linear fitting of N_{upset}/N_{total} and φ which can be calculated by the formula (1), where N_{total} is memory capacity of the SRAM device. φ is total neutron fluence, and N_{upset} is total upset numbers of SRAM.

$$\sigma = \frac{N_{upset}}{N_{total} \times \varphi}$$
(1)

Table 1 shows the upset cross sections of SRAM with different power supply when reactor operates in steady state. The upset cross sections of four SRAMs are very close. The maximum upset cross section and the minimum upset cross section have discrepancy about 9%. We can also see that 2# and 4# SRAM's upset cross section are bigger than 1# and 3# SRAM's upset cross section. That is maybe due to the environment noise feeding in long cable that is used to power 2# and 4# SRAM. As 1# and 3# SRAM are powered by power chip, the output voltage is relatively stable because the input voltage of power chip is ranging from 6 V to 40 V.

Table 1 Upset cross sections of SRAM with different power supply

Power supply mode	Serial Number of SRAM	Upset Cross Section $(cm^{-2} \cdot s^{-1})$	Upset Number (bits)
Power chip	1#	1.74×10^{-15}	19182
	3#	1.73×10^{-15}	18811
DC power	2#	1.86×10^{-15}	20253
	4#	1.90×10^{-15}	20849

From Fig. 5 we can see that before the neutron fluence reaches to 9.2×10^{12} cm^{-2} when the power chip still can function well, the upset numbers of all the SRAMs increase with time linearly. Therefore, during this time the upset of all the SRAMs are caused by the neutron induced single event effect. The neutron induced single event effect is caused by ionizing energy deposition which is due to the interactions of neutrons with matter and then produce secondary charged particles which can cause atomic ionization during transport[5-6]. The ionizing energy deposition changes the concentration of carriers and the charge states of defects but it is short time and repairable.

Hence, we can see that before the neutron fluence reaches to the failure threshold of power chip, the upset of all the SRAMs is caused by neutron induced single event upset effect. When the neutron reaches to threshold, the power chip can't function well due to displacement damage effect and SRAM will upset drastically. However, if the SRAM is powered by DC power, the upset of SRAM is caused by the neutron induced single event upset as the upset number increases with time linearly.

4. Conclusion

From the experiment results, we can see that when a system consisting of a power chip and a SRAM chip irradiated by the neutron of the reactor, the power chip's output voltage will decrease and can't function well when the neutron fluence reaches up to 9.2×10^{12} cm^{-2}. And then the SRAM devices

which is powered by the power chip lost its all data. Hence, the displacement damage effect of power chip when the neutron fluence of reactor reaches the failure threshold caused the loss of SRAM's data as the upset number have a spurt growth. When the SRAM was powered by the DC power, the main reason caused SRAM upset is neutron induced single event effect, the upset number caused by this factor is growing linearly with time. Hence, the power supply has an important impact on the radiation effect electronic system.

References

1. J. M. Armani, G. Simon, and P. Poirot, "Low-energy neutron sensitivity of recent generation SRAMs," *IEEE Trans. Nucl. Sci.*, vol. **51**, no. 5, pp. 2811–2816, 2004.
2. J. R. Srour, "A Framework for Understanding Displacement Damage Mechanisms in Irradiated Silicon Devices", *IEEE Trans. Nucl. Sci.,* vol. **53**, no. 6, pp. 3610–3620, Dec. 2006
3. E. Ibe, H. Taniguchi, Y. Yahagi, K. Shimbo, and T. Toba, "Impact of Scaling on Neutron-Induced Soft Error in SRAMs From a 250 nm to a 22 nm Design Rule," *IEEE Trans. Electron Devices*, vol. **57**, pp. 1527–1538, Jul. 2010.
4. T. Borel, F. Roig, et al, "A typical Effect of Displacement Damage on LM124 Bipolar Integrated Circuits," *IEEE Trans. Nucl. Sci.,* vol. **65**, no. 1, pp. 71–77, Jan. 2018
5. S. Wen, R. Wong, M. Romain, and N. Tam, "Thermal neutron soft error rate for SRAM in the 90-45 nm technology range," in *Proc. IEEE Int. Reliab. Phys. Symp.*, pp. 1036–1039, May. 2010.
6. Weulersse, N. Guibbaud, A. Beltrando, et al, "Preliminary Guidelines and Predictions for 14-MeV Neutron SEE Testing," *IEEE Trans. Nucl. Sci.*, vol. **64**, pp. 2268–2275, Aug. 2017.

Transient Ionizing Dose Effect on Neutron Irradiated SRAMs

Y. Liu[a,b], C.H. He [a*], W. Chen [b], G.Z. Wang [b], R.B. Li [b], J.L. Li [b], S.C. Yang [b]

[a] *School of Nuclear Science and Technology, Xi'an Jiaotong University, 710049, Xi'an, China;*
[b] *State Key Laboratory of Intense Pulsed Irradiation Simulation and Effect, Northwest Institute of Nuclear Technology, P.O.Box 69-10, 710024, Xi'an, China)*

Abstract:

Two feature-sized static random access memories (SRAM) are irradiated by different level 1 MeV equivalent reactor neutrons, and are performed transient ionizing dose effect study subsequently. The latch up and data upset threshold dose rate of SRAMs are obtained by experimental research, respectively. The relationship between threshold dose rate and neutron irradiation fluence are gained; Transient ionizing currents in displacement damaged PN junction are studied using MEDICI toolkit. Results indicate the neutron irradiation could enhance the transient ionizing latch up and data upset threshold dose rate value, neutron induced gain reduction on parasitical transistors and carrier lifetime reduction are the main reason.

Keywords: Transient radiation effect; neutron; latch up; data upset; SRAM

1. Introduction

As semiconductor devices become more integrated, more and more CMOS integrated circuits are used in various electronic systems to achieve more advanced performance. Static random access memory (SRAM) has been the most commonly used storage device for microprocessors and many electronic systems due to its low power consumption. Transient ionizing dose effects on electronics is one of the most serious radiation effects on electronic devices, which can generate photocurrent inside the CMOS device in a very short time, leading to data upset, functional failure, or even burn out[1-4].

In this paper, different level neutron irradiation treatments were carried out for IDT6116 SRAM with a feature size of 0.8microns and HM628512C SRAM with a feature size of 0.18microns, and then a transient ionizing dose experiment was carried out on the "Qiangguang-I" accelerator platform. The latch up dose rate threshold and the data upset dose rate threshold of the SRAMs after different neutron fluences were obtained. The relationship between threshold value and neutron fluence is compared and analyzed, and the effect mechanism is analyzed.

2. Experimental details

The SRAM devices were irradiated with neutrons using Xi'an pulse reactor (XAPR), during irradiation the circuits were shorted and connected to the ground. The XAPR was operated with the power of 100kW, the 1MeV equivalent neutron flux is $5.84 \times 10^9 \, \text{cm}^{-2} \cdot \text{s}^{-1}$ and the neutron/gamma ray ratio (n/γ ratio) is $7.7 \times 10^9 \, \text{cm}^{-2} \cdot \text{rad(Si)}^{-1}$. The SRAM devices accumulated five fluences perpendicular to the direction of the neutron beam, with five devices per irradiance being irradiated, respectively. The

1MeV equivalent neutron fluence of irradiation were: 5.0×10^{10} n·cm^{-2}, 1.0×10^{11} n·cm^{-2}, 5.0×10^{11} n·cm^{-2}, 8.0×10^{12} n·cm^{-2}, 6.0×10^{13} n·cm^{-2}. Neutron flounce is measured by activation foil.

In order to ensure the function and parameters of the devices after neutron irradiation, the parameters of the devices before and after neutron irradiation were tested by large-scale integrated circuit tester. Displacement damage induced by neutron irradiation is a permanent damage, the tests were performed after one week of neutron irradiation per batch.

Table 1 shows the test results of partial parameters before and after neutron irradiation in IDT6116 SRAMs. The parameter test results are in accordance with the specifications of the device datasheet except the 6.0×10^{13} n·cm^{-2} neutron irradiated samples. The failed sample may be due to the total ionizing dose effect caused by neutrons induced secondary particles and the accompanying gamma rays. However, due to the physical structure of the latch-up effect still exists, it will be used as a compared sample in this paper.

Table 1 Partial parameters of IDT6116 SRAM before and after neutron irradiation

1MeV equivalent neutron fluence / n·cm^{-2}	I_{cc} (nA)	I_{sb} (nA)	Function	t_{AA} (ns)	t_{AW} (ns)
Pre-rad(0)	57	71	Pass	18.0	4.4
5.0×10^{10}	17	55	Pass	17.6	4.4
5.0×10^{11}	63	67	Pass	17.6	4.2
8.0×10^{12}	52	69	Pass	16.6	4.4
6.0×10^{13}	51	64	Fail	20.0	799

Table 2 Partial parameters of HM628512C SRAM before and after neutron irradiation

1MeV equivalent neutron fluence / n·cm^{-2}	I_{cc} (nA)	I_{sb} (nA)	Function	t_{AA} (ns)	t_{AW} (ns)
Pre-rad(0)	0.5	0.5	Pass	42.0	9.0
5.0×10^{10}	31	3.3	Pass	37.6	9.6
1.0×10^{11}	27	1.9	Pass	39.0	10.0
5.0×10^{11}	0.5	0.4	Pass	45.0	9.4
8.0×10^{12}	31	10.0	Pass	36.0	9.2
6.0×10^{13}	51	6.2	Pass	37.0	9.3

The test results of partial parameters before and after neutron irradiation in HM628512C SRAMs are shown in Table 2. The parameter test results are in accordance with the specifications of the device datasheet, and the devices read and write normally.

Pulsed X-ray irradiation was carried out on "Qiangguang-I" accelerator platform. The pulsed X rays are generated by high-speed electrons striking the tantalum target. The pulse duration is about 50 ns (equivalent pulse width is 25 ns), and the average photon energy is approximately 1 MeV. The PIN detector is used to measure the pulsed gamma-ray waveform, and LiF thermoluminescent dosimeters are used to measure the deposit total dose in pulsed irradiation. Dose rate is calculated from the ratio of the deposit total dose and equivalent pulse width in one pulse. It is simple to adjust the value of dose rate via changing the distance between the devices and the target. In addition, the measurement uncertainty of dose rate is kept at a level less than 20% (coverage factor $k = 2$).

The irradiated devices in neutron exposure and the pristine ones (as a contrast) were placed in the pulsed X-ray environment. All devices were write in 55H, and were biased to the nominal voltage. The

status of latch-up can be judged by observing the current flowing through the Vdd pin. If the current increases suddenly from several milliampere to hundreds of milliampere or more, latch-up effect occurs; whereas there is no change of the current, indicating latch-up is not triggered. Then read back storage data and compare with the initial data to calculate the data upset. The dose rate can be flexibly adjusted by changing the distance of the devices and the beam source, and the thresholds of the devices can be find out via several times experiments.

3. Experimental results

Fig.1 shows the latch-up effect of IDT6116 SRAMs after different neutron irradiation. The normal operating current of this device is less than 0.06 amps, which will increase to more than 0.12 amps when the latch-up effect occurs. It can be judged whether the device is latched by the change of current.

Fig.1 Transient ionizing latch-up effect of neutron irradiated IDT6116 SRAMs.

The results of latch-up threshold measurements in the devices irradiated by neutron are represented in Table 3. It can be seen that latch-up threshold increases evidently when neutron flux is up to 8.0×10^{12} n·cm^{-2}. However, as neutron flux is up to 6.0×10^{13} n·cm^{-2}, the threshold of latch-up drops sharply. That is mainly because the concomitant γ rays with neutron exposure enhance the trapped charges in the oxide layer, and increase the sensitivity of latch-up.

Data upsets in SRAMs are mainly due to the fact that when the photocurrent is large enough, due to the capacitive charging, when the transistor is turned on or off or the output voltage exceeds the device 0 and 1 noise margin, the data upset occurs.

Fig.2 shows the data upset effect of HM628512C SRAMs after different neutron irradiation, the transient ionizing dose rate ranges from 3.9×10^{6} Gy(Si)/s to 7.6×10^{7} Gy(Si)/s. It can be seen from the figure that the transient ionizing dose rate effect of the 0.18 micron feature size SRAMs is mainly reflected in data upset, and the effect has significant threshold characteristics. The results of data upset threshold measurements in the devices irradiated by neutron are represented in Table 4.

Table 3 Change of latch-up threshold after neutron exposure

neutron flux (1MeV equivalence)/n·cm^{-2}	Latch-up threshold
Pre-rad(0)	5.9×10^7Gy(Si)/s
5.0×10^{10}	4.4×10^8Gy(Si)/s
5.0×10^{11}	5.7×10^8Gy(Si)/s
8.0×10^{12}	$>1.5\times10^9$Gy(Si)/s
6.0×10^{13}	3.3×10^6Gy(Si)/s
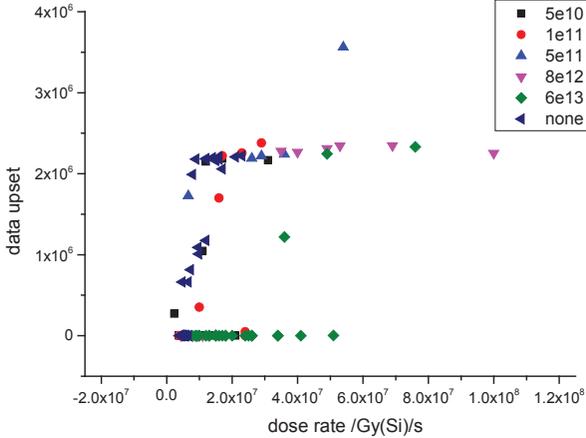
Fig.2 Transient ionizing upset effect on neutron irradiated HM628512C SRAMs.

Table 4 Change of data upset threshold after neutron exposure

neutron flux (1MeV equivalence)/n·cm^{-2}	Data upset threshold
Pre-rad(0)	4.7×10^6Gy(Si)/s
5.0×10^{10}	1.0×10^7Gy(Si)/s
1.0×10^{11}	1.5×10^7Gy(Si)/s
5.0×10^{11}	2.0×10^7Gy(Si)/s
8.0×10^{12}	3.0×10^7Gy(Si)/s
6.0×10^{13}	4.0×10^7Gy(Si)/s

It can be seen that the neutron pre-irradiation significantly improves the device's ability to resist transient ionizing dose rate induced data upset.

4. Discussion

Parasitic P-N-P-N structure in CMOS circuits and the equivalent circuitry are exhibited in figure 3. Under pulsed X-ray irradiation, the largest photocurrent in the P-N-P-N structure is from the junction of N-well and P-epi, namely the dominant portion to trigger latch-up, flowing through R_{sub} and the

base of Q_n. Because of current amplification of Q_n, the current from the collector of Q_n is β_n times the current injected into the base of Q_n, then leading to the base current of Q_p augment. In other words, the necessary and sufficient condition for latch-up occurrence is that the primary photocurrent, flowing through the circuitry in one circulation, results in more current.
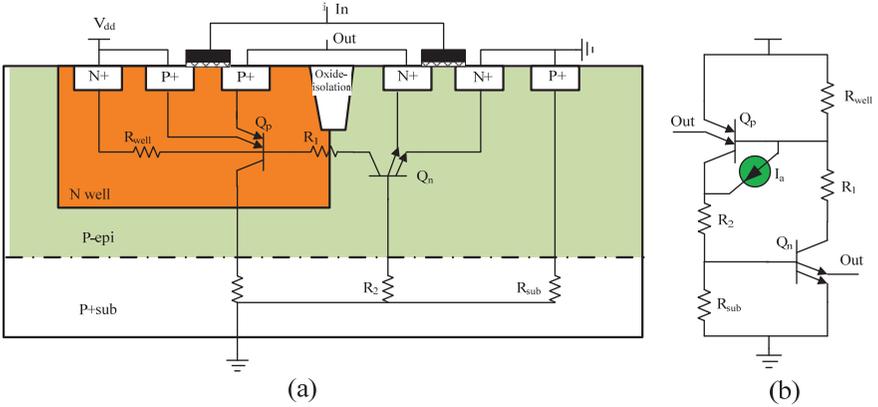
Fig.3 The parasitic P-N-P-N structure in CMOS devices and the equivalent circuitry:
(a) the parasitic P-N-P-N structure, (b) the equivalent circuitry.

The latch-up holding current is an important parameter of the latch-up effect and can be defined as the minimum on-current required to maintain the latch-up state. As shown in equation (1):

$$I_H = \frac{\beta_{npn}(\beta_{pnp}+1)I_{RW} + \beta_{pnp}(\beta_{npn}+1)I_{RS}}{\beta_{npn}\cdot\beta_{pnp}-1} \tag{1}$$

Here the β_{pnp} and β_{npn} are the gain of parasite transistors in the P-N-P-N structure, I_{RW} represents the current flowing through R_W, while I_{RS} represents the current flowing through R_S. Obviously, the smaller the product of the current gain, the larger the required latch-up holding current. An infinitely great current is needed to hold the latch-up while $\beta_{pnp}\cdot\beta_{pnp}$ degrade to 1. This means neutron induced gain degradation [5] of parasite transistor could enhance the anti-latch-up ability of SRAMs.

In order to further analyze the effect of neutron irradiation on the transient photocurrent caused by carrier lifetime degradation, the physical process of the effect was calculated based on the two-dimensional PN junction structure using the MEDICI software. Simulation results indicates the carrier lifetime does not affect the time response of the photocurrent induced by transient ionizing radiation. But the magnitude of the photo current is significantly reduced while the carrier lifetime reduces, as shown in Fig.4. The reduction of the photocurrent would improve the device's ability to resist transient ionizing dose rate induced data upset.
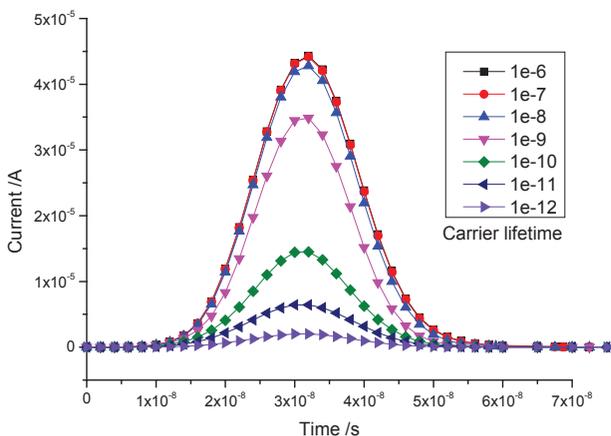
Fig.4 Simulation result of Photo current versus carrier lifetime.

In order to further analyze the effect of neutron irradiation on the transient photocurrent caused by carrier lifetime degradation, the physical process of the effect was calculated based on the two-dimensional PN junction structure using the MEDICI software. Simulation results indicates the carrier lifetime does not affect the time response of the photocurrent induced by transient ionizing radiation. But the magnitude of the photo current is significantly reduced while the carrier lifetime reduces, as shown in Fig.4. The reduction of the photocurrent would improve the device's ability to resist transient ionizing dose rate induced data upset.

5. Conclusion

Neutron pre-irradiation could significantly improve the transient ionizing latch-up and data upset threshold dose rate value of SRAMs. Also, the reactor neutron and parasite gamma ray induced total ionizing dose effect should not be neglected. Displacement damage induced gain reduction and carrier lifetime degradation are the main reason for this effect.

References
1. CoppageF N, Evans D C. Characteristics of destruction from latchupin CMOS[J]. IEEE Trans. Nucl. Sci., 1977, NS-24: 2226–2233.
2. Qin J R, Chen SM, Liu B W, et al. Research on single event transientpulse quenching effect in 90 nm CMOS technology[J]. Sci. China Tech. Sci., 2011, **54**(11): 3064–3069.
3. Alexander D R. Transient ionizing radiation effects in devices andcircuits[J]. IEEE Trans. Nucl. Sci., 2003, 50: 565–580.
4. Deval Y, Lapuyade H. Evaluation of a design methodology dedicatedto dose-rate-hardened linear integrated circuits[J]. IEEE Trans. Nucl. Sci., 2002, 49: 1468–1473.
5. J. R. Srour, "A Framework for Understanding Displacement Damage Mechanisms in Irradiated Silicon Devices", IEEE Trans. Nucl. Sci., vol.**53**, NO. 6, PP.3610-3620, Dec. 2006.

DESIGN AND IMPLEMENTATION OF MATRYOSHKA-TYPE NEUTRON SPECTROMETER

Lv Ning, Guo Huiping, Lv Wenhui, Lv Jinxu, Xiao Qizhan, Sun Mingyan

Xi'An Research Institute of Hi-Tech, Xi'an, China

Abstract: Aiming at the portability and mobility, the design and implementation of a portable neutron spectrometer, namely Matryoshka-type neutron spectrometer (MNS), was completed consulting the idea of a Bonner sphere spectrometer (BSS). The MNS used a spherical He-3 proportional counter as a thermal neutron detector. A series of cylindrical acrylic cups with diameters from 4 cm to 40 cm were made as containers of water moderator. The Monte Carlo method was adopted to obtain the energy response matrix of the MNS. During the measurement, each acrylic cup contained water as a moderator, and the He-3 proportional counter was placed at the geometric center to perform neutron counting. With the energy response matrix obtained above, the neutron spectrum was solved through a classical inversion algorithm. After the measurement, water was drained and the acrylic cups were placed one by one like a Matryoshka doll. The design of MNS has reduced the mass and volume of BSS, and was easy to carry around. Comparison test of acquiring background and Am-Be source neutron spectra between MNS and BSS proved the effectiveness of the MNS.

Key words: neutron detection, neutron spectrum, neutron spectrometer, full energy range

1. Introduction

As its wide energy response range, simple operation and ingenious calculation, multisphere neutron spectrometer is widely used to determine neutron spectrum for the purpose of neutron ambient dose equivalent measurement. For multisphere neutron spectrometer was invented by Bramblett R.L., Ewing R.I. and Bonner T.W. in 1960, it is also called Bonner sphere spectrometer (BSS) [1], which was composed of a series of polyethylene moderator balls and a thermal neutron detector in center. Since then, more mature products of BSS have been gradually coming out, including the NEMUS BSS jointly designed by the British Centronic Company and PTB, the LUDLUM 42-5 BSS, the ROSPEC BSS, etc. In China, MNSIL 100 BSS [2] was jointly developed by Tsinghua University and Tongfang Weishi; many other research institutes have developed a variety of prototypes for their own special needs [3, 4].

Although operation process is simple, the polyethylene moderator balls of BSS are inconvenient to be moved from one radiation field to another because their weight and volume. In this article, moderators were designed as a series of cylindrical acrylic cups filled with water, which could be drained out while acrylic cups could be placed into another one by one like a Matryoshka doll. In this way, the weight and volume of the whole neutron spectrometer are reduced sharply. The neutron spectrometer becomes portable and lightweight to carry around.

The advantage is that the initialization conditions of the neutron spectrum are not too strict. As long as the shapes are roughly similar, the iterative formula will adjust the neutron spectrum with reference to the measured values and the response matrix, and finally get a better result. If there is no prior information of the preset spectrum, it can be replaced by a uniform distribution.

3 Measurements and Analysis

3.1 Measurements

The MNS was used to acquire the neutron spectrum of Am-Be neutron source radiation field. The laboratory is 12 m (long) × 6 m (wide) × 4 m (high). It is a reinforced concrete structure with indoor space. The Am-Be neutron source was 1.2 m high away from the ground and was located at the center of the ground plane. The geometric center of the thermal neutron detector was 0.5 m away from the Am-Be neutron source. Before Am-Be neutron source radiation field spectrum measurement, background neutron spectrum measurement of this lab was under consideration. The measurement results are shown in Table 1.

Table 1 Neutron counting rate for three kinds of radiation fields

Diameter /cm	Background /cps	Am-Be neutron source /cps
6	0.00465	2.42
8	0.00549	5.25
10	0.00553	8.48
12	0.00641	12.76
14	0.00576	16.12
16	0.00630	16.30
18	0.00613	17.43
20	0.00523	16.68
22	0.00595	19.27
24	0.00539	16.13
26	0.00520	18.69

3.2 Analysis

Neutron energy analysis interval was limited between 1×10^{-9} and 10 MeV. With the Algorithm introduced above, the inversed neutron spectra of radiation field are shown in Fig. 4 and Fig. 5.

Fig. 4 illustrates the background neutron spectrum of the lab. The dotted line was the result obtained by MNS this paper designed, compared with solid line, which was the result obtained by BSS. There exist two peaks in the spectrum:

i. Evaporation neutron zone [6]. The neutron energy in this region is between 0.1 MeV and 10 MeV, the main source is the resonance nuclear reaction between neutrons and atmosphere or with buildings. The energy of the neutron generated by the de-excitation is 0.1 ~10 MeV.

ii. Thermal neutron zone. The neutron energy of this region is less than 0.4 eV, and the most probable distribution is between 10^{-8}~10^{-7} MeV, which is basically consistent with the Maxwell distribution [6]. The neutron is derived from the collision of neutrons in the air with the walls of the laboratory, the ground and other materials, and finally reaches the thermal equilibrium state, finally forming a thermal neutron peak on the background neutron energy spectrum.
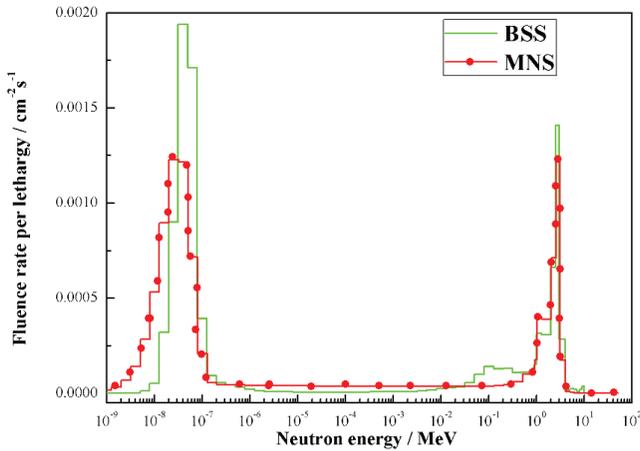
Fig. 4 Background neutron spectrum of laboratory

Fig. 5 illustrates the neutron spectrum of Am-Be neutron source radiation field. The dotted line was the result obtained by MNS this paper designed, compared with solid line, which was the result obtained by BSS. There exist three peaks in the spectrum:

i. Fast neutron zone. The neutron peak region of the Am-Be source is mainly between 1 MeV and 10 MeV, which is consistent with ISO 8529-1, in which the extreme values around 3.1 MeV, 4.4 MeV, 6.6 MeV, 7.7 MeV, 9.8 MeV[7], shown in Fig. 6.
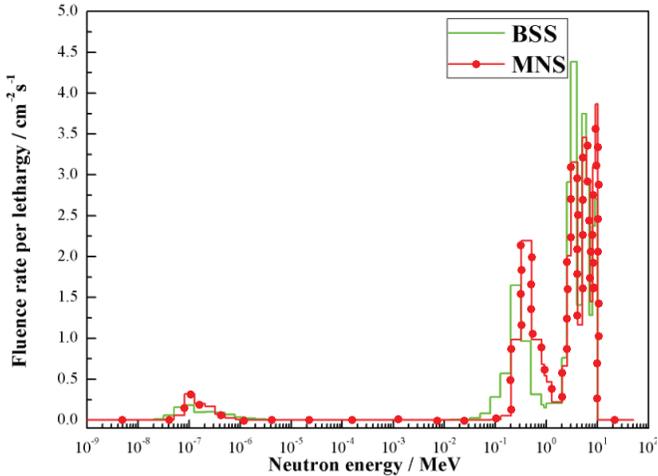
Fig. 5 Neutron spectrum of Am-Be neutron source radiation field

ii. Evaporation neutron zone. The neutron energy in this region is between 10^{-1} MeV and 1 MeV. Since the neutron collimator was not applied in this experiment, the 1 MeV ~ 10 MeV neutron emitted from Am-Be neutron source collided with the concrete wall around, lost a certain amount of energy, and then entered the detector. Its essence is the secondary neutron spectrum of the Am-Be neutron source [6].

iii. Thermal neutron zone. The peak position is around 1×10^{-7} MeV. The neutrons originally emitted by Am-Be neutron source, scattering neutrons, and environmental background neutrons collide with various materials such as the walls of the laboratory and the ground, and finally reach a thermal equilibrium state, forming the thermal neutron zone.
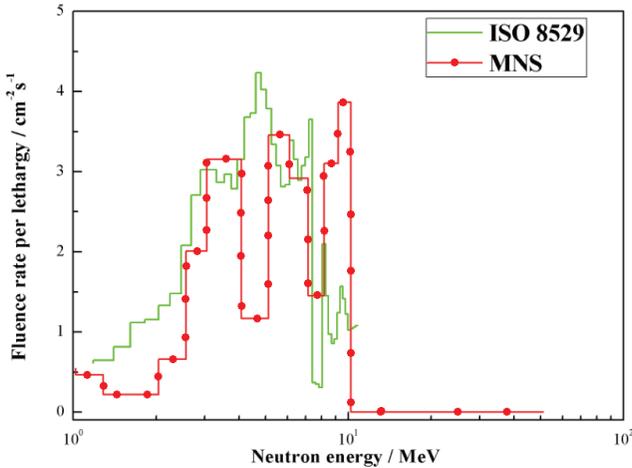
Fig. 6 Neutron spectrum of Am-Be neutron source between 1 MeV and 10 MeV

4 Comparison and Results

Furthermore, we divided the full energy range of neutron into different region, compared neutron fluence rate of each region between MNS and BSS, as shown in Table 2.

Table 2 Comparison of neutron fluence rate between MNS and BSS/ cm^{-2}·s^{-1}

Radiation fields	Fluence rate	Thermal neutron < 0.4 eV	Slow neutron 0.4 eV ~100 keV	Fast neutron 100 keV~10 MeV
Background	BSS	3.25×10^{-3}	2.44×10^{-4}	1.32×10^{-3}
	MNS	3.42×10^{-3}	2.63×10^{-4}	1.27×10^{-3}
Am-Be neutron source	BSS	2.66×10^{-1}	8.61×10^{-1}	6.61
	MNS	2.86×10^{-1}	0.82×10^{-1}	6.75

Generally speaking, from the result of Comparison, neutron energy distribution inversed by MNS is consistent with BSS as shown in Fig. 4 and Fig. 5, which illuminates the correctness of MNS design.

Compare two sets of moderator between MNS and BSS, 13 hollow acrylic cups V.S. 13

polyethylene balls, diameters from 3 inch to 15 inch:

i. To the volume. During the carrying process after measurement, because the smaller acrylic cup could be placed into a bigger cup one by one like a Matryoshka doll, the space MNS occupied is only decided by the biggest cup, which is 43.4 L, 35% of all the 13 polyethylene balls of BSS.

ii. To the weight. During the carrying process after measurement, water could be drained out, the weight of 13 hollow acrylic cups is 5.75 Kg, only 5% of 13 polyethylene balls of BSS.

Under the precondition of acquiring neutron spectrum successfully, the Matryoshka-type neutron spectrometer makes the weight and volume of the whole neutron spectrometer reduced sharply, and becomes portable and lightweight to carry around.

References

1. Bramblett R.L., Ewing R.I., Bonner T.W. A new type of neutron spectrometer. Nuclear Instruments and Methods, 1960, **9**(1): 1–12.

2. HU Qingdong, ZENG Zhi, MA Hao, *et al*. Measurement of indoor natural neutron spectrum with a bonner sphere spectrometer [J]. Tsinghua University (Science & Technology), 2015, **55**(12): 1332–1334.

3. LI Yan, CHENG Fanjie, CHENG Yuting, *et al*. Neutron spectrum measuring of critical assembly by BF_3 multi-column spectrometer [J]. Atomic Energy Science and Technology, 2017, **51**(2): 319–322.

4. FU Xin. Research and development of an extended range multi-sphere neutron spectrometer [D]. Beijing: University of Chinese Academy of Sciences, 2016.

5. CHEN Yonghao. Fast neutron energy spectrum measuring and unfolding research by proton recoils method [D]. Lanzhou: Lanzhou University, 2013.

6. LIU Shengkang. Neutron physics [M]. Beijing: Atomic Energy Press, 1986: 144–145.

7. ISO 8529–1:2001, IDT. Reference neutron radiations- Part 1: Characteristics and methods of production.

Modeling and Simulation of Activated Corrosion Products Behavior Under Design-Based Variation of Neutron Flux Rate in AP-1000

F. Mahmood, H. Hu[a], L. Cao and G. Lu

School of Nuclear Science and Technology, Xi'an Jiaotong University, Xi'an, China
fiazmahmood@stu.xjtu.edu.cn

Abstract: The research on Activated Corrosion Products (ACPs) is gaining more significance motivated by the growing trend of innovative reactor designs in world energy market. In this research, application of a locally developed code CPA-AP1000 is extended to study progression of ACPs in primary circuit of AP-1000 under full power neutron flux and design based variation in the flux rate. The programing is executed in MATLAB while MCNP code is used to compute the neutron flux distribution in reactor core, under particular operating conditions. The mathematical model in the program is handled to account for calculation of ACPs for full power flux and varying flux rate scenarios. The simulations are carried out for steady state operation up to Middle of Cycle (MOC) and afterwards slow changes in neutron flux rate, derived by the Mechanical Shim (MSHIM) based power maneuvers, are introduced in the system. The results for major ACPs demonstrate that during period of normal full power operation short-lived ACPs build up promptly, rendering an immediate radiation source for inspection and maintenance crews. When neutron flux rate is slowly reduced and ultimately settled to a lower value, the saturation specific activity of corresponding radioisotopes changes accordingly. The short-lived ACPs rapidly attain a new lower saturation value of specific activity but those having long half-lives sluggishly decay and ultimately produce radiation sources, which hold for a longer period of time. The studies are further extended to compare the build-up and decay pattern of ^{56}Mn in primary coolant, core scale and piping structure. The specific activity due to ^{56}Mn in all parts (coolant, core and piping) of primary circuit builds up promptly under normal full power operation and rapidly declines following the reduction in neutron flux rate. The simulation results reveal that specific activity due to *ACPs* in core scale is the largest source under all operating conditions.

Key Words: Activated Corrosion Products, specific activity, CPA-AP1000, power maneuvering, neutron flux rate variation

1 Introduction

The ACPs impose a major radiological burden during routine surveillance, equipment handling and maintenance activities of RCS. The estimation of radiation dose caused by the ACPs in RCS of nuclear power plant (NPP) is effective for job planning and assessment of ORE to the surveillance

---

[a] Corresponding author

Tel: +86-29-82668648, Fax: +86-29-82667802

Email address: huasi_hu@mail.xjtu.edu.cn

and maintenance workers. The optimization of ORE caused by ACPs is mostly executed through the planning of routine maintenance during reactor shutdown periods. However, daily surveillance and emergency maintenance put forwards need of an urgent approach to RCS. Therefore, evaluation of activity caused by ACPs during various plant operating conditions is of utmost importance. When primary coolant containing ACPs passes through the flow channels of the primary coolant circuit it deposits the dissolved and suspended radionuclides on the cooling system inner surfaces [1]. The types of radionuclides formed, the levels of equilibrium activity reached and the rate at which the equilibrium is reached all are functions of various operating parameters of the reactor. These also include the composition of the materials in contact with the coolant, amount and the types of the impurities present in the coolant, operating power of the reactor, residence time of the coolant in the reactor core, temperatures and pressures, coolant flow rate, corrosion rate and filter efficiency. The major corrosion products and their reaction properties are described in Table 1 [2].

The radiological inventory of RCS mainly depends on the amount of ACPs present in primary coolant and deposited on the inner surfaces of the system walls, if fuel failure is ignored. The evaluation of radioactive crud sources in RCS of NPPs highly depends on plant operating conditions and design specifications. New operational strategies of modern reactor designs are coming up with effective contribution to meet variable demands in world energy. However, estimation of variation in activity level in RCS during application of design based operational strategies has turned out more challenging. In previous studies, typical PWRs are most widely focused in the subjected area of research. Recently, ACPs behavior in innovative reactor designs has also been studied [3-5]. The research efforts have been dedicated to understand the corrosion kinetics by developing CAT code [6]. Subsequently, another computer code CPA-AP1000 is locally developed to study the behavior of ACPs in the AP-1000 [7]. In this study, activity levels of the major corrosion products in RCS are evaluated during reactor full power operation and design based slow changes in neutron flux employing the CPA-AP1000.

Table 1. Corrosion products and their reaction properties

Sr.#	Reaction	Activated CP	Activation cross section	γ-ray energy
1	^{23}Na (n, γ) ^{24}Na (E_n >11.60 MeV)	^{24}Na ($T_{1/2}$=15.40 h)	0.53 b	4.10 MeV
2	^{58}Fe (n, γ) ^{59}Fe (E_n is thermal)	^{59}Fe ($T_{1/2}$=45.10 h)	0.90 b	1.17 MeV (99.99%) 1.33 MeV (99.99%)
3	^{98}Mo (n, γ) ^{99}Mo (E_n >3.10 MeV)	^{99}Mo ($T_{1/2}$=67.00 h)	0.45 b	0.78 MeV (8%) 0.74 MeV (8%)
4	^{59}Co (n, γ) ^{60}Co	^{60}Co ($T_{1/2}$=5.30 y)	20.00 b	1.17 MeV (99.99%) 1.33 MeV (99.99%)
5	^{55}Mn (n, γ) ^{56}Mn (E_n is thermal)	^{56}Mn ($T_{1/2}$=2.58 h)	13.40 b	2.13 MeV (15%) 1.81 MeV (24%) 0.85MeV (99%)

2 Mathematical model

The time-dependent model of activity in the primary coolant circuit is established by balancing the rate of production and loss of radioactive nuclei due to different exchange pathways. The pathways include activation of CPs due to power dependent value of flux, purification of coolant, deposition of the materials on surfaces, leakage from the system and radioactive decay of activated products. Different pathways leading to these production and loss mechanisms are schematically described in Fig. 1.
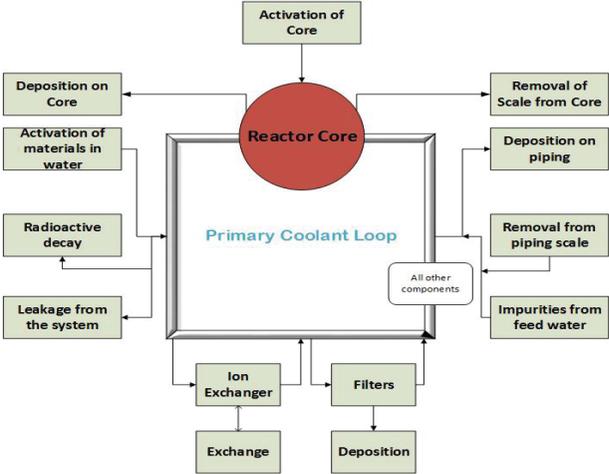
Fig. 1. Schematic of exchange pathways for modeling activation products in the primary coolant circuit

The mathematical model of the time-dependent behavior of dominant CPs in the primary coolant circuit of AP-1000 is based on the following assumptions.

- o The composition of CPs corresponds to the chemical composition of originally corroding material.
- o The material of walls of cooling system corrodes uniformly and homogeneously.
- o The intrinsic activity is considered negligible.
- o The deposition on surfaces in contact with cooling water is proportional to the concentration of CPs in water.
- o The ion-exchangers and filters remove impurities in proportion to their concentration in the coolant.

The design-based variation in neutron flux rate is introduced into the system by Mechanical Shim (MSHIM) based power maneuvers. The neutron flux is treated as representative of reactor operating power. The change in neutron flux rate is modeled as directly affected by variation in reactor operating power. In order to incorporate the effect of power maneuverings, the power levels are modeled with the subsequent scheme. The time-dependent operating power $p(t)$ is defined in terms of normalized power parameter $f(t)$ and Rated Thermal Power (RTP) p_0 as following;

$$p(t) = f(t)p_0 \tag{1}$$

The parameter $f(t)$ is capable of describing reactor operation at various power levels and under *MSHIM* based power transients. The power parameter $f(t)$ describes any linear increase or decrease in reactor operational power as following;

$$f(t) = \begin{cases} p_1 & , t < t_s \\ p_1 - \mu(t - t_{ts}) & , t_{ts} \le t < t_{te} \\ p_2 & , t \ge t_{te} \end{cases} \tag{2}$$

where p_1 and p_2 represent operating power in terms of percentage *RTP* before start and end of power maneuvering at time t_{ts} and t_{te} respectively, and μ is the slope of linear increase or decrease operating power.

The activation of CPs is affected by the time taken by a particle for traversing through the primary coolant circuit, and length of time it is exposed to the neutron flux. The effective neutron flux density ϕ_ϵ (n/cm².sec) links both of these time intervals as following;

$$\phi_\epsilon = \frac{1 - e^{-\lambda T_c}}{1 - e^{-\lambda T_L}} \phi_0 \tag{3}$$

where ϕ_0 is thermal neutron flux density (n/cm².sec) averaged over the geometry of core, λ is decay constant (sec⁻¹) of the activated nuclide of interest, T_c is time length for which a particle of coolant is exposed to the neutron flux and can be estimated as $H\rho A/w(t)$. The parameter H is core height, ρ is the density of the coolant at operating temperature and pressure, and $w(t)$ is time dependent mass flow rate. The circulating time of a particle through the primary coolant system is denoted by T_L for loop length L of the primary circuit and can be estimated as LT_c/H.

The concentration of target nuclides (atoms/cm³) in the primary coolant, on piping and core surfaces have been denoted by N_w, N_p and N_c respectively. The concentrations of activated nuclides (atoms/cm³) in the primary coolant water, on the inner walls of piping and core surfaces have been denoted by n_w, n_p, and n_c respectively. The rate of change of active material concentration in primary coolant is given by;

$$\frac{dn_w}{dt} = \sigma f(t) \phi_\epsilon N_w - \left(\sum_j \frac{\varepsilon_j Q_j}{V_w} + \sum_k \frac{l_k}{V_w} + \lambda \right) n_w + \frac{k_p}{V_w} n_p + \frac{k_c}{V_w} n_c \tag{4}$$

where σ is the group constant for the production of ithe sotope from target nuclide. The sum over j for $\varepsilon_j Q_j$ is given as following;

$$\varepsilon_j Q_j = \varepsilon_i Q_i + \varepsilon_f Q_f + \varepsilon_c Q_c + \varepsilon_p Q_p \tag{5}$$

where the quantities $\varepsilon_i Q_i$, $\varepsilon_f Q_f$, $\varepsilon_c Q_c$, $\varepsilon_p Q_p$ are removal rates (cm³/sec) induced by ion exchanger, filter, core and pipe surfaces respectively. The term l_k is rate (cm³/sec) at which the primary coolant is lost during kth leak, k_p and $k$the $_c$ are rates (cm³/sec) at which isotopes are removed from the scale on piping and core respectively. The first term in equation (4) represents the production of radioactive isotopes. The second term is rate at which active the nuclides are lost because of purification by the ion-exchanger and filter, deposition on the piping and core and decay of the activated nuclei. The third and fourth terms are the rates at which activity is re-introduced into the water because of erosion or dissolution of activity deposited on inner surfaces of piping and reactor core. The rate of change in target nuclide concentration in coolant water can be written as;

$$\frac{dN_w}{dt} = -\left(\sum_j \frac{\varepsilon_j Q_j}{V_w} + \sum_k \frac{l_k}{V_w} + \sigma f(t) \phi_\epsilon \right) N_w + \frac{k_p}{V_w} N_p + \frac{k_c}{V_w} N_c + S_w \tag{6}$$

$$S_w = \frac{C_0 S N_0 f_n f_s}{V_w A} \tag{7}$$

236

3.1 Computing Scheme

Based on the above model, a computer program namely Corrosion Products Activity in AP-1000 (CPA-AP1000), has been developed by executing programming in MATLAB. The overall computational scheme is as shown in Fig. 3. The CPA-AP1000 contains two loops; one loop calculates specific activity under steady-state or power maneuvering conditions, and other moves over different isotopes. After initialization, the program first calculates group fluxes using Tally-4 of the MCNP code. Since the MCNP results are normalized to one source neutron, the result has to be properly scaled in order to get the absolute comparison to the measured quantities of flux. Therefore, the scaling factor is applied in data processing and F4 tally results of core averaged group fluxes are scaled to the desired fission neutron source (power) level using equation 13. The system of coupled differential equations is solved using fourth order Runge-Kutta method.
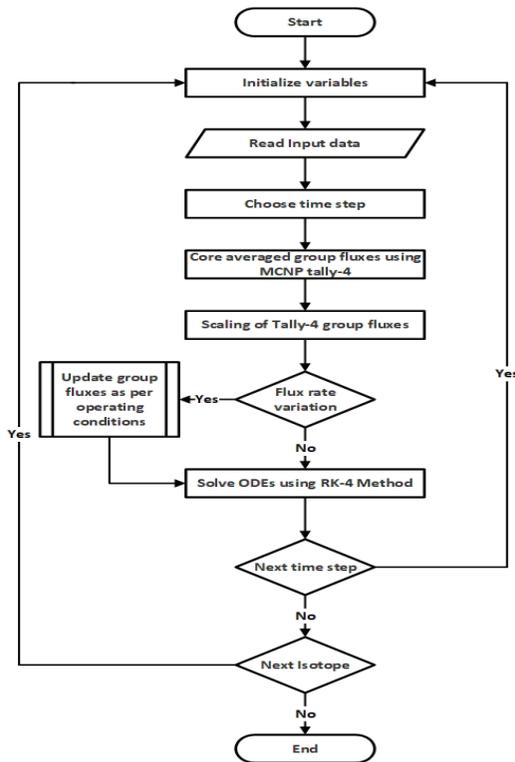
Fig. 3. Flowchart of CPA-AP100 for computing CPA under steady-state operation and flux rate vitiation

4   Results and Discussions

The simulations were started at time t= 0, when reactor was considered to be operating in steady state having no impurities at the initial stage. It has been assumed that the system material corrodes uniformly and homogeneously with constant corrosion rate. The experimental values of different factional exchange rates employed in the present analysis are shown in Table 3 [2,7]. The ion-exchanger removal is the most sensitive parameter to effect CPA values. The detailed effect of ion-exchange removal on saturation specific activity of ^{24}Na was studied using an approach adopted in our previous study [7]. The specific activity of ^{24}Na as a function of reactor operation time was calculated for various values of ion-exchanger removal rate. The aim of the calculation was to demonstrate the well-defined effect of ion-exchanger removal rate on saturation specific by selecting the sufficient data points. The resulting saturation specific activity of ^{24}Na as a function of different ion-exchange removal rate is as shown in Fig. 4.
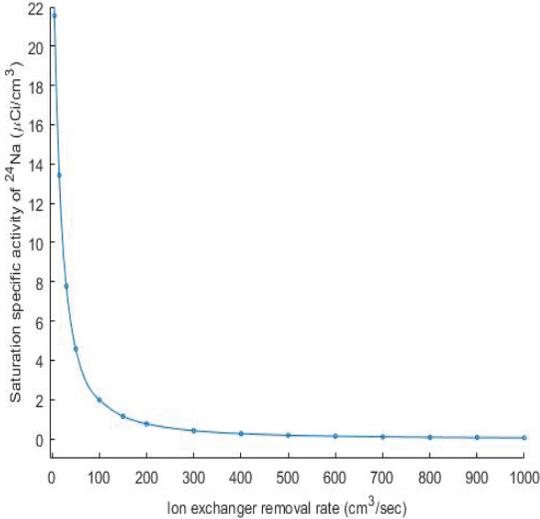
Fig. 4. Saturation specific activity of ^{24}Na as a function of ion-exchange removal rate in primary coolant of AP-1000

The results depicted that the saturation activity is higher enough for low ion-exchanger removal rate and it decreases nonlinearly as ion-exchanger removal rate is increased. When value of $\varepsilon_I Q_I$ approaches 400 cm^3/sec, saturation activity varies with a minor slope and becomes almost constant at 600 cm^3/sec. Therefore, the optimal value of ion-exchange removal rate of 600 cm^3/sec was selected in our subsequent evaluations. The selection of more data points in this study has demonstrated the more clear effect of ion-exchange removal rate on saturation activity, however, trend of the results is the same as obtained in the previous investigation.

Table 3. Fractional exchange rates of a typical PWR

Rate Description	Value1 and Unit	Value2 and Unit
Deposition on core	$\varepsilon_c Q_c/V_w = 5.835x10^{-5} sec^{-1}$	$\varepsilon_c Q_c/V_c = 8.81x10^{-6} sec^{-1}$
Deposition on piping	$\varepsilon_p Q_p/V_w = 1.00x10^{-6} sec^{-1}$	$\varepsilon_p Q_p/V_c = 1.00x10^{-5} sec^{-1}$
Ion-exchanger removal	$\varepsilon_I Q_I/V_w = 5.70x10^{-5} sec^{-1}$	
Resolution ratio for core	$K_c/V_w = 2.918x10^{-6} sec^{-1}$	$K_c/V_c = 4.406x10^{-6} sec^{-1}$
Resolution ratio for piping	$K_p/V_w = 5.0x10^{-7} sec^{-1}$	$K_p/V_p = 5.0x10^{-6} sec^{-1}$
Volume of primary coolant	$V_w = 1.37x10^7 cm^3$	
Volume of scale on core	$V_c = 9.08x10^6 cm^3$	
Average corrosion rate	$C_0 = 2.40x10^{-13} g/cm^2.sec$	

4.1 Evaluation of ACPs in the primary circuit

The specific activity behavior of ACPs in primary coolant circuit of AP-1000 was studied under full- power neutron flux and design based variation in the flux rate. A typical pattern of neutron flux rate was introduced into the system for this purpose. It was considered that reactor was continuously operated at 100% RTP up to 750 h (i.e. MOC) and then flux rate was slowly reduced. The flux was reduced at a slow rate of 16.67 % of full power flux per hour, which ultimately lead the reactor to operate at 50 % of RTP in almost 3 hours. It was considered that after this variation induced by MSHIM based power transients, reactor operated at 50% of RTP for the rest of the cycle. A typical time-dependent flux pattern depicting such changes in neutron flux with time is shown in Fig. 5.
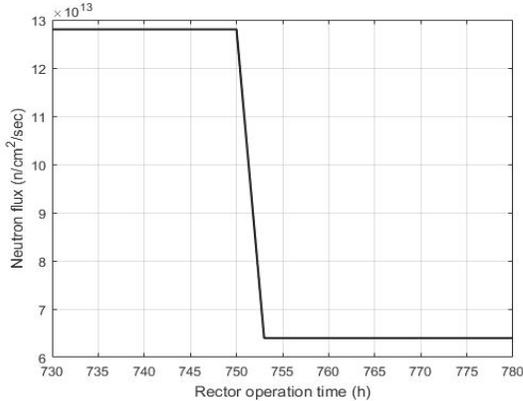
Fig. 5. The variation of neutron flux as a function of reactor operation time

4.1.1 Evaluation of ACPs in the primary coolant

The results for the specific activity buildup behavior of dominant ACPs ([24]Na, ^{59}Fe, [99]Mo, ^{60}Co, [56]Mn) in the primary coolant are presented in this section. The simulations for a typical flux rate variation as described in the previous section were run using CPA-AP1000 code. The reactor was operated at 100% RTP without any operational transient up to MOC. After the continuous operation of the reactor at 100% RTP for 750 hours, a slow variation in flux rate variation lead the reactor to 50%

RTP in almost 3 hours. The simulation results showing the behavior of dominant CPs in primary coolant during the complete cycle are presented in Fig. 6. The behavior of various ACPs is described for normal full power operation up to MOC, and for flux rate variation after MOC in following sections.
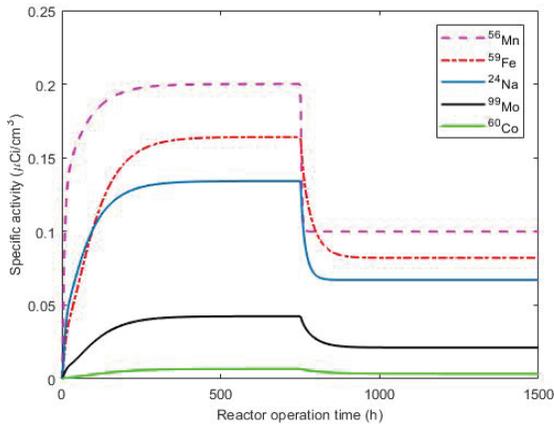
Fig. 6. The Specific activity r of ACPs in primary coolant under normal operation and the design-based variation in neutron flux rate

4.1.1.1 The behavior of ACPs up to Middle of Cycle (MOC)

The response curves of ACPs up to MOC have shown initially rapid increases in activity concentration during normal full power operation, as shown in Fig. 6. The initial rapid increase in specific activity is due to higher corrosion rates during the initial operating period of the reactor. This results in a rapid production of target materials at the beginning and ultimately production of more ACPs. The ACPs start accumulating on the coolant channel piping inner walls surfaces and on the core structures after passing sometime. Furthermore, the ACPs are also removed due to continuous ion-exchange operation and the use of filters. A balance between the removal rate and accumulation of the ACPs on piping and cores surfaces leads to a saturation specific activity value after passing sometime. The ^{56}Mn is the largest contributor to the total specific activity. Its specific activity is about 36.51% of the total specific activity in primary coolant. It has a saturation value of 0.2000 µCi/cm^3. The specific activity response of ^{56}Mn is rapid as compared to all of the other ACPs; it is mainly due to the short half-life as compared to other ACPs of interest. The ^{56}Mn reaches 90% of its saturation value after 100 h of startup time. The ^{59}Fe increases slowly as compared to ^{24}Na. The contribution of ^{59}Fe and ^{24}Na to the total activity is 29.97% and 24.51% respectively. The ^{59}Fe finally approaches a higher saturation value of 0.1641 µCi/cm^3 as compared to the saturation value of 0.1342 µCi/cm^3 for ^{24}Na. The saturation concentrations for ^{59}Fe and ^{24}Na reach 90% of their values in about 200 h and 165 h respectively. The ^{99}Mo and ^{60}Co have longer half-lives as compared to other ACPs under study and they contribute less towards the total specific activity during reactor operation. The contribution
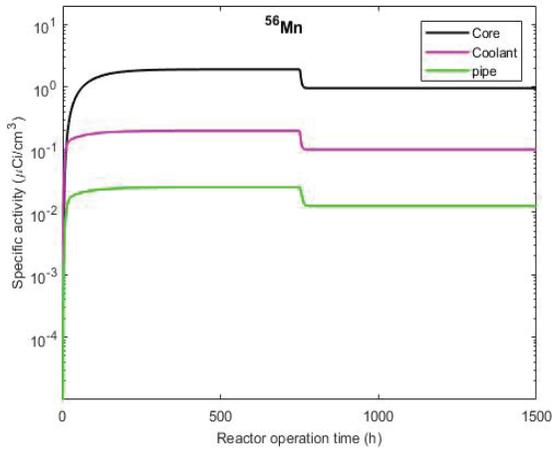
Fig. 9. The specific activity of ^{56}Mn in primary coolant and on inner walls of the primary system during normal operation and design-based variation in neutron flux rate

5 Conclusions

This study has been focused to envisage the specific activity behavior in various zones of the primary circuit of a fresh reactor design. A home developed code CPA-AP1000 is employed to compute the specific activity of ACPs in primary coolant circuit of AP-1000. The activity behavior due to major ACPs is investigated in primary coolant under the steady-state operation and the design-based variation in the neutron flux rate. The results depicted that during normal full power operation, all of ACPs build up at different rates, and finally saturate to constant values. The ACPs have demonstrated time-dependent behaviors during the period of flux variation. When flux rate variation was terminated and the reactor was onward operated at a new power level, all of ACPs attained a new reduced saturation value. The investigations are further extended to compare activity behavior of ^{56}Mn in primary coolant, on inner walls of structural components inside the core, and piping outside the core. The results have shown that specific activity on the surfaces of the structure inside the core is the highest followed by that of coolant. The specific activity on the inner surfaces of the piping structure outside of the core is minimum among all other zones. During the period of design based flux rate variation, the specific activity is also reduced in all zones of the circuit. The specific activity reduction pattern follows a similar trend in all parts of the circuit. When flux rate variation is terminated, specific activity in all parts of the circuit also attains a new saturation value. The estimation of activity behavior of ACPs under normal operation and design-based variation of flux rate is helpful in envisaging the corresponding radiation levels. The detailed behavior of other major ACPs in different parts of the primary circuit needs further investigations.

6   References

[1] Rafique M, Mirza N, Mirza S, et al. Review of computer codes for modeling corrosion product transport and activity build-up in light water reactors. NUKLEONIKA, 2010, 55: 263-269.

[2] Mirza A, Mirza N, Mir I. Simulation of corrosion product activity in pressurized water reactors under flow rate transients. Annals of Nuclear Energy, 1998, 25 (6): 331-345.

[3] Génin JB, Brissonneau L, Gilardi T. OSCAR-Na: A New Code for Simulating Corrosion Product Contamination in SFR. 2016, 3. **DOI:** 10.1007/s40553-016-0094-9

[4] Song JS, Cho HJ, Jung MY, et al. A Study on the Application of CRUDTRAN Code in Primary Systems of Domestic Pressurized Heavy-Water Reactors for Prediction of Radiation Source Term. Nuclear Engineering and Technology, 2017, 49 (3): 638-644. **DOI:** 10.1016/j.net.2016.11.005

[5] Li L, Zhang J, He S, et al. The development of two-phase three-node model used to simulate the transport of ACPs. 2017, 97: 99-105. **DOI:** 10.1016/j.pnucene.2016.12.015

[6] Shuran M, Jia J, Yichen B, et al. Modelling of materials corrosion inside RCS based on mixed-conduction model. Proceedings of 8th International Symposium on Symbiotic Nuclear Power Systems for 21st Century Chengdu, China, September 26-28, 2016.

[7] Mahmood F, Hu H, Cao L. Dynamic response analysis of corrosion products activity under steady state operation and Mechanical Shim based power-maneuvering transients in AP-1000. Annals of Nuclear Energy, 2018, 115: 16-26. **DOI:** 10.1016/j.anucene.2018.01.009

[8] Westinghouse. AP1000 Design Control Document, Rev. 19, 2011. https://www.nrc.gov/docs/ML1117/ML11171A500.html

[9] Stefani GL, Rossi PR, Maiorino JR, et al. Neutronic and thermal-hydraulic calculations for the AP-1000 NPP with the MCNP6 and Serpent codes. 2015 International Nuclear Atlantic Conference - INAC 2015, São Paulo, Brazil, October 4 - 9, 2015.

[10] Elsawi MA, Hraiz ASB. Benchmarking of the WIMS9/PARCS/TRACE code system for neutronic calculations of the Westinghouse AP1000™ reactor. Nuclear Engineering and Design, 2015, 293: 249-257. **DOI:** 10.1016/j.nucengdes.2015.08.008

Table 1. Simulate Results

Diamond detector	neutron （MeV）	gamma （MeV）
Energy deposition	1.0524E-01	1.0202E-03

The simulation results show that the accumulative deposition energy of neutron is two orders of magnitude higher than that of gamma ray deposition, which is mainly caused by two reasons. First, the shielding materials of the radiation experimental apparatus absorb most thermal neutrons, epithermal neutrons and gamma rays in the radiation field. The residual neutron in the radiation field is mainly fast neutrons and a small amount of residual gamma rays, and the ratio of neutron and gamma is relatively high. Secondly, the diamond materials used in the diamond detector have a low atomic number and a thin thickness, and the gamma ray can only have a very low mass energy absorption coefficient, and it is difficult to deposit all the energy of the secondary electrons produced by the action in such a thin detector. Therefore, it can be inferred from the simulation results that the signal in the current mode detector is mostly the contribution of neutrons, and the contribution of gamma rays to the signal can be neglected. The simulation results show that the diamond detector has a very high signal-to-noise ratio (SNR) without any converters and can be used to measure the neutron flux rate in the radiation field of the reactor.

System and experiment

Hence the current signal can be ignored that generated by gamma ray, the diamond detector used to measure neutron Flux rate in pulsed radiation field works in current mode, In order to obtain the neutron flux over time, single crystal diamond detector working in current mode has been adopted, whose signal can be recorded by oscilloscope and electrometer for measuring pulse, trailing-edge respectively.
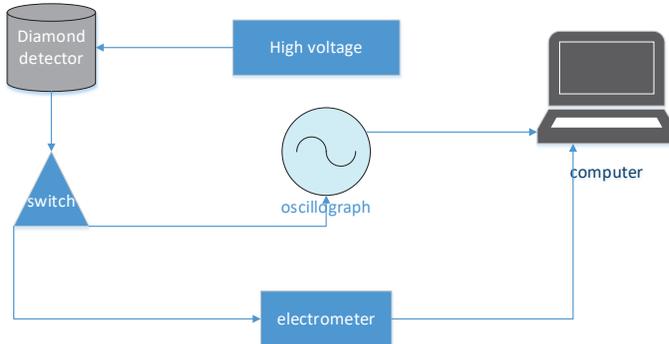
Fig. 3. Diamond detector measuring circuit.

The system used for neutron flux measurement in reactor irradiation experiment apparatus includes diamond detector and package, high voltage power supply, oscilloscope, electrometer and signal recording device, etc. The destination of this experiment is to measure

the variation of neutron flux rate along the pulse and back edge with time. The measurement of diamond detector signal is divided into two parts: the oscilloscope is used to record the detector current signal during the pulse process. Because the signal resolution of the oscilloscope decreases during the descent of the pulse, it is needed to switch the detector current signal to the electrometer in the process of the signal descent. The measuring circuit is shown in Fig. 3.

In this experiment, the working condition of Xi'an pulsed reactor is $3.2 and $2.0, and the corresponding half maximum width of the pulse is about 10 ms – 20 ms. The response of diamond detector to sub-nanosecond pulse X-ray is about 2.2 ns, which fully meets the measurement requirement of the pulse radiation field. In order to increase the signal-to-noise ratio (SNR) of the post-pulse signal, the measurement system is set up to switch the signal measurement from oscilloscope to electrometer after the oscilloscope triggers 25ms. After measurement, the signal of oscilloscope and galvanometer should be combined to obtain the complete signal of pulse radiation field. When diamond detector is used to measure the neutron flux rate, the relative neutron rate variation in the pulse radiation process can be obtained. In the radiation field pulse, the post-accumulative neutron flux is measured by activation method.

Results and discussion

When the XAPR working at $3.2 and $2.0, the measuring results in the displacement damage effect experiment apparatus are shown in the figure below. The full width at half maximum (FWHM) of the pulse is coincidence well with the Pulse Power Meter, the result are shown in Fig. 4.
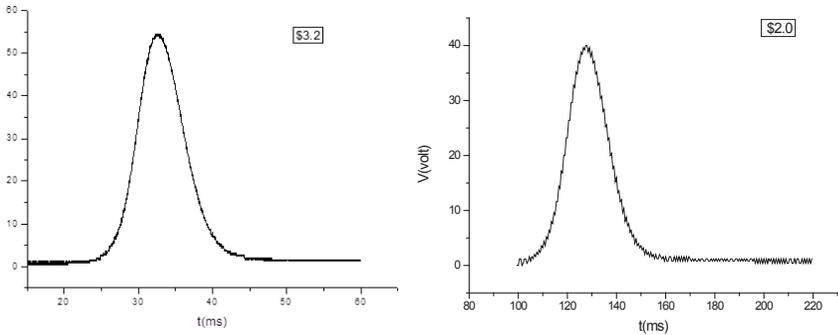
Fig. 4. Results for $3.2 and $2.0.

The current signal pulse in diamond and trailing-edge within a certain time has been integrated and normalized according to the activation measuring result of the cumulative neutron flux in different period of time, the analysis results are shown in table 2.

The current signal of single crystal diamond detector can reflect the changing of neutron flux over time, thus the radiation information such as accumulative neutron injection and peak neutron flux in different time periods can be obtained.

Therefore, the current diamond detection system can be used to monitor the neutron injection rate in the irradiated experimental device, and the output amplitude of the pulse signal is relatively linear to reflect the peak injection rate.

Table 2. Result for $3.2 and $2.0

Reactivity ($)	FWHM (ms)	Accumulative Neutron (neutrons*cm^{-2})	Peak Neutron Flux (neutrons*cm^{-2}*s^{-1})
3.2	9.8	8.32 E+12	7.42E+14
2.0	15.3	4.71 E+12	2.86 E+14

Conclusion

The single crystal diamond detection system adopted working in current mode can be used to monitor the pulse neutron flux in the displacement damage effect experiment apparatus , so as to obtain radiation parameters, such as full width at half maximum, neutron flux over time.

References

1. L.Y. Liu, X.P. Ouyang, J.F. Zhanga, et al. Properties comparison between nanosecond X-ray detectors of polycrystalline and single-crystal diamond[J]. Diamond & Related Materials **73** (2017) 248–252.
2. P. Lardon, C. Mer, P. Delacour, et al. Investigations of high quality diamond detectors for neutron fluency monitoring in a nuclear reactor [J]. Diamond & Related Materials **15** (2006) 815–821.
3. M. Pillon, M. Angelone, P. Batistoni, et al. Characterization of a diamond detector to be used as neutron yieldmonitor during the in-vessel calibration of JET neutron detectors inpreparation of the DT experiment[J]. Fusion Engineering and Design **106** (2016) 93–98.
4. Y. Uchihori, T. Kashiwagi, K. Hibino, et al. Investigation of Synthetic Diamond Radiation Detector Using Heavy Ion Beams [J]. IEEE Nuclear Science Symposium Conference Record 2005 N35-65.

MEASUREMENT OF ENERGY SPECTRUM OF BETATRON X-RAYS FROM LASER-PLASMA ACCELERATION

Xiufeng Weng, Fuli Wei, Zichuan Zhang, Jihu Wang, Zhaohui Song

Northwest Institute of Nuclear Technology, NINT, Xi'an 710024, Shaanxi, China
Corresponding author: nandswk@163.com

ABSTRACT

Betatron X-ray radiation can be generated by transverse betatron motion in the laser-plasma wake field. It has a comparatively small scale and a femtosecond duration. Therefore, betatron X-rays is advantageous to be used in femtosecond pump detection; meanwhile it has prospective applications in material science and bioscience. Measurement of its energy spectrum is valuable to learn the quality of betatron X-rays and its radiation sources. In our research, transmission attenuation method was used to measure its spectrum. A detection system was tailor-designed and fabricated for the betatron X-ray source of SIOM (Shanghai Institute of Optics and Fine Mechanics, Chinese Academy of Sciences) to meet the demand that the energy spectrum of each X-ray pulse be acquired through every pulse within a small angle. The reconstruction algorithm to solve the energy spectrum was also well optimized correspondingly. To test the properties of the system and the developed algorithm, we did comparison measurement experiments using the fabricated system and commercial HPGe detector respectively on Philips X'Unique II current steady X-ray source. The measured spectrum gained by our detection system fit quite well with that measured by HPGe detector. On the basis, the developed system was successfully applied in detection of X-ray spectra of Tesla repetitive frequency X-ray source.

Keywords: energy spectrum measurement; transmission attenuation; pulsed gamma; Betatron; laser-plasmas;

1. INTRODUCTION

Since their discovery in 1896[1], X-rays have a profound impact on science, medicine, and technology. In order to meet the scientific needs on faster time and smaller spatial scales, new x-ray sources became hotspot in research. When an intense femtosecond laser pulse interacts with gas, a plasma is formed and the ponder motive force of the pulse generates a large amplitude plasma wave[2-3]. This wave break, trap, accelerate electrons; and then short-duration of x-rays, which is called betatron radiation, burst into generation. One of the key features of betatron X-rays enabling their new applications is ultrafast pulse duration below 100 femtoseconds. Characterization of the time profile as well as the energy profile is crucially important for understanding and analyzing the physical phenomena and for its development and application. As far as the time profile is concerned, it is still an obstacle to measure the radiation pulse with sub-picosecond, which is not discussed in the paper. As regards the energy profile, the measurement of energy spectrum of pulsed γ/X rays has baffled us over a long period of time. It is more challenging and difficult especially to get energy spectra through one single pulse in a small bunch. In this paper, we developed the transmission attenuation method to determine the energy spectrum for pulsed X-ray sources.

SIOM betatron radiation source[4] driven by laser-plasma wake field is expected to generate betatron X-ray with its energy over 10 keV–1 MeV, pulse duration about several

femtoseconds, total flux $10^7 \sim 10^{12}$ particles per pulse and beam profile $\Phi 10 \sim 50$ mm. In terms of the parameters, we put forward two measurement systems to measure its energy spectrum—CCD camera with attenuators and photomultipliers coupled delaying optical fiber with attenuators, both of which can obtain the energy spectrum of each X-ray pulse for every pulse within a small angle. The expectation maximum algorithm was utilized to reconstruct the spectrum from transmission data. Based on the available sources, we conduct experiments to validate the CCD camera with attenuator system including spectrum unfolding algorithm on Philips X'Unique II current steady X-ray source. As an application sample, the developed photomultipliers coupled delaying optical fiber with attenuator system is applied in energy spectrum detection of Tesla repetitive frequency X-ray source[5].

2. METHODS

When a beam of gamma/X with the photon fluence F is casting on a detector, the signal measured can be expressed as

$$T(0) = \int_0^\infty F_E S(E)\, \mathrm{d}E, \tag{1}$$

where $F_E = dF/dE$ is the derivative energy spectrum, $S(E)$ is the energy response of detectors to gamma/X rays with energy E, i.e. the signal produced by unit fluence of photon with energy E.

Once a filter with the thickness of x is placed in the beam path, the spectrum of the photon changes to $F_E = F(0)\mathrm{e}^{-\mu(E)x}$, while the signal T becomes

$$T(x) = \int_0^\infty F_E\, \mathrm{e}^{-\mu(E)x} S(E)\, \mathrm{d}E, \tag{2}$$

where $\mu(E)$ is the filter's attenuation coefficient to photons with energy E. The discretization form of the equation can be displayed as

$$T(x_i) = \sum_{j=1}^{n} a_{ij}\rho_j, \tag{3}$$

of which $a_{ij} = \mathrm{e}^{-\mu(E_j)x_i}\, s(E_j)\Delta E$, where x_i (i=1,2, …, m) denotes thickness of the ith attenuator, $T(x_i)$ denotes the intensity signal of the corresponding i^{th} attenuator, ρ_j (j = 1, 2, ..., n) denotes the intensity of gamma in the jth energy zone under the condition of that the total energy zone is divided into n-1 intervals with each $\Delta E = (E_{max} - E_{min})/(n-1)$. Since a series of m (m=16 in the paper) attenuators are employed, sixteen equations can be formulated. To solve the combined linear equations, the unfolding algorithm of Expectation Maximization Method[6-12] was developed to solve the problem, which has been tested to have good validation and strong robust in the well-designed experiments carried out on Philips X'Unique II X-ray source ahead with a good agreement of the spectra simulated by Monte Carlo method.

Based on theoretical parameters of SIOM betatron radiation source, two different spectrum measurement systems are designed to obtain all attenuation transmission data in solely one pulse, as shown in Fig. 1 and Fig. 2. CCD camera imaging system shown in Fig.1 can be used for both constant and pulsed gamma/X source. It has a characterization of low sensitivity, not so complicated setup but with a relatively low dynamic range. Optical fiber array time-delay spectrum measurement system based on photomultiplier is well designed only applicable in detection of energy spectrum of pulsed gamma/X sources, especially for low-intensity and narrow-duration gamma/X sources.
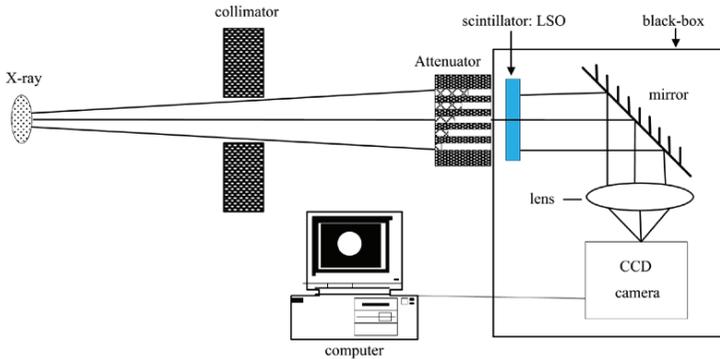
Fig.1 CCD camera imaging energy spectrum measuring system for pulsed gamma/X. Gamma/X rays are collimated to parallel beams, and irradiated directly onto the 16 holes of attenuators and the rear scintillator (e.g. LSO). The emission light is reflected by a mirror to the lens of CCD camera. The CCD signal is transferred to computer and can be displayed through developed software. The grey levels represent the intensity of incident gamma/X measured.
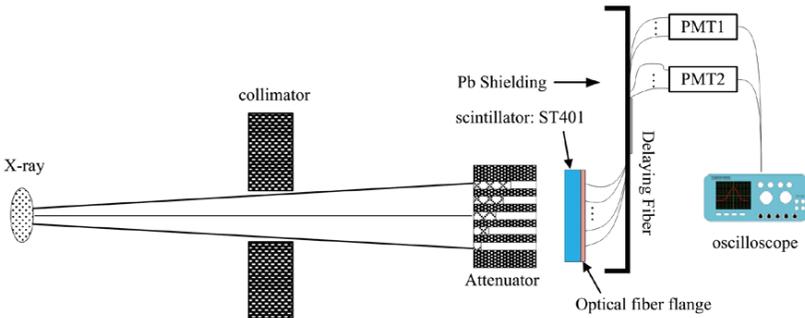
Fig.2 Optical fiber array energy spectrum measuring system for pulsed gamma/X. Gamma/X rays are collimated to parallel beams, and irradiated directly onto the 16 holes of attenuators and the rear scintillator (e.g. ST401). On the back panel of the scintillator, it is coupled with optical time delaying fiber in the rear position of corresponding hole of attenuator. The fibers are fixed by fiber flange. The length of the delaying fiber is 3 m more than the shorter one. The longer 8 paths of fibers are connected with one PMT while the shorter ones are connected with the other PMT. Both signals of the PMTs are transferred and recorded by an oscilloscope. The integral area of each waveform represents the intensity of incident gamma/X measured.

3. EXPERIMENTS

For experiments of gamma/X energy spectrum detection, we have developed and fabricated the above two measuring systems, displayed in Fig. 3. Based on the current constant X-ray source Philips X'Unique II (shown in Fig. 4), we carried out experiments to test the camera imaging system and spectra reconstruction. After this, the optical fiber array measuring system is applied in measuring energy spectrum of Tesla repetitive frequency X-ray source (displayed in Fig. 5), which is capable of producing tunable, hard X-ray pulses at maximum about 400 keV with short durations of ~400 ps.

REFERENCES

1. W.C. Roentgen, 1896, Nature, Vol. **53**, pp 274.
2. G. Genoud, et al., Appl. Phys. B, Vol. **105**, pp 309–316.
3. Silvia Cipiccia1, et al., 2011, Nature Phys. Vol. **7**, pp 867–871.
4. Changhai Yu, et al., 2016, Scientific Reports, 6:29518.
5. L. Quan, et al., 2007, Laser and Particle Beams, 2007, Vol. **19**, pp 1049–1052 (in Chinese).
6. Wang Jihu, et al., 2014, Modern Applied Physics, Vol.**5**, pp169–173 (in Chinese).
7. L. Silberstein, 1932, J. Opt. Soc. Am., Vol. **22**, pp265–280.
8. P.H. Huang, et al., 1981, Med. Phys., Vol. **8**, pp 368–374.
9. P.H. Huang, et al., 1982, Med. Phys., Vol. **9**, pp 695–702.
10. R.G. Waggener, et al., 1999, Med. Phys., Vol. **26**, pp1269–1278.
11. E.Y. Sidky, et al., 2005, J. Appl. Phys., Vol. **95**, pp 1–11.
12. J.H. Wang, et al., 2014, Modern Appl. Phys., Vol. **5**, pp169–173.
13. BRIESMEISTER J B, 1998, LA-12625-M-Manual.

Fission

ANGULAR DISTRIBUTIONS AND ANISOTROPY OF FISSION FRAGMENTS FROM NEUTRON-INDUCED FISSION OF [232]Th, [233]U, [235]U, [238]U, [239]Pu, [nat]Pb AND [209]Bi IN INTERMEDIATE ENERGY RANGE 1–200 MeV

A.M. Gagarski[1], A.S. Vorobyev[1], O.A. Shcherbakov[1], L.A. Vaishnene[1], A.L. Barabanov[2,3]

[1]*NRC "Kurchatov Institute", B.P. Konstantinov Petersburg Nuclear Physics Institute, 188300, Gatchina, Leningrad district, Russia*
[2]*NRC "Kurchatov Institute", 123182, Moscow, Russia*
[3]*Moscow Institute of Physics and Technology, 141700, Dolgoprudny, Moscow Region, Russia*

Abstract

Angular distributions of fission fragments from the neutron-induced fission of [232]Th, [233]U, [235]U, [238]U, [239]Pu, [nat]Pb and [209]Bi have been measured in neutron energy range 1–200 MeV at the neutron TOF spectrometer GNEIS based on the spallation neutron source at 1 GeV proton synchrocyclotron of the NRC KI – PNPI (Gatchina, Russia). The multiwire proportional counters have been used as a position-sensitive fission fragment detector. A description of the experimental equipment and measurement procedure is given. The anisotropy of fission fragments deduced from the data on measured angular distributions is presented in comparison with experimental data of other authors, first of all, the recent data from LANL and CERN. The data on anisotropy and angular distributions of fission fragments in neutron energy range above 20 MeV for [233]U, [239]Pu, [nat]Pb and [209]Bi have been obtained for the first time.

1. Introduction

Neutron-induced fission cross-sections and angular distributions of fission fragments are the main sources of information about fission barrier structure and nuclear transitional states on the barrier. The relevant experimental data have been accumulated over decades, mostly for $E_n < 20$ MeV (E_n is the energy of incident neutrons). These data are not only of high scientific value, but of great significance for nuclear technologies as well. Nowadays, a discussion on accelerator-driven systems for nuclear power generation and nuclear transmutation has created considerable interest to nuclear fission at intermediate ($E_n < 200$ MeV) and higher neutron energies.

Angular distributions of fission fragments are associated with two phenomena. First, an ensemble of spins of fissioning nuclei is to be aligned and, second, distribution of transitional states over the projection K of nuclear spin on the fission axis should be non-uniform. The first factor is determined by the processes which precede fission, while the latter one is given by the mechanism of fission. At the energies much exceeding the fission barrier, the fission is preceded by the multi-step particle emission. A relative contribution of equilibrium and non-equilibrium processes into the dynamics of highly excited nuclei is not clear up to now. The measurements of angular distributions of fragments from neutron-induced fission at the energies up to 200 MeV may shed some light on this question.

In this report, we summarize the results of the measurements carried out at the neutron time-of-flight (TOF) spectrometer GNEIS [1, 2] of the NRC KI – PNPI during the last few years. In a series of journal articles [3–5], we have reported the data on angular distributions and anisotropy of fragments from neutron-induced fission of the target nuclei [235]U, [238]U and

[232]Th [3], [233]U and [209]Bi [4], [239]Pu and [nat]Bi [5] in the intermediate energy range 1–200 MeV. Some more details of the measurements, as well as the results, can be found elsewhere [6–10].

2. General description of the experiment

The measurements were carried out at the 36 m flight path of the neutron TOF-spectrometer GNEIS. A schematic view of the experimental set-up is shown in Fig. 1. Detailed description of the set-up and 8-input readout system based on two DC-270 Acqiris waveform digitizers can be found in our previous publications [3-10].

The targets of [232]Th (100 %) and [235]U (90 % enrichment) ~150–200 µg/cm^2 of thickness were produced by vacuum deposition of tetrafluorides of these materials on a 2 µm thick Mylar foil. The [233]U (82.9 %) target ~200 µg/cm^2 of thickness and [238]U (natural uranium) target 350 µg/cm^2 of thickness were made by painting technique with U_3O_8 deposits on a 100 µm thick Al foil. The [239]Pu (99.76 %) target ~300 µg/cm^2 of thickness was made using the same technique with a PuO_2 deposit. The targets of [nat]Pb and [209]Bi ~150–1000 µg/cm^2 of thickness were produced by vacuum deposition of high purity metal on a 2 µm thick Mylar foil.

The fission fragment registration was performed by two coordinate-sensitive multiwire proportional counters D1 and D2 (MWPC) 140×140 mm^2 of size. The fragment counters D1 and D2 were placed close to the target in the beam one after the other. The neutron beam axis came through the geometrical centers of the target and the MWPC's electrodes being perpendicular to them. In order to have a possibility to take into account for the linear momentum contribution into the measured angular distribution, the measurements with two set-up orientations relative to the beam direction (downstream and upstream) were performed.

Time and pulse-height analysis of the signal waveforms allowed to derive the neutron energy and the fission fragment coordinates on the MWPCs, and, hence, the angle information. A value of cos(θ), where θ is an angle between neutron beam axis and fission fragment momentum, can be derived easily from the coordinates of the fission fragment measured by two counters.
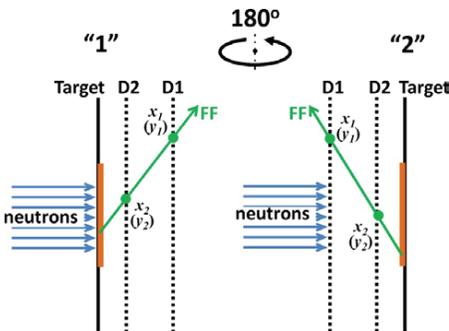
Fig. 1a. Schematic view of the experimental set-up at two orientations relative to the neutron beam direction (downstream and upstream).
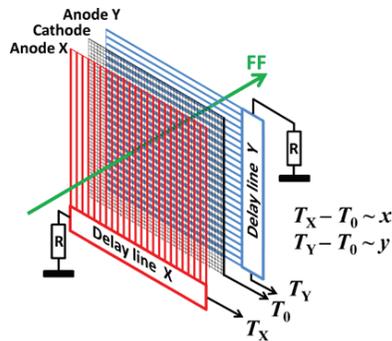
Fig. 1b. Construction of the MWPC. The coordinates are determined from the time delay of signals from anodes (T_X and T_Y) with respect to a signal from the cathode (T_0).

The measured angular distributions for selected fission fragment events were corrected for the efficiency of fission fragment registration. This efficiency was calculated by means of the Monte-Carlo method taking into account following parameters: the electrode wire structure, distances between MWPCs and target, sizes of electrodes and distances between them, sizes of the target and neutron beam, the position (angular) resolution (~2 mm). Also, the additional corrections due to the differential nonlinearity of the delay line chips and the mutual influence (signal cross-talk) of the anodes of two adjacent MWPCs were taken into account [4].

An anisotropy $W(0^o)/W(90^o)$ of angular distributions of fission fragments in the center-of-mass system were deduced from the corrected $\cos(\theta)$ angular distributions in the laboratory system for two set-up orientations relative to the neutron beam direction ($\cos(\theta)$ bins were equal to 0.01) by fitting them in the range $0.24 < \cos(\theta) < 1.0$ by the sum of even Legendre polynomials up to the 4-th order.

3. Results and discussion

Until 2000, practically all measurements [11–23] of the fission fragment angular distributions were carried out using beams of monoenergetic neutrons in energy range below 14 MeV (sometimes up to 24 MeV) at the Van-de-Graaff and Cockroft-Walton accelerators, as well as in the energy range 20–100 MeV at the cyclotron of the TSL (Uppsala) [21,24].

A new age in experimental investigations of the fission fragment angular distributions started when new experiments dedicated to this problem have been initiated nearly simultaneously by the GNEIS team at NRC KI – PNPI [3–10], the n_TOF Collaboration at CERN [25–29], and the NIFFTE Collaboration in Los Alamos [30, 31]. The pulsed high-intensity "spallation" neutron sources of these facilities enable to carry out TOF-measurements of the neutron-induced fission cross sections and fission fragment angular distributions in intermediate neutron energy range 1–300 MeV. The other two principally important features of the experimental techniques employed by these research groups are usage of the multichannel position-sensitive detectors of fission fragments of different degree of complexity (MWPCs, PPACs, TPC), and application of the wave-form digitizers for detector pulse processing.

The anisotropy $W(0^o)/W(90^o)$ obtained at the GNEIS by fitting the fission fragment angular distributions measured for ^{232}Th, ^{233}U, ^{235}U, ^{238}U, ^{239}Pu, ^{nat}Pb and ^{209}Bi in the neutron energy range 1–200 MeV is shown in Fig. 2–8. The figures also show experimental data obtained by other authors [11–31]. It can be stated that the results obtained at the GNEIS below ~ 20 MeV adequately represent the structures in energy behavior of the anisotropy observed in early measurements, and this circumstance ensures reliability of the experimental technique employed. At present, a comparison of our results obtained in the energy range 20–200 MeV for ^{232}Th, ^{235}U and ^{238}U can be done with analogous data measured at LANL and n_TOF. Fig. 3 displays obvious disagreement between our data for ^{235}U [3] and those obtained by n_TOF (Leal-Cidoncha [28]) and LANL (Kleinrath [30]) in a whole energy range 1-200 MeV. The latest data sets presented by n_TOF [29] and LANL [31] collaborations shown in Fig. 8 significantly improved agreement with our data though their numerical data still are absent in the EXFOR data base. Large uncertainties of the ^{238}U data presented by n_TOF (Leal-Cidoncha [29]) do not allow to make an unambiguous conclusion about agreement between our data sets above ~ 20 MeV (Fig. 4), whereas data by Ryzhov [25] are definitely higher that our data above ~ 40 MeV. In a case of ^{232}Th shown in Fig. 5, one of two data sets obtained by n_TOF [25–27] agrees within experimental uncertainties with our data above ~ 20 MeV (Leong [25]), while the other (Tarrio [27]) is much higher. And again,

data by Ryzhov [25] are higher than all other data sets. The observed disagreements leave a space for thorough analysis of the possible systematic errors specific for every experimental procedure used in the measurements mentioned above.
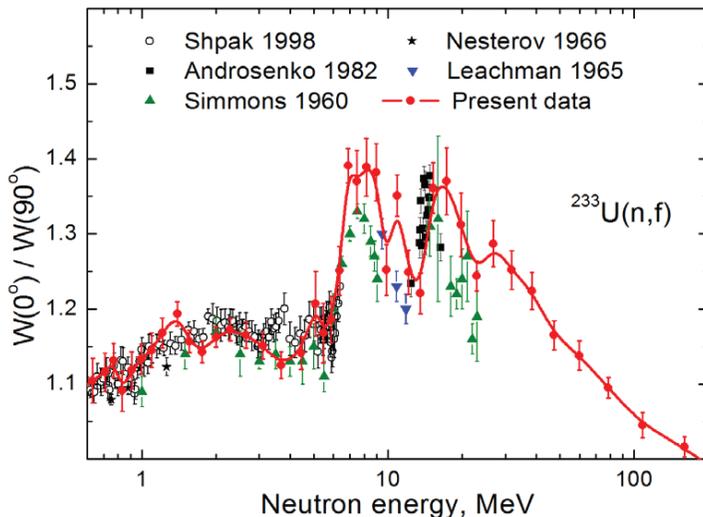
Fig. 2. Anisotropy of fission fragments of ^{233}U.
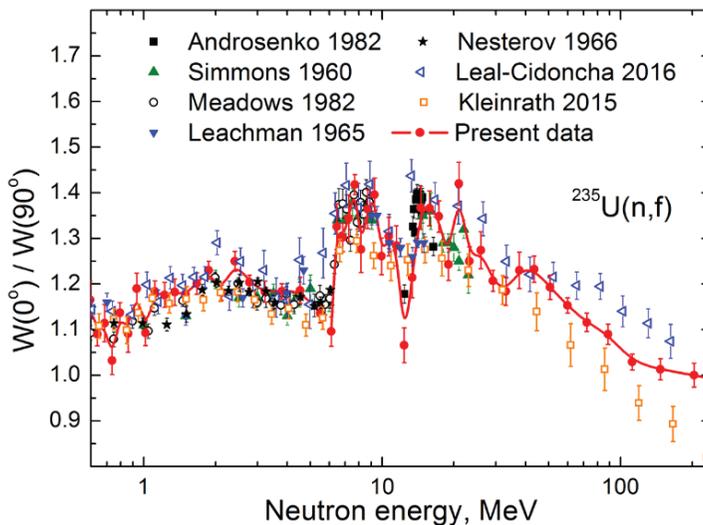
Fig. 3. Anisotropy of fission fragments of ^{235}U.
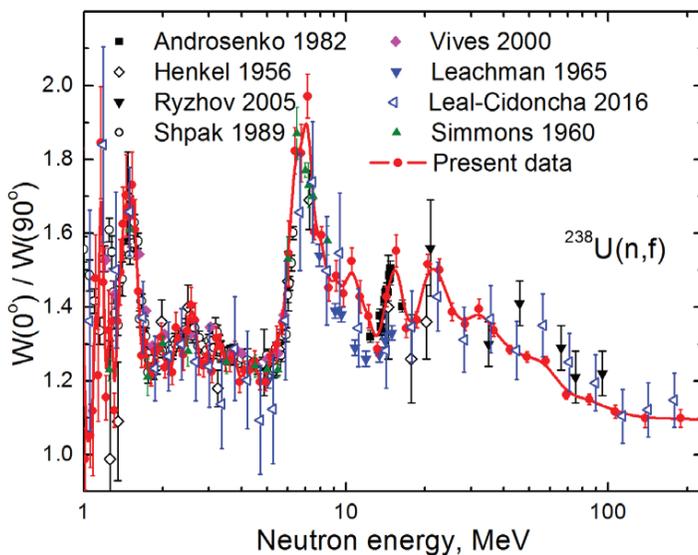
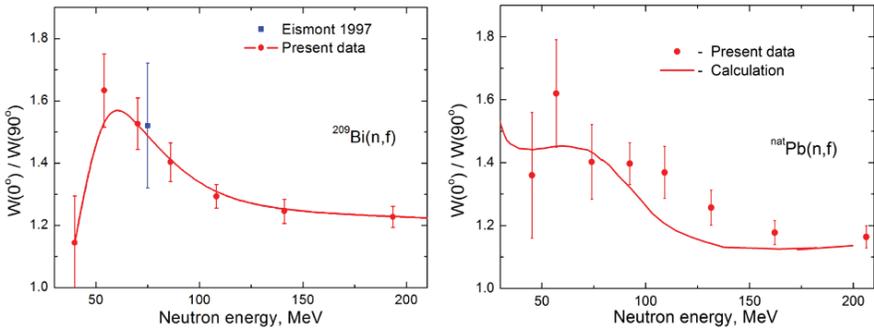Fig. 4. Anisotropy of fission fragments of ^{238}U.
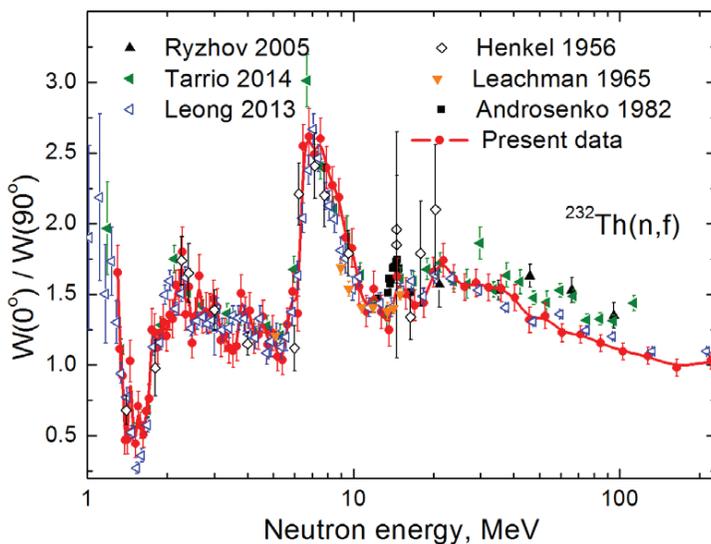
Fig. 5. Anisotropy of fission fragments of ^{232}Th.
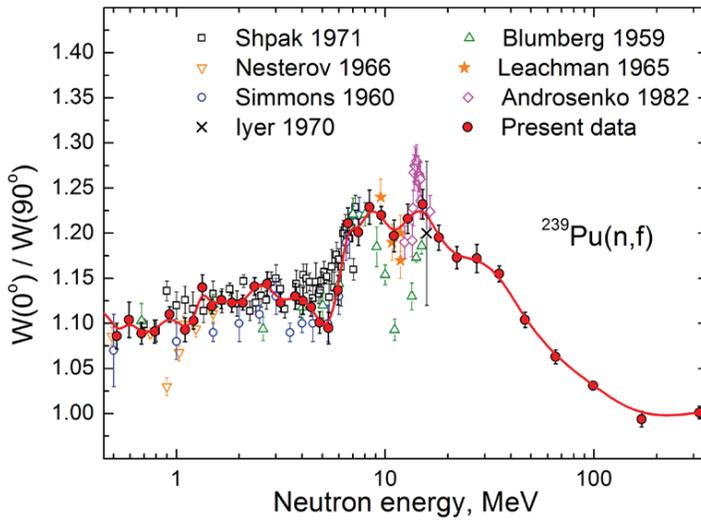
Fig. 6. Anisotropy of fission fragments of ^{239}Pu.

Fig. 7. Anisotropy of fission fragments of ^{209}Bi (left) and ^{nat}Pb (right).

An undoubted achievement of present work is the fact that experimental data on fission fragment angular distributions above ~ 20 MeV for ^{233}U, ^{239}Pu, ^{nat}Pb and ^{209}Bi have been obtained for the first time. For ^{nat}Pb and ^{209}Bi the measurements are especially difficult because neutron-induced fission cross sections of these nuclei are 10–100 lower than those of actinides. As a consequence, background problems and low counting statistics lead to vast machine-time expenditures.

Our next goal is a measurement of the fission fragment angular distributions for ^{237}Np. The only one data set for this nucleus was obtained in neutron energy range from 0.1 MeV up to 1 GeV at the n_TOF (Leong [25]). Unfortunately, it is characterized by large error bars and, therefore, can't be treated as a completed research. An upper neutron energy range of the

other (comparatively old) experimental data for [237]Np included in the EXFOR data base do not exceeds 15 MeV.
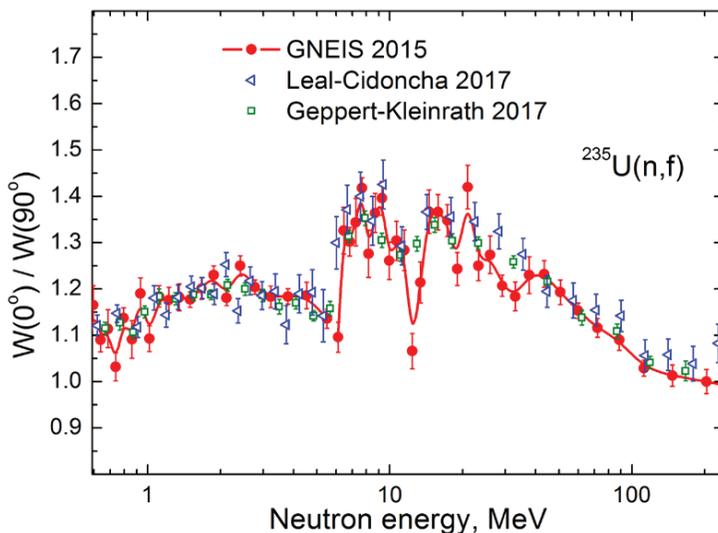
Fig. 8. Anisotropy of fission fragments of [235]U.

Acknowledgments

References

1. N.K. Abrosimov, G.Z. Borukhovich, A.B. Laptev, V.V. Marchenkov, G.A. Petrov, O.A. Shcherbakov, Yu.V. Tuboltsev, and V.I. Yurchenko, Nucl. Instrum. Methods Phys. Res. A **242**, 121 (1985).
2. O.A. Shcherbakov, A.S. Vorobyev, and E.M. Ivanov, Phys. Part. Nucl. **49**, 81 (2018).
3. A.S. Vorobyev, A.M. Gagarski, O.A. Shcherbakov, L.A. Vaishnene, and A.L. Barabanov, JETP Letters **102(4)**, 203 (2015).
4. A.S. Vorobyev, A.M. Gagarski, O.A. Shcherbakov, L.A. Vaishnene, and A.L. Barabanov, JETP Letters **104(6)**, 365 (2016).
5. A.S. Vorobyev, A.M. Gagarski, O.A. Shcherbakov, L.A. Vaishnene, and A.L. Barabanov, JETP Letters **107**(9), 521 (2018).
6. A.S. Vorobyev, A.M. Gagarski, O.A. Shcherbakov, and L.A. Vaishnene. In book "XXIII International Seminar on Interaction of Neutrons with Nuclei", Dubna, May 25–29, 2015. JINR, E3-2016-12, 2016, p.73.

7. A.S. Vorobyev, A.M. Gagarski, O.A. Shcherbakov, L.A. Vaishnene. In book "XXIV International Seminar on Interaction of Neutrons with Nuclei", Dubna, May 24–27, 2016. JINR, E3-2017-8, 2017, p.343.

8. A.S. Vorobyev, A.M. Gagarski, O.A. Shcherbakov, L.A. Vaishnene, and A.L. Barabanov. In book "XXIV International Seminar on Interaction of Neutrons with Nuclei", Dubna, May 24–27, 2016. JINR, E3-2017-8, 2017, p.413.

9. A.S. Vorobyev, A.M. Gagarski, O.A. Shcherbakov, L.A. Vaishnene, and A.L. Barabanov. In book "XXV International Seminar on Interaction of Neutrons with Nuclei", Dubna, May 22–26, 2017. JINR, E3-2018-12, 2018, p.343.

10. A.S. Vorobyev, A.M. Gagarski, O.A. Shcherbakov, L.A. Vaishnene, and A.L. Barabanov, Proc. of the Int. Conf. "Nuclear data for Science and Technology ND-2016", September 11–16, 2016, Bruges, Belgium. EPJ Web of Conferences **146**, 04011 (2017).

11. R.L. Henkel and J.E. Brolley Jr, Phys. Rev. **103**, 1292 (1956).

12. L. Blumberg, R.B. Leachman, Phys. Rev. **116**, 102 (1959).

13. J.E. Simmons and R.L. Henkel, Phys. Rev. **120**, 198 (1960).

14. R.B. Leachman and L. Blumberg, Phys. Rev. **137**, B814 (1965).

15. V.G. Nesterov, G.N. Smirenkin, and D.L. Shpak, Yadernaya Fizika **4(5)**, 993 (1966).

16. R.H. Iyer, M.L. Sagu, in Proc. of the Nuclear Physics and Solid State Physics Symposium, Dec. 27–30, 1970; Madurai, India: Nuclear Physics, Vol. **2**, p.57 (1970).

17. D.L. Shpak, Yu.B. Ostapenko, G.N. Smirenkin, Sov. J. of Nucl. Physics **13**, 547 (1971).

18. Kh.D. Androsenko, G.G. Korolev, and D.L. Shpak, VANT, Ser. Yadernye Konstanty **46(2)**, 9 (1982).

19. J.W. Meadows and C. Budtz-Jorgensen, Proc. of the Conf. on Nuclear Data for Science and Technology, Antwerp 1982, p.740.

20. D.L. Shpak, Yadernaya Fizika, Vol. **50(4)**, 922 (1989).

21. V. Eismont, A. Kireev, I. Ryzhov, et al., in Proc. of the Int. Conf. on Nuclear Data for Science and Technology, May 19–24, 1997; Trieste, Italy, Conf. Proc., **59**, 658 (1997).

22. D.L. Shpak, Physics of Atomic Nuclei, 61(8), 1333 (1998).

23. F. Vives, F.-J. Hambsch, G. Barreau, et al., Nucl. Phys. **A662**, 63 (2000).

24. I.V. Ryzhov, M.S. Onegin, G.A. Tutin, et al., Nucl. Phys. **A760**, 19 (2005).

25. L.S. Leong, PhD Thesis, Universite Paris Sud, CERN-Thesis-2013-254.

26. L.S. Leong, L. Tassan-Got, D. Tarrio, et al., Proc. of the Int. Conf. "Nuclear data for Science and Technology ND-2013", March 4–8, 2013, New York, USA. EPJ Web of Conferences **62**, 08003 (2013).

27. D. Tarrio, L.S. Leong, L. Audouin et al., Nuclear Data Sheets, **119**, 35 (2014).

28. E. Leal-Cidoncha, I. Duran, C. Paradela, et al., Proc. of "4th International Workshop on Nuclear Data Evaluation for Reactor applications WONDER-2015", October 5–8, 2015, Aix-en-Provence, France. EPJ Web of Conferences **111**, 10002 (2016).

29. E. Leal-Cidoncha, et al., FIESTA 2017, LANL FIESTA Fission School & Workshop, Santa Fe, 17–22 September 2017. https://t2.lanl.gov/fiesta2017/Talks/Leal-Cidoncha.pdf

30. V. Kleinrath, PhD Thesis, Technischen Universitat Wien, 2015.

31. V. Geppert-Kleinrath, F. Tovesson, J.S. Barrett, et al., arXiv: 1710.00973v1 [nucl-ex] 3 Oct 2017.

The Wall Effect of the Sample Position Well in the Measurement of Fission Fragments

Huaiyong Bai, Haoyu Jiang, Yi Lu, Zengqi Cui, Jinxiang Chen, Guohui Zhang[*]

State Key Laboratory of Nuclear Physics and Technology, Institute of Heavy Ion Physics, Peking University, Beijing 100871, China

Yu.M. Gledenov, M.V. Sedysheva
Frank Laboratory of Neutron Physics, JINR, Dubna 141980, Russia

G. Khuukhenkhuu
Nuclear Research Centre, National University of Mongolia, Ulaanbaatar, Mongolia

*Corresponding author: guohuizhang@pku.edu.cn

Abstract: The twin-gridded ionization chamber is widely used in the measurement of charged particles from neutron induced reactions. In many cases, a ^{238}U sample is mounted in the sample position well at the common cathode to monitor the neutron flux. In the experiments, some of the fission fragments with emission angle near 90° will collide with the inner wall of the sample position well, leading the measured pulse height to be lower, i.e. the wall effect of the sample position well. The wall effect of the sample position well is affected by the working gas pressure and the dimension of the ^{238}U sample and the sample position well. In the present work, simulations and experiments are performed to quantify the influence of the working gas pressure and the dimension of the ^{238}U sample and the sample position well on the wall effect of the sample position well in the measurement of ^{238}U fission fragments.

Key words: ionization chamber; wall effect; sample position well; fission fragments

1. Introduction

The measurement of neutron induced fission fragments is highly concerned in radiation measurement for the following two aspects. Firstly, the standard cross sections are useful in monitoring the neutron flux [1,2], i.e. ^{235}U(n, f) and ^{238}U(n, f). Secondly, the research on neutron induced fission fragments is important in nuclear physics and applications [3,4]. Gridded ionization chambers are widely used in measuring the neutron induced fission fragments because of its high detection efficiency, γ insensitive and radiation resistant, et al. [4–7]. In many cases, the prepared fissile samples are mounted in a sample position well to simultaneously measure the emitted fission fragments in both the forward and the backward directions, or to replace the samples conveniently [8,9]. In these situations, the fission fragment may collide with the inner wall of the sample position well and only a part of its kinetic energy can be deposited in the working gas. Thus, the measured pulse amplitude of the corresponding event will be lower [7]. This is the wall effect of the sample position well for fission fragments which is simplified as the wall effect below.

The wall effect can decrease the proportion of the fission events above the measurement threshold, which means that the determined detection efficiency will be overestimated if the wall effect is ignored. Because the wall effect is more significant for fission fragments with lager emission angle, especially with emission angles near 90º, the measured angular distribution will be incorrect. Therefore, the wall effect for neutron induced fission fragments is important.

271

In the present work, the wall effect for neutron induced fission fragments is studied using Monte Carlo simulation reliability of which is validated by the experiment. In section 2, the measurement of the energy spectrum of neutron induced fission fragments is illustrated, and the Monte Carlo simulation of the energy spectrum is introduced. In section 3, the factors of the wall effect is studied using the Monte Carlo simulation. Finally, the conclusions are drawn in section 4.

2. The experiment and the simulation

2.1 The experiment

The sketch of the experimental setup, including a neutron source and a gridded ionization chamber, is presented in Fig. 1. The 5.5 MeV neutrons were generated using a deuterium gas target bombarded by the deuteron beam. The pressure of the gas target was ~0.30 MPa and the length was ~2.0 cm. The deuteron beam ~2.5 μA was accelerated by the 4.5 MV Van de Graff accelerator of Peking University.

The gridded ionization chamber, details of which were presented in Ref. [9], was used as the detector of the charged particles. The separation of the cathode-grid was ~61.0 mm and that of the grid-anode was ~15.0 mm. The working gas was Kr + 2.7% CO_2 mixtures 0.052 MPa in pressure. The grid shielding inefficiency was about 0.017 [7, 10]. The data acquisition system (DAqS), with which the cathode-anode coincident signals can be recorded, was introduced in Ref. [11].
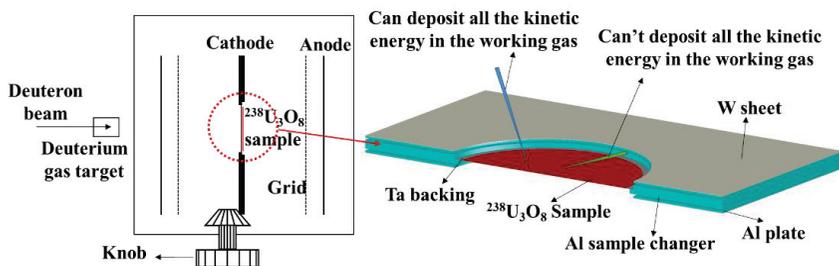
Fig. 1. The sketch of the experimental setup.

At the cathode of the gridded ionization chamber, there was a sample changer with five sample position wells. Back-to-back samples can be mounted in each of them as shown in Fig. 1. The sample changer was made of aluminum. Except for the measured sample, the samples mounted in the other sample position wells were covered by aluminum plates at both sides [7]. To decrease the background of neutron induced charged particles, the whole cathode was covered by tungsten sheets at both sides. The thicknesses of the tungsten sheets were 0.1 mm. The radii of the sample position wells were ~24.0 mm and the depths were ~2.0 mm [7].

A highly enriched $^{238}U_3O_8$ sample (> 99.999%) was used in the experiment [12]. This $^{238}U_3O_8$ sample was prepared using painting method with 22.5 mm in radius. The thickness of the $^{238}U_3O_8$ sample was about 605 μg/cm^2 with non-uniformity ~1.00 [13]. The sample was mounted in one of the five sample position wells as shown in Fig. 1. The backing was a tantalum sheet 0.1 mm in thickness.

The measured energy spectrum of the neutron induced fission fragments is illustrated in Fig. 2. The energy of the higher energy peak is ~90 MeV according to the simulation

introduced below. Since the position of the peak is not very clear, a little deviation of the determined energy is expected.
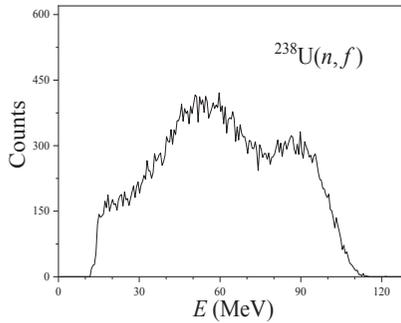
Fig. 2. The measured energy spectrum of the neutron induced fission fragments.
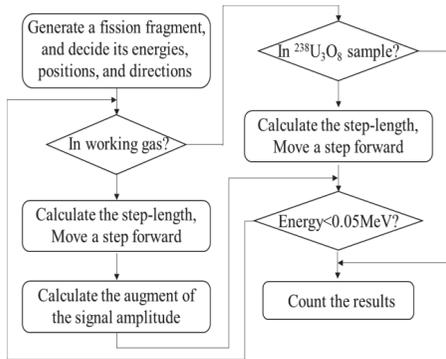
Fig. 3. The flowchart of the Mote Carlo simulation.

2.2 The simulation

The simulation is based on Monte Carlo method which is similar to that introduced in Ref. [13]. According to Ref. [13], the effect of the scattering of the fission fragment can be ignored without inducing noticeable deviations, and only those fission fragments with orientations toward the working gas need to be tracked.

The flowchart of the simulation is presented in Fig. 3. In the simulation, A fission fragment (atomic number, mass and yield) is sampled from the cumulative fission products yields taken from ENDF/B-VII.1 library [14,15]. The fission fragments with yields which are lower than 1/1000 of the highest one are ignored in the simulation to improve the efficiency of the simulation. The energy of the fission fragment E_f is determined by its mass using the results of Ref. [4]. As the energies of different fragments with the same mass may be different, a random number E_w is sampled from normal distribution $N(0, \sigma_w)$ where σ_w is the width of the energy as a function of the mass published by Birgersson [4]. The initial energy of the fission fragment in the simulation is $E_f + E_w$. The (x, y) position of the fission fragment is

sampled randomly with the restriction of $x^2 + y^2 \leq r^2$ ($r = 22.5$ mm which is the radius of the $^{238}U_3O_8$ sample). The thickness h of the $^{238}U_3O_8$ sample at (x, y) equals to the average thickness multiplying w which is a weight factor sampled from the normal distribution $N(1.00, 1.00)$ because the non-uniformity of the $^{238}U_3O_8$ sample is 1.00 [13]. If the sampled w is negative or bigger than 10, a new w will be sampled to make sure that the thickness of the $^{238}U_3O_8$ sample is reasonable. The z position of the fission fragment is randomly sampled from [0 h]. The orientation of the fission fragment is sampled from isotropic distribution [15]. Since the probability of the fission reaction is proportional to the thickness, the weight of the fission fragment is wy where y is the yield of the fission fragment taken from ENDF/B-VII.1 library [15].

The fission fragment moves forward step by step. In each step the energy loss is set to be 0.05 MeV with step length decided by the stopping power calculated using SRIM-2013 Code [16]. If the fission fragment entrances the working gas, the energy ΔE deposited in each step will increase the anode signal amplitude of the gridded ionization chamber by ΔA calculated using

$$\Delta A = \Delta E \left(1 - \eta \frac{d}{D_{cg}}\right), \tag{1}$$

where η is the grid shielding inefficiency, d is the distance from the cathode to the spot where the energy ΔE is deposited, and D_{cg} is the separation of the cathode-grid. It should be pointed out that the stopping powers of the fission fragments with the same atomic number are assumed to be the same, and this will not induce noticeable deviations as explained in Ref. [13].

The fission fragment will not stop unless its energy is degraded below 0.05 MeV or it collides with the inner wall of the sample position well. After it stops, the fission fragment will be counted. The simulated results of 10^5 fission fragments are shown in Fig. 4. In the simulated energy spectrum of the neutron induced fission fragments, the valley near 0 MeV is caused by the gap between the inner wall of the sample position well and the edge of the $^{238}U_3O_8$ sample, and the counts at 0 MeV is caused by the self-absorption effect.
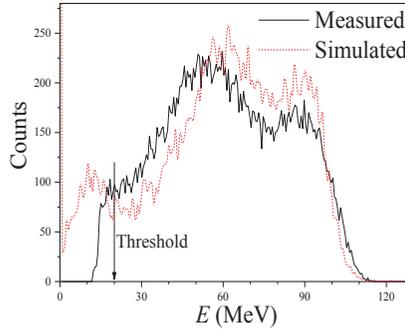
Fig. 4. The energy spectra of neutron induced fission fragments. The solid line and the dashed line are the measured and simulated ones, separately.
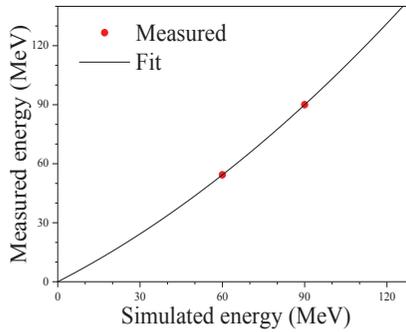
Fig. 5. The relationship between the measured energy and the simulated energy of the neutron induced fission fragments.
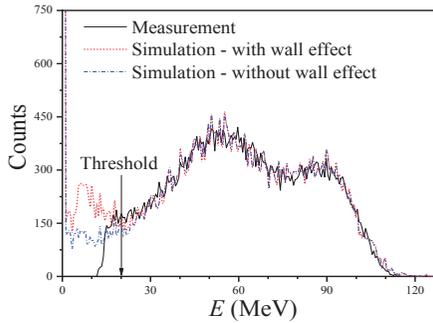
Fig. 6. The energy spectra of the neutron induced fission fragments. The solid line is the measured one. The dashed line and the dash dotted line are the simulated ones with and without considering the wall effect, respectively.

Since the Pulse Height Defect (PHD) effect is not considered in the simulation, the energy of the measured lower energy peak is lower than that of the simulated one. Actually the energy of the measured higher energy peak should also be lower than that of the simulated one due to the PHD effect. Because the PHD effect is generally more significant for heavy fission fragments which correspond to the lower energy peak [17], the energy of the measured lower energy peak is still lower than that of the simulated one even if the energy of the measured higher energy peak is assumed to be equal to that of the simulated one [13]. The PHD effect has not been measured by us, and there is no related data which can be used according to our knowledge. The simulated energy of the neutron induced fission fragment is adjusted using [13]

$$E_M = aE_s + bE_s^2, \qquad (2)$$

where E_M and E_S are the energies of the two peaks of the measured and the simulated energy spectra, separately, a and b are the fitting parameters. Because the PHD effect is more noticeable for heavy fission fragments [8], the increase of the measured energy is slower in lower energy region as shown in Fig. 5. After the energy scaling, the simulated energy spectra

accords well with the measured one as presented in Fig. 6, and this proves that the simulated result is reliable.

As shown in Fig. 6, the difference between the simulations with and without considering the wall effect is obvious in low energy regions. If the wall effect is ignored, the detection efficiency above the measurement threshold will be overestimated by 5% which proves the significance of the wall effect.

3. Discussions about the wall effect

To illustrate the wall effect more clearly, simulation, in which the self-absorption and the PHD effects are ignored to exclude their interferences, is performed. In this case, only the wall effect can affect the energy deposition in the working gas and the result indicates that ~14% of the fission fragments will be affected by the wall effect. As shown in Fig. 7, the tail below 50 MeV is caused by the wall effect.
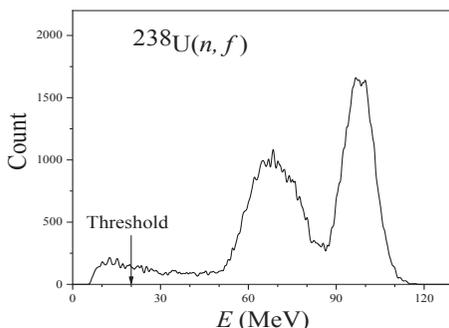
Fig. 7. The simulated energy spectrum of the neutron induced fission fragments.
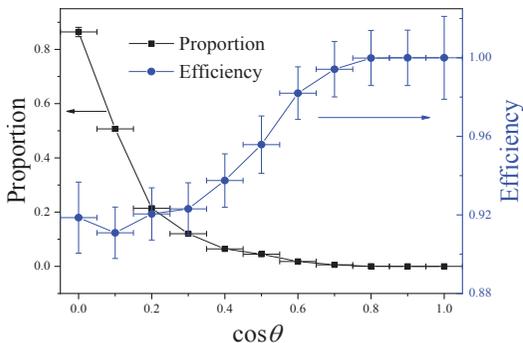
Fig. 8. The proportion of the fission fragments with the wall effect (square) and the detection efficiency of the fission fragments (circle) as functions of the cosine of the emission angle.

3.1 The wall effect for fission fragments with different emission angles

If the fission fragment collides with the inner wall of the sample position well, only a part of its energy will be deposited in the working gas. Thus, the signal amplitude of the fission fragments may be decreased to below the measurement threshold, so that the corresponding detection efficiency may be decreased. In Fig. 8, the proportion of the fission

fragments with the wall effect and the detection efficiency of the fission fragments as functions of the cosine of the emission angle are presented. If the emission angle is bigger than 45° ($\cos\theta < 0.7$) the wall effect will be noticeable. As shown in Fig. 8, the bigger of the emission angle, the higher proportion of the fission fragments with the wall effect and the lower detection efficiency of those fission fragments are. This indicates that if the wall effect is ignored, the detection efficiency will be overestimated and the measured angular distribution will be incorrect.

3.2 Factors which influence the wall effect

The wall effect can be influenced by some factors which will affect the collisions between the fission fragments and the inner wall of the sample position well. In general, the lower pressure of the working gas (the longer range of the fission fragment), the bigger radius of the $^{238}U_3O_8$ sample, the smaller radius and the deeper depth of the sample position well, the stronger of the wall effect is. To illustrate the influences of these factors, simulations are performed and the results are illustrated in Fig. 9.
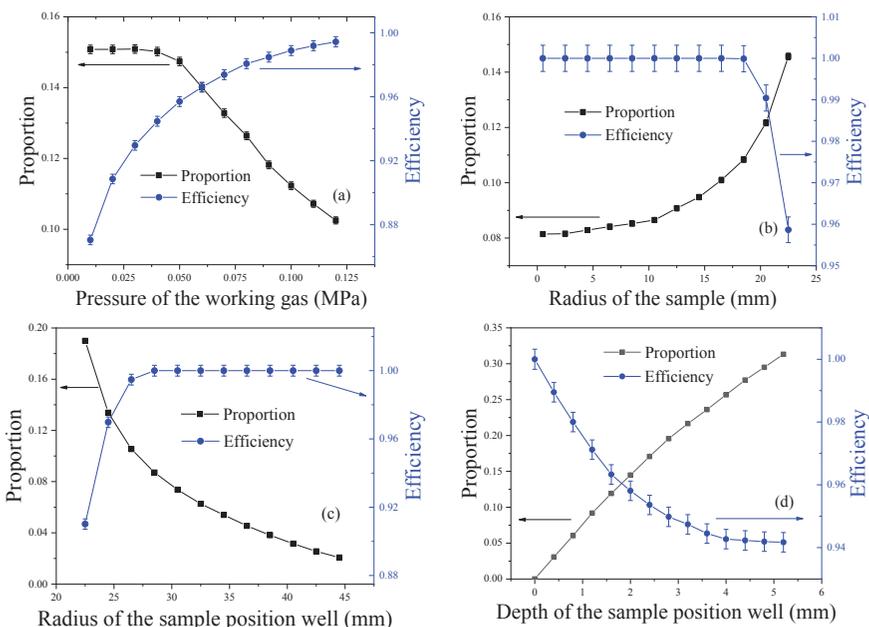
Fig. 9. The proportion of the fission fragments with the wall effect (square), and the detection efficiency of the fission fragments (circle). (a), the influence of the working gas pressure (the radius of the sample is 22.5 mm, the radius and the depth of the sample position well are 24.0 and 2.0 mm, separately); (b), the influence of the radius of the $^{238}U_3O_8$ sample (the working gas pressure is 0.052 MPa, the radius and the depth of the sample position well are 24.0 and 2.0 mm, respectively); (c), the influence of the radius of the sample position well (the working gas pressure is 0.052 MPa, the radius of the sample and the depth of the sample position well are 22.5 and 2.0 mm, separately); and (d), the influence of the depth of the sample position well (the working gas pressure is 0.052 MPa, the radii of the sample and the sample position well are 22.5 and 24.0 mm, respectively).

As shown in Fig. 9(a), the proportion of the fission fragments with the wall effect decreases with the increase of the working gas pressure because more fission fragments will be stopped before they reach the inner wall of the sample position well. As a result, the detection efficiency will be higher since the wall effect is weaker.

In Fig. 9(b), the proportion of the fission fragments with the wall effect increase with the increase of the radius of the sample, because the fission fragments generated near the inner wall of the sample position well are more likely to collide with the inner wall of the sample position well. Although the proportion of the fission fragments is higher and higher, the detection efficiency of the fission fragments will not change if the radius of the sample is smaller than 16.5 mm. This is because the separation between the sample's edge and the inner wall of the sample position well is big enough so that the deposited energies of the fission fragments are high enough to surpass the measurement threshold.

Contrary to the situation in Fig. 9(b), the proportion of the fission fragments with the wall effect decreases with the increase of the radius of the sample position well as shown in Fig. 9(c). Thus, the detection efficiency of the fission fragment increase with the increase of the radius of the sample position well. If the radius of the sample position well is bigger than 28.5 mm, all the fission fragments will be detected although some fission fragments are still affected by the wall effect. This is because before the fission fragment reaches the inner wall of the sample position well, the deposited energy will be high enough to surpass the measurement threshold.

Fig. 9(d) shows that the proportion of the fission fragments with the wall effect increases with the increase of the depth of the sample position well, because the fission fragment with smaller emission angle may collide with the inner wall of the sample position well if the sample position well is deeper. The detection efficiency of the fission fragments thus decreases with the increase of the depth of the sample position well.

4. Conclusions

In the present work, the wall effect of the fission fragments is illustrated using Monte Carlo simulation. According to the simulation, the proportion of the fission fragments with the wall effect can be as big as 14%, and the wall effect is more significant for the fission fragment with larger emission angle. Because the detected energy of the fission fragments with the wall effect may degraded below the measurement threshold, the determined detection efficiency of the fission fragments will be overestimated if the wall effect is ignored.

Since the conditions of the experiments may be various, the significance of the wall effect should be different. In general, the wall effect will be more significant if the working gas pressure is lower (the range of the fission fragment is longer), or the radius of the sample is bigger, or the radius of the sample position well is smaller, or the sample position well is deeper.

References

1. A.D. Carlson, V.G. Pronyaev, D.L. Smith et al., Nuclear Data Sheets 110 (2009): 3215–3324.
2. Neutron Cross-section Standards, 2006, https://www-nds.iaea.org/standards/.
3. F. Vives, F.J. Hambsch, H. Bax et al., Nuclear Physics **662** (1) (2000):63–92.
4. E. Birgersson, A. Oberstedt, S. Oberstedt et al., Nuclear Physics A **817** (2009): 1–34.
5. G. Zhang, Y.M. Gledenov, G. Khuukhenkhuu et al., Physical Review C **82** (2010): 054619.
6. G.A. Tutin, I.V. Ryzhov, V.P. Eismont et al., Nuclear Instruments and Methods in Physics Research A **457** (2001): 646–652.
7. H. Bai, Z. Wang, L. Zhang et al., Applied Radiation and Isotopes **125** (2017): 34–41.
8. D.L. Duke, F. Tovesson, A.B. Laptev et al., Physical Review C **94** (2016): 054604.
9. Z. Chen, X. Zhang, Y. Chen et al., Nuclear Physics Review **16** (1) (1999): 31–36.
10. O. Bunemann, T.E. Cranshaw, J.A. Harvey, Canadian Journal of Research A **27** (5) (1949): 191–206.
11. G. Zhang, H. Wu, J. Zhang et al., Eur. Phys. J. A **43**, 1 (2010).
12. G. Zhang, X. Liu, Z. Gao et al., Applied Radiation and Isotopes **70** (2012): 888–892.
13. H. Bai, H. Jiang, Z. Cui et al., Determination of the amount of ^{238}U target nuclei and simulation of the neutron induced fission fragment energy spectrum, submitted to Applied Radiation and Isotopes.
14. C. Jammes, P. Filliatre, P. Loiseau et al., Nuclear Instruments and Methods in Physics Research A **681** (2012): 101–109.
15. ENDF/B-VII.1, 2011, U.S. Evaluated Nuclear Data Library, https://www-nds.iaea.org/exfor/endf.htm.
16. J.F., Ziegler, 2013, SRIM -2013, http://www.srim.org/#SRIM.
17. D.L. Duke, F. Tovesson, A.B. Laptev et al., Physical Review C **94** (2016): 054604.

Measurement Technology for Primary Fission Products

Jiang Wengang[1], Qian Shaojun[1], Zhou Zuying[2], Shi Quanlin[1], Liu Shilong[2],
Li Xuesong[1], Xie Feng[1], Dai Yihua[1], Yang Yi[2], Liang Jianfeng[1]

[1]*Northwest Institute of Nuclear Technology, Xi'an 710024, Shaanxi, China*
[2]*China Nuclear Data Center, China Institute of Atomic Energy, Beijing 102413, China*

Abstract: The measurement of primary fission products is very important for the research on fission yields and the fission phenomena. It is necessary to jointly measure the mass, charge and kinetic energy of fission product. This paper mainly introduces the following four aspects: 1) Research on time-of-flight measurement of primary fission products; 2) Developing a Frisch-grid ionization chamber with silicon nitride film for measuring kinetic energy E_k of primary fission products; 3) Using the ^{252}Cf spontaneous fission source to verify the method of measuring the mass distribution of primary fission products; 4) Study on the charge measurement of the primary fission products based on its specific energy losses.

Keywords: Primary fission products, time-of-flight measurement, Frisch-grid ionization chamber, silicon nitride film, ^{252}Cf spontaneous fission, mass distribution, specific energy losses

1. Introduction

There are many programs aimed to investigate the neutron-induced fission, such as VERDI (IRMM) [1-3] and SPIDER (LANL)[4.] Those investigations are very important for inferring the independent yield of fission yield, prompt neutron and fission model about the neutron-induced fission of uranium and plutonium. But now the resolution of flight time and energy are dissatisfactory, and the charge of primary fission products cannot be measured feasible. So this paper will try to measure the charge of primary fission products using the specific energy losses obtained by the Frisch-grid ionization chamber.

2. Experimental

Measurement of primary fission product requires measuring mass, kinetic energy and charge simultaneously. The mass is acquired from the flight time and kinetic energy. The flight time is measured by a couple of time pick-up detectors. The kinetic energy is measured by a Frisch-grid ionization chamber with silicon nitride film. And the charge is measured based on specific energy losses of primary fission product.

A schematic representation of the experimental arrangement is shown in Fig. 1. Two secondary electron detectors [5, 6] are used as time pick-up detector pairs for time of flight measurement. Particle trajectories on the order of 775 mm are determined accurately within 0.5 mm.
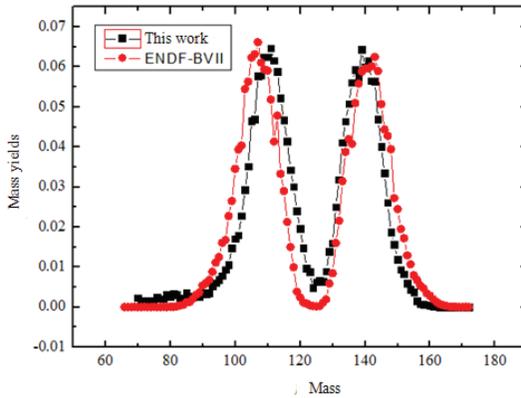
FIG.5. The mass distribution of primary fission products of ^{252}Cf.

As the same principle to a Bragg curve counter [7-9], the current signal (seen in Fig. 6.) output from the Frisch-grid ionization chamber can be used to measure the specific energy losses of primary fission products in working gas. And the nuclear stopping power of the primary fission products in working gas of the ionization chamber has been studied. There was a certain difference in the nuclear stopping power between light and heavy fission products, but the charge number Z could not be measured directly.
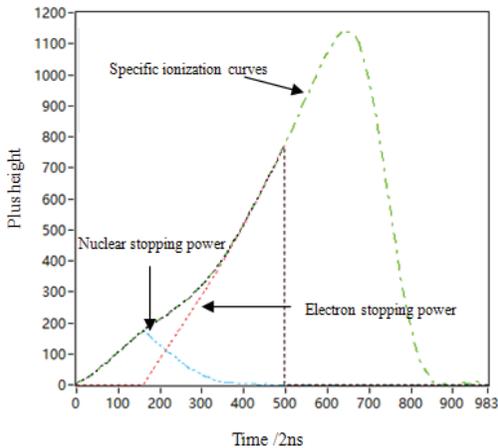
FIG.6. The specific energy losses of primary fission products obtained by the Frisch-grid ionization chamber.

References

1. M.O. Frégeau1, et al, The VERDI fission fragment spectrometer [Z]. EPJ Web of Conferences 62, 2013.
2. S. Oberstedt, et al, VERDI – a double (v, E) fission-fragment spectrometer [Z]. EFNUDAT Slow and Resonance Neutrons, Budapest (HU), Sep., 2009.
3. M.O. Frégeau, First results from the new double velocity–double energy spectrometer VERDI [J]. Nuclear Instruments and Methods in Physics Research A, 2016, **817**: 35–41.
4. C.W. Arnold, Development of position-sensitive time-of-flight spectrometer for fission fragment research [J]. Nuclear Instruments and Methods in Physics Research A, 2014, **764**:53–58.
5. Mikko Laitinen, et al, Secondary electron flight times and tracks in the carbon foil time pick-up detector [J]. Nuclear Instruments and Methods in Physics Research B, 2014, **336**: 55–62.
6. K.M. Kosev, A high-resolution time-of-flight spectrometer for fission fragments and ion beams [D]. Technische Universität Dresden, 2008.
7. T. Sanami, et al, A Bragg curve counter with an active cathode to improve the energy threshold in fragment measurements [J]. Nuclear Instruments and Methods in Physics Research A, 2008, **589**:193–201.
8. T. Sanami, et al, A Bragg curve counter with an internal production target for the measurement of the double-differential cross-section of fragment production induced by neutrons at energies of tens of MeV [J]. Nuclear Instruments and Methods in Physics Research A, 2009, **610**:660–668.
9. R. Barna, et al, PISA – an experiment for fragment spectroscopy at the Internal Beam of COSY: application of an Axial Ionization Chamber [J]. Nuclear Instruments and Methods in Physics Research A, 2004, **519**: 610–622.

MANIFESTATION OF PEAR-SHAPED CLUSTERS IN COLLINEAR CLUSTER TRI-PARTITION (CCT)

Yu.V. Pyatkov[1,2], D.V. Kamanin[2], A.A. Alexandrov[2], I.A. Alexandrova[2], Z.I. Goryainova[2], V. Malaza[3], E.A. Kuznetsova[2], A.O. Strekalovsky[2], O.V. Strekalovsky[2], V.E. Zhuchko[2]

[1]National Nuclear Research University MEPhI (Moscow Engineering Physics Institute), Moscow, Russia
[2]Joint Institute for Nuclear Research, Dubna, Russia
[3]University of Stellenbosch, Faculty of Military Science, Military Academy, Saldanha 7395, South Africa

INTRODUCTION

The majority of our experiments of recent years were dedicated to the study of new multibody at least ternary decay channel of low excited heavy nuclei [1, 2]. Due to specific features of the effect, it was called collinear cluster tri-partition (CCT). Now we have an entire collection of different CCT manifestations observed through the linear structures in the mass correlation distributions M_1–M_2 of decay products. Some of the structures look like strait lines M_1 = const or M_2 = const. The most populated structures of such sort are aggregated in so called "Ni-bump" which was analyzed in details in our previous publications [3, 4]. More specific structures satisfying the condition $M_1 + M_2$ = const, while the total mass of the fragments involved is less than the mass of the fissioning nucleus were revealed in our recent experiment at the COMETA spectrometer (JINR). The analysis of these structures is presented below.

EXPERIMENTS AND RESULTS

Our latest experiments were dedicated to searching for rare decay modes of low excited actinide nuclei with a special attention the reliability of identification of such events. The improvement of our experimental methods has been achieved by digitizing of a signal from each detector and off-line processing of the signal images. Here we present the results of the experiment (Ex1) performed using such approach. The scheme of the setup is shown in Figure 1. We used the double-armed time-of-flight spectrometer of fission fragments (FFs). Two "start" micro-channel plates based timing detectors *St1* and *St2* were placed in the center of the experimental vacuum chamber. The ^{252}Cf (sf) source was located between the detectors. Four mosaics of eight PIN diodes each provided measuring of both the FF energy and time-of-flight.

The data acquisition system consisted of the fast flash-ADC (Amplitude to Digital Convertor) CAEN DT574 multichannel digitizer, logic blocks providing trigger signals, and a personal computer. Current value of the signal was measured by the digitizer every 0.2 ns.

Time reference point on the PIN diode signal was calculated using a new algorithm proposed by us earlier [5]. The algorithm approximates the initial part of a leading edge of the signal by a parabolic curve under condition that the parabola vertex lies on the mean value of the base line. The second condition to be met consists in sewing of the parabolic curve with a line approximating the linear part of the leading edge. This means that both the values and derivatives of the parabolic and linear functions must be equal in the sewing point. The

parameters of the curve are estimated by a minimization of a χ^2 using some points of the leading edge located above the three sigma (standard deviation of the base line values) level. Experimental testing proved this method to give unbiased "true" time reference corresponding to the real beginning of the signal [5]. Thus, distortion of the time-of-flight due to so called "plasma delay" (PD) [6] is excluded.
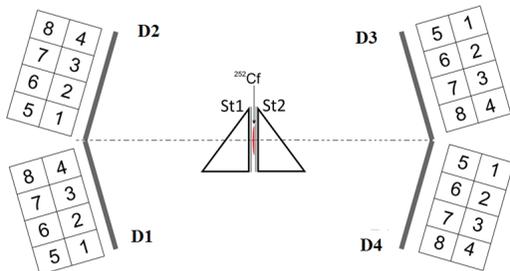

FIGURE 1. Ex1: layout of the experimental setup. The ^{252}Cf (sf) source is placed between two "start" micro-channel plates based timing detectors *St1* and *St2*. Four mosaics (D1÷D4) of eight PIN diodes each provide measuring of both the FF energy and time-of-flight.

Calculation of the FF mass taking into account pulse-height-defect (PHD) based on the parametrization proposed in [7] was performed in the iterative procedure described in [8].

FFs mass correlation distribution in the region of the "Ni-bump" [3] is presented in Figure 2(a). Due to the background conditions of this experiment, the events with the energy of the light fragment in the range $E_2 = (6÷30)$ MeV were selected.
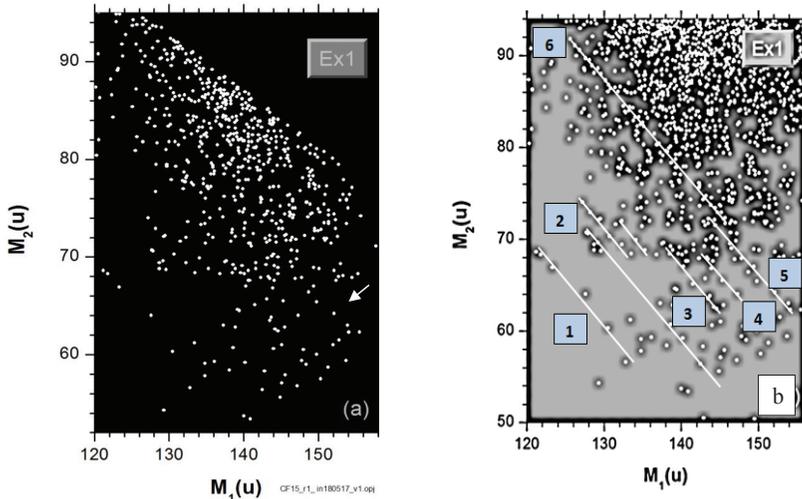
FIGURE 2. FFs mass correlation distributions from ^{252}Cf(sf) obtained in Ex1 – (a). Specific rhombic-spiral structure in the bottom of the figure ("nuclear rose") is marked by an arrow. The same distribution is shown in different graphic presentation in (b). The tilted lines marked by the numbers 1–6 meet the condition $M_1 + M_2 = $ const.

286
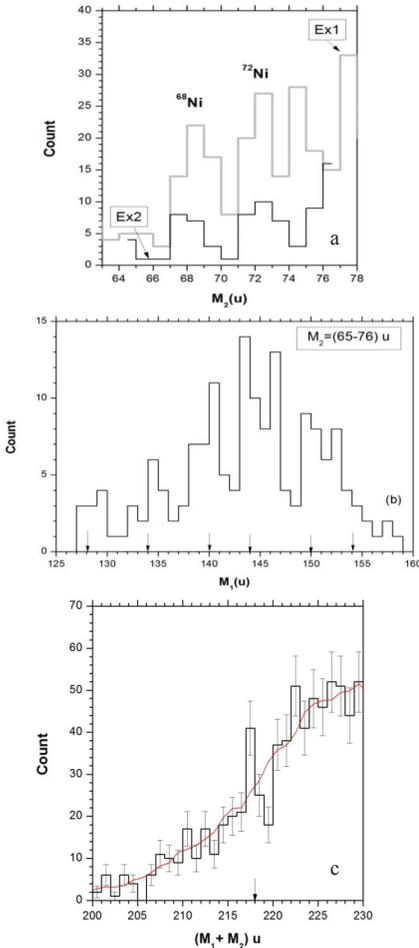
FIGURE 3. Different projections of the mass correlation distribution from Ex1 (Figure 2). Projection of the distribution is compared with that obtained earlier in Ex2 [1] – (a). Projection of the distribution onto M_1 axis under condition that $M_2 = (65–76)$ u – (b). Positions of the magic nuclei are marked by the arrows. Projection of the distribution along the direction $M_1 + M_2 = $ const – (c). The peak centered at the mass 218u is marked by the arrow. See text for details.

Different projections of the mass correlation distribution from Ex1 are shown in Figure 3.

As can be inferred from the Figure 2a the statistics in Ex1 is approximately three times more than that in Ex2 [1]. A total yield of two Ni peaks in Ex1 does not exceed 10^{-4} per binary fission which agrees with our previously obtained value. The data of Ex2 indicated that the heavy clusters in the ternary prescission configurations are predominantly magic nuclei (Table 1 in [3]). Noticeably large statistics in Ex1 allowed us to confirm previous observation. The projection of the distribution shown in Figure 2(b) onto M_1 axis for the range of $M_2 = (65–76)$ u clearly demonstrates increased yield of the heavy fragments corresponding to the magic isotopes of ^{128}Sn, ^{134}Te, ^{140}Xe, ^{144}Ba, ^{150}Ce, ^{154}Nd (their masses are marked in Figure 3(b) by the arrows).

The data from Ex1 along with the presence of the lines at the mass numbers A = 128, 68, 72 (Figure 2(a)) similar to those observed in Ex2 show some additional structures. A rhombic-spiral structure in the lower right corner of Figure 2(a) that resembles a rose depiction was called "nuclear rose". It consists of the family of lines $M_1 + M_2 \approx$ const and several lines almost perpendicular to them. The lines of the first sort (marked by the numbers 1–6 in Figure 2(b)) will be analyzed in the next section while a discussion of the latter is below the scope of this paper.

The longest line 6 in Figure 2b manifests itself not so obviously as the others. Nevertheless, projection of the mass correlation distribution along the direction $M_1 + M_2 =$ const demonstrates a statistically significant peak corresponding to this line (Figure 3c). The smoothed background in the figure is shown by the smooth curve.

Figure 4 demonstrates the linear structures from Figure 2b in detail. Presumable prescission cluster composition of the fissioning system for some point lying on the analyzed line is shown in the panels. Corresponding missed cluster in each case is shown first. Nuclear composition of the heavy magic core is marked below the line underlying the chemical symbols of two detected fragments.
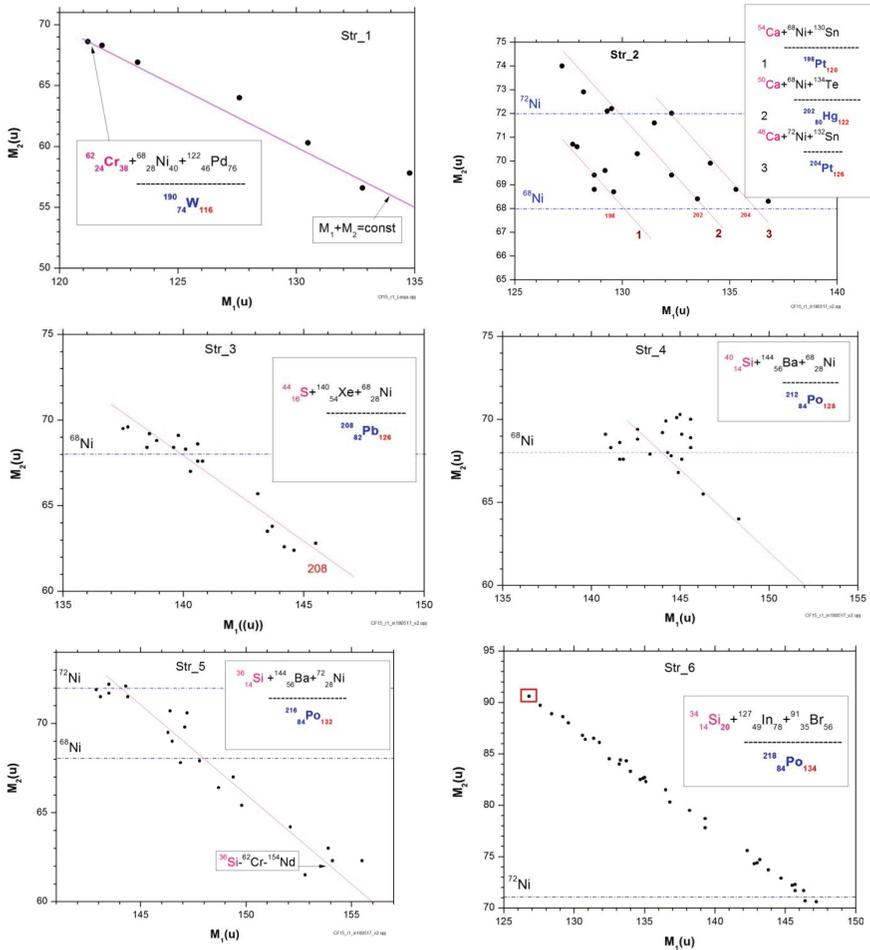
FIGURE 4. Linear structures from Figure 2b shown in detail. Presumable prescission cluster configurations of the decaying system for some points are presented in the panels. Corresponding missed cluster in each case is shown first.

Table 1. Parameters of the linear structures shown in Figure 2b.

Str №	Missing fragment	Heavy magic core	Number of neutrons	Experiments
		Parameters of the structures observed		
1	^{62}Cr	^{190}W	116	Ex1
2	$^{48, 50, 54}$Ca	^{198}Pt, ^{202}Hg, ^{204}Pt	120, 122, 124	Ex1 & Ex2
3	^{44}S	^{208}Pb	126	
4	^{40}Si	^{212}Po	128	Ex1 & Ex3
5	^{36}S	^{216}Po	132	
6	^{34}Si (N = 20)	^{218}Po	134	Ex1
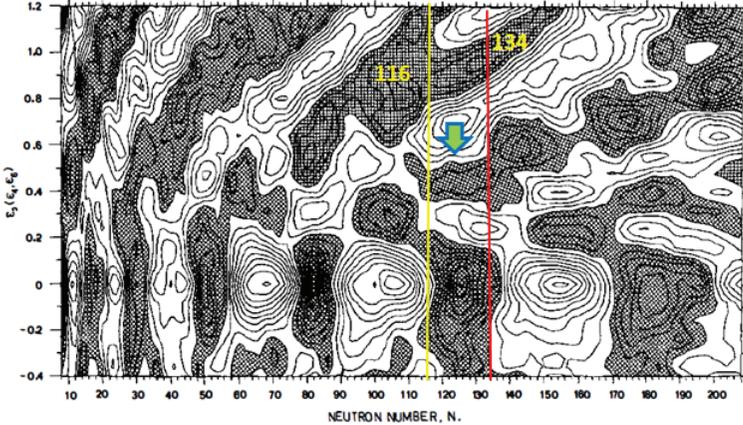
FIGURE 5. Shell energy diagram [10] depending on neutron number and deformation. Areas corresponding to negative shell energy are shaded, and the contour separation is 1 MeV.

DISCUSSION

For the first time we observed the linear structures meeting the condition $M_1 + M_2 = $ const in our experiment (Ex3) at the FOBOS setup based on the gas-filled detectors [9]. The linear ridges corresponding to the constant missing masses were revealed as a fine structure in the mass correlation plot collected with good statistics. Later using the COMETA spectrometer based on the mosaics of PIN diodes, we also observed the structures under discussion (Ex2), but the data suffered from small statistics [1]. Parameters of all linear structures observed so far in the region of so called "Ni-bump" are presented in Table 1. As can be inferred from Figure 5, showing the shell corrections map [10], the numbers of neutrons in the heavy magic cores (the forth column in Table 1) manifest themselves through the discussed structures correspond to the valley of negative shell corrections. In the recent publication [11] on the study of pear-shaped nuclei, it was noted that octupole correlations enhanced at the magic neutron numbers 34, 56, 88, 134. Thus, it is reasonable to expect that the nuclei having 116–134 neutrons would be pear-shaped and show magic properties. According to the calculations,

for instance [12], fissioning system becomes pear-shaped at the beginning of the descent from the fission barrier, at least in the most populated fission valley of the potential energy surface.

We propose the following scenario of the process leading to the formation of the structures under discussion. At the initial stage of the descent from the fission barrier the fissioning nucleus undergoes transformation from a prolate to more complicated shape. The nucleus of such shape consists of a heavy magic octupole deformed core and the light cluster in contact with the thin edge of the "pear". At further elongation the core takes dumb bell-like shape with more and more long neck between the heavy and light parts of the dumb bell. The mass of the light cluster stays unchanged. After the first rupture in the neck, a heavy fragment and a di-nuclear system consisting of the light cluster and some part of the neck fly apart. Later, due to the second rupture, the light cluster and the light FF become free. In general, the cinematics of the process seems to be similar to that discussed in [3].

CONCLUSIONS

Based on the new data we clarify a mechanism of the CCT mode similar to heavy ion radioactivity [9]: octupole deformed magic core plays the same role as magic Pb cluster in the "Lead radioactivity".

ACKNOWLEDGMENTS

REFERENCES

1. Yu.V. Pyatkov et al., Eur. Phys. J. A 48 (2012) 94–110.
2. D.V. Kamanin, Yu. V. Pyatkov, "Clusters in Nuclei – Vol.3" ed. by C. Beck, Lecture Notes in Physics 875, pp. 183–246 (2013).
3. Yu.V. Pyatkov et al., Phys. Rev. C 96, №6, 064606 (2017).
4. Yu.V. Pyatkov et al., Proc. of the 25th Int. Seminar on Interaction of Neutrons with Nuclei, Dubna, Russia, 22-26 May 2017. Dubna 2018, p. 409-414.
5. D.V. Kamanin et al., Izvestiya Rossiiskoi Akademii Nauk. Seriya Fizicheskaya, 2018, V. 82, No. 6, pp. 804-807.
6. H.O. Neidel et al., Nucl. Instr. Meth. V. 178 (1980) P. 137.
7. S.I. Mulgin et al., NIM A 388 (1997) 254-259.
8. Yu.V. Pyatkov et al., Journal of Physics: Conference Series, V. 675, (2016), Int. Conf. on Particle Physics and Astrophysics (ICPPA-2015), 5–10 October 2015, Moscow, Russia, 042018.
9. Yu.V. Pyatkov et al., Eur. Phys. J. A 45 (2010) 29–37.
10. S. Aberg et al., Annu. Rev. Nucl. Part. Sci. 1990.40: 439-527.
11. L. P. Gaffne et al., Nature. V. 497 (2013).
12. Yu. V. Pyatkov, V. V. Pashkevich, et al., Nucl. Phys. A 624 (1997) 140.

SEARCH FOR SCISSION NEUTRONS IN THE MEASUREMENT OF ANGULAR AND ENERGY DISTRIBUTIONS OF THE PROMPT FISSION NEUTRONS FOR ^{233}U, ^{235}U, ^{239}Pu AND ^{252}Cf

A.S. Vorobyev, O.A. Shcherbakov, A.M. Gagarski, G.V. Val'ski

B.P. Konstantinov Petersburg Nuclear Physics Institute of National Research Centre "Kurchatov Institute", Gatchina, Leningrad district, 188300, Russia

Abstract

The measurements of angular and energy distributions of the prompt fission neutrons from thermal neutron-induced fission of ^{233}U, ^{235}U, ^{239}Pu and from spontaneous fission of ^{252}Cf were carried out at the WWR-M research reactor in Gatchina, Russia. Some peculiarities were found in the angular distribution of the prompt fission neutrons. It is possible to explain them by assuming that in the center-of-mass system of fission fragment the neutrons are more likely emitted along fission direction than in the perpendicular one. The value of anisotropy of neutrons emission in the center-of-mass system of fission fragment was found to be equal to 6-8% for all nuclei under investigation. The yields of "scission" neutrons have been estimated: 1.5÷2.7% (^{233}U), 1.8÷2.6% (^{235}U), 3.6÷4.5% (^{239}Pu) and 2.0÷3.0% (^{252}Cf) with the average uncertainty 0.8%.

Introduction

As a result of experimental studies of the emission of prompt fission neutrons (PFNs) [1, 2], it was found that neutrons are emitted primarily in the direction of motion of fragments and that the proposed hypothesis of evaporation of neutrons from fully accelerated fragments [3] provides the general description of observed features [4]. For the detailed description of angular and energy distributions of PFNs, it is necessary to assume the existence of "scission" neutrons, i.e., neutrons whose emission mechanism differs from evaporation of neutrons from fully accelerated fragments (emission of neutrons before or at the time of scission of a fissioning nucleus or in the process of acceleration of produced fission fragments). In particular, for the most studied case of spontaneous fission of ^{252}Cf(sf), estimates of the contribution of "scission" neutrons obtained from the analysis of independent experimental data range from 1 to 20% of the total number of neutrons per fission event (Fig. 1 upper part). The information on the anisotropy of the PFNs emission in the center-of-mass system of fission fragments obtained from the experiment is even more scarce than information on the yield of "scission" neutrons (Fig. 1 lower part).

The main purpose of this work was the experimental investigation of the emission mechanism of PFNs by the coincidence measurements of angular and energy distributions of neutrons and fission fragments. The experimental data needed for such investigation, ideally, should be obtained using the same set-up and data processing for many nuclei at different excitation energies. Therefore, using the same experimental set-up and data processing, a few experiments have been carried out at NRC KI PNPI (Gatchina, Russia) to measure the angular and energy distributions of prompt neutrons from thermal neutron-induced fission of ^{233,235}U,

[239]Pu and spontaneous fission of [252]Cf [5-9]. In this paper, some results of this investigation are presented.
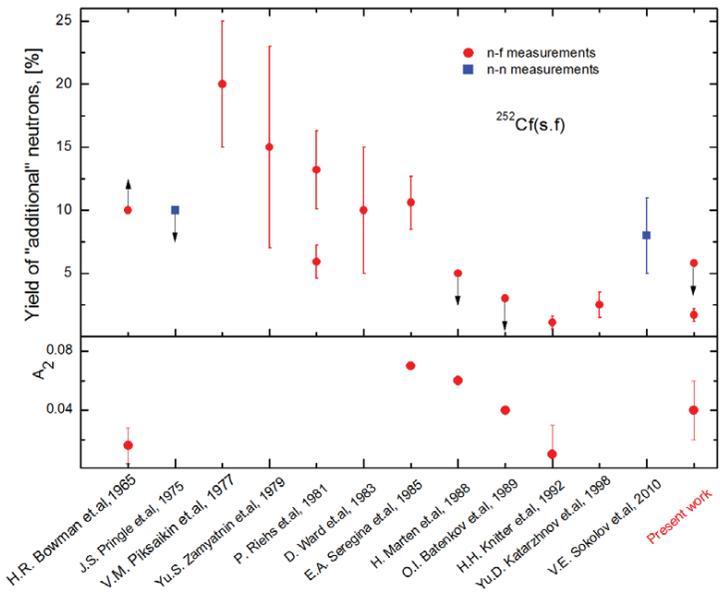

Fig. 1. Main results of previous investigations of PFN emission mechanism for [252]Cf: upper part - yield of "scission" neutrons (downward and upward arrows indicate the upper and lower bounds, respectively); lower part - anisotropy of the angle distribution of PFNs in the center-of-mass system of fission fragments.

1. Experiment overview

The measurements of angular and energy distribution of PFNs were carried out at the research reactor WWR-M of PNPI. The fission fragments and prompt neutrons time-of-flights were measured simultaneously for 11 fixed angles, θ, between the axis of neutron detector and normal to the surface of stop multi-wire proportional detectors (MWPDs) (coming through its center) in the range from 0° to 180° in 18° intervals. The schematic view of the experimental set-up is shown in Fig. 2. The neutron beam was coming along the chamber axis normally to the Fig. 2 plane.

It should be noted that realized scheme of the experimental set-up guarantees identity of conditions of the neutron spectra measurements at various angles relative to the fission axis, namely: the magnitude and composition of the background, the efficiency of the neutron detectors, and neutron re-scattering by the parts of experimental set-up. Also, the use of two neutron detectors with slightly different characteristics enables to estimate probable systematic errors of the data obtained.

At the same time, the existing calculation methods used in practice to describe angular and energy distributions of PFNs do not provide necessary accuracy. For example, the total PFNs of ^{235}U calculated by different commonly used codes [10] are presented in Fig. 3, where the spectra calculated assuming that PFNs are emitted from fully accelerated fragments and using the same input parameters are shown as a ratio to Maxwell distribution. It is seen that the existing calculation methods do not provide necessary accuracy to describe experimental data while the method realized in this work gives accuracy not worse than those of commonly used codes and does not require knowledge of a large number of input parameters.

3. Results and discussion

On the whole, the calculated model energy and angular distributions agree rather well with the experimentally obtained distributions. It is also possible to describe the total PFN spectrum in the laboratory system above 1 MeV and their average number of PFNs per fission event. However, there is a minor distinction which is observable for all investigated nuclei [6, 10-12]. For example, in Fig. 4, the PFN spectrum measured for angle 90° relative to fission fragment direction and the total PFN spectrum obtained by summing over angles for ^{239}Pu(n,f) are compared with the corresponding calculated values. The observed differences may be interpreted as a manifestation of "scission" neutrons and the average energy of these neutrons and their yield can be estimated.
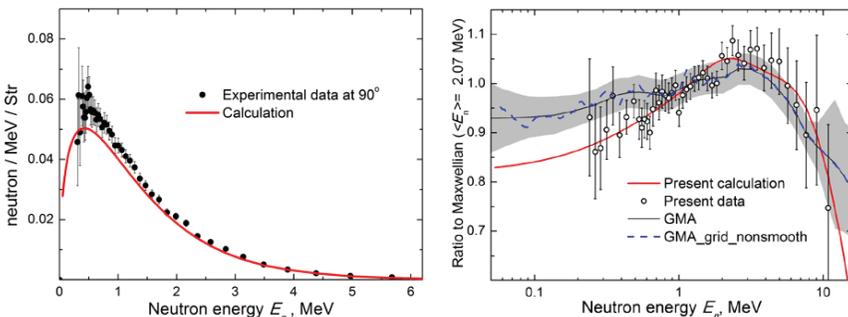
Fig. 4. Left – the PFN spectrum measured for angle 90° relative to the fission fragment direction. Right – the total PFN spectrum of ^{239}Pu(n,f) obtained by summing over angles θ are shown as a ratio to Maxwell distribution. GMA – generalized least square fit of PFN spectra measured by different experimental groups (non-model evaluation) – taken from ref. [10].

The systematic difference between calculated total PFN spectra and total PFN spectra measured by different experimental groups (evaluated spectrum – GMA fit) is visible in the neutron energy range lower than 0.6 MeV. The "scission" neutron spectrum can obtained as a difference between evaluated total PFN spectra (GMA fit) and model calculation. To verify this statement, the PFN spectra measured for angles close to 90° relative to the direction of the light fragments' movement, were compared with calculated PFN spectra at the same angles. The "scission" neutron spectrum was obtained with the use of the difference spectra obtained as the difference between the measured and model spectra for angles of 72.2°, 90° and 107.8° with respect to the direction of motion of the light fragment. To compare the two

estimates, the "scission" neutron spectrum obtained in the first way was multiplied by 4π (it was assumed that the distribution of "scission" neutrons in the laboratory system was isotropic). A comparison of the spectra obtained in this manner shows the agreement (within the errors of the experimental data) between the results from estimates performed in different ways. For example, in Fig. 5 these difference spectra for ^{252}Cf and ^{239}Pu are presented.

Since the relative contribution from "scission" neutrons should be largest at angles Ω close to 90°, the yield of these neutrons from the fission of the investigated nuclei was estimated using the spectrum obtained in the second way: with least squares approximated by functions (1) and (2):
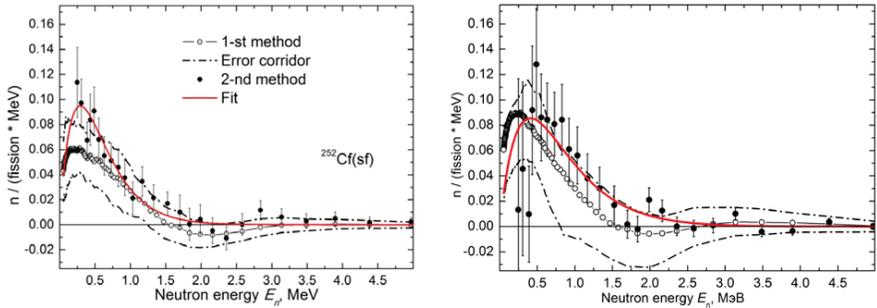
Fig. 5. Spectrum of "scission" neutrons: left - for ^{252}Cf(sf); right - for ^{239}Pu(n,f). Points - the difference spectrum obtained using spectra measured at 72.2°, 90° and 107.8° relative to the direction of motion of the light fission fragment and the corresponding ones calculated under the assumption that all prompt neutrons are emitted from the accelerated fragments. Circles - the difference between total PFN spectrum obtained by experiment (estimated data and it's errors) and calculated assuming that all prompt neutrons are evaporated from accelerated fragments. Solid line - fit of experimental data marked with points by the equation (1).

Table 1. Main characteristics of "scission" neutrons.

	^{233}U(n,f)	^{235}U(n,f)	^{239}Pu(n,f)	^{252}Cf(sf)
Approximation using function (1)				
Yield, %	1.5 ± 0.6	1.8 ± 0.6	3.6 ± 0.6	2.0 ± 0.6
Average energy, MeV	0.53 ± 0.08	0.47 ± 0.05	0.91 ± 0.19	0.58 ± 0.06
Approximation using function (2)				
Yield, %	2.7 ± 0.8	2.6 ± 0.8	4.5 ± 0.9	3.0 ± 0.8
Average energy, MeV	1.7 ± 0.2	1.4 ± 0.2	1.6 ± 0.2	1.5 ± 0.2

$$p_S(E) = \frac{p_0}{4\pi} \cdot \frac{E}{T_0^2} \cdot \exp\left(-\frac{E}{T_0}\right) \tag{1}$$

$$p_S(E) = \frac{p_0}{4\pi} \cdot \frac{E}{T_0^2} \cdot \exp\left(-\frac{E}{T_0}\right) + \frac{p_1}{4\pi} \cdot \frac{E}{T_1^2} \cdot \exp\left(-\frac{E}{T_1}\right) \tag{2}$$

The parameters p_0, T_0, p_1 and T_1 were varied. The results of these approximations are given in Table 1.

Conclusion

To estimate the yield of "scission" neutrons in fission the measurements of angular and energy distributions of PFNs from thermal neutron-induced fission of ^{233,235}U, ^{239}Pu and spontaneous fission of ^{252}Cf have been carried out at the WWR-M research reactor in NRC KI PNPI (Gatchina, Russia). The analysis of these data demonstrates a general agreement between experimental data and model calculations performed assuming that PFNs are emitted from fully accelerated fission fragments. But there are some differences which cannot be explained within the model of neutron emission from fully accelerated fragments. These differences can be eliminated by assuming that there were ~2–4% of "scission" neutrons. It should be noted that these estimations of properties of "scission" neutrons were performed assuming isotropic emission of "scission" neutrons in the laboratory system. Probably, this assumption is very close to the real situation, because in the measurements of the angular dependency of the neutron-neutron coincidence curves, which are very sensitive to isotropic component in the laboratory system, the same values of "scission" neutron yield were obtained within experimental errors [13].

The nature of the observed neutron excess can be determined after a thorough comparison of the experimental data and the calculations using theoretical models that allow for possible PFNs emission mechanisms in fission.

References

1. R.R. Wilson, Phys. Rev. **72**, 189 (1947).
2. J.S. Fraser, Phys. Rev. **88**, 536 (1952).
3. V. Weisskopf, Phys. Rev. **52**, 295 (1937).
4. J. Terrell, Phys. Rev. **113**, 527 (1959).
5. A.S. Vorobyev, O.A. Shcherbakov, Yu.S. Pleva, A.M. Gagarski, G.V. Val'ski, G.A. Petrov, V.I. Petrova, T.A. Zavarukhina, *et. al.*, *Nucl. Instr. and Meth.* **A598**, 795 (2009).
6. A.S. Vorobyev, O.A. Shcherbakov, A.M. Gagarski, G.V. Val'ski, G.A. Petrov, EPJ Web of Conference **8**, 03004 (2010).
7. A.S. Vorobyev, O.A. Shcherbakov, Yu.S. Pleva, A.M. Gagarski, G.V. Val'ski, G.A. Petrov, V.I. Petrova, T.A. Zavarukhina, Proc. of the XVII-th International Seminar on Interaction of Neutrons with Nuclei "Neutron Spectroscopy, Nuclear Structure, Related Topics", ISINN-17, Dubna, May 27-29, 2009, ed. A.M. Sukhovoj, JINR, Dubna, E3-2010-36, 2010, p. 60.
8. A.S. Vorobyev, O.A. Shcherbakov, VANT, Ser. Nuclear Constants, Issue 1–2, 37 (2011–2012) [report INDC(CCP)-0455, IAEA, Vienna, 2014].
9. A.S. Vorobyev, O.A. Shcherbakov, VANT, Ser. Nuclear Constants, Issue 2, 52 (2016).
10. R. Capote, Y.-J. Chen, F.-J. Hambsch, N.V. Kornilov, J.P. Lestone, O. Litaize, B. Morillon, D. Neudecker, S. Oberstedt, T. Ohsawa, N. Otuka, V.G. Pronyaev, A. Saxena, O. Serot, O.A. Shcherbakov, N.-C. Shu, D.L. Smith, P. Talou, A. Trkov, A.C. Tudora, R. Vogt, A.S. Vorobyev, Nuclear Data Sheets, **131**, 1 (2016).
11. A.S. Vorobyev, O.A. Shcherbakov, A.M. Gagarski, G.A. Petrov, G.V. Val'ski, JETP **125(4)**, 619 (2017).
12. A.S. Vorobyev, O.A. Shcherbakov, A.M. Gagarski, G.A. Petrov, G.V. Val'ski, T.V. Kuzmina, JETP **127(4)**, 659 (2018).
13. I.S. Guseva, A.M. Gagarski, V.E. Sokolov, G. A. Petrov, A.S. Vorobyev, G.V. Val'sky, T.A. Zavarukhina, Physics of Atomic Nuclei **81(4)**, 447 (2018).

Prompt Fission Neutron Investigation in ^{235}U(n_{th},f) and ^{252}Cf(sf) Reactions

Shakir Zeynalov, Pavel Sedyshev, Valery Shvetsov and Olga Sidorova

Joint Institute for Nuclear Research, 141980 Dubna, Moscow region, Russia

Abstract. The prompt neutron emission in thermal neutron induced fission of ^{235}U and spontaneous fission of ^{252}Cf investigated applying digital signal electronics. The goal was to check new revised data analysis software with fission fragment (FF) kinetic energy corrections after prompt fission neutron (PFN) emission. The revised software was used to reanalyze old data measured in EC-JRC-IRMM, where ^{252}Cf(sf) reaction was investigated. Both measurements were done using similar twin Frisch grid ionization chamber for fission fragment detection with NE213 equivalent fast neutron detector. In total about $0.5 \cdot 10^6$ FF with PFN coincidences have been analyzed in both measurements. The fission fragment kinetic energy, mass and angular distribution has been investigated along with prompt neutron time of flight and pulse shape analysis using a six channel synchronous waveform digitizer (WFD) with sampling frequency of 250 MHz and 12 bit resolution in ^{235}U(n_{th},f) reaction investigation. Similar WFD with sampling frequency 100 MHz was used for PFN investigation in ^{252}Cf(sf) reaction. These two experiments was considered as a reference for further investigations with a new setup composed of position sensitive ionization chamber as FF detector and array of 32 liquid scintillator PFN detectors recently constructed in Dubna.

1 Introduction

The nuclear fission is considered as the process of charged drop development under competition between attractive nuclear and repulsing coulomb forces, leading eventually to the split of the nucleus mainly into two parts of comparable masses. The main part of FF excitation energy is released by the prompt fission neutrons, emitted by FF after full acceleration by coulomb forces. The experimental investigations of various characteristics of PFN emission is needed to understand the nuclear fission dynamics from the scission point down to rupture. One of the interesting observation is the increasing $\bar{\nu}(A)$ from the heavy fragment with increase of the excitation energy of the fissioning system [1] still has no clear explanation. Therefore, further systematic study of correlations between fragments and neutron characteristics is needed. The studies of PFN emission in fission induced by neutrons from energies extending from resonances up to a few MeV could possibly contribute to better understanding the mechanism of PFN emission from the excited FF. The experiments on sub-barrier fission, induced by thermal neutrons are of particular interest because of no measurements was done so far on mass and energy distributions for this systems [2]. In this work we report results of PFN investigation in thermal neutron-induced fission of ^{235}U and spontaneous fission of ^{252}Cf. The main goal of the experiments was the feasibility check of the apparatus and data analysis procedure.

2 Experimental Setup and FF data analysis

A convenient way to study of PFN emission in neutron-induced fission is to use a conventional twin back-to-back ionization chamber, with two chambers sharing a common cathode as was done by Budtz-Jorgensen and Knitter [3]. The cathode was made from a thin

conductive foil and at the same time served as backing for the fissile deposit. For binary fission events two complementary FF are simultaneously detected in two independent chambers. Free electrons released by FF deceleration are induced pulses on the chambers anodes and on the common cathode during drift along the applied externally electric field. The pulse height in each chamber was proportional to corresponding FF kinetic energy release and the FF pulse shape conveys information on the FF angle (Θ) in respect to the electric field applied in the direction of the normal to the cathode plane. From the correlated energies obtained in the above double-energy (2E) experiment, FF masses and velocities could be found in the way similar to that in book [4]. If the fissile target is located on the common cathode and the fast neutron detector positioned at the certain distance along the normal to the target the angle between FF and PFN emission would be equal to Θ. The PFN velocity may be determined from the known flight path and the measured time delay between cathode and ND pulses. Measured FF and PFN velocity vectors then may be used for PFN emission kinematics. The PFN multiplicity distributions in respect to FF kinetic energy release and mass split may be reconstructed by comparison of two sets of FF measurements. In the first experiment fission fragment mass and kinetic energy release should be evaluated from the measurement independent from ND. In the second experiment FF mass and kinetic energy release should be evaluated for the FF coincided with ND. The detailed information on PFN emission in fission is available from the measured dependence of the number $\nu(A,TKE)$ of PFN emitted by the FF with mass number A and TKE release of two fission fragments [3-4]. The late function allowed obtaining of averaged characteristics on $\overline{\nu}(A)$ or $\overline{\nu}(TKE)$ by integrating over respective variable, if the mass yield matrix - $Y(A,TKE)$ is known, for example:

$$\overline{\nu}(A) = \frac{\int_0^\infty \nu(A,TKE\,)Y(A,TKE\,)dTKE}{\int_0^\infty Y(A,TKE\,)dTKE},$$

$$\overline{\nu} = \int_0^\infty \nu(A,TKE\,)Y(A,TKE\,)dTKE\,dA,$$

$$200 = \int_0^\infty Y(A,TKE\,)dTKEdA\ .$$

(1)

Similar relation could be written for averaging over A:

$$\overline{\nu}(TKE\,) = \frac{\int_0^\infty \nu(A,TKE\,)Y(A,TKE\,)dA}{\int_0^\infty Y(A,TKE\,)dA},$$

$$\overline{\nu} = \int_0^\infty \nu(A,TKE\,)Y(A,TKE\,)dTKE\,dA,$$

$$200 = \int_0^\infty Y(A,TKE\,)dTKEdA\ .$$

(2)

$\nu(A), \nu(TKE)$ can be easily determined if the distributions of $P(A,TKE)$ and $Y(A,TKE)$ are known. The experimental method and data analysis procedure implemented in this work was adopted from Ref. [3], where it was described in detail. For each fission event the FF and PFN kinetic energies, FF masses along with the angle between PFN and FF motion should be determined. All this information can then be used to reconstruct the PFN emission kinematics both in the laboratory (LF) and in the centre of mass (CMF) frames. The measurements were carried out using the experimental setup presented in Fig. 1. Reaction kinematics is sketched is sketched Reaction kinematics is sketched in Fig. 2.
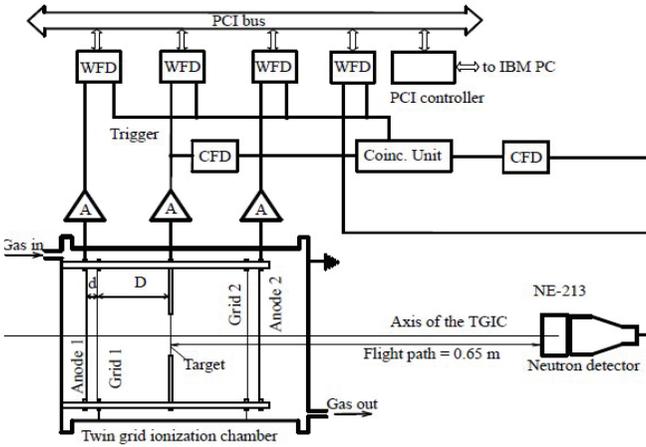
Fig. 1. Experimental Setup.

The experimental setup consisted of the twin back-to-back ionization chamber (TIC), which was designated for FF kinetic energy release and the cosine of angle between fission axis and the cathode plane normal measurement.
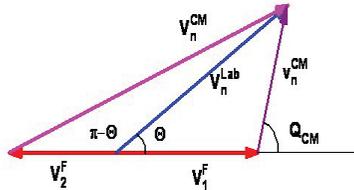

Fig. 2. Vector diagram for PFN emission from FF.

The experimental data was collected using a digital pulse processing (DPP) system, consisting of six synchronous waveform digitizers (12 bit, 250 MS/sec). The FF energies and angles were obtained from the chamber signal waveforms using DPP, realized in form of recursive procedures. The neutron energy was derived from time-of-flight (TOF) calculated as delay between the cathode and the neutron detector pulses. The measured FF energy release should be corrected for energy losses in the target layer and target backing if the cosine of angle Θ is known. In this work anode current pulse waveform was derived from the output pulse of charge sensitive preamplifier and the pulse "centre of gravity" (T) calculated as described in Ref. [5]. The relation between T and the cos(Θ) was derived in Ref. [6] using Ramo-Shokley theorem and numerically calculated weighting potentials:

$$\cos(\Theta) = (T_{90} - T)/(T_{90} - T_0),$$

(3)

300

where the used variables have the following meaning: D-is the cathode-anode distance, d - is the grid-anode distance, σ-is the Frisch grid inefficiency value, $T_0 = T(\cos(\Theta) = 1)$, $T_{90} = T(\cos(\Theta) = 0)$. The below formula was used to correct anode signal pulse heights for grid inefficiency:

$$P_A^C = P_A / (1 - \sigma(1 - \frac{T}{T_{90}}) \cdot (1 + \frac{d}{2D})). \tag{4}$$

After the emission angle was calculated the average anode pulse height versus $1/\cos(\Theta)$ was plotted for both chambers to find energy loss correction for FF detected in each chamber. The data sets are fitted as a linear function of $1/\cos(\Theta)$, the slopes of which were assigned to energy loss correction in respective chamber. The correction for FF pulse height caused by momentum transfer to working gas atoms by FF (non ionizing collisions) during its deceleration – is called pulse height defect (PHD). The PHD depends on the FF mass and kinetic energy and was corrected in data analysis using parameterization suggested in Ref. [6]:

$$E = \alpha \cdot PH + \beta + PHD(A_{post}, E_{post}), \tag{5}$$

where E_{post}, A_{post} - FF kinetic energy and mass respectively after neutron emission. The fitting parameters α and β - are chosen to arrive at the values of *TKE* and $<A_H>$ as given in Ref. [4] p. 323. After all corrections have been implemented we went to reconstruct the mass yield for investigated reaction. To do so we needed $\bar{\nu}(A)$ from literature and we used data from Ref. [8] and from Ref. [2]. The mass yield curve was obtained using $\bar{\nu}(A)$ for $^{235}U(n_{th},f)$ reaction from Ref. [2] is shown in Fig. 4 in comparison with result published in Ref. [4] p. 300.
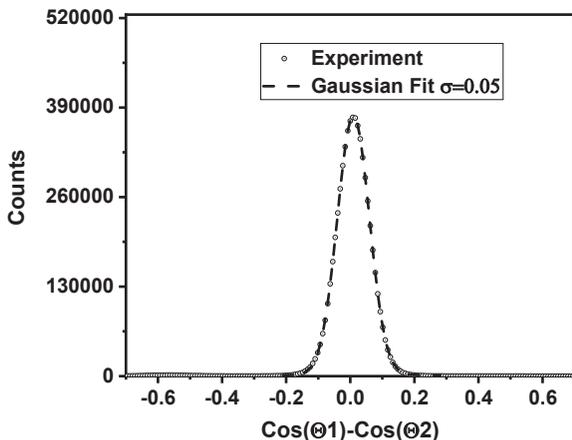
Fig. 3. Demonstration the precision of $\cos(\Theta)$ measurement in the range $0.5 < \cos(\Theta) < 1.0$.
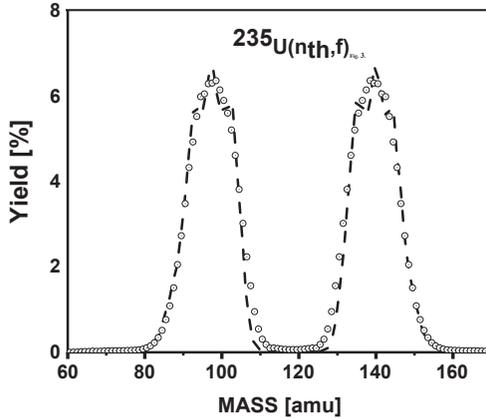
Fig. 4. Comparison of measured mass yield (dots) with data (solid line) taken from Ref.[4].

For calculations the successive approximation procedure to obtain pre-PFN emission mass described in Ref. [3] was used.

3 PFN data analysis

Measurement of PFN time-of-flight in present experiment was done using cathode pulse of TIC as a "T-zero" signal and the ND signal as "Stop" signal. The signals were digitized with 250 MHz sampling rate and stored during experiment for further off-line data analysis. Time difference between these two signals was analyzed implementing standard constant fraction time marking (CFTM) algorithm both to the cathode and to the ND waveforms. The realization of the algorithm described in Ref. [9] and was applied to the cathode waveform. The copy of the original signal is delayed by approximately 0.4 of the cathode signal rise time (~1000 ns) and summed with scaled and inverted original signal. The "T-zero" time is assigned to the crossing point of resulting signal with time axis. The crossing point was calculated using parabola interpolation between two successive samples, first of which has positive and second the negative values. The time mark for the ND signal was found in the similar way. It should be noted that to achieve the best timing resolution in CFTM realization one should convert sampled waveform to continuous form using Shannon's sampling formula [9]. Unless we do not deal with energy spectrum reconstruction, the resolution (~2.5 ns) provided in this simple implementation we found sufficient for PFN analysis. The neutron multiplicity was estimated by counting the number of coincidence between cathode pulse and PFN signal of ND. Due to high gamma radiation background both from the target and surrounding materials the PFN counts need to be separated from the gamma radiation using pulse shape analysis as described in Ref. [9].

The PFN detected by ND mainly is emitted from FF moving towards the ND, but the probability, that it was emitted by FF moving in opposite direction (complementary FF) is not zero and these events should be considered as the background. The background created by the complementary FF was investigated in Ref. [5] and was slightly modified in our approach.

According to the reaction kinematics depicted in Fig. 2, the kinetic energy of the second FF in the CMF, must be much higher than the kinetic energy of the first FF. Bearing in mind the exponential drop of the PFN energy spectrum in the CMF, the contribution to the PFN from both FFs could be evaluated using the probabilities defined as:

(5)

$$W_x = 1/(1+\exp(E_{CM}^x - E_{CM}^y)),$$
$$W_y = \exp(E_{CM}^x - E_{CM}^y)/(1+\exp(E_{CM}^x - E_{CM}^y)) \ ,$$

where W_x, W_y - are probabilities of PFN emission with CM kinetic energies $E_{CM}^{x,y}$ of FF and its complement respectively. A comparison of the mass distributions plotted using measured data and probabilities, defined by eq. (5) are similar to Ref. [3], where the background from the complementary fragments for ^{252}Cf(SF) was found to be small.

The angular distribution of PFN emitted in FF CM reference frame is plotted in Fig. 5, proving that almost all of the PFN are emitted from fully accelerated FFs. The transformation from the LAB to CM reference frame was done using the following formula:

$$\cos(\Theta_{CM}) = (v_n^{Lab} \cdot \cos(\Theta) - v_1^F)/v_{CM} \ . \tag{6}$$

4 PFN analysis in ^{235}U(n$_{th}$,f) reaction

The PFN distribution was evaluated considering neutron emission from the fully accelerated FF, using the reference frame moving along with the FF towards the ND. We used the Jacobian factor and conversion formulae from CM to LAB reference frame as was described in Ref. [10]:

$$\overline{v}(A,TKE) = \int_0^\infty \frac{Yc(A,TKE,V_{LAB}) \cdot V_{CM} \cdot (V_{LAB} - V_F \cdot \cos(\Theta))}{\varepsilon(V_{LAB}) \cdot V_{LAB}^2} dV_{LAB} / Y(A,TKE) \tag{7},$$
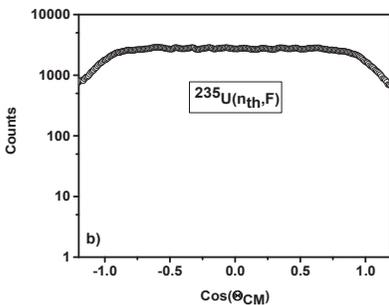
Fig. 5. The angular distribution of PFN emission measured in the FF CM frame.
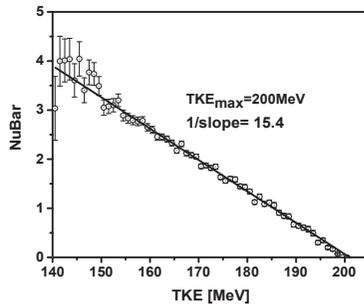
Fig. 6. The average PFN emission distribution mass dependence, measured in ^{235}U(n$_{th}$,f)reaction in comparison with data from Ref. [7].

efficiency dependence on PFN velocity in LAB frame, V_{LAB} - the PFN velocity measured in LAB frame, V_F - FF fragment velocity in LAB frame, V_{CM} is the PFN velocity in CM frame.

The distribution $Y(A,TKE)$ calculated without demanding coincidence with ND as was described above, but distribution $Yc(A,TKE,V_{LAB})$ calculated with FF energy corrected due to FF recoil after PFN emission as was described in Ref. [12].
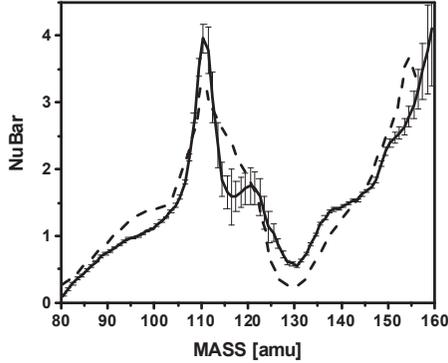
Fig. 7. The average PFN emission distribution dependence on FF TKE, measured in ^{235}U(n$_{th}$,f) reaction with Q$_{max}$= ~205 MeV.
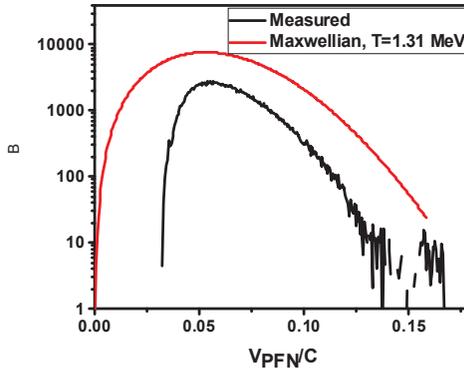
Fig. 8. Comparison of PFN velocity distribution, measured in ^{235}U(n$_{th}$,f) reaction with Maxwell distribution with temperature parameter kT=1.31 MeV.

Dependence of average PFN multiplicity on TKE was evaluated in the similar manner using formulae (2) and plotted in Fig. 7. The PFN velocity distribution was evaluated from

collected data and plotted in Fig. 8 along with the Maxwell distribution with temperature parameter T=1.313 MeV. The PFN detection efficiency was evaluated as the ratio of the measured PFN and plotted in Fig. 9.

It should be noticed that measurement of $\bar{\nu}(A)$ in ^{235}U(n_{th},f) was more complicated in comparison with ^{252}Cf(sf) due to very high peak to valley ratio in FF mass distribution for ^{235}U. Low statistics in the valley area of mass distribution makes data analysis very sensitive to background. That is why in this report we reanalyzed the data with the same data analysis software as was used in analysis of ^{235}U(n_{th},f) reaction. The test of our data analysis procedure in ^{252}Cf(sf) reaction was necessary for confidence in our results for ^{235}U(n_{th},f) which is more precisely reproduce mass distribution of the reaction.
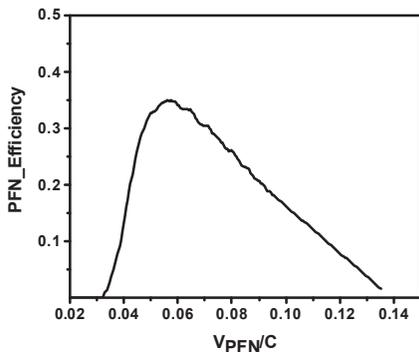
Fig. 9. PFN detection efficiency dependence on velocity measured in speed of light (C) units.

5 PFN analysis in ^{252}Cf(sf) reaction

Investigation of PFN in spontaneous fission of ^{252}Cf was done in 2007-2009 at IRMM with the experimental setup similar to presented in Fig.1. The ionization chamber was absolutely
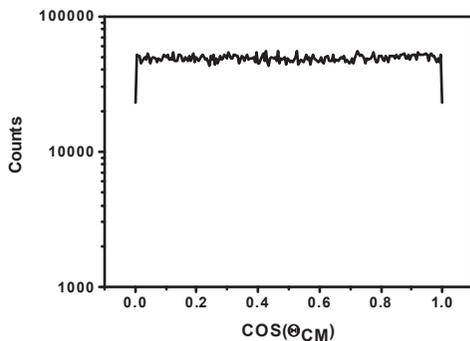
Fig. 10. PFN angular distribution for ^{252}Cf(sf) reaction in CM reference frame.

identical to the chamber used in above reported study. The PFN detectors were the same   size but in case of experiment with Cf-target the distance between target and PFN detector was 0.725 m. Measurement was done with data acquisition hardware   and software was identical to reported above (except sampling frequency of WFD, which was 100 MHz). Data analysis was done using procedure as described above. The PFN angular distribution in CM reference frame was evaluated from data measured in laboratory reference frame and presented in Fig. 10. Cosine of angle between FF motion direction and PFN emission was evaluated using Eq. (6). The cosine distribution of neutron emission angle, measured in FF CM frame, was found to be almost homogeneous, proving that majority of PFN emitted from fully accelerated FF. Comparison of PFN velocity distribution with Maxwell distribution of PFN velocity is presented in Fig. 11.
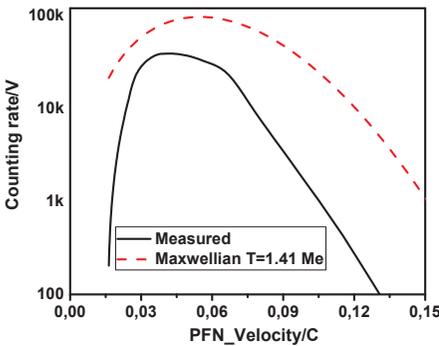
Fig. 11. Comparison of measured PFN velocity distribution with Maxwell distribution in ^{252}Cf(sf) experiment.
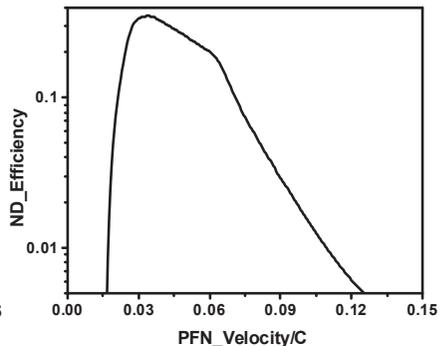
Fig. 12. PFN detection efficiency in reaction ^{252}Cf(sf) as function of the ratio of PFN speed, measured in units of speed-of-light (C).

The recommended value for temperature factor kT=1.41 MeV was used in this study. The PFN detection efficiency dependence on neutron velocity was evaluated as a ratio between measured PFN velocity distribution and Maxwell distribution. The dependence of PFN detection efficiency on the neutron speed presented in Fig. 12.

In both the ^{235}U(n_{th},f) and ^{252}CF(sf) experiments we implemented similar neutron-gamma separation procedure based on the difference between fast and slow scintillation decay time. Two values based on integrating the total charge over two different time periods conveyed information on the type of the detected particle. The plots in Fig. 13 demonstrate how the high and low kinetic energy region of PFN was separated from the background by increase of the threshold in total charge integral over longer time interval. It should be noted that the plots 1 and 2 in Fig. 13 were obtained without application of the neutron gamma separation criterion using only the threshold. The plot 3 was obtained with application of neutron-gamma separation criterion. It should be pointed out that in both experiments the background in PFN distribution was practically completely removed with the applied threshold value corresponding to PFN kinetic energy of ~0.5 MeV.
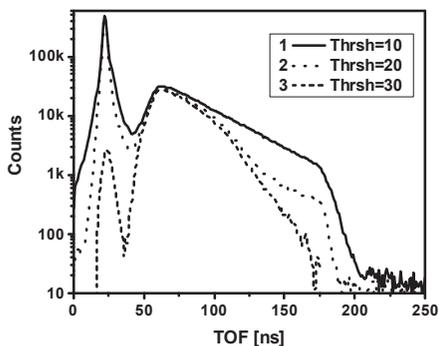
Fig. 13. Dependence of background in high and low PFN kinetic energy spectra on the threshold in total charge integrated over long time interval.

6 Conclusions and outlook

The average PFN emission was evaluated using the same data analysis software as was used in the analysis of ^{235}U(n$_{th}$,f) reaction described in above section. Results of average PFN emission dependence on FF mass and TKE are presented in Fig. 14 and Fig. 15 respectively.
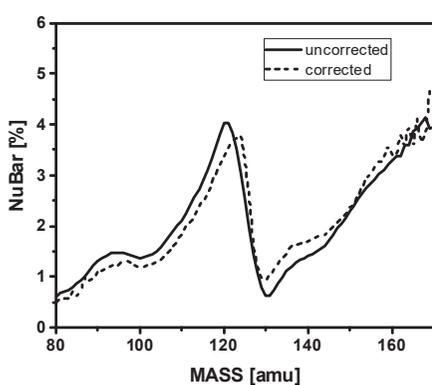

Fig. 14. Mass dependence of average PFN emission in ^{252}Cf(sf).
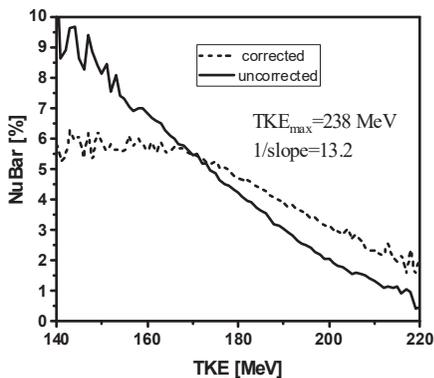
Fig. 15. $\bar{\nu}(TKE)$ dependence in ^{252}Cf(sf) reaction. The maximum TKE release, when PFN emission became impossible PFN indicated in figure.

The distributions presented for FF recoil taken into account and ignored in order to demonstrate the effects of corrections according to Ref. [11]. It should be noted that the average neutron number also should be corrected according to formula (11) from Ref. [11]. We found this correction very small both in $^{235}U(n_{th},f)$ and $^{252}Cf(sf)$ reactions in full agreement with Ref. [11]. The difference between uncorrected and corrected distributions on Fig. 14 was quite significant, which we explain with formula (4) used for pulse height correction due to Frisch-grid inefficiency. Detailed description and derivation of the formula can be found in research paper [8]. As was pointed out in review paper [12], the use of large

$X1=(A-D)/(A+D)$
$X2=(B-C)/(B+C)$
$Y1=(A-B)/(A+B)$
$Y2=(D-C)/(D+C)$
$PH=A+B+C+D$
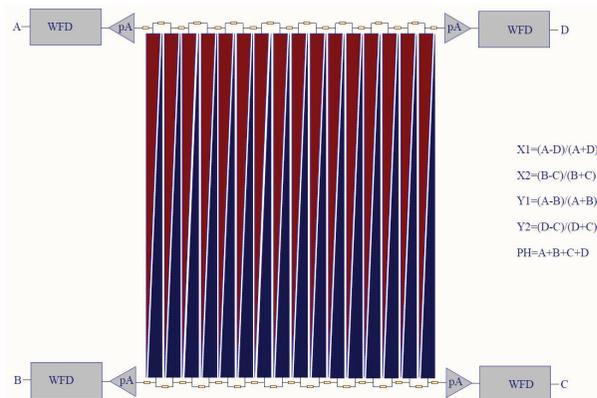
Fig. 16. One of the anodes of position sensitive twin ionization chamber.

neutron detectors (with higher PFN detection efficiency) in many aspects was preferable in PFN investigations. Bearing this in mind we started investigations, which would combine the properties of both detectors with high and low efficiency. Before development of new experimental setup for PFN we have developed position sensitive twin fission chamber with capability of reconstruction the orientation of fission axis in 3D [13]. The twin chamber consisted of common cathode, where fissile target can be located. Two segmented anodes located at 40 mm distance symmetrically from the both sides of the cathode plane plain.
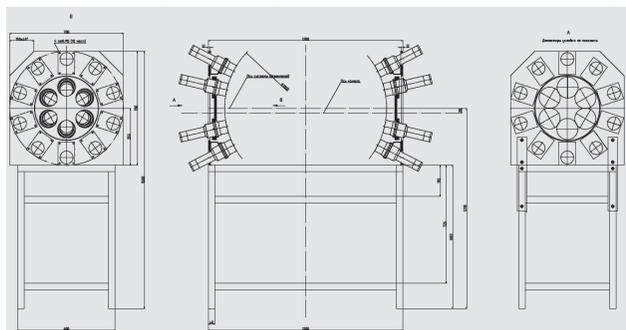

Fig. 17. Fast neutron detector composed of 32 liquid scintillation modules with position sensitive twin ionization chamber in centre (not shown in figure)

Segmented anodes consisted of triangular strips, electrically isolated from each other as demonstrated in Fig. 16. Each strip as shown in the figure connected to the nodes of the resistive chain filter. Operational principle of position sensitive ionization chamber, formulae for FF "charge centre-of gravity" and FF orientation evaluation was provided in Refs. [8,13]. Fast neutron detector consisted of 32 type VS-0499-100 scintillation detector modules of diameter 76 mm and 51 mm from SCIONIX HOLLAND BV (Fig. 17). The setup was planned to use in experiment to the end of this year at IREN –resonance neutron source in Dubna.

Acknowledgements

References

1. A.A. Naqvi, F. Kappeler, and F. Dickmann, Phys. Rev. **C34**, 218 (1986).
2. A. Al-Adili, D. Tarrio, F.-J. Hambsch, A. Gook, K. Jansson, A. Solders, V. Rakopoulos, C. Gustavson, M. Lantz, A. Materrs, S. Oberstedt, A.V. Prokofiev, M. Viladi, M. Osterlund, and S. Pomp, *EPJ Web of Conferences* **122**, 01007 (2016).
3. C. Budtz-Jorgensen and H.-H. Knitter, Nucl. Phys., **A490**, 307 (1988).
4. C. Wagemans, *The Nuclear Fission Process*, CRC Press, Boca Raton, FL, 1991.
5. S. Zeynalov, O. Zeynalova, F.-J. Hambsch and S. Oberstedt, Bull. Russ. Acad. Sci.: Phys. **73**,506 (2009).
6. Zeynalov, S., Hambsch, F.-J., Oberstedt, S., 2011. Jour. Korean Phys. Soc. **59**, 1396.
7. V.F. Apalin, Yu. N. Gtitsuk, I.E. Kutikov, V.I. Lebedev, and L.A. Mikaelyan, Nucl. Phys., **55**, 249 (1964).
8. O. Zeynalova, Sh. Zeynalov, M. Nazarenko, F.-J. Hambsch, and S. Oberstedt, *AIP Conf. Proc*. **1404**, 325(2011).
9. G. Knoll, *Radiation Detection and Measurement*, John Willey & Sons, Inc, Third edition, 2001.
10. H.R. Bowman, J.C.D. Milton, S.G. Thompson, and W.J. Swiatecki, Phys. Rev. **129** (1963) 2133.
11. A. Gavron, Nucl. Instrum. and Meth., **115** (1974) 99.
12. H. Nifenecker, C. Signarbieux, R. Babinet, J. Poitou, *Neutron and gamma emission in fission*, IAEA-SM-174/207.
13. Sh. Zeynalov, P. Sedyshev, O. Sidorova, V. Shvetsov, Applications of Nuclear Techniques (CRETE17), *International Journal of Modern Physics: Conference Series*, Vol. **48** (2018) 1860123.

THERMAL NEUTRON INTENSITY MEASUREMENT WITH FISSION CHAMBER IN CURRENT, PULSED AND CAMPBELLING MODES

Sh. Zeynalov[1], V. Kuznetsov[1], P. Sedyshev[1], V. Shvetsov[1], O. Sidorova[1],
Youngseok Lee[2], Uk-Won Nam[3]

[1]*Joint Institute for Nuclear Research, Frank Laboratory of Neutron Physics,*
141980 Joliot-Curie 6, Dubna Moscow region, Russia
[2]*National Fusion Research Institute, Daejeon, South Korea*
[3]*Korea Astronomy & Space Science Institute, Daejeon Science Town, South Korea*

Abstract

In thermal nuclear reactors, most of the power is generated by thermal neutron induced fission. Therefore, fission chambers with targets that responds directly to slow neutrons are of great interest for thermal neutron flux measurements due to relatively low sensitivity to gamma radiation. However, the extreme conditions associated with experiments at very low cross section demand highly possible thermal neutron flux, leading often to substantial design changes. In this paper we report design of a fission chamber for wide range (from 10 to 10^{12} n/cm^{2}sec) measurement of thermal neutron flux. Test experiments were performed at the first beam of IBR2M pulsed reactor using digital pulse processing (DPP) technique with modern waveform digitizers (WFD). The neutron pulses detected by the fission chamber in each burst (5 Hz repetition rate) of the reactor were digitized and recorded to PC memory for further on-line and off-line analysis. New method is suggested to make link between the pulse counting, the current mode and the Campbell technique.

Introduction

In recent decade digital pulse processing (DPP) is considered as very powerful alternative to traditional analogue pulse processing (APP) in experimental nuclear physics research. Mainly it happened due to a diversity of data analysis options were provided in data analysis and the flexibility of data treatment, which very unlikely can be provided by APP. In this work we demonstrated the power of DPP implemented in thermal neutron counting with fission chamber (FC) in the various modes developed in the reactor instrumentation, namely the counting, the current and the Campbelling techniques. We demonstrated how to implement DPP making direct link between the counting and the current mode measurement with the thermal neutron sensor based on gas filled detectors. It should be noticed that absolute thermal neutron flux measurement in the wide intensity range was very unlikely possible with the same mode. The main problem was in the response function of the sensor, which has limit in the width about few ns. When the distance between pulses became comparable with this limit, then separation of the individual pulses was impossible. In that case measurement usually was possible to perform in the current mode, using the proportionality of the measured current to the neutron intensity. The main problem is how to

make link between the counting and the current modes. In this work we propose a solution which we believe able to provide the link.

Experimental Setup and Results

In reported experiment we used the fission chamber with ^{235}U target (99,999% enrichment) mounted on the common cathode of a twin parallel plate ionization chamber shown in Fig. 1. The target thickness was 0.5 mg/cm^2 of uranium smeared on the both sides of aluminium backing foil. Ionization chamber was operated at constant flow 50 ml/min of working gas P10. Negative high voltage (500 V) was applied to the common cathode allocated between two anodes at distances of 40 mm from each of them. Due to thickness of the target and backing foil only one of two fission fragments (FF) was detected on thermal neutron induced fission event. Working gas pressure was stabilized at 1.05 bar using a gas pressure controller. Fission chamber was located at distance 27 m from the pulsed nuclear reactor IBR2M with the following main parameters: average power 1.8 MW, fast neutron pulse duration 200 us, the pulse repetition rate 5Hz, the thermal neutron intensity at the target position was about 10^6 n/cm^2 per second. Fission fragments (FF) were decelerated in the working gas of FC producing free electrons which were drifted towards the anodes under the applied uniform electric field, inducing electric current pulses on the cathode circuit. The cathode current was amplified and recorded by the WFD, triggered by the IBR2M "T-zero" signal. The WFD sampling frequency (200 kHz) and the number of samples (4096) were
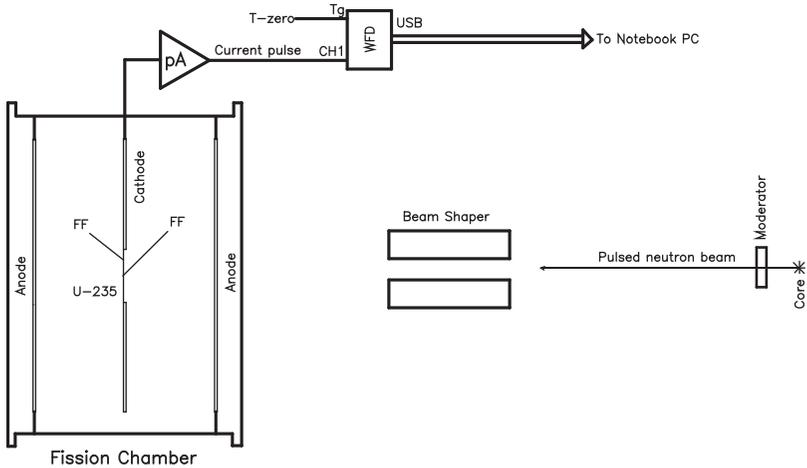

Figure 1. Fission chamber with associated preamplifier, WFD and beam shaping equipment.

selected in order to cover the full thermal neutron burst duration about 20 ms. Sequential reactor bursts were digitized and recorded to the notebook computer's hard disk for further off-line data analysis. One of the recorded reactor bursts presented in Fig.2. It should be noticed that because of the overlapped pulses baseline was distorted and must be restored

using special electronic modules to stabilize the base line for proper counting when the APP was implemented. Use of the DPP avoided the problem in the elegant way, using sequential flow of the reactor bursts. To remove the baseline fluctuation we have used the following method: each recorded waveform of the burst was subtracted from the waveform of previous one, creating waveform shown in Fig. 3. It was easy to see that resulted distribution composed of bipolar waveform with removed baseline and the data obtained was satisfying to the second Campbell theorem [1,2]. According to the theorem the variance of the current's AC component from the randomly distributed in time (Poisson distribution) current pulses is proportional to the average pulse rate and the mean square charge per pulse:

$$\langle I(t) \rangle = \int_0^\infty h(t) dt \cdot \sum_{i=0}^m \langle n_i \rangle \cdot \langle q_i \rangle \tag{1}$$

$$\langle I(t)^2 \rangle - \langle I(t) \rangle^2 = \int_0^\infty h(t)^2 dt \cdot \sum_{i=0}^m \langle n_i \rangle \cdot \langle q_i^2 \rangle \tag{2}$$

where, $h(t)$ the circuit's response to a single pulse of a unit charge, $\langle q_i \rangle$ the mean charge per pulse, $\langle q_i^2 \rangle$ the mean square charge per pulse, $\langle n_i \rangle$ the average pulse rate in a fixed interval of measurement. In current measurement, $\langle I(t) \rangle^2 = 0$, because the current waveform $I(t)$ was difference of two sequential waveforms. So the Eq. 2 reduced to Eq. 3:

$$\langle I(t)^2 \rangle = \int_0^\infty h(t)^2 dt \cdot \sum_{i=0}^m \langle n_i \rangle \cdot \langle q_i^2 \rangle \tag{3}$$
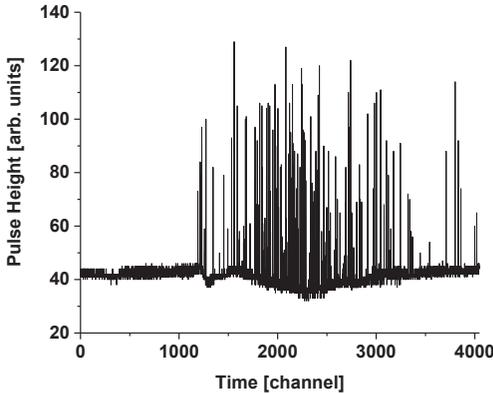

Figure 2. Recorded waveform of single burst of the IBR2M (full range is 20500 us).

To investigate the Campbell theorem experimentally we divided whole measurement consisting of more than 160000 of reactor bursts into the pieces of 12000 bursts. For each reactor burst we measured the number of detected neutrons, which was fluctuating from burst to burst making distribution presented in Fig.4. There were main group of bursts with the
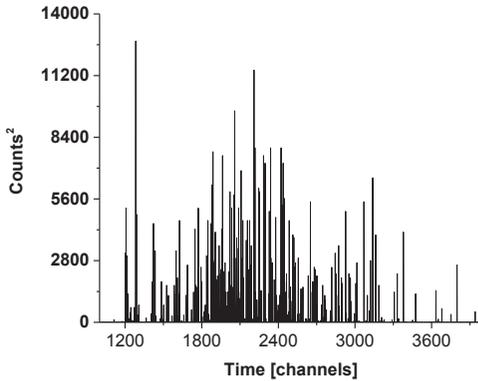
Figure 6. Autocorrelation function calculated after subtraction of two successive reactor bursts.
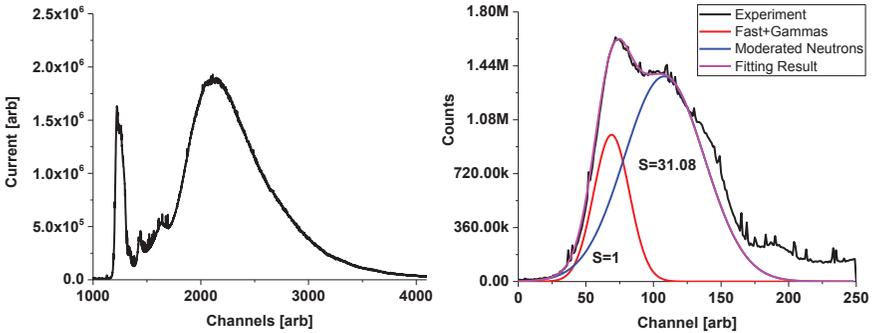

Figure 7. On the left: FC pulses summed for 160000 reactor bursts. On the right: radiation from the reactor burst with decomposition into the neutron (partially moderated/resonance) and gamma plus fast neutrons, escaped the moderator, represented by Gaussians. S indicates relative area under the Gaussians.

Finally in Fig.8 we have presented results of the current mode and the Campbelling techniques of the pulse rate measurement using FC. Each point was obtained by summing the pulses from the sequential reactor bursts incrementally: the second group burst pulses were added to the first one, the third group of burst pulses was added to the second one and so on.
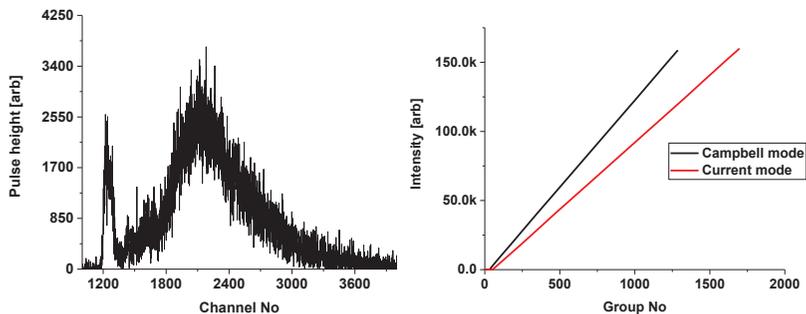
Figure 8. On the left; group waveform composed of 100 sequential waveforms; on the right comparison of intensity measurement in Campbell and current modes demonstrates very good linearity.

Each group consisted of waveforms acquired in 100 sequential bursts. For the analysis the waveforms were summed creating almost continuous distribution as shown on the left graph of the Fig. 8. Then for the current mode measurement the components of the distribution from Fig.8 (left) was integrated producing the number proportional to the pulse intensity in the given group. For the Campbelling technique the components of distribution was squared before integration then the square root of integral was considered as measure of the flux intensity for the given group. Results for the current and Campbelling technique were plotted on the left of Fig. 8 both demonstrating very good linearity.

Conclusions

In this paper we report results of out-of-core thermal neutron flux measurement on pulsed nuclear reactor IBR2M using the counting, the current and Campbelling techniques. Counting mode was used to make direct link between the number of detected neutrons and the current flowing through the FC. Pulsed neutron source provided unique possibility to achieve a variable neutron flux density in the same data set. The neutron induced signals result in pulses with much greater charges than pulses from gammas, the mean square signal will weigh the neutron component by the square of the ratio of neutron signal neutron- to gamma ray induced signal [2]. In our work we find this ratio not less than 7000 from rough estimate of experimental data.

References

1. N.R. Campbell, V.J. Francis, "Theory of Valve and Circuit Noise, JIEE, Vol. **93**. Part III, 1946; DOI:10/1049/ji-3-2.1946.0009.

2. G.F. Knoll, *Radiation detection and measurements*, (Wiley, New York, 2000), p. 522, Chapter 14, IV, Reactor Instrumentation).

3. L. Svetov, O. Sidorova, Sh. Zeinalov. *In proc. of XXIV International Seminar on Interaction of Neutrons with Nuclei*, Dubna, May 24-27, 2016, JINR E3-2017-8, p. 430.